8-1-2014

CFD Simulation of the Thermal Performance of a Parallel Counter-Parallel Flow Heat Exchanger for the Treatment of Hypothermia

Alex Heller
University of Nevada, Las Vegas, helleralex2@gmail.com

CFD SIMULATION OF THE THERMAL PERFORMANCE OF A PARALLEL COUNTER-PARALLEL FLOW HEAT EXCHANGER FOR THE TREATMENT OF HYPOTHERMIA

By

Alex Junzo Heller

Bachelor of Science in Mechanical Engineering
University of Nevada Reno
2009

A thesis submitted in partial fulfillment
of the requirements for the

Master of Science - Biomedical Engineering

Department of Mechanical Engineering
Howard R. Hughes College of Engineering
The Graduate College

University of Nevada, Las Vegas
August 2014

UNIVERSITY OF NEVADA LAS VEGAS

THE GRADUATE COLLEGE

We recommend the thesis prepared under our supervision by

Alex Junzo Heller

entitled

CFD Simulation of the Thermal Performance of a Parallel Counter-Parallel Flow Heat Exchanger for the Treatment of Hypothermia

is approved in partial fulfillment of the requirements for the degree of

Master of Science in Biomedical Engineering

Department of Mechanical Engineering

Samir Moujaes, Ph.D., Committee Co-Chair

Hui Zhao, Ph.D., Committee Co-Chair

Alexander Barzilov, Ph.D., Committee Member

Moses Karakouzian, Ph.D., Graduate College Representative

Kathryn Hausbeck Korgan, Ph.D., Interim Dean of the Graduate College

August 2014

ABSTRACT

CFD Simulation of the Thermal Performance of a Parallel Counter-Parallel Flow Heat Exchanger for the Treatment of Hypothermia

By

Alex J. Heller

Samir F. Moujaes, Ph.D.,P.E., Examination Committee Chair
Professor, Department of Mechanical Engineering
University of Nevada, Las Vegas

Hypothermia is a life-threatening condition. Currently, active warming methods are the most effective treatment for dysthermic patients. The aim of this study is to investigate the use of computational fluid dynamics (CFD) in evaluating the thermal performance of a parallel/counter-parallel flow heat exchanger used as part of a fluid warmer to treat Hypothermia. The 3D model of the heat exchanger is divided into three regions; Infusate (fluid to be heated), Hot Water (heating fluid), and a Solid Region (wall). At the end of the heat exchanger, an elbow section is used to create the counter-parallel flow arrangement specific to this design.

The primary focus of this study involves evaluating heat transfer between the Infusate and Hot Water regions. Several simulations were performed for varying heat exchanger lengths (0.6, 1.2, 1.8, and 2.4m). The current CFD predicted values were compared to previously collected experimental data. In the experimental set-up, the outlet temperature was evaluated using a center-point temperature probe. The current CFD study evaluated the outlets in terms of mean bulk temperature to better characterize the thermodynamic average with respect to fluid flow. Despite this difference, the CFD results of the Infusate outlet temperatures were within 20% of the previously published experimental values. Using a center-point temperature probe, the CFD simulations were within 8% of the experimental values. It was concluded that the CFD

model accurately represented the thermodynamic characteristics of the heat exchanger and can be used for future design purposes.

The Hot Water region features a unique geometric variation on the traditional concentric annulus; a separation along the mid-plane confines the flow to have the area of a true concentric annulus. As such, CFD was used to investigate the thermalhydraulic effects within the Hot Water region (semi-annulus). Correlations were developed to predict the hydrodynamic and thermal developing lengths within the Hot Water region. These correlations were determined for developing flow at the inlet and after the elbow sections of the Hot Water region. CFD simulations of the Hot Water region demonstrated increasing hydrodynamic and thermal developing lengths for increasing Reynolds Number under laminar and turbulent flow. Increased mass flow rates produce increased forces within the flow area, requiring increased axial length for thermal and hydrodynamic profiles to stabilize.

Developing effects within a concentric annulus has been addressed in the literature; however the flow characteristics within the proposed semi-annulus are not as well understood. A comparative study was performed evaluating the studied Hot Water semi-annulus against a true concentric annulus. The CFD developed hydrodynamic entrance length correlation for the Hot Water region (semi-annulus) under laminar flow was compared to a known entrance length correlation for a true concentric annulus. Due to the separation along the mid-plane of the Hot Water region, the flow area and wetted perimeter of a true concentric annulus is expected to be greater than that of the semi-annular geometry. Greater flow interaction with the wall in the semi-annulus increases the viscous drag on the fluid, resulting generally in a lower non-dimensionalized developing length as a function of Reynolds Number.

Pressure drop within the Hot Water region was also evaluated and compared to known properties of a true concentric annulus within the fully developed region. Under both laminar

and turbulent flow, the studied semi-annulus of the Hot Water region demonstrated greater pressure drop than a true concentric annulus with similar dimensions and flow conditions. The elbow section of the Hot Water region produced a significant pressure drop, which may be due to the abrupt change in flow direction resulting in increased centrifugal forces and recirculation zones.

The thermal and hydrodynamic properties revealed in the CFD simulations can be used to improve future design considerations, which may lead to improved Hypothermia treatment protocols and patient care.

ACKNOWLEDGMENTS

I would like to express my sincere gratitude to Dr. Samir Moujaes, my advisor, for his invaluable help throughout this process - of which I would not have finished without his guidance and expertise. I would also like to thank those on my committee Dr. Alexander Barzilov, Dr. Hui Zhao, and Dr. Moses karakouzian – who have helped make this thesis possible. I would also like to make special mention of Joan Conway, who was always happy to answer my never ending questions and kept me organized.

To my mother, Rae Heller, who has always been proud of me and encouraged me to pursue my interests. I would be nothing without her. To my grandparents, Lillian and Kenneth Kusunoki, who have always supported and believed in me. To my brother, Daniel Heller, who is also a graduate engineering student, for helping me get through and understand the coursework. I would also like to thank my father, Peter Heller, for supporting me in my endeavors. Also, my better half – Lauren Hastings, who has put up with me through this stressful but rewarding experience. She helped me stay grounded and understand what is important. Finally, I would like to thank my family and friends for their support and encouragement.

TABLE OF CONTENTS

LIST OF TABLES

LIST OF FIGURES

CHAPTER 1

LITERATURE REVIEW

Trauma patients are especially susceptible to Hypothermia due to reduced metabolic activity, exposure to the environment, blood-volume loss, or disrobing/infusion of cold fluids during resuscitation. Currently, passive and active warming methods are used to treat Hypothermic patients. A 1990 paper by Gentilello et. al described a warming method which showed faster rewarming times than any other method previously evaluated. Continuous Arteriovenous Rewarming (CAVR), utilizes a fluid warmer which features a parallel/counter-parallel flow heat exchanger [13]. As part of this study, a thermodynamic model was developed to predict the progression of the patient's temperature over time. Figure 1.1 illustrates the schematic diagram of the thermodynamic system analyzed.

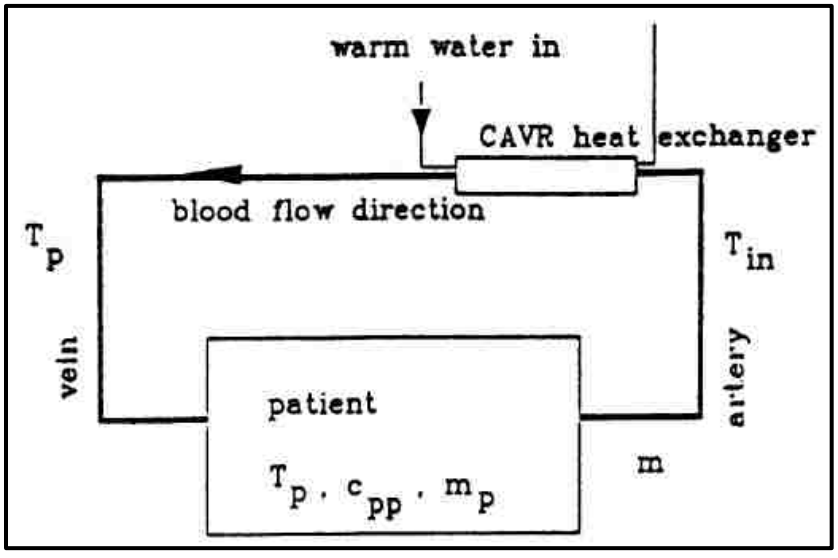

Figure 1.1 Schematic Diagram of Thermodynamic System Analyzed [13]

In a later study done by Moujaes and Oliver (1998), the previously described thermodynamic model was expanded to a 1D numerical simulation to further characterize the thermal properties of the heat exchanger design. A finite difference approach was used to solve a two-point boundary value problem. The numerical model was shown to predict outlet temperatures within 10% of the experimental values [27]. This thesis focuses on expanding upon this previous work to develop a 3D CFD model to predict the thermal properties of the heat exchanger, as it is felt that the experimental data provided in the previous study did not adequately represent the averaged thermodynamic temperatures at the fluid outlets. In the experimental study, a center-point temperature probe was used at the fluid outlets. In the current CFD study, mean bulk temperature was evaluated at the fluid outlets instead.

The Hot Water region (semi-annulus) of the proposed heat exchanger features a unique variation on the traditional concentric annulus geometry; a separation along the center-plane confines the flow area to half of that of a true concentric annulus. Understanding the fully developed regime within a given geometry is a critical metric in terms of design applications. Developing effects within a concentric annulus has been addressed in the literature; however the flow characteristics within the proposed semi-annulus are not as well understood. Lin et al. (2000) derived a correlation for the hydrodynamic entrance length of annular-ducts within the laminar regime [24]. However, this correlation is only applicable to annular-sector ducts within a range of apex angles. Previous studies by Heaton el al. [17] and Sparrow and Lin [37] utilized linearization methods to derive correlations for calculating entrance lengths within concentric annuli as a function of the inner and outer radii. Nouar et al. (1995) provides a review of different methods for evaluating the entrance effects within a concentric annulus [28]. In a more recent study, Poole (2010) in a numerical study discusses the developing region characteristics of a concentric annulus for a range of inner and outer radii ratios [30]. To

characterize the developing region of the Hot Water semi-annulus, a comparative study was performed with known properties of a concentric annulus.

CHAPTER 2

INTRODUCTION

Hypothermia is a life-threatening condition, whose effect can be more pronounced in certain patient populations, specifically trauma patients with comorbid hypothermia. Current treatment of hypothermia involves active and passive methods. Active warming methods have been shown to be the most effective, but require specialized equipment. Additionally, there are two forms of active warming methods; invasive and non-invasive. Invasive methods involve the administration of warmed fluids to patients either intravenously or intra-arterially. Non-invasive methods utilize warmed forced-air or circulating water blankets which are placed over patients to maintain normal body temperature. In this study the heat exchanger component of a fluid warmer (Invasive active warmer) was modeled and evaluated using CFD software. The proposed heat exchanger consists of two fluid regions; fluid to be warmed (Infusate) and the heating fluid (Hot Water). This model was used to evaluate heat transfer between the Infusate and Hot Water region, and also characterize the hydrodynamic properties within the Hot Water region.

2.1 Hypothermia

Normal human body temperature is defined as 37^{o}C. The human body has several methods of thermoregulation; sweating, vasoconstriction, vasodilation, metabolic rate, and shivering. Hypothermia occurs when heat lost to the environment surpasses the body's ability to generate heat. There are several degrees of Hypothermia [12]:

- Mild (36.5^{o}C – 32^{o}C)
- Moderate (32^{o}C – 28^{o}C)
- Severe (28^{o}C – 20^{o}C)
- Profound (<20^{o}C)

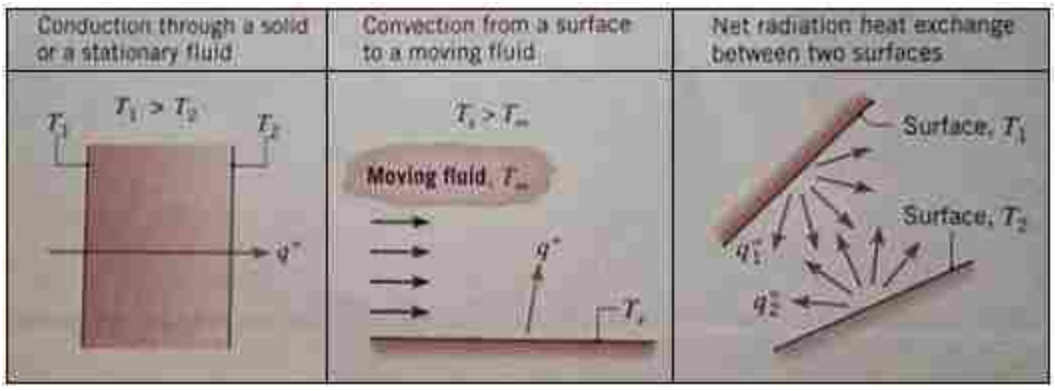

Figure 2.1 Conduction, Convection, and Radiation Heat Transfer Modes [18]

Maintenance of normthermia (normal body temperature) in humans is dependent on the body's ability to adapt to changing environmental conditions. There are three main types of heat transfer that impact human thermoregulation; conduction, convection, and radiation. Conduction refers to heat transfer across a temperature gradient through a solid medium. In humans, conduction typically accounts for 15% of total body heat loss [21]. Convection heat transfer refers to the thermal interaction of a solid surface with a moving fluid (gas or liquid) [20]. With respect to human thermoregulation, convection involves heat loss or gain through the interaction of moving fluids over the skin. Thermal radiation refers to emission of heat energy as electromagnetic waves. Radiation is a major form of heat transfer in humans, accounting for as much as 55 – 65% of total body heat loss [6]. Although radiation can account for a majority of total body heat loss, this can easily be mitigated by decreasing skin exposure to the environment. Figure 2.1 depicts the three main mechanisms of heat transfer (conduction, convection, and radiation) [18].

Hypothermia is a serious medical condition that impacts several physiological processes and is often associated with other conditions. Trauma patients are especially susceptible to comorbid hypothermia. Several factors may predispose trauma patients to comorbid

hypothermia; blood loss, environmental exposure, age, central nervous system injury, or cutaneous injuries (burns/open wounds) [12]. Studies have shown better outcomes for patients with either trauma or hypothermia alone, as opposed to patients with concurrent trauma and hypothermia [2-3,12,15,23,39]. Currently, the most effective treatments for dysthermic patients involve active convective heating/cooling devices [2,12,15,23,33-34,39]. Specifically, invasive methods such as the arteriovenous fluid warmer have demonstrated faster rewarming times when compared to non-invasive methods [13].

2.2 Treatment of Hypothermia

Current treatment for hypothermia focuses on balancing the effects of heat loss with the body's natural ability to thermoregulate. Thermoregulation is tightly regulated through sweating, shivering, vasoconstriction, and vasodilation. Under cold ambient temperatures, blood vessels constrict directing blood to the core to conserve heat. Conversely, under hot ambient conditions, blood vessels dilate directing blood to the periphery to aid in heat dissipation [7]. Under normal physiological conditions, core temperature fluctuations of a few tenths of a degree Celsius triggers thermoregulatory responses (shivering or sweating) [29]. However, when the human thermoregulatory system is compromised (trauma, blood loss, or extreme ambient conditions) the body is unable to compensate and temperature fluctuations may be more severe.

Treatment for hypothermia involves passive and active efforts. Passive methods involve removing wet clothing, increasing ambient room temperature, placing blankets on the patient, and minimizing air flow over the patient. Active rewarming methods can be further classified as invasive and non-invasive. Non-invasive active rewarming methods include forced-air warming blankets, heat lamps, or circulating water blankets. Invasive active rewarming methods involve

the use of fluid warmers which warm fluids for intravenous or intraarterial administration to the patient [25].

2.2.1 Active Rewarming Methods

Current Hypothermia protocols involve the use of active rewarming medical devices. As previously mentioned, these methods can further be classified as invasive and non-invasive. Though active rewarming methods have been shown to be more effective at maintaining normothermia, a combination of passive and active efforts are utilized in the treatment of hypothermic patients. Currently there are several commercially available body temperature regulation systems. Common non-invasive active rewarming devices currently used include the Bair Hugger (by 3M) and Blanketrol II (by Cincinnati Sub Zero). Figure 2.2 depicts the forced air warming device by 3M. This type of active rewarming method uses heated air which continuously cycles through the inflatable blanket which is placed over the patient. The blanket contains perforations on the patient side which allows the warm air to flow over the patient. Additionally, the air inside the inflated blanket acts as an insulation layer to minimize heat loss from the patient [1]. Figure 2.3 depicts the circulating water blanket produced by Cincinnati Sub Zero. This body temperature regulation system comprises a type of vapor compression cycle to heat/cool a fluid which is circulated throughout the blanket and then returned to the device for re-heating/cooling. This unit consists of programmable manual, automatic, or gradient controls which minimize the temperature fluctuations in the circulating water. In the gradient or automatic setting, the unit is able to input current patient core temperature within a feedback loop, adjusting the water temperature accordingly [9].

Figure 2.2 3M Forced Air Warming Device for the Treatment of Hypothermia [1]

Figure 2.3 Cincinatti Sub Zero Circulating Water Blanket for the Treatment of Hypothermia [9]

Invasive active rewarming method involve intravenous or intraarterial administration of warmed fluids. A common commercially available fluid warmer used for the treatment of Hypothermia is the Level 1 by Smiths Medical. Figure 2.4 depicts the Level 1 produced by Smiths Medical. This unit features a countercurrent heat exchanger which warms fluids or blood up to body temperature to be administered to patients. The current model uses an Aluminum heat

exchanger, which has significantly higher thermal conductivity than traditional medical grade plastics [36]. The Aluminum heat exchanger allows for rapid heating of fluids, which is crucial for patients with significant blood loss or severe Hypothermia.

Figure 2.4 Smiths Medical Level 1 used for the Treatment of Hypothermia [36]

CHAPTER 3

CFD BACKGROUND

3.1 CFD Modeling

Computational Fluid Dynamics (CFD) utilizes existing physics principles of fluid mechanics and heat/mass transfer with the computational approach of numerical methods. Generally, there are three approaches to solving fluid flow problems; Analytical, Experimental, and Numerical. The analytical approach has the advantage of providing exact solutions to flow problems, however due to the complexity of fluid mechanics analytical solutions are only possible for a limited range of problems. The experimental method involves building physical models of the problem to be tested within a lab setting. Experimental methods provide accurate solutions to the defined problems, but are usually costly and can be time consuming to refine the set-up to the desired conditions. The Numerical approach or CFD method involves using computational methods to determine a relatively accurate approximation to a set of partial differential equations. The advantage of the CFD method includes; universality, flexibility, accuracy, and cost [40]. The obvious disadvantage to the CFD approach is that an exact solution is not obtained. However, CFD can be used to determine a reasonable approximation which can be used to refine a design or determine initial boundary conditions before beginning costly experimental analysis.

3.2 STAR-CCM+

STAR-CCM+ is a commercially available comprehensive CFD package created by CD-Adapco. This software allows the user to complete all of aspects of CFD modeling in one integrated package. *STAR-CCM+* encompasses the following features; 3D modeling, Surface Preparation, Mesh Generation, Physics Modeling, Turbulence Modeling, and Post-Processing.

STAR-CCM+ is based on the finite volume method, and is capable of solving a wide range of physics problems [38].

3.3 General Workflow of CFD Analysis

Figure 3.1 outlines the general workflow of a CFD analysis from start to finish. The first step of any CFD analysis is to model the geometry to be analyzed (2D or 3D). This is also the appropriate time to repair the surface of any holes or overlapping faces. Once the geometry is generated, the user is able to define the surface topology (walls, inlets, outlets, or interfaces). The mesh generation is the next step in the overall workflow. This is a critical step, as the rest of the process is dependent on the quality of the mesh generated. The first step in generating the mesh is to choose the desired meshing models. *STAR-CCM+* has two surface mesher models to improve the quality of the surface mesh (surface remesher, surface wrapper). Re-meshing the surface is particularly important when the geometry is imported from outside CAD software. *STAR-CCM+* also has several volume mesh models to choose from; Polyhedral, Tetrahedral, Trimmer, Prism Layer, Thin Mesher, Generalized Cylinder, and Extruder. Next the physics models need to be defined. This is entirely dependent on the type of solution desired. *STAR-CCM+* includes several physics models to choose from; single/multi-phase fluid flow, turbulence, heat transfer, compressibility, combustion reactions, and many others [38]. This is also the time to define the initial and boundary conditions. After the physics models have been chosen, monitors or plots need to be defined based on the needs of the user. This also includes desired stopping criteria. The solution is now ready to run. After the solution has converged, the results can be analyzed and graphed according to the users preferences.

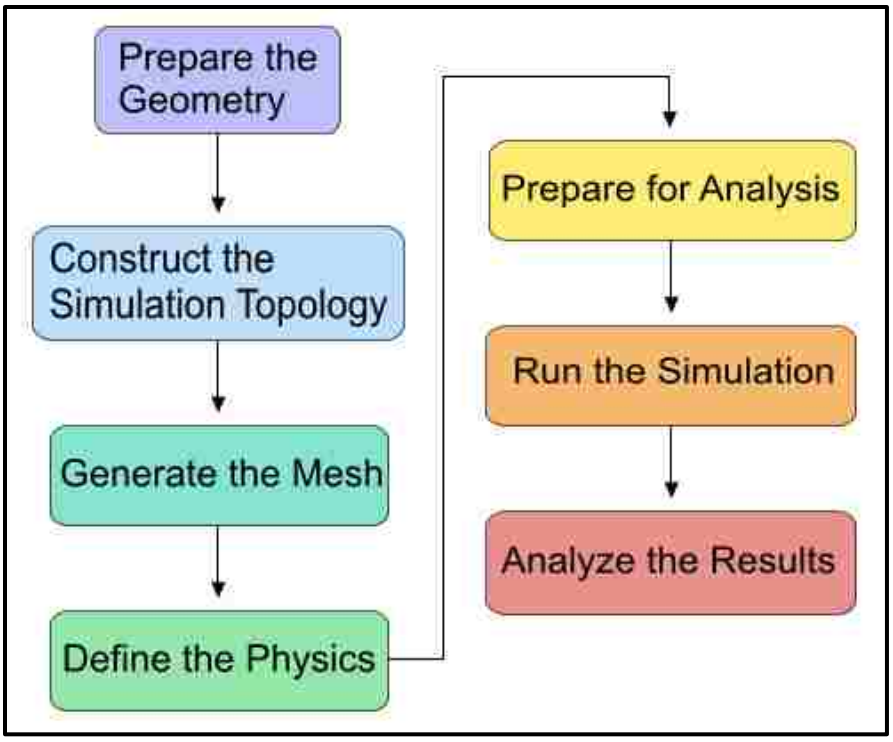

Figure 3.1 General Workflow of CFD Analysis [38]

3.4 Mathematical Models

The system of governing equations to describe the flow consists of the continuity, conservation of momentum, and the conservation of energy system of equations. Additionally, the Hot Water region was modeled as turbulent flow. The k-ε turbulent model was chosen for the Hot Water region.

The Continuity Equation:

The continuity equation describes the conservation of mass and is expressed in cylindrical coordinates as follows [20]:

$$\frac{\partial \rho}{\partial t} + \frac{1}{r}\frac{\partial}{\partial r}(\rho r v_r) + \frac{1}{r}\frac{\partial}{\partial \theta}(\rho v_\theta) + \frac{\partial}{\partial z}(\rho v_z) = 0 \qquad [1]$$

Where:

v_r, v_θ, v_z = Velocity components in the r, θ, z directions (Figure 3.2)

ρ = Fluid density

t = Time

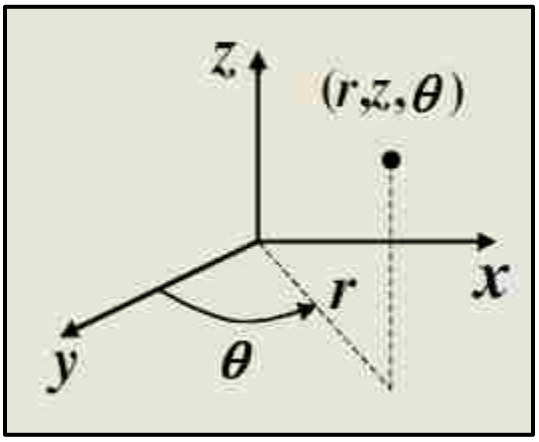

Figure 3.2 Cylindrical Coordinate System [20]

For incompressible flow the continuity equation reduces to [20]:

$$\frac{1}{r}\frac{\partial}{\partial r}(rv_r) + \frac{1}{r}\frac{\partial v_\theta}{\partial \theta} + \frac{\partial v_z}{\partial z} = 0 \qquad [2]$$

Conservation of Momentum Equations:

The conservation of momentum equations, also known as the Navier-Stokes equations, follows Newton's second law of motion: the rate change of momentum of a body is equal to the net force acting on it [40]. There are two types of forces acting on a finite volume element; body forces and surface forces. Body forces act directly on the fluid from an outside source. Examples of body forces include gravity, electro-magnetic, or Lorentz forces. Surface forces include pressure or frictional forces which act between adjacent fluid elements or between fluid elements and a wall [40]. The three Navier-Stokes equations in cylindrical coordinates, assuming constant density, Newtonian fluid, and constant viscosity are expressed as follows [20]:

$$\rho\left(v_r\frac{\partial v_r}{\partial r}+\frac{v_\theta}{r}\frac{\partial v_r}{\partial \theta}-\frac{{v_\theta}^2}{r}+v_z\frac{\partial v_r}{\partial z}+\frac{\partial v_r}{\partial t}\right)=\rho g_r-\frac{\partial p}{\partial r}+\mu\left[\frac{\partial}{\partial r}\left(\frac{1}{r}\frac{\partial}{\partial r}(rv_r)\right)+\frac{1}{r^2}\frac{\partial^2 v_r}{\partial \theta^2}-\frac{2}{r^2}\frac{\partial v_\theta}{\partial \theta}+\frac{\partial^2 v_r}{\partial z^2}\right] \quad [3]$$

$$\rho\left(v_r\frac{\partial v_\theta}{\partial r}+\frac{v_\theta}{r}\frac{\partial v_\theta}{\partial \theta}+\frac{v_r v_\theta}{r}+v_z\frac{\partial v_\theta}{\partial z}+\frac{\partial v_\theta}{\partial t}\right)=\rho g_\theta-\frac{1}{r}\frac{\partial p}{\partial \theta}+\mu\left[\frac{\partial}{\partial r}\left(\frac{1}{r}\frac{\partial}{\partial r}(rv_\theta)\right)+\frac{1}{r^2}\frac{\partial^2 v_\theta}{\partial \theta^2}-\frac{2}{r^2}\frac{\partial v_r}{\partial \theta}+\frac{\partial^2 v_\theta}{\partial z^2}\right] \quad [4]$$

$$\rho\left(v_r\frac{\partial v_z}{\partial r}+\frac{v_\theta}{r}\frac{\partial v_z}{\partial \theta}+v_z\frac{\partial v_z}{\partial z}+\frac{\partial v_z}{\partial t}\right)=\rho g_z-\frac{\partial p}{\partial z}+\mu\left[\frac{1}{r}\frac{\partial}{\partial r}\left(r\frac{\partial v_z}{\partial r}\right)+\frac{1}{r^2}\frac{\partial^2 v_z}{\partial \theta^2}+\frac{\partial^2 v_z}{\partial z^2}\right] \quad [5]$$

Where:

g_r, g_θ, g_z = Body Forces (component direction)
μ = Fluid Viscosity
P = Hydrostatic Pressure
v_r, v_θ, v_z = Velocity components in the r, θ, z directions
ρ = Fluid density
t = Time

Conservation of Energy Equation:

The principle for the Conservation of Energy equation is based on the first law of Thermodynamics: Energy can neither be created nor destroyed. Neglecting nuclear, electromagnetic, or radiation energy transfer the conservation of energy equation can be expressed as [20]:

$$\rho c_p\frac{DT}{Dt}=\nabla\cdot k\nabla T+\beta T\frac{Dp}{Dt}+\mu\Phi \quad [6]$$

Where:

c_p = Specific heat at constant pressure
k = Thermal Conductivity
p = Pressure
β = Coefficient of thermal expansion
Φ = Dissipation function

The coefficient of thermal expansion can be expressed as [20]:

$$\beta=-\frac{1}{\rho}\left[\frac{\partial\rho}{\partial T}\right]_p \quad [7]$$

The dissipation function accounts for energy loss due to friction, which is essential when modeling high velocity flow or fluids with high viscosity properties. The dissipation function can be expressed in cylindrical coordinates for an incompressible fluid as [20]:

$$\Phi = 2\left(\frac{\partial v_r}{\partial r}\right)^2 + 2\left(\frac{1}{r}\frac{\partial v_\theta}{\partial \theta}\right)^2 + 2\left(\frac{\partial v_z}{\partial z}\right)^2 + \left(\frac{\partial v_\theta}{\partial r} - \frac{v_\theta}{r} + \frac{1}{r}\frac{\partial v_r}{\partial \theta}\right)^2 + \left(\frac{1}{r}\frac{\partial v_z}{\partial \theta} + \frac{\partial v_\theta}{\partial z}\right)^2 + \left(\frac{\partial v_r}{\partial z} + \frac{\partial v_z}{\partial r}\right)^2 \quad [8]$$

Turbulence Modeling:

For the turbulent regime in the Hot Water region, a Reynolds-Averaged Navier-Stokes (RANS) model was used. The RANS model is the oldest method of turbulence modeling still utilized in CFD analysis. The advantages of the RANS model include simplicity, low computational cost (relative to more complicated models), and a broad selection of models to choose from. The RANS equation can be written as [40]:

$$\rho\frac{\partial\langle u_i\rangle}{\partial t} + \rho\frac{\partial}{\partial x_j}\left(\langle u_i\rangle\langle u_j\rangle\right) = -\frac{\partial\langle p\rangle}{\partial x_i} + \mu\nabla^2\langle u_i\rangle - \frac{\partial\tau_{ij}}{\partial x_j},\ \frac{\partial\langle u_i\rangle}{\partial x_i} = 0 \quad [9]$$

Where:

τ_{ij} = Reynolds stress tensor

k-ε (Two-Equation model):

One commonly used method in the RANS family is the two-equation model. In the two equation model, the velocity and length scale of turbulence are determined via the addition of two partial differential equations [40]. Since the velocity and length scales are evaluated as functions of space and time with respect to the local flow field, this model is generally applicable to any flow configuration. For this study the most common two-equation model (k-epsilon) was utilized. The two variables being modeled in the k-ε model are k (turbulent kinetic energy) and ε (rate of viscous dissipation). The respective transport equations for the k-ε model are written as follows [40]:

For k,

$$\rho\frac{\partial k}{\partial t} + \rho\langle u_j\rangle\frac{\partial k}{\partial x_j} = \underset{1}{-\tau_{ij}\frac{\partial\langle u_i\rangle}{\partial x_j}} \underset{2}{-\rho\varepsilon} + \underset{3}{\frac{\partial}{\partial x_j}\left[\mu\frac{\partial k}{\partial x_j}\right]} - \underset{4}{\frac{\partial}{\partial x_j}\left[\frac{\rho}{2}\langle u_i' u_i' u_j'\rangle + \langle p' u_j'\rangle\right]} \quad [10]$$

The first two terms form the material derivative of k, which describe the rate of change of k with respect to a fluid particle transported by the mean flow. The physical interpretation of the terms on the right side of the equation is [40]:

1. Rate of energy production
2. Effect of viscous dissipation
3. Molecular diffusion of k
4. Diffusion by turbulent motion

For ε,

$$\rho\frac{\partial\varepsilon}{\partial t}+\rho\langle u_j\rangle\frac{\partial\varepsilon}{\partial x_j}=C_{\varepsilon1}P_k\frac{\varepsilon}{k}-C_{\varepsilon2}\rho\frac{\varepsilon^2}{k}+\frac{\partial}{\partial x_j}\left[\left(\mu+\frac{\mu_t}{\sigma_\varepsilon}\right)\frac{\partial\varepsilon}{\partial x_j}\right] \quad [11]$$

Where P_k is the turbulent kinetic energy production determined by:

$$P_k\equiv-\tau_{ij}\frac{\partial\langle u_i\rangle}{\partial x_j}=-\rho\langle u_i'u_j'\rangle\frac{\partial\langle u_i\rangle}{\partial x_j}=2\mu_t\langle S_{ij}\rangle\frac{\partial\langle u_i\rangle}{\partial x_j} \quad [12]$$

Five model constants are necessary to solve the system of partial differential equations. These five constants may differ slightly based on given flow conditions, however the most common values used are given in Table 3.1.

Table 3.1 Closure Coefficients for k-ε Model [40]

k-epsilon Model	
Coefficient	**Value**
C_μ	0.09
$C_{\varepsilon1}$	1.44
$C_{\varepsilon2}$	1.92
σ_ε	1.3
σ_k	1.0

STAR-CCM+ Turbulence Modeling:

STAR-CCM+ has four major classes of turbulence models to select from; Spalart-Allmaras models, k-epsilon, k-omega, and Reynolds stress transport models. The Spalart-Allmaras model is usually used for flow conditions in which the boundary layer is mostly attached, and it typically used for aerospace applications. Reynolds stress transport model is the most complex, and as such the most computationally heavy model. This type of model is typically reserved for applications in which the turbulence is strongly anisotropic. The k-epsilon and k-omega models are similar in that two-transport equations are solved. The k-epsilon model is a good compromise between computational cost and accuracy [38]. The k-epsilon model was chosen for the applications of this study.

Realizable Two-Layer k-epsilon turbulent model:

This turbulent model combines the Realizable k-epsilon model with the two-layer approach. The Realizable k-epsilon model was developed by Shih et. al (1994) [32]. The transport equations and descriptions of the Realizable k-epsilon model are fully described in the *STAR-CCM+* user manual [38].

Two-Layer Turbulent Approach:

This turbulent model was first described by W. Rodi in 1991 [31]. The two-layer approach combines a one-equation model with the two-equation k-epsilon model. The one-equation model solves for turbulent kinetic energy (k), and uses the k-epsilon model to determine the rate of viscous dissipation (ε) algebraically with the distance from the wall. The description and formulation for the two-layer turbulent model is fully described in the *STAR-CCM+* user manual [38].

Realizable Two-Layer k-epsilon Turbulence Model:

This turbulence model combines the Realizable k-ε model with the two-layer approach. The advantage of using this approach is ability to use an all y+ wall treatment, which is able to approximate near-wall turbulence for a variety of mesh densities. This turbulence model was chosen to model the turbulent flow within the Hot Water region.

Near-Wall Treatment Methods:

Near-wall modeling can impact the accuracy of numerical simulations, specifically in turbulent regimes as vorticity and turbulent fluctuations are strong near the wall [40]. There are several problems with the RANS model in regards to near wall turbulence. The mean flow velocity decreases as it approaches a no-slip boundary, as the mean velocity decreases so does the Reynolds number. At some point near the wall (with decreasing Reynolds number) the flow transitions from turbulent to laminar. Turbulent fluctuations continue to decrease as the wall is approached; the wall tends to prevent such fluctuations. This phenomenon is known as the viscous sub-layer [20]. The length scale computed by the RANS turbulence model decreases near the wall, which requires a reduction in the number of grid steps in the direction normal to the wall [40]. Another issue of the decreasing turbulent fluctuations near the wall is the inability of the RANS model to accurately model the turbulent stresses. Even with a high mesh density near the wall, the RANS model over-predicts the turbulent stress near the wall. This is further compounded by inaccurate predictions of near-wall momentum estimations leading to inaccurate modeling of the entire flow field. One method of resolving this issue is increasing the mesh density near the wall. However, this greatly increases the computational power needed. Additionally, the viscous sub-layer is so thin for high Reynolds numbers that it becomes

impractical to simply increase the mesh density near the wall to compensate. An alternate approach to model the turbulent fluctuations near the wall involves using wall functions [40].

When using wall functions, turbulence modeling is only applied up to a certain distance away from the wall. Near the wall, the solution is approximated using wall functions which are a set of mathematical relations that are used to obtain the boundary conditions near the wall for the continuum equations. There are several assumptions utilized when using wall functions [38]:

- Consistent set of assumptions regarding the velocity, turbulence, and other scalar quantity distributions.
- Assumption that the chosen turbulence model is only valid outside the viscous dominated region of the boundary layer.
- The centroid of the near-wall cell lies within the logarithmic region of the boundary layer.

The advantage to using wall functions is the increased accuracy of the solution near the wall and a significant computational savings due to the ability to use a coarser mesh density.

Wall Treatment STAR-CCM+:

STAR-CCM+ utilizes wall treatments as opposed to wall functions. The difference is that a wall treatment is a set of near-wall modeling assumptions, where as a wall function uses only one type of wall treatment. Depending on the flow conditions modeled, *STAR-CCM+* has three types of wall treatments [38]:

- High-y+ wall treatment: Applies wall-function approach, assumes that the near-wall cell lies within the logarithmic region of boundary layer.
- Low-y+ wall treatment: This treatment is only suitable for low-Reynolds number flows, and assumes the viscous sub-layer is properly resolved.

- All-y+ wall treatment: A hybrid of the high-y+ and low-y+ wall treatments. This treatment emulates the high-y+ treatment for coarse meshes and the low-y+ treatment for fine meshes. This method is also suitable for intermediate mesh densities.

Wall Law Formulations:

The wall law formulation to estimate near wall turbulence is fully described in the *STAR-CCM+* user guide [38].

CHAPTER 4

DESCRIPTION OF PROBLEM GEOMETRY

Figure 4.1 depicts the schematic diagram of a cross section of the proposed heat exchanger. The cross section shows two concentric rings connected by a thin wall which runs the length of the heat exchanger. Four different heat exchanger lengths were evaluated in this study; 0.6m, 1.2m, 1.8m, and 2.4m. The fluid to be warmed (Infusate) flows inside the center pipe (3.0mm diameter), which runs the length of the heat exchanger. The warmer fluid (Hot Water) flows along the outer annulus in both a parallel and counter-parallel flow arrangement. The entrance section of Hot Water region is parallel to the flow of the Infusate region. At the end of the heat exchanger, an elbow allows the Hot Water flow to return in a counter-parallel arrangement to the Infusate region. The elbow consists of a spherical cross section with a diameter of 9.5mm. Separating the Infusate and Hot Water fluid regions is a thin wall section or solid region. The Wall region is composed of a thermally conductive plastic material which allows heat transfer between the Infusate and Hot Water regions.

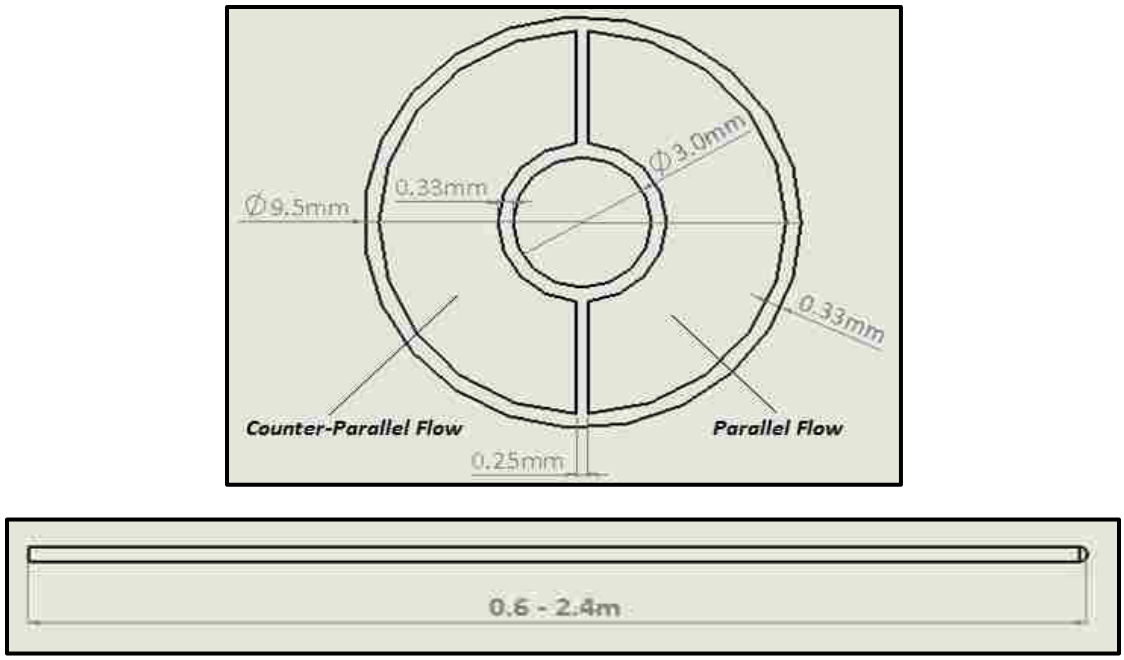

Figure 4.1 Schematic Diagram of Proposed Heat Exchanger (Length Varies 0.6 – 2.4m)

4.1 3D Modeling of the Geometry

The 3D geometry was generated using the modeling software *Solidworks*. Figure 4.2 depicts the flow orientation of the heat exchanger being evaluated. The Infusate region consists of a cylindrical pipe with a diameter of 3.0mm which runs the length of the heat exchanger. The Infusate region is heated by the warmer fluid (Hot Water region), which flows in a parallel and counter-parallel arrangement to the Infusate region. The parallel/counter-parallel flow arrangement is achieved through an elbow section at the end of the heat exchanger. Figure 4.3 illustrates the relation between the Infusate and Hot Water regions, as well as the configuration of the elbow section.

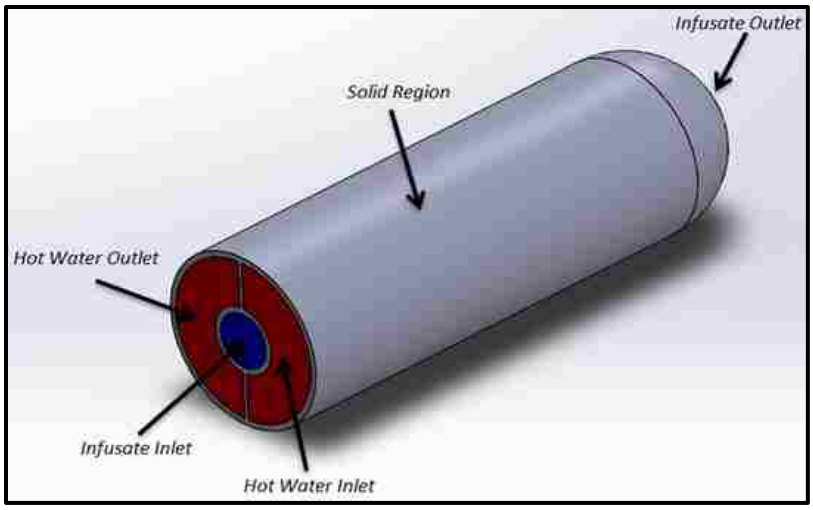

Figure 4.2 Flow Orientation of the Evaluated Heat Exchanger

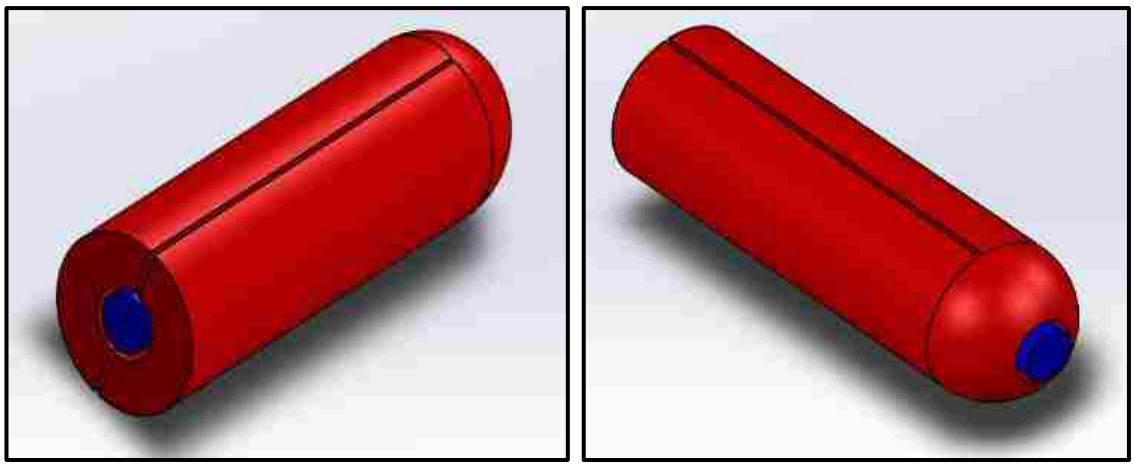

Figure 4.3 3D Model of Hot Water Region (Red) and Infusate Region (Blue)

CHAPTER 5

MESHING AND BOUNDARY CONDITIONS

5.1 Mesh Generation

The 3D geometry created in *SolidWorks* was imported into the commercial CFD software *STAR-CCM+* to complete the mesh generation and numerical solution.

5.1.1 Infusate Region Mesh

Mesh Selection:

Surface Mesh:

Mesh generation was completed using *STAR-CCM+* after importing the 3D geometry from *Solidworks*. The initial surface did not adequately capture the geometry of the Infusate region and required refinement. The model "Surface Remesher" was used to improve the surface quality of the imported geometry. Surface Remesher re-triangulates the imported geometry surface, making the surface more optimal when generating the volume mesh. Figure 5.1 shows the initial imported geometry mesh and the remeshed surface for the Infusate region. The remeshed surface is much finer, which more accurately captures the details of the imported geometry.

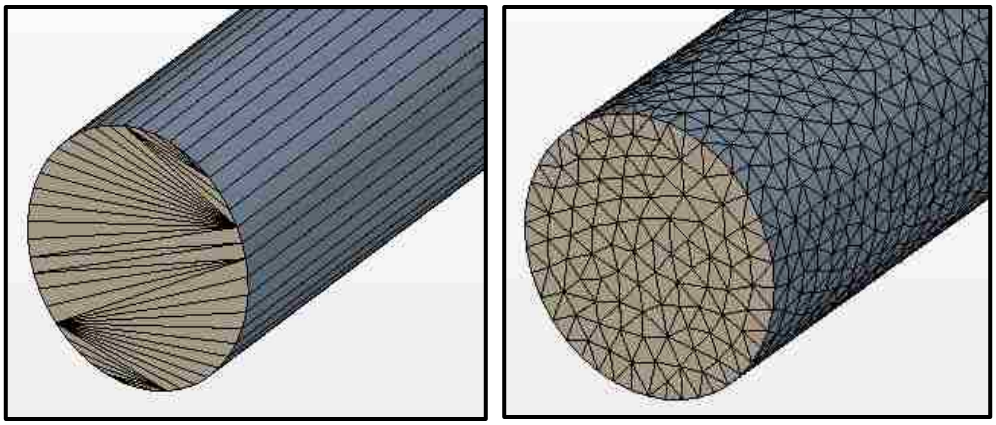

Figure 5.1 Initial Surface vs. Remeshed Surface of Infusate Region

Volume Mesh:

For the Infusate region of the geometry, three volume mesh models were chosen; prism layer, generalized cylinder, and polyhedral. The polyhedral model was chosen as the core volume mesher based on its general solution accuracy and ability to achieve equivalent accuracy to tetrahedral models using several times fewer cells. The prism layer module was chosen to improve the accuracy of the flow solution near the wall. This particular model is specifically important in determining the forces and heat transfer near the walls. The generalized cylinder model was chosen to help increase the efficiency of the solution. This type of model is best suited for geometries that are roughly cylindrical in shape, such as pipe flow. For pipe flow, the solution can be solved more efficiently if the mesh is oriented parallel to the fluid flow. Figure 5.2 depicts the generated volume mesh of the Infusate region, highlighting the different volume mesh models utilized.

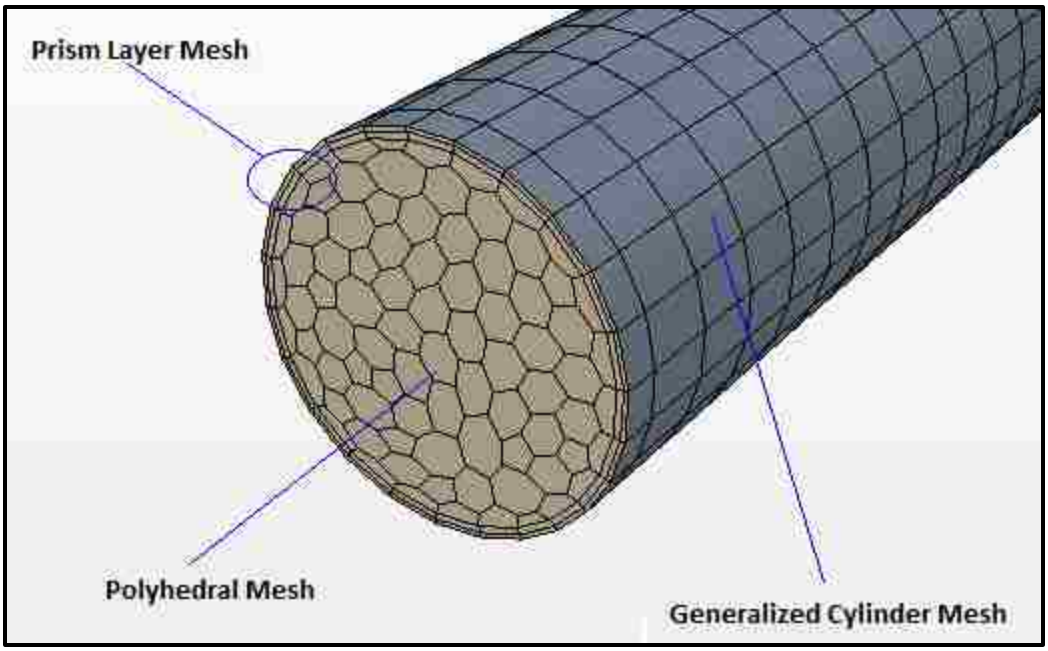

Figure 5.2 Generated Volume Mesh for Infusate Region

Grid Independency Infusate Region:

When performing a CFD analysis, it is crucial to the accuracy of the final solution that the grid independency criterion is satisfied. Grid independency occurs when the solution no longer varies with increased mesh density. The Infusate region was modeled as laminar flow in the CFD analysis, so a grid independency was performed to ensure solution accuracy while minimizing required computational power. Using a mesh density greater than what is discovered during the grid independency would likely only result in a negligible increase in solution accuracy. However, the computational requirements will be much greater and require more time to solve the system partial differential equations.

Due to the similar geometries of the different heat exchanger lengths, a grid independency was performed for the 0.6m geometry and the determined mesh conditions utilized for the remaining heat exchanger lengths. A volumetric flow rate of 15ml/min (Reynolds Number 81) was used for the grid independency of the Infusate region. A coarse mesh of about

80,000 cells and a fine mesh of about 1,000,000 cells were used for this analysis. Figure 5.3 depicts the generated volume meshes for the range of mesh densities tested (80,000 – 1,000,000 total cells). The axial velocity along the center-line of the Infusate region outlet was evaluated (Figure 5.4). Table 5.1 documents the mesh conditions used for each run of the grid independency.

Table 5.1 Mesh Conditions Used for Variation of Mesh Density (80,000 – 1,000,000 total cells)

	Run 1	Run 2	Run 3	Run 4
Total Cells	84,040	126,060	436,435	1,061,960
Base Size [mm]	1.50	0.35	0.15	0.10
Number Prism Layers	2	2	2	2
Prism Layer Thickness [mm]	0.375	0.09	0.0375	0.025
Target Surface Size [mm]	1.5	0.35	0.15	0.1

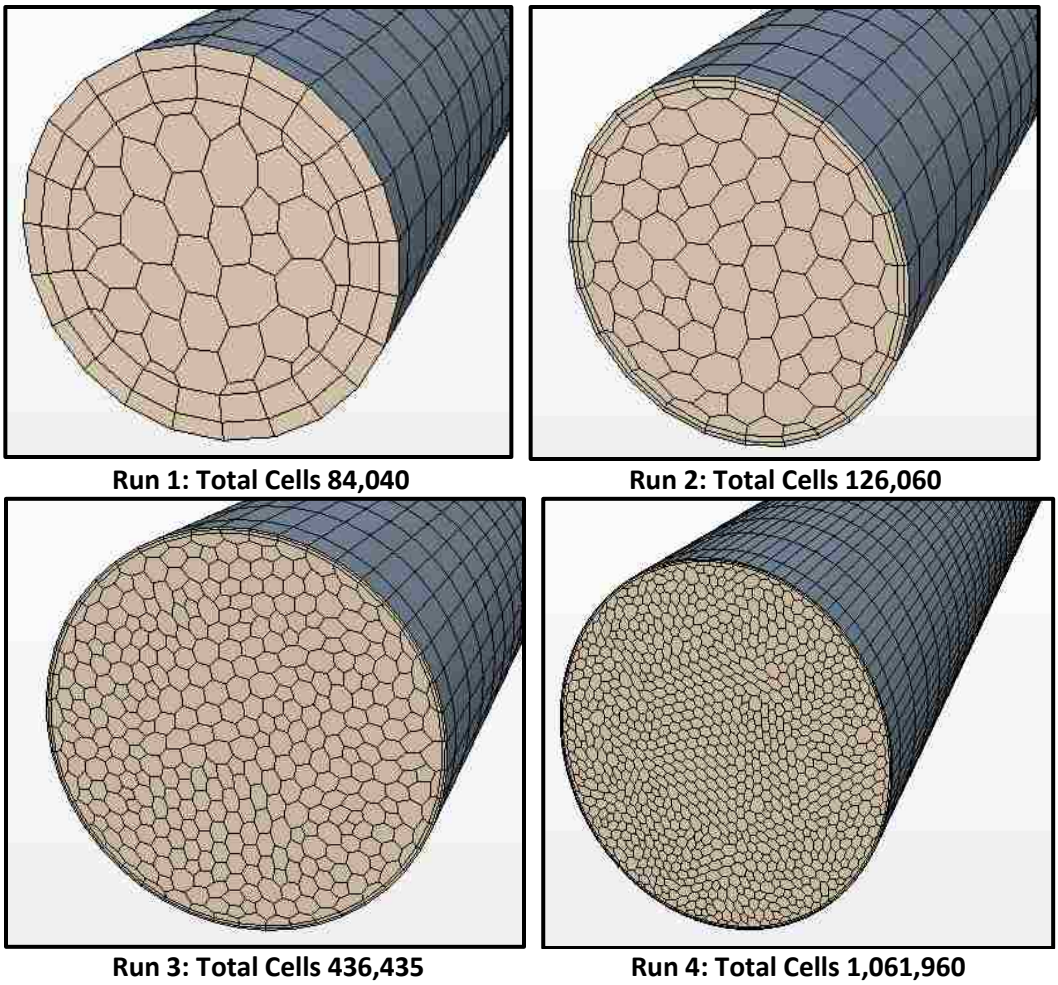

Figure 5.3 Generated Volume Mesh Densities Used in Grid Independency

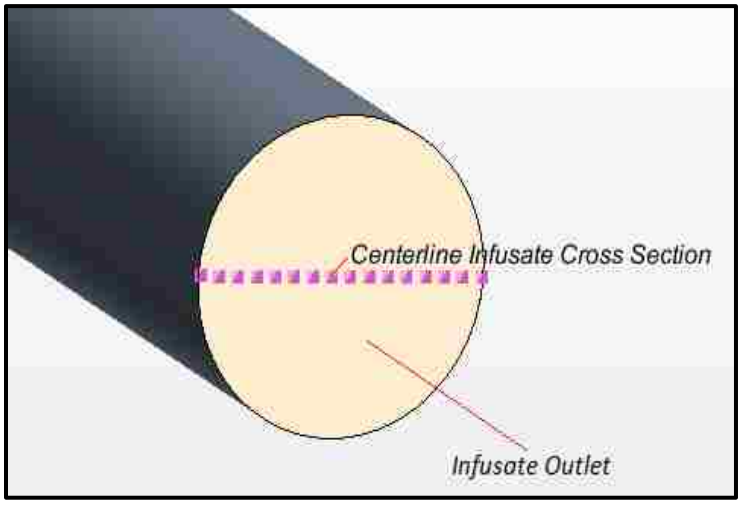

Figure 5.4 Cross Section Used for Axial Velocity Profile in the Grid Independency

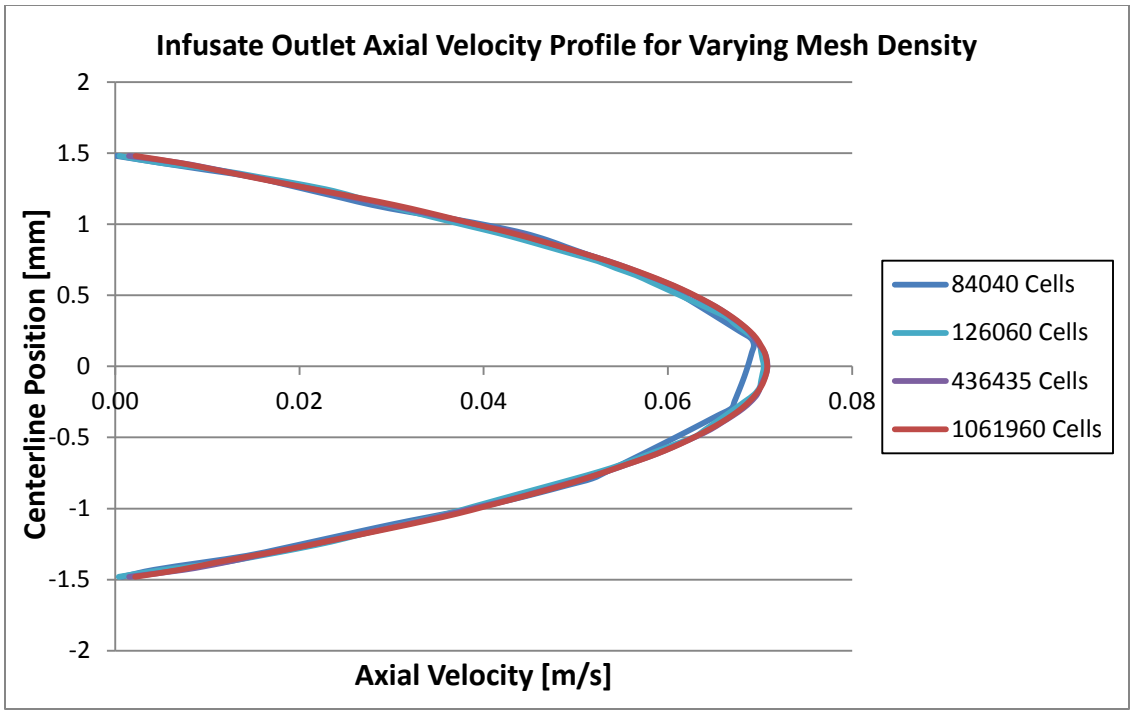

Figure 5.5 Comparison of Axial Velocity Profiles at Infusate Outlet for Increasing Mesh Density

Figure 5.5 depicts the axial velocity profile at the Infusate outlet for the increasing mesh densities evaluated in the grid independency. The average difference between the axial velocity for the 126K and 1,000,000 mesh densities is less than 2%. As such, the mesh density of 126K was determined to be acceptable for the purpose of this study. As the total number of cells increase, the required computational power and solution time increases proportionally. The chosen mesh conditions were determined to accurately capture the flow conditions while efficiently utilizing computational resources. As such, the mesh conditions for the 126K mesh density were utilized for the production runs (Refer to Table 5.1). These mesh conditions were used for the additional heat exchanger lengths evaluated, which resulted in an increase in total cells proportional to the increase in heat exchanger length.

5.1.2 Hot Water Region Mesh

Mesh Selection:

Surface Mesh:

The surface remesher model was also used for the Hot Water region to improve the overall surface quality of the imported geometry tessellation. Figure 5.6 depicts the initial surface and the remeshed surface for the Hot Water region.

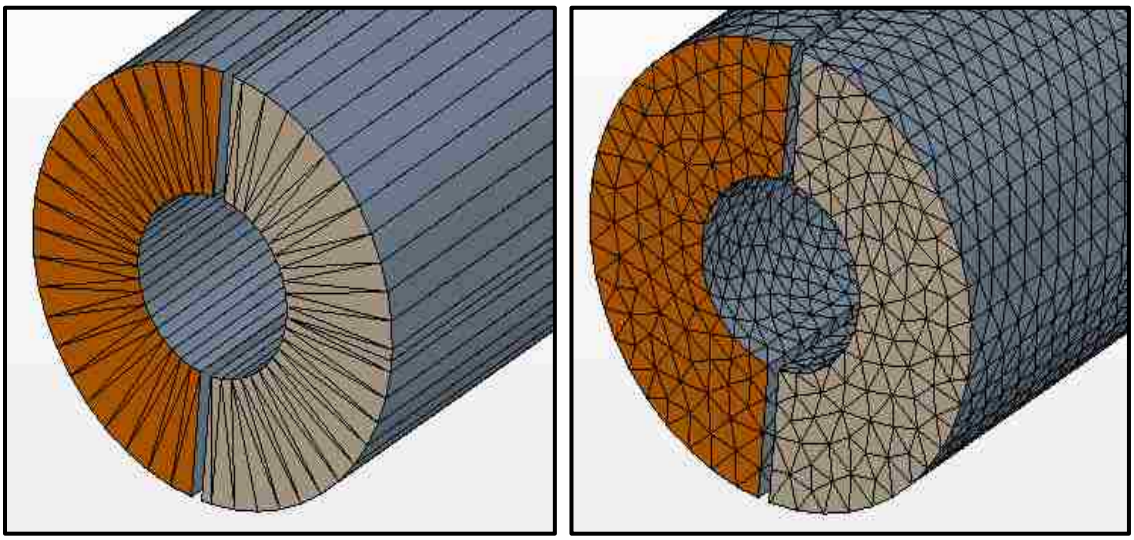

Figure 5.6 Initial Surface vs. Remeshed Surface of Hot Water Region

Volume Mesh:

For the Hot Water region, two volume mesh models were utilized; prism layer and polyhedral. As with the Infusate volume mesh, the polyhedral model was chosen as the core volume mesh model based on its general solution accuracy. The prism layer module was also chosen to improve the accuracy of the flow solution near the wall. The generalized cylinder mesh was not chosen due to the sharp turn in the elbow section, which made using this type of

volume mesh model impractical. Figure 5.7 depicts the generated volume mesh for the Hot Water region, highlighting the different volume mesh models utilized.

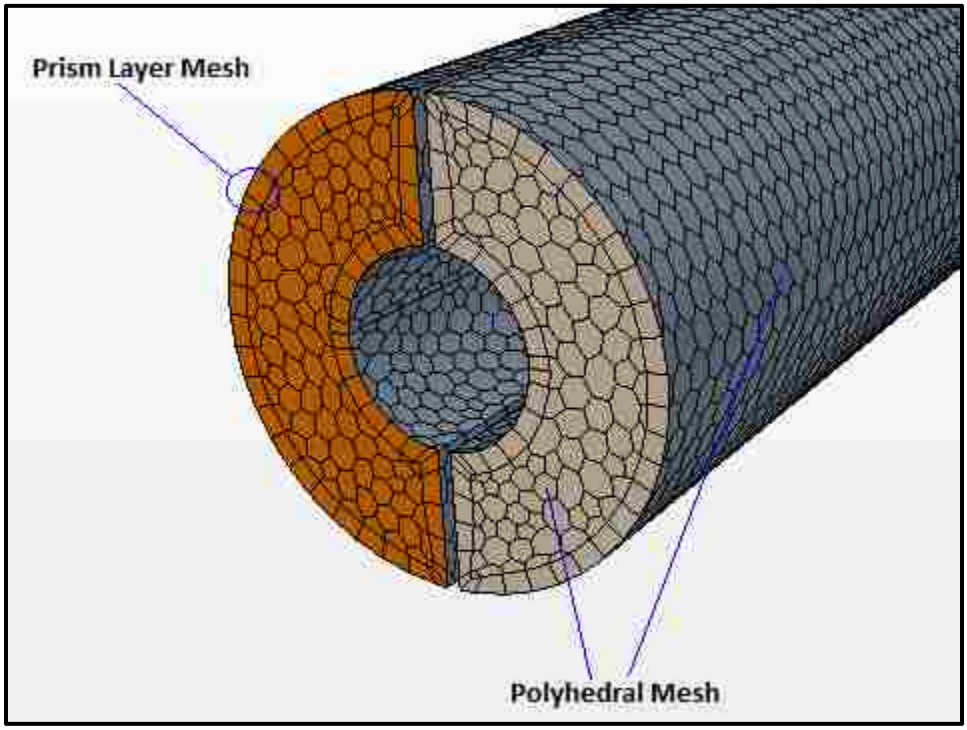

Figure 5.7 Generated Volume Mesh for Hot Water Region

Determining the Accuracy of the Hot Water Volume Mesh:

The Hot Water region was modeled as turbulent flow based on estimated Reynolds numbers. Specifically, a realizable two-layer K-epsilon turbulence model was chosen for the Hot Water region. The default wall treatment for this model is the all-y+ wall treatment. This is a hybrid wall treatment which provides the most flexibility in terms of mesh density. The all-y+ wall treatment emulates the high-y+ treatment for coarse meshes and the low-y+ treatment for fine meshes. This method is also suitable for intermediate mesh densities. For the best solution accuracy, *STAR-CCM+* recommends that the Wall Y+ values be in the range of 1 – 60 when using the all-y+ wall treatment [38]. Figures 5.8 – 5.11 depict the Wall Y+ distribution near the wall of

the Hot Water region for the evaluated heat exchanger lengths (0.6, 1.2, 1.8, and 2.4m). Table 5.2 documents the Hot Water region mesh conditions for the different heat exchanger lengths evaluated. The Wall Y+ values were within the *STAR-CCM+* recommended range, and the chosen mesh conditions were determined to be acceptable for the production runs.

Table 5.2 Hot Water Region Mesh Conditions for Evaluated Heat Exchanger Lengths

	0.6m HE	1.2m HE	1.8m HE	2.4m HE
Total Cells	239,540	466,613	764,740	954,623
Base Size [mm]	0.60	0.60	0.60	0.60
Number Prism Layers	1	1	1	1
Prism Layer Thickness [mm]	0.39	0.6	0.75	1.05
Surface Size Range [mm]	0.24 - 0.75	0.2 - 0.8	0.2 - 0.8	0.2 - 0.8

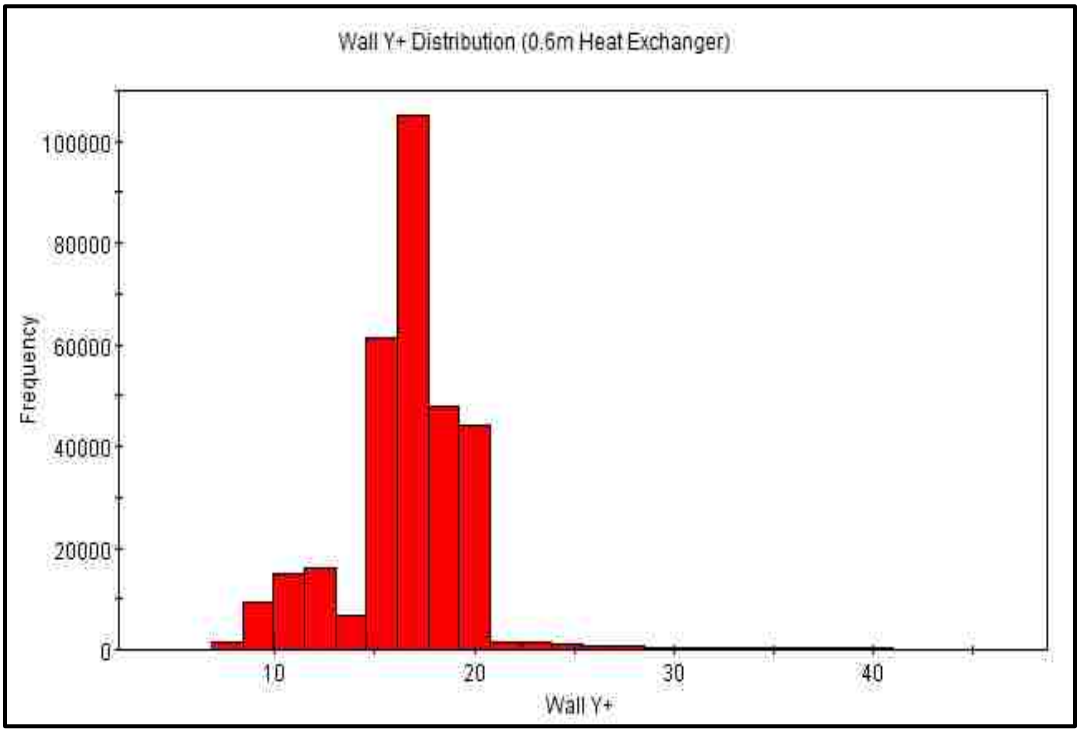

Figure 5.8 Wall Y+ Distribution of Hot Water Region (0.6m Heat Exchanger)

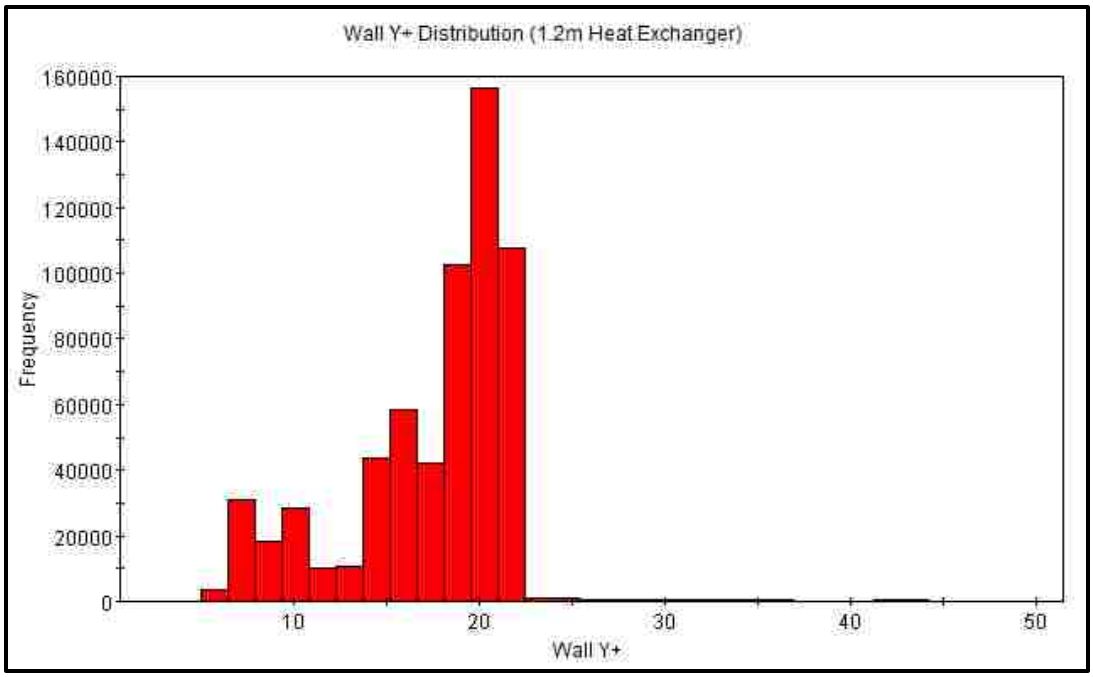

Figure 5.9 Wall Y+ Distribution of Hot Water Region (1.2m Heat Exchanger)

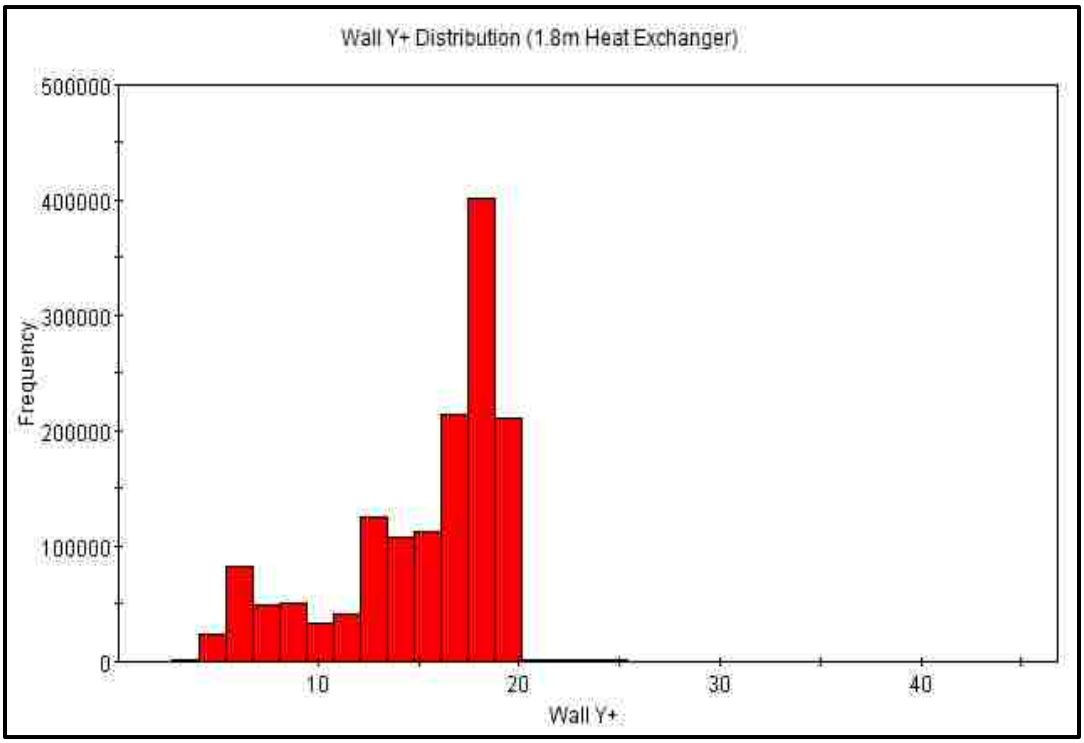

Figure 5.10 Wall Y+ Distribution of Hot Water Region (1.8m Heat Exchanger)

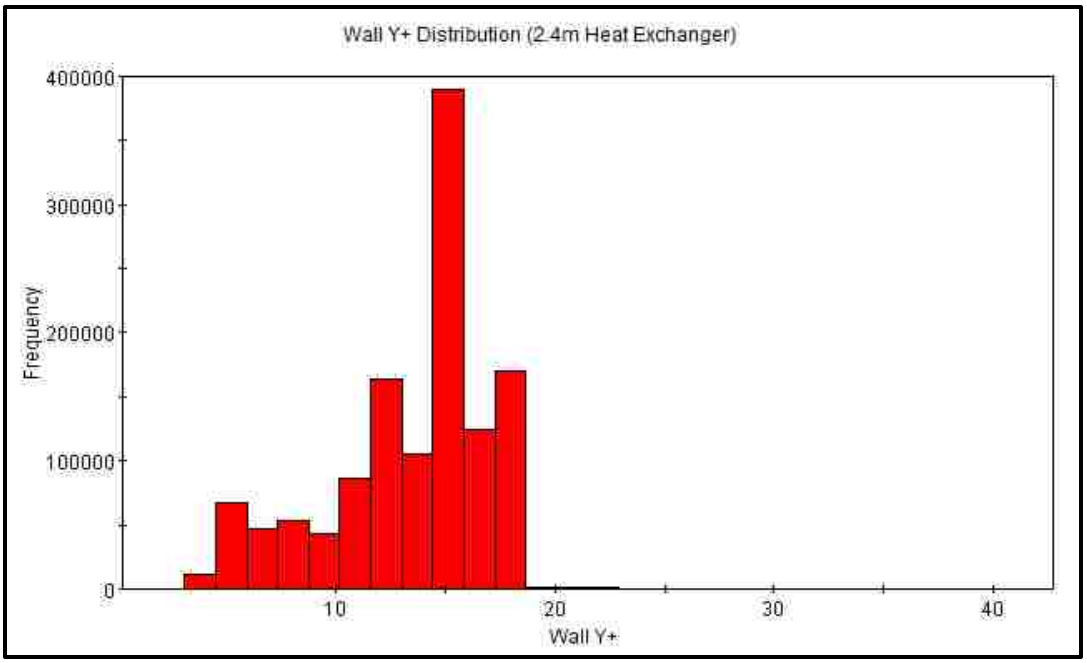

Figure 5.11 Wall Y+ Distribution of Hot Water Region (2.4m Heat Exchanger)

5.1.3 Wall Region Mesh

Mesh Selection:

Surface Mesh:

The surface remesher model was also used for the Wall region to improve the overall surface quality of the imported geometry tessellation. Figure 5.12 depicts the initial surface and the remeshed surface for the Wall region.

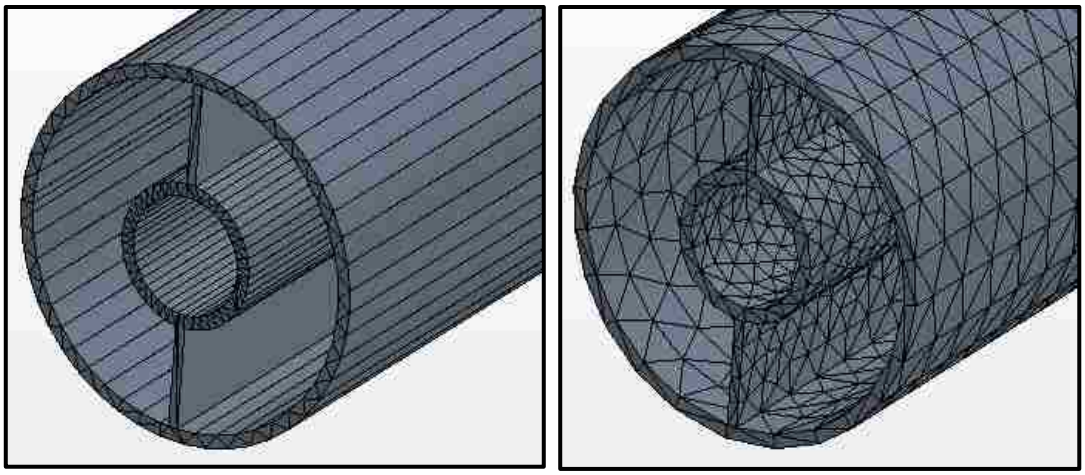

Figure 5.12 Initial Surface vs. Remeshed Surface of Wall Region

Volume Mesh:

For the Wall region only one type of volume mesh model was used. The thin mesher model is specifically designed for thin regions. The thickness of the Wall region is approximately 0.33mm. The thin mesher model generates a prism layer type volume mesh in thin regions. This type of model is also able to determine whether or not portions of the geometry are considered “thick” or “thin”. The portions the model recognizes as thin are modeled as a prism type volume mesh. The portions the model recognizes as thick are modeled as a polyhedral type volume mesh. Figure 5.13 depicts the generated volume mesh for the Wall region for the 0.6m heat exchanger. Similar mesh conditions were used to generate the volume mesh for the Wall region for the additional heat exchanger lengths evaluated.

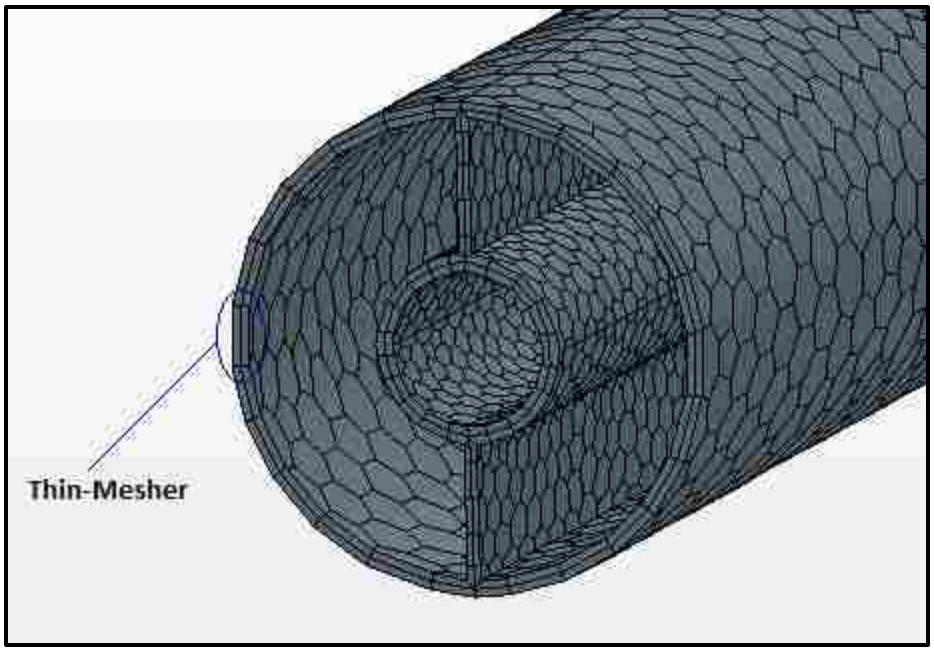

Figure 5.13 Generated Volume Mesh for Wall Region

5.2 Significance of Research

A correlation has been developed to determine the theoretical impact the infusion of fluids have on core temperature [4]:

$$\Delta T_{core} = \frac{Thermal\ Stress\ of\ infused\ fluids}{(W \times C_{p,patient})} \quad [13]$$

$$Thermal\ Stress = \left[\left(T_{core} - T_{fluids}\right) \times C_{p,fuids} \times V_{fluids}\right] \quad [14]$$

Where:

W = Weight of patient (kgs)
$C_{P,patient}$ = Specific heat of patient (0.83 kcal/L/^{o}C) [10]
T_{core} = Patient core temperature
T_{fluids} = Temperature of infused fluids
$C_{P,fluids}$ = Specific heat of infused fluids
V_{fluids} = Volume of infused fluids

Bondok described a typical trauma scenario with the infusion of room temperature fluids to an adult patient. Based on the above correlation, the infusion of 4.3L of room

temperature fluids to the patient would result in a decrease of 1^{o}C core temperature in an awake/alert patient and 1.5^{o}C core temperature decrease in an anesthetized patient. This is a significant change in core temperature, especially considering the increased risk of Hypothermia in trauma patients. A study by Boyan and Howland in 1961 first demonstrated the harmful effects of infusion of cold fluids. They showed a reduction of 0.5 – 1.0^{o}C in core temperature of anesthetized cancer patients following the infusion of 0.5L of cold blood [5].

In regards to fluid warmers, studies have shown that blood can safely be warmed to 42^{o}C for infusion without causing hemolysis [35]. This is a critical metric in the design of fluid warmers for the treatment of Hypothermia. CFD simulations can be used to help predict the right combination of flow rate and heating fluid temperature to regulate the desired Infusate outlet temperature, prior to setting up costly experiments.

5.3 Model Description

This particular heat exchanger is used as part of a medical device to warm hypothermic patients. The device is designed to warm fluids or blood which is then provided to the patient intravenously or intra-arterially. It was assumed that heat transfer would occur between the Infusate and the Hot Water regions along the parallel and counter-parallel side. Additionally, the outer-surface of the heat exchanger was assumed to be adiabatic, so all heat transfer would occur locally between the Infusate and Hot Water regions. For the purposes of this simulation, water was chosen as the working fluid for both the Infusate and Hot Water regions. The Wall region was modeled as a thermally conductive polymer. The specific material properties used in the simulation are given in Table 5.3.

Table 5.3 Material Properties for Fluid and Solid Regions

Material Properties		
	Water	Thermally Conductive Polymer
Density [kg/m^3]	997.561	1840
Specific Heat [J-kg/K]	4181.72	900
Thermal Conductivity [W/m-K]	0.62027	20

5.4 Boundary Conditions

As previously mentioned, heat transfer was considered between the Infusate and Hot Water regions. The outer-surface of the heat exchanger was considered to be adiabatic. Two main boundary conditions for the solution were the inlet temperature of the Hot Water and Infusate regions. Both regions were modeled with a uniform entrance temperature. Additionally, the mass flow rate at the inlet for both the Hot Water and Infusate regions were modeled as a constant uniform entrance flow rate. The final boundary condition imposed involved the Hot Water and Infusate outlet, which were assumed to be at atmospheric pressure (1 atm). A basic energy balance was performed between the Hot Water and Infusate regions. The solution was allowed to run until the percent difference between the heat gained by the Infusate region and heat lost by the hot water region was less than 2.0%.

The heat lost by the hot water region was calculated using the following equation:

$$-Q = m_H C_{P,H}(T_{o,H} - T_{i,H}) \quad [15]$$

Where:

m_H = Mass Flow Rate Hot Water
$C_{P,H}$ = Specific Heat Hot Water Region
$T_{i,H}$ = Inlet Temperature Hot Water Region
$T_{o,H}$ = Outlet Mean Bulk Temperature-Hot Water Region

The heat gained by the Infusate region was calculated using the following equation:

$$Q = m_I C_{P,I}(T_{o,I} - T_{i,I}) \quad [16]$$

Where:

m_I = Mass Flow Rate Infusate
$C_{P,I}$ = Specific Heat Infusate Region
$T_{i,I}$ = Inlet Temperature Infusate Region
$T_{o,I}$ = Outlet Mean Bulk Temperature-Infusate Region

Mean bulk temperature is often used as a local reference temperature when evaluating convective heat transfer, especially when considering pipe flow. Mean Bulk temperature is defined as follows [20]:

$$mC_pT_m = \int_0^{r_0} \rho C_p v_x T \, 2\pi r dr \quad [17]$$

Where:

Mass flow rate is given by:

$$m = \int_0^{r_0} \rho v_x 2\pi r dr \quad [18]$$

Assuming constant properties, combining [18] into [17] yields:

$$T_m = \frac{\int_0^{r_0} v_x T r dr}{\int_0^{r_0} v_x r dr} \quad [19]$$

Mean Bulk temperature is typically evaluated over a specific cross-sectional area within the flow field. Since the calculation of the mean bulk temperature takes into account the mass flow rate of the moving fluid, this method provides a more accurate representation of the average temperature of the moving fluid when compared to a simple surface average temperature. In the previous experimental study [27], the outlet temperature was measured using a single center-point temperature probe. In the current study, 3D CFD modeling was used to more accurately represent the entire flow area, allowing for the calculation of mean bulk temperature over the entire cross-sectional area at the outlets. Evaluating in terms of mean bulk temperature more accurately characterizes the thermal properties of the heat exchanger.

In this thesis, a 3D CFD model was developed to accurately capture physical characteristics of the parallel/counter-parallel flow heat exchanger. Simulations were run for four different heat exchanger lengths (0.6m, 1.2m, 1.8m, and 2.4m). Additionally, four different sets of boundary conditions were considered in this study. The first set of conditions evaluated the effect of heat exchanger length on Infusate outlet temperature. Infusate inlet mass flow rate and temperature were held constant for each heat exchanger length (15ml/min and 10^{o}C). This study was repeated for an Infusate inlet mass flow rate of 50ml/min. Next, the effect of Infusate inlet mass flow rate on outlet temperature was evaluated. Only the 2.4m heat exchanger was considered in this study, with constant Hot Water inlet temperature and mass flow rate (42^{o}C and 750ml/min). The Infusate inlet temperature was held constant at 10^{o}C with increasing inlet mass flow rate. This study was repeated for an Infusate inlet temperature of 20^{o}C. The boundary conditions used in the current CFD analysis were chosen based on a previous study by Moujaes and Oliver (1998). The results of the previous experimental study were then compared to the current CFD results. The boundary conditions used in the CFD comparison to the experimental data are given in Tables 5.4 – 5.7. Additional simulations were run to develop hydrodynamic and thermal entrance length correlations for the Hot Water region under laminar and turbulent flow.

Table 5.4 Boundary Conditions Evaluating Infusate Outlet Temperature vs. Exchanger Length

Infusate Outlet Temp vs. Exchanger Length (Boundary Conditions)				
Heat Exchanger Length [m]	Infusate Inlet Temp [C]	Infusate Inlet Mass Flow Rate [ml/min]	Hot Water Inlet Temp [C]	Hot Water Inlet Mass Flow Rate [ml/min]
0.6	10	15	41.6	1700
1.2	10	15	41.55	1165
1.8	10	15	41.65	920
2.4	10	15	41.58	785

Table 5.5 Boundary Conditions Evaluating Infusate Outlet Temperature vs. Exchanger Length (Increased Infusate Inlet Flow Rate)

Infusate Outlet Temp vs. Exchanger Length (Boundary Conditions)				
Heat Exchanger Length [m]	Infusate Inlet Temp [C]	Infusate Inlet Mass Flow Rate [ml/min]	Hot Water Inlet Temp [C]	Hot Water Inlet Mass Flow Rate [ml/min]
0.6	10	50	41.6	1700
1.2	10	50	41.55	1165
1.8	10	50	41.55	920
2.4	10	50	41.6	785

Table 5.6 Boundary Conditions Evaluating Infusate Outlet Temperature vs. Infusate Inlet Flow Rate

Infusate Outlet Temperature vs. Infusate Inlet Mass Flow Rate (Boundary Conditions)				
Heat Exchanger Length [m]	Infusate Inlet Temp [C]	Infusate Inlet Mass Flow Rate [ml/hr]	Hot Water Inlet Temp [C]	Hot Water Inlet Mass Flow Rate [ml/min]
2.4	10	500	42	750
2.4	10	1500	42	750
2.4	10	2500	42	750
2.4	10	3500	42	750
2.4	10	5000	42	750

Table 5.7 Boundary Conditions Evaluating Infusate Outlet Temperature vs. Infusate Inlet Flow Rate (Increased Infusate Inlet Temperature)

Infusate Outlet Temperature vs. Infusate Inlet Mass Flow Rate (Boundary Conditions)				
Heat Exchanger Length [m]	Infusate Inlet Temp [C]	Infusate Inlet Mass Flow Rate [ml/hr]	Hot Water Inlet Temp [C]	Hot Water Inlet Mass Flow Rate [ml/min]
2.4	20	500	42	750
2.4	20	1500	42	750
2.4	20	2500	42	750
2.4	20	3500	42	750
2.4	20	4500	42	750
2.4	20	6000	42	750

The following assumptions were made for the simulations:

- The outer-surface of the heat exchanger was assumed to be adiabatic
- Convection heat transfer was assumed between the Infusate and Hot Water regions.
- No-slip condition at the walls of the fluid regions

- Laminar flow in the Infusate region
- Turbulent flow in the Hot Water region
- Incompressible

To help characterize the hydrodynamic properties of the heat exchanger, as well as determine the correct physics models to utilize within the CFD simulations, Reynolds Numbers were determined. The Reynolds Number for the Infusate region was calculated using the following equation for pipe flow [20]:

$$R_e = \frac{VD_h}{\nu} \quad [20]$$

Where:

V = Mean Fluid Velocity
D_h = Hydraulic Diameter
υ = Kinematic Viscosity

The Hydraulic Diameter can be calculated using the following equation [20]:

$$D_h = \frac{4A_f}{P} \quad [21]$$

Where:

A_f = Flow Area
P = Wetted Perimeter

The mean fluid velocity was calculated based on the inlet mass flow rate according to the equation:

$$Q = AV \quad [22]$$

Where:

Q = Volumetric Flow Rate
A = Cross Sectional Area
V = Flow Velocity

The diameter of the flow area in the Infusate region is 3.0mm. The Hydraulic Diameter for the Infusate region was calculated based on the Flow Area and Wetted Perimeter (Table 5.8). Table 5.9 lists the calculated Reynolds Numbers of the Infusate region for the different flow conditions

used in the CFD simulations. In the CFD simulations, the Infusate region was evaluated as laminar flow based on the calculated Reynolds Numbers.

Table 5.8: Properties for the Infusate Region

Infusate Region	
Flow Area [mm^2]	7.069
Wetted Perimeter [mm]	9.42
Hydraulic Diameter [mm]	3.001
Kinematic Viscosity [m^2/s]	1.308×10^{-6}

Table 5.9: Calculated Infusate Region Reynolds Numbers for Associated Flow Conditions

Infusate Volumetric Flow Rate [ml/min]	Mean Fluid Velocity [m/s]	Reynolds Number
8.33	0.02	45.06
15	0.04	81.14
25	0.06	135.23
41.67	0.10	225.41
50	0.12	270.47
75	0.18	405.70
83.33	0.20	450.77
100	0.24	540.94

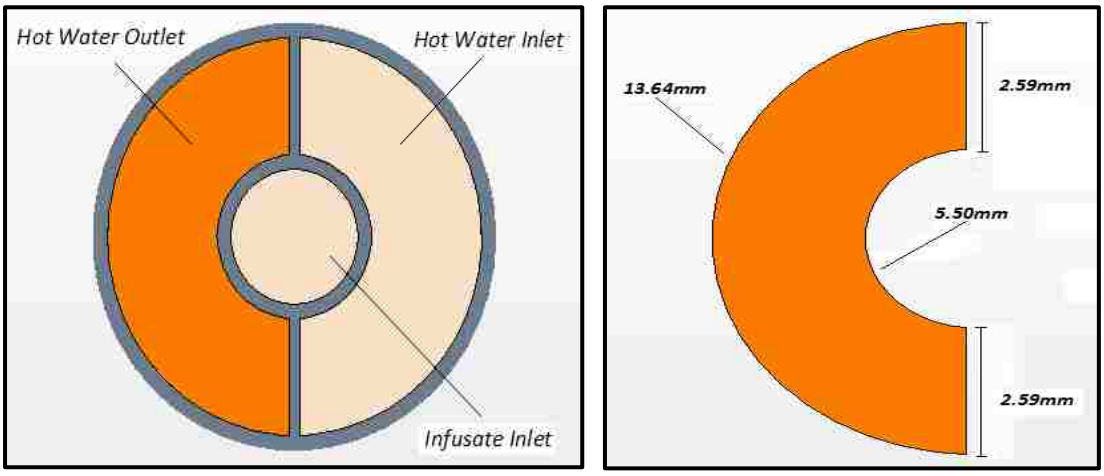

Figure 5.14 Inlet/Outlet Configuration and Wetted Perimeter Dimensions of Hot Water Region

The Reynolds Number for the Hot Water region was estimated based on (Eqs. [20] and [21]). Figure 5.14 illustrates the flow configuration of the proposed heat exchanger, as well as the perimeter dimensions for the flow area of the Hot Water region. The Hydraulic Diameter for the Hot Water region was calculated based on the Flow Area and Wetted Perimeter (Table 5.10). Table 5.11 lists the calculated Reynolds Numbers of the Hot Water region for the different flow conditions used in the CFD simulations. In the CFD simulations, the Hot Water region was evaluated as turbulent flow based on the calculated Reynolds Number.

Table 5.10: Properties for the Hot Water Region

Hot Water Region	
Flow Area [mm^2]	24.78
Wetted Perimeter [mm]	24.315
Hydraulic Diameter [mm]	4.076
Kinematic Viscosity [m^2/s]	0.64025×10^{-6}

Table 5.11: Calculated Hot Water Reynolds Numbers for Associated Flow Conditions

Heat Exchanger Length [m]	Hot Water Volumetric Flow Rate [ml/min]	Mean Fluid Velocity [m/s]	Reynolds Number
0.6	1700	1.14	7279.15
1.2	1165	0.78	4988.36
1.8	920	0.62	3939.31
2.4	750	0.50	3211.39
2.4	785	0.53	3361.26

CHAPTER 6

RESULTS AND DISCUSSION

6.1 Outlet Temperature vs. Heat Exchanger Length

The Infusate outlet temperature was evaluated in terms of the heat exchanger length. The boundary conditions used for these simulations are given in Table 5.4. The results of the current CFD simulations were compared to experimental results collected in a paper published in 1998 [27]. Figure 6.1 compares the current CFD predicted outlet temperatures with the experimental results. It is important to note that the outlet temperature measured in the experiments was localized to a center-point temperature probe. In the current CFD simulations, bulk temperature was used as the measure for the outlet temperatures. This difference in outlet temperature measurement should account for the difference in reported results. Despite this observation, the CFD predicted outlet temperatures were within 8% of the experimental values.

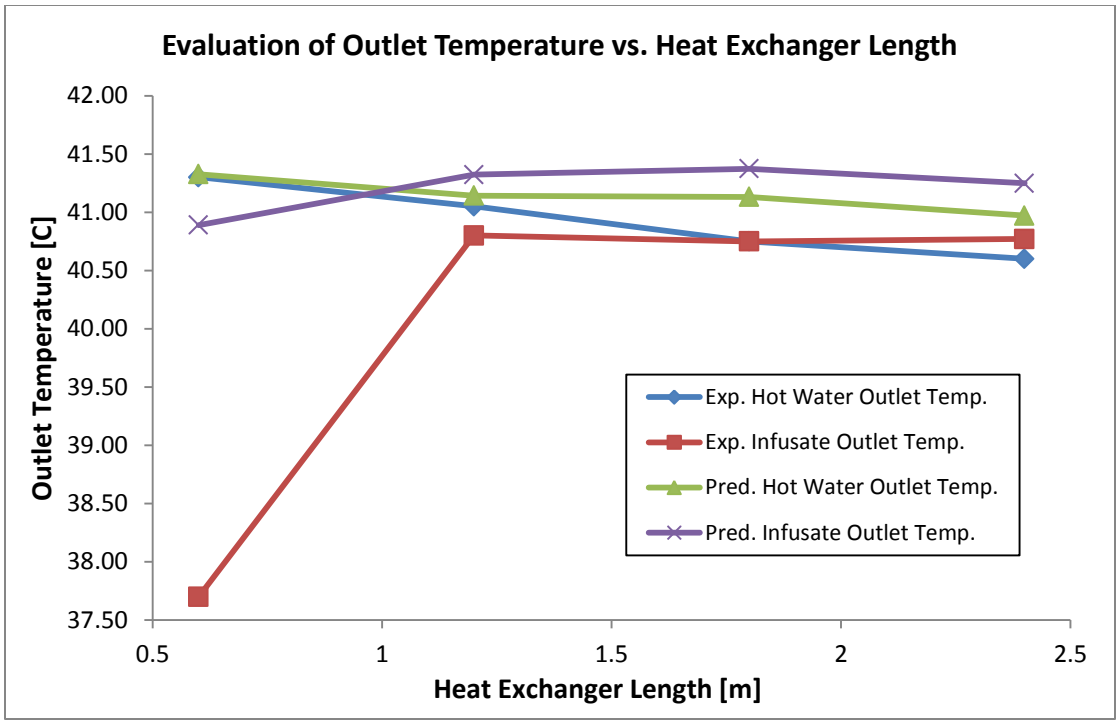

Figure 6.1 Comparison of Outlet Temperatures (CFD Predicted vs. Experimental Results [27])

6.1.1 Infusate Region

Of particular interest to the current study was the characterization of the thermal profile of the Infusate region. As previously mentioned, blood can be safely warmed to 42°C for infusion without causing hemolysis. As such, it is imperative that the fluid within the Infusate region does not rise above 42°C. To depict the thermal profile of the Infusate region along the length of the heat exchanger, a center plane of the Infusate region was plotted in terms of cylindrical geometry of the Infusate region. A uniform temperature profile of 10°C was applied at the inlet of the Infusate region for all heat exchanger lengths evaluated. Heat transfer occurs along the length of the heat exchanger across the temperature gradient between the Infusate and Hot Water regions. The independent variable in these simulations was heat exchanger length. The mean bulk temperature at the outlet of the Infusate region is expected to increase with increasing heat exchanger length, but at a diminishing rate. As axial distance from the inlet

of the Infusate region increases, the temperature gradient (ΔT) between the Infusate and Hot Water regions decreases. As such, heat transfer would decrease until equilibrium is reached between the Infusate and Hot Water regions. This results in the temperature profile within the Infusate region approaching a uniform temperature near the end of the heat exchanger, assuming appropriate flow conditions and heat exchanger length. This was observed for all heat exchanger lengths evaluated. As such, it does not seem necessary to require a heat exchanger length much greater than 0.6m to achieve the desired outlet temperature for the given boundary conditions. Thermal equilibrium was not reached for any of the heat exchanger lengths evaluated, as the outlet temperatures of the Infusate and Hot Water regions were not equal. The parallel/counter-parallel flow orientation of the Hot Water region may account for this observation, as heat transfer at the inlet of the Infusate region interacts with both the inlet and outlet of the Hot Water region.

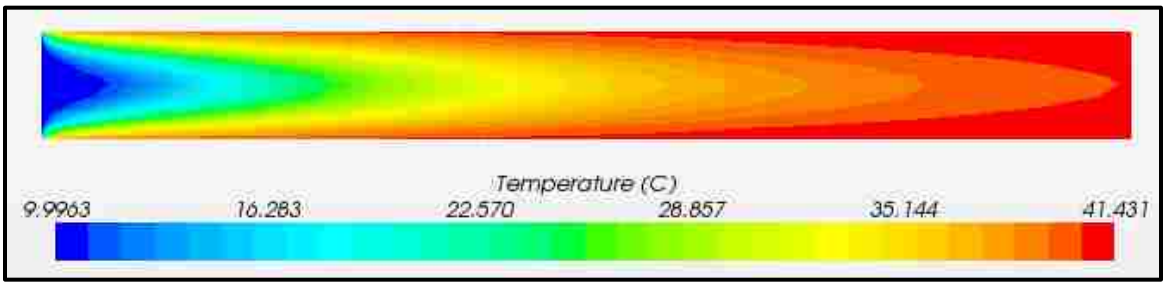

Figure 6.2 Infusate Length Center-Plane Temperature Profile (0.6m Heat Exchanger)

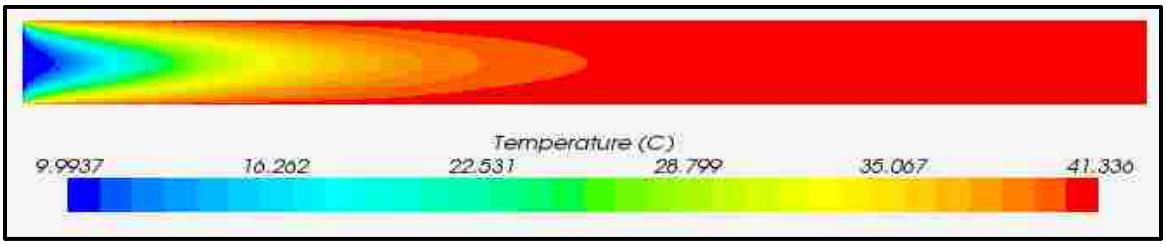

Figure 6.3 Infusate Length Center-Plane Temperature Profile (1.2m Heat Exchanger)

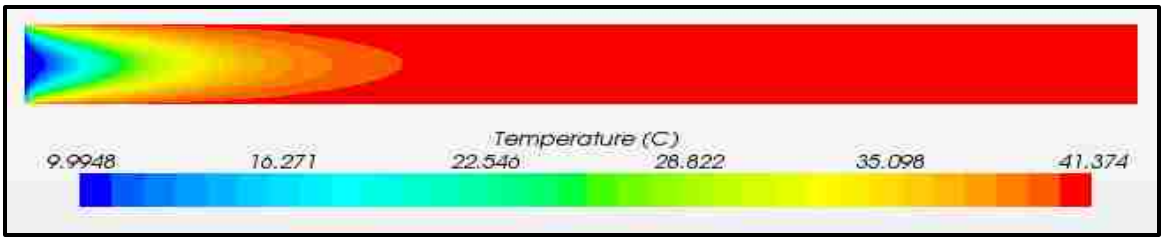

Figure 6.4 Infusate Length Center-Plane Temperature Profile (1.8m Heat Exchanger)

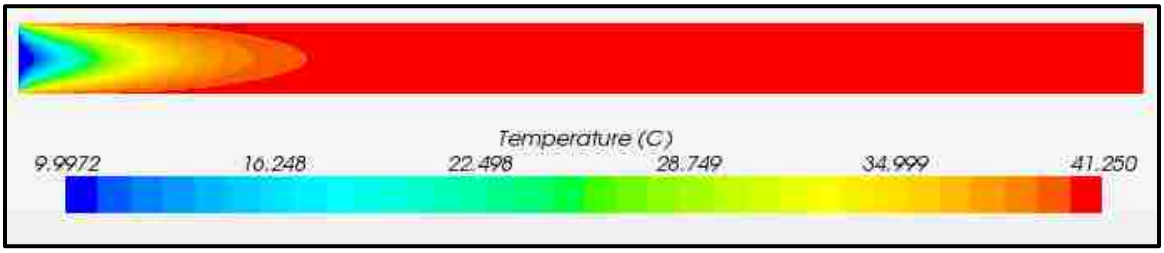

Figure 6.5 Infusate Length Center-Plane Temperature Profile (2.4m Heat Exchanger)

The temperature profile at the outer-surface of the Infusate region was also examined (Figures 6.6-6.9). Again, heat transfer occurs across the temperature gradient between the Infusate and Hot Water regions. The outer-surface of the Infusate region is closer in proximity to the Hot Water region. This results in the outer-surface reaching a uniform temperature profile closer to the inlet than the interior of the Infusate region for all heat exchanger lengths examined.

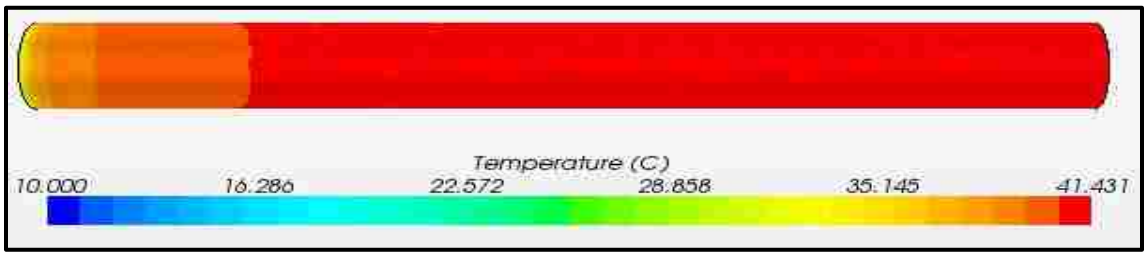

Figure 6.6 Infusate Length Outer-Surface Temperature Profile (0.6m Heat Exchanger)

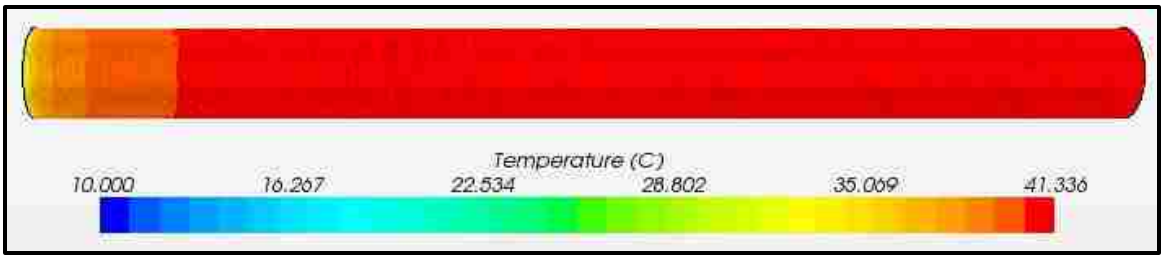

Figure 6.7 Infusate Length Outer-Surface Temperature Profile (1.2m Heat Exchanger)

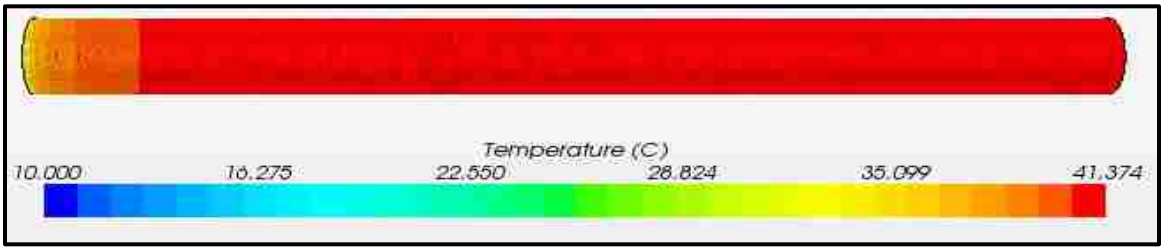

Figure 6.8 Infusate Length Outer-Surface Temperature Profile (1.8m Heat Exchanger)

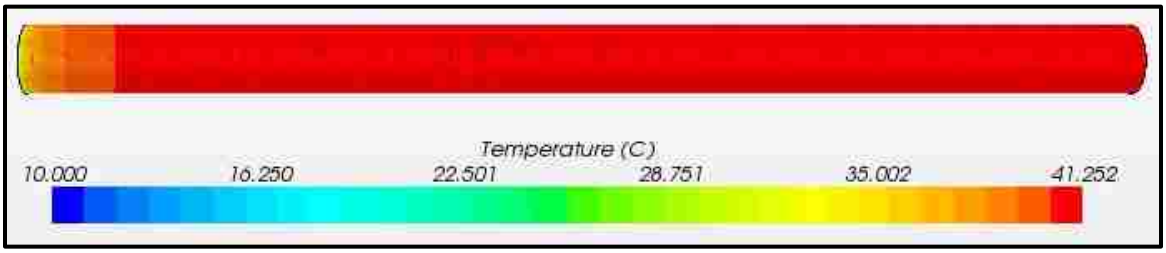

Figure 6.9 Infusate Length Outer-Surface Temperature Profile (2.4m Heat Exchanger)

This study was also interested in characterizing the hydrodynamic properties of the parallel/counter-parallel flow heat exchanger. The geometry of the Infusate region is a common cylindrical pipe. The hydrodynamic properties of pipe flow have been well studied and documented. As such, this study is mostly concerned with characterizing the hydrodynamic properties of the Hot Water region, as this geometry is a unique variation of the common concentric annulus. However, a center-plane section over the length of the Infusate region was plotted in terms of the velocity magnitude to demonstrate the validity of the CFD model (Figures 6.10-6.13). The velocity profile appears to reach fully developed flow a short distance from the

inlet with the expected parabolic axial velocity profile. A no-slip condition was imposed at the walls of the Infusate region. The velocity magnitude at the walls is equal to zero, which is consistent with a no-slip condition. These properties are consistent with known hydrodynamic properties of pipe flow, and help demonstrate overall solution accuracy.

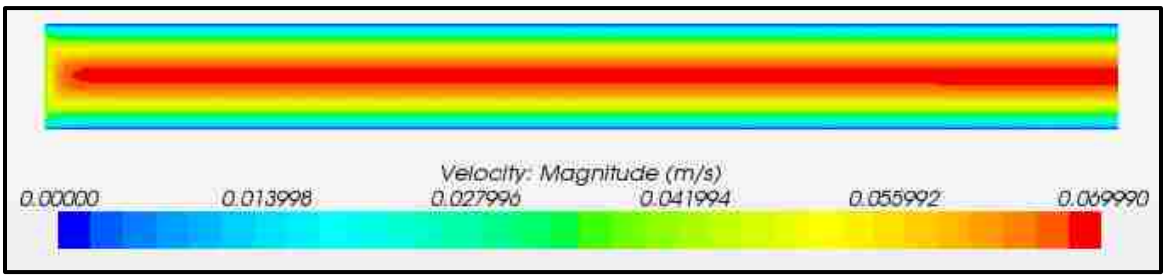

Figure 6.10 Infusate Length Center-Plane Velocity Profile (0.6m Heat Exchanger)

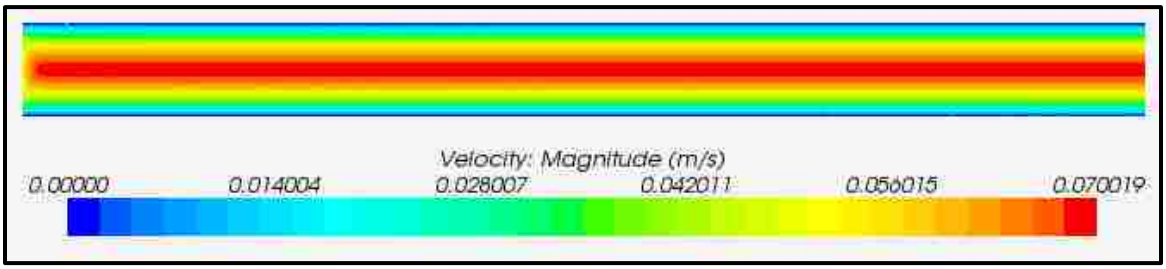

Figure 6.11 Infusate Length Center-Plane Velocity Profile (1.2m Heat Exchanger)

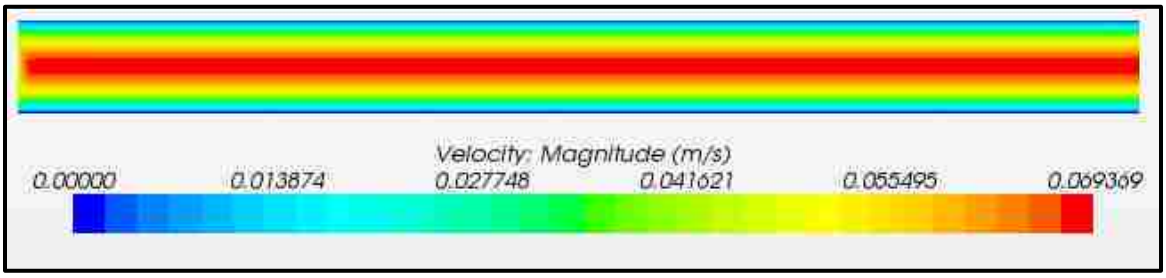

Figure 6.12 Infusate Length Center-Plane Velocity Profile (1.8m Heat Exchanger)

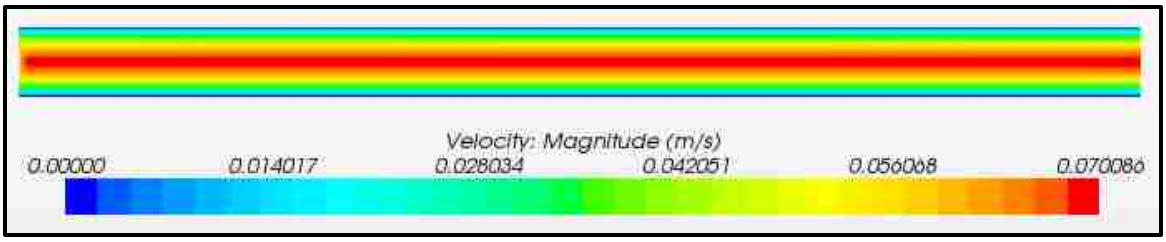

Figure 6.13 Infusate Length Center-Plane Velocity Profile (2.4m Heat Exchanger)

6.1.2 Hot Water Region

Similar to the Infusate region, this current study focused on characterizing the thermal properties of the Hot Water region. Additionally, this study was also interested in examining the hydrodynamic effects within the unique geometry of the Hot Water region. The Hot Water geometry consists of concentric rings like a traditional annulus, but also features a separation along the mid-plane which confines the flow area to half of a true concentric annulus.

To help characterize the thermal profile within in the Hot Water region, a center-plane along the length of heat exchanger was plotted in terms of temperature (Figure 6.14-6.17). Due to the length of the heat exchanger, the subsequent figures were scaled to accommodate the entire length into one figure. The figure was scaled along the z-axis or the length of the heat exchanger. The Infusate inlet temperature is much lower than the Hot Water inlet temperature (10^{o}C vs. ≈41.6^{o}C). As such, heat is lost by the Hot Water region and gained by the Infusate region. Additionally, the outer-surface of the heat exchanger was defined as adiabatic. This results in the temperature of the Hot Water region remaining relatively uniform near the outer surface of the heat exchanger. This also explains the temperature profile along the inner-wall of the Hot Water region near the Infusate region, as heat transfer can only occur across the boundary between the Infusate and Hot Water regions. Due to the parallel/counter-parallel arrangement, heat transfer occurs along both sides of the Infusate region. This explains the more varied temperature profile on both sides of the Hot Water region near the Infusate inlet.

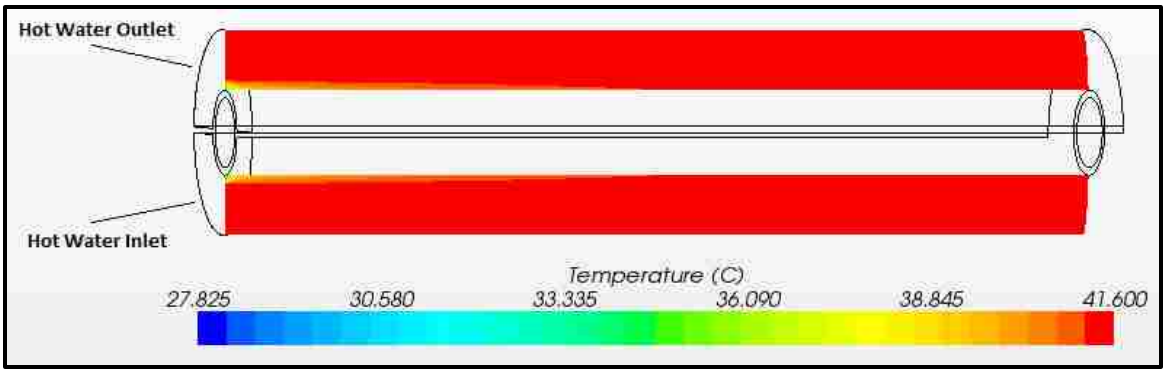

Figure 6.14 Hot Water Length Center-Plane Temperature Profile (0.6m Heat Exchanger)

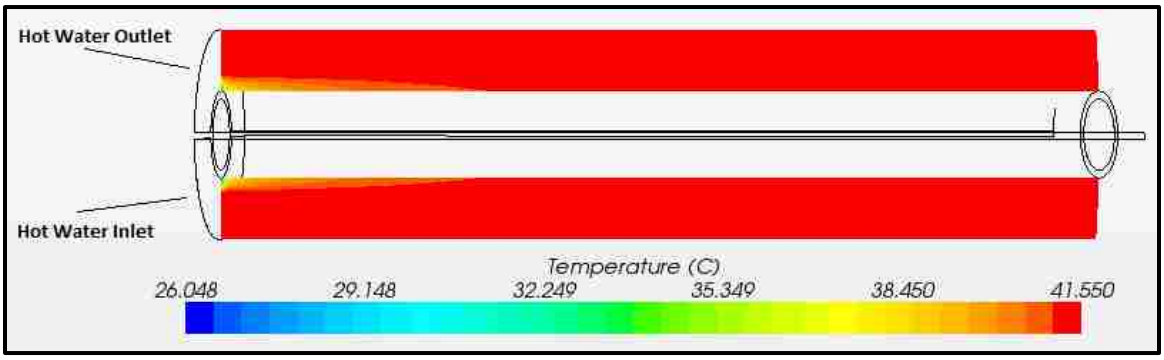

Figure 6.15 Hot Water Length Center-Plane Temperature Profile (1.2m Heat Exchanger)

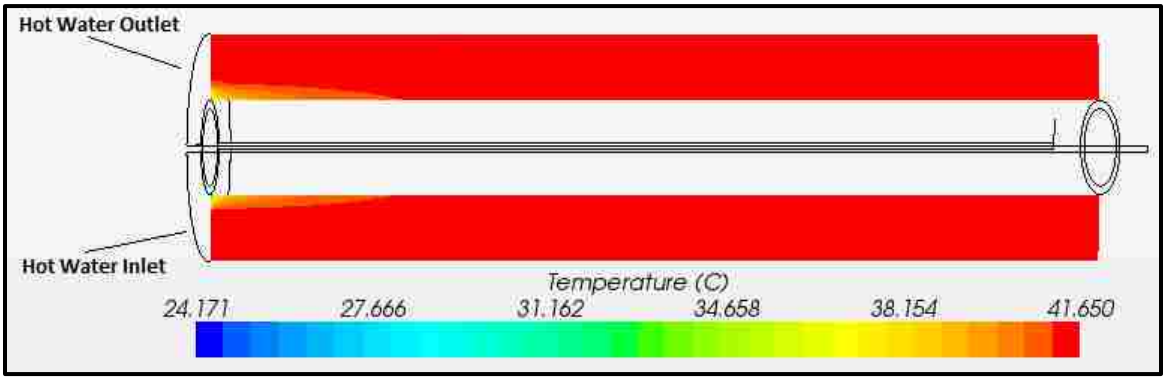

Figure 6.16 Hot Water Length Center-Plane Temperature Profile (1.8m Heat Exchanger)

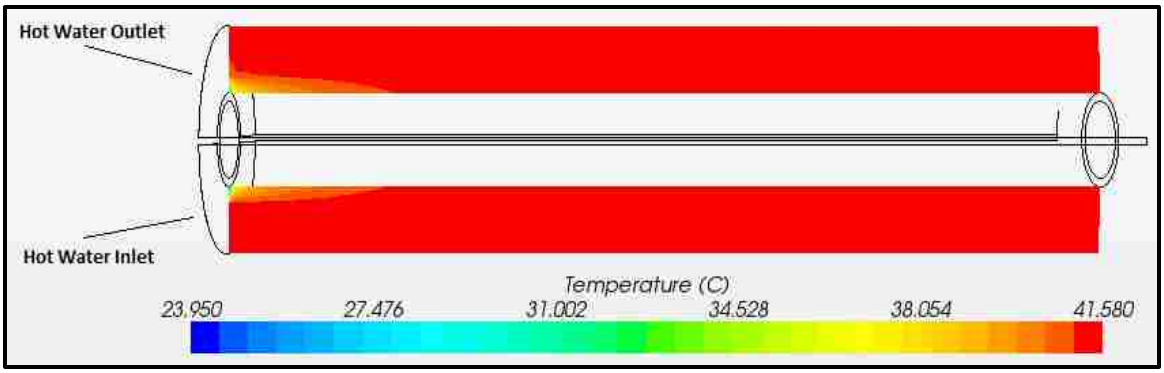

Figure 6.17 Hot Water Length Center-Plane Temperature Profile (2.4m Heat Exchanger)

To highlight the temperature distribution within the Hot Water region, cross-section temperature profiles were plotted for the different heat exchanger lengths examined (0.6m, 1.2m, 1.8m, and 2.4m). Temperature cross sections were plotted at ¼ and ¾'s of the given heat exchanger length. Figures 6.18 – 6.21 depict the cross-section temperature profiles for the different heat exchanger lengths evaluated. As expected, temperature within the Hot Water region increases from the center (near the Infusate region) outward. Again, this is due to the adiabatic condition at the heat exchanger outer surface, which only allows heat transfer between the Infusate and Hot Water regions. Similar boundary conditions were applied at the inlet sections for all heat exchanger lengths evaluated. As such, a uniform temperature profile within the Hot Water region is reached at similar distances from the inlet for all heat exchanger lengths evaluated. This results in the temperature profile near the end of the heat exchanger being more uniform as the heat exchanger length increases. Since heat transfer occurs along the length of the heat exchanger, the temperature profile within the Hot Water region should decrease as it approaches the outlet. This results in the return section having a lower temperature profile than the entrance section of the Hot Water region.

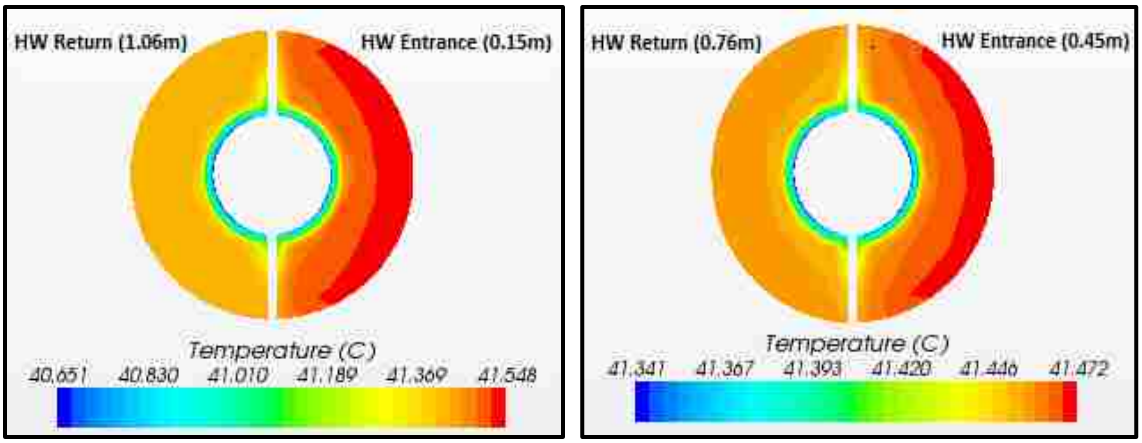

Figure 6.18 Cross-Section Temperature Profile Hot Water Region (0.6m HE)

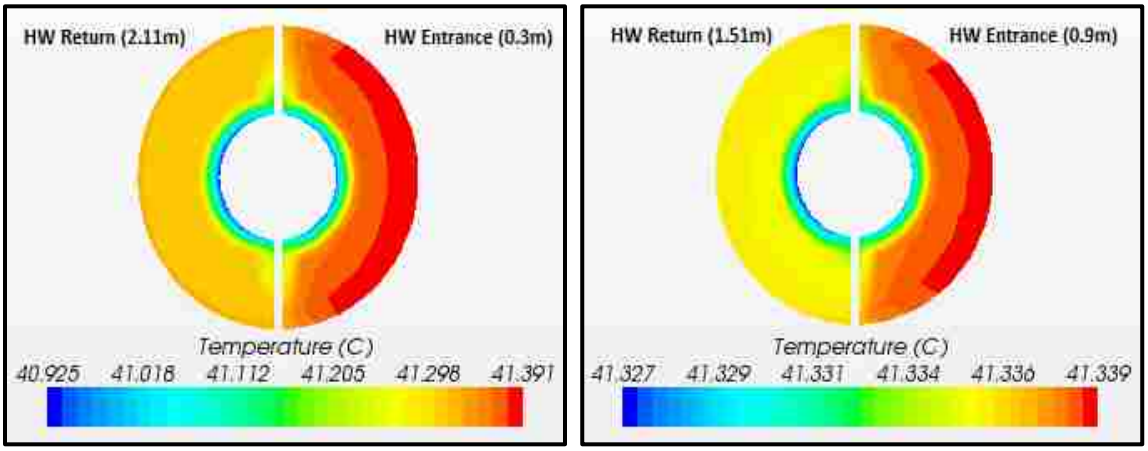

Figure 6.19 Cross-Section Temperature Profile Hot Water Region (1.2m HE)

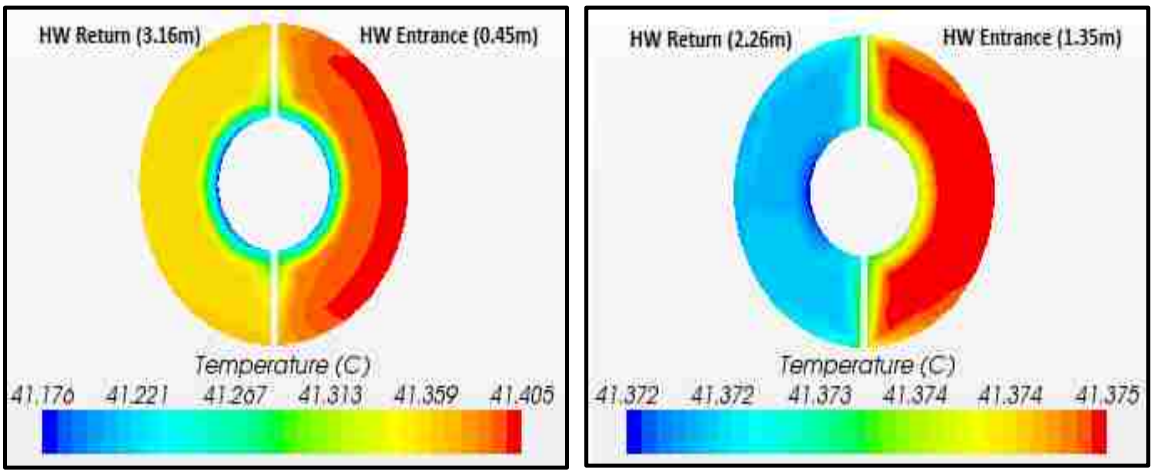

Figure 6.20 Cross-Section Temperature Profile Hot Water Region (1.8m HE)

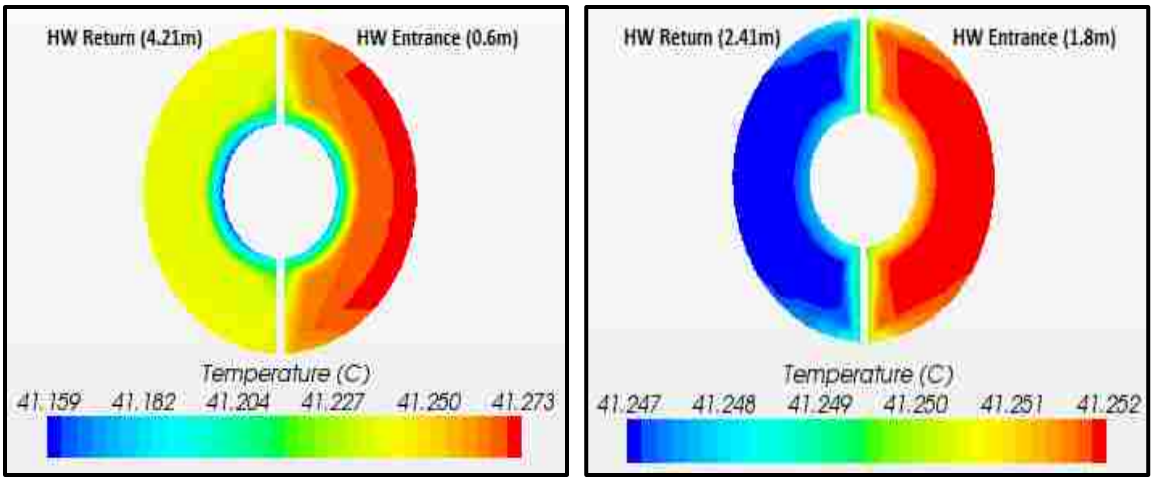

Figure 6.21 Cross-Section Temperature Profile Hot Water Region (2.4m HE)

To help visualize the hydrodynamic effects within the Hot Water region, a center-plane along the length of the heat exchanger was plotted in terms of velocity magnitude (Figures 6.22-6.25). Again, the subsequent figures were scaled to accommodate the entire length of the heat exchanger into one figure. However, it is apparent from these plots that axial velocity becomes fully developed a short distance from the inlet of the Hot Water region. Turbulent flow was simulated in the Hot Water region for all heat exchanger lengths evaluated. Typically, the hydrodynamic entrance length is much shorter for turbulent flow than for laminar [20]. Additionally, there is a significant increase in velocity magnitude at the exit of the elbow section of the Hot Water region, which results in an additional developing region. The elbow section of the Hot Water region creates an abrupt change in flow direction over a short length (approximately 0.01m). Centrifugal forces at the elbow section may result in a significant pressure drop. The centrifugal forces and pressure drop along the short length (relative to heat exchanger length) of the elbow section may account for the increase in flow velocity observed.

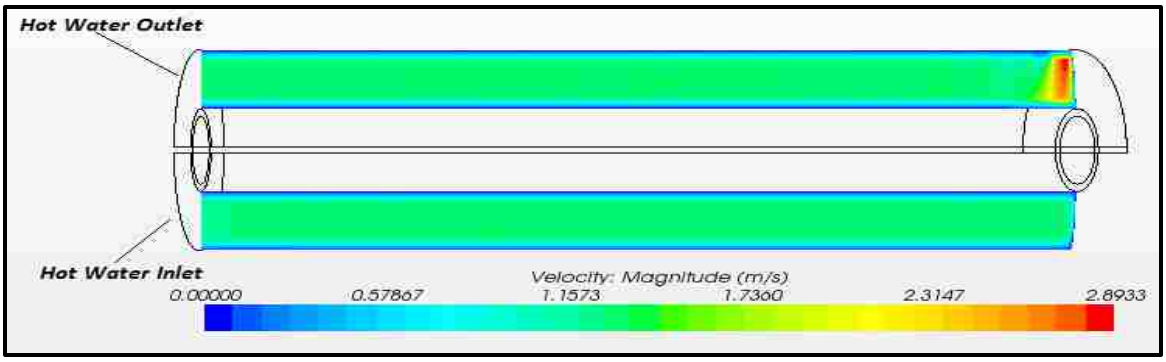

Figure 6.22 Hot Water Length Center-Plane Velocity Profile (0.6m Heat Exchanger)

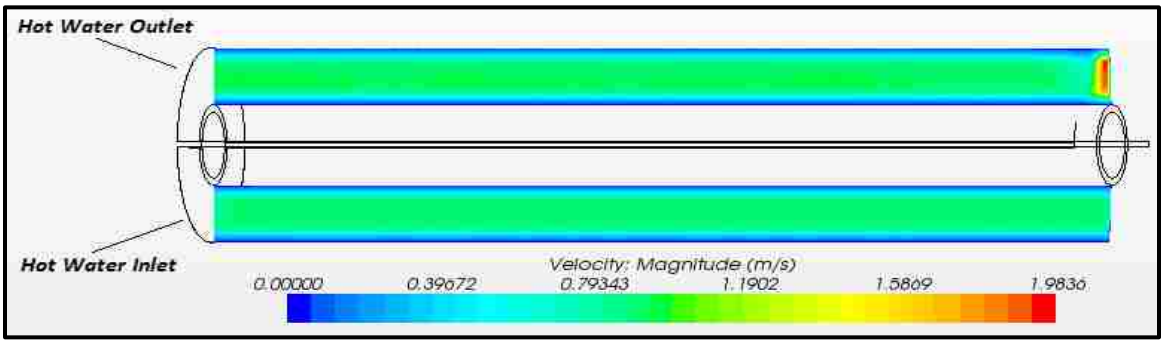

Figure 6.23 Hot Water Length Center-Plane Velocity Profile (1.2m Heat Exchanger)

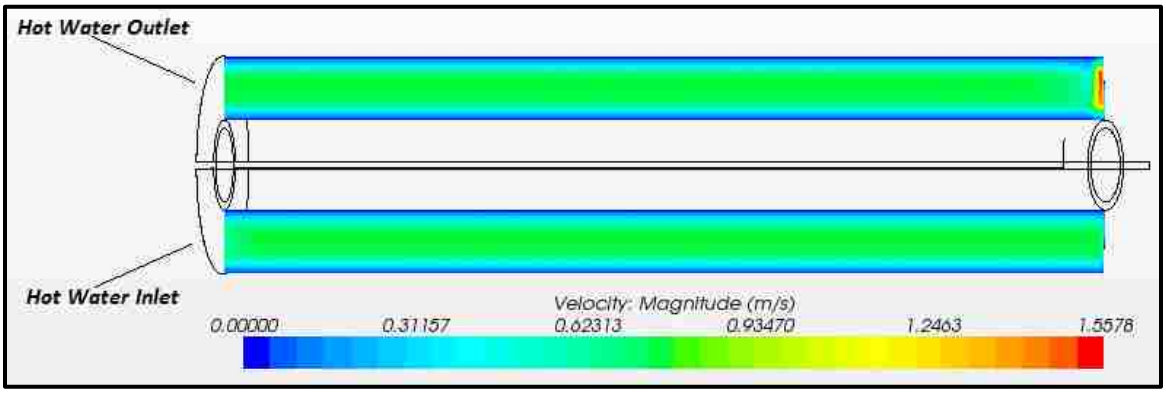

Figure 6.24 Hot Water Length Center-Plane Velocity Profile (1.8m Heat Exchanger)

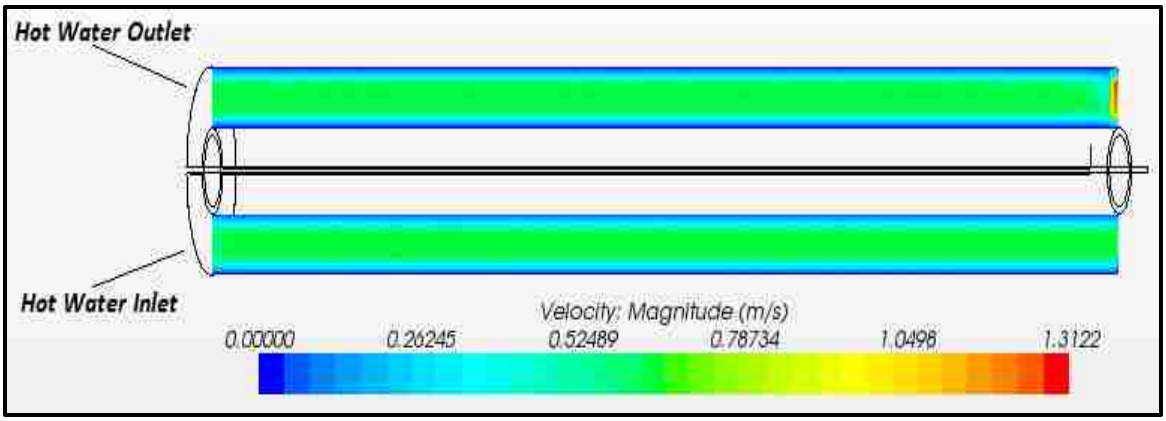

Figure 6.25 Hot Water Length Center-Plane Velocity Profile (2.4m Heat Exchanger)

An unscaled velocity magnitude plot centered on the elbow section of the Hot Water region was also plotted to highlight the unique hydrodynamic effects. Figures 6.26-6.29 depict the unscaled velocity magnitude plot focusing on the elbow section of the Hot Water region. A significant velocity increase is observed at the outlet of the elbow section. Again, centrifugal forces and pressure drop within the elbow section would account for the increase in velocity at the outlet of the elbow section. Additionally, the abrupt change in flow direction within the elbow results in a new developing region after the elbow section of the Hot Water region. Approximations of the distance after the elbow for the flow to become fully developed were 0.16m, 0.148m, 0.14m, and 0.13m for the respective heat exchanger lengths (0.6m, 1.2m, 1.8m, and 2.4m). As the volumetric flow rate at the inlet of the Hot Water region decreases, the entrance length after the elbow also decreases. Decreased flow rate may result in a decrease in turbulent fluctuations, which may account for the observed decrease in entrance length. The axial velocity along the centerline of the flow area was plotted for increasing axial distance (x) away from the elbow section of the Hot Water region to confirm the entrance length approximations. Figure 6.30 depicts the axial length and centerline locations for the axial velocity profiles. Figures 6.31-6.34 depict the axial velocity profiles of the developing flow area immediately after the elbow section of the Hot Water region.

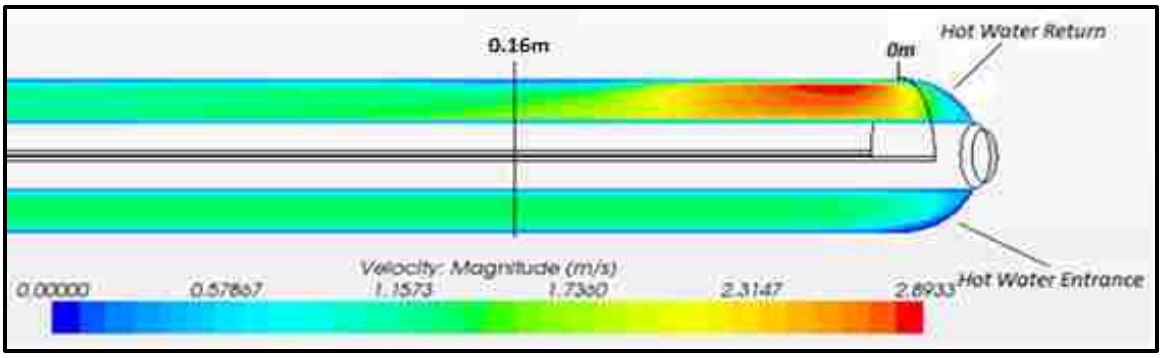

Figure 6.26 Unscaled Velocity Profile of Elbow Section-Hot Water Region (0.6m HE)

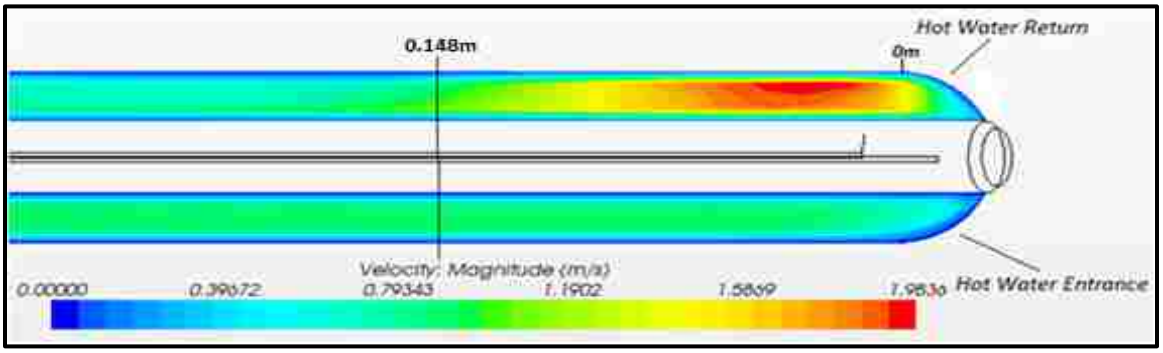

Figure 6.27 Unscaled Velocity Profile of Elbow Section-Hot Water Region (1.2m HE)

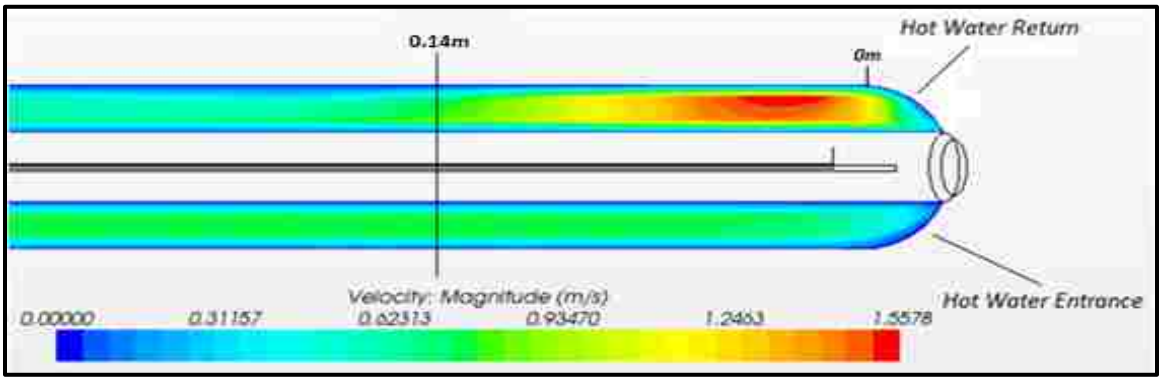

Figure 6.28 Unscaled Velocity Profile of Elbow Section-Hot Water Region (1.8m HE)

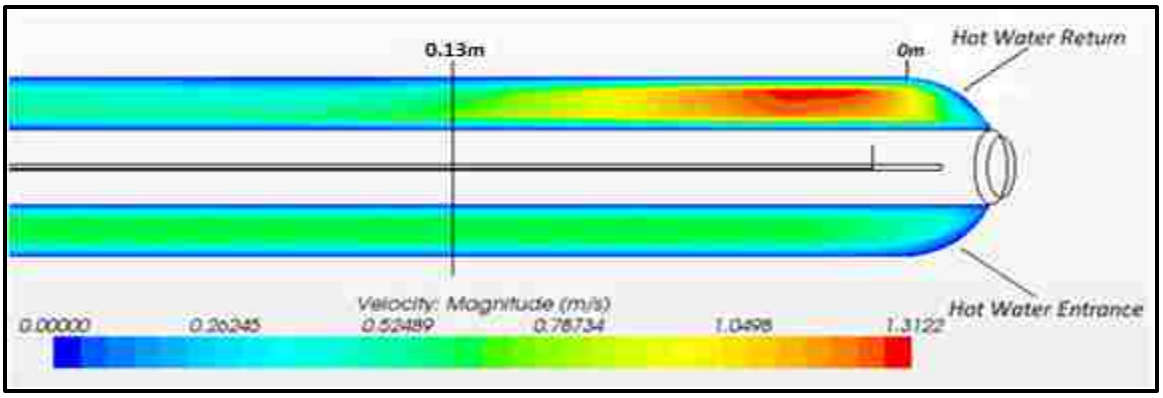

Figure 6.29 Unscaled Velocity Profile of Elbow Section-Hot Water Region (2.4m HE)

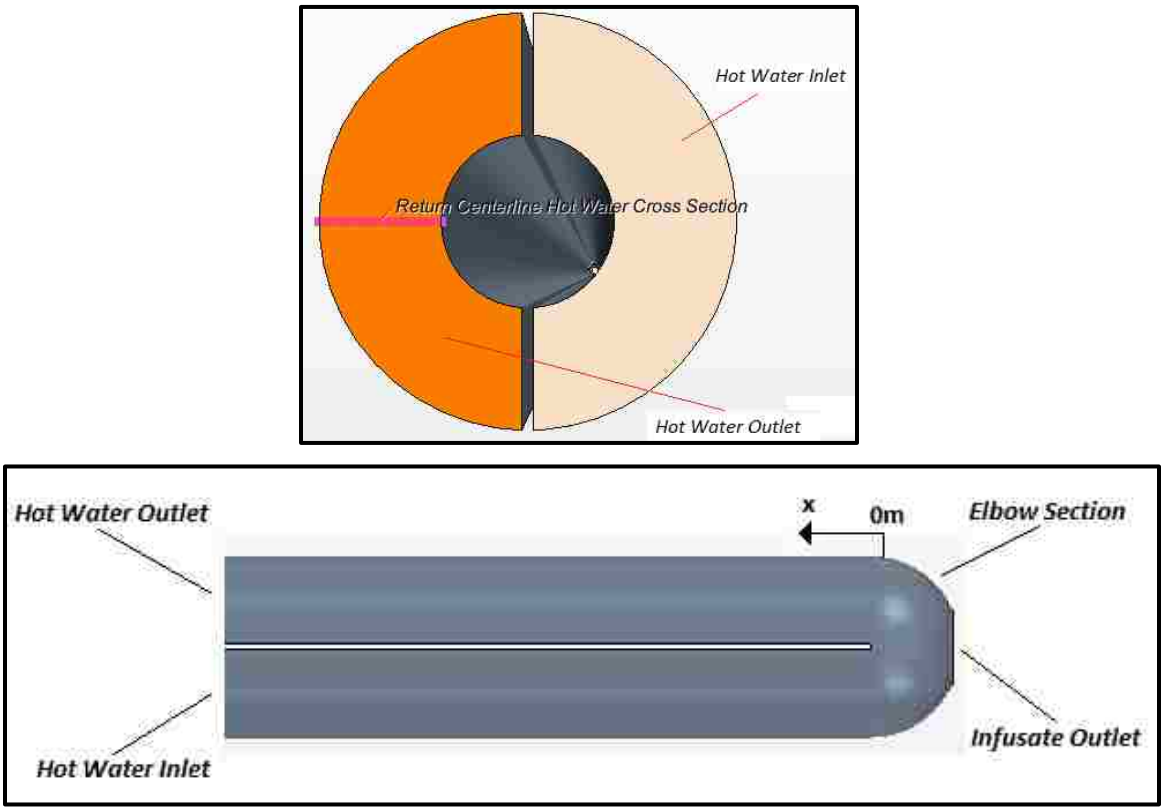

Figure 6.30 Hot Water Centerline/Axial length Locations for Subsequent Velocity Profile Data

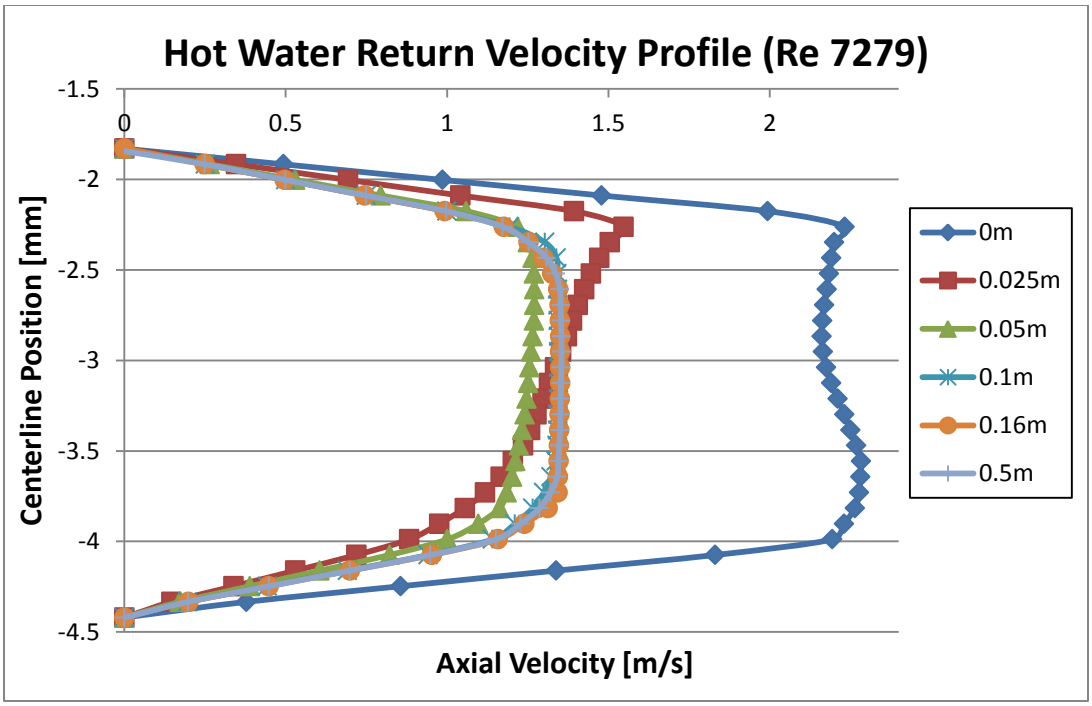

Figure 6.31 Axial Velocity Profile of Developing Flow After Elbow of Hot Water Region (0.6m HE)

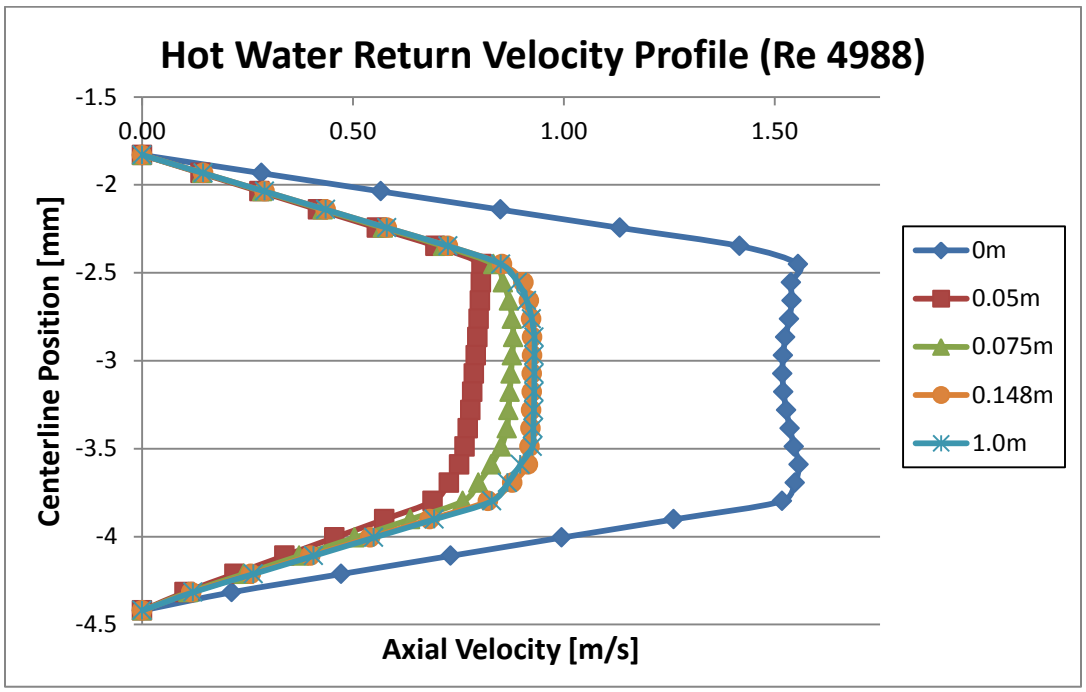

Figure 6.32 Axial Velocity Profile of Developing Flow After Elbow of Hot Water Region (1.2m HE)

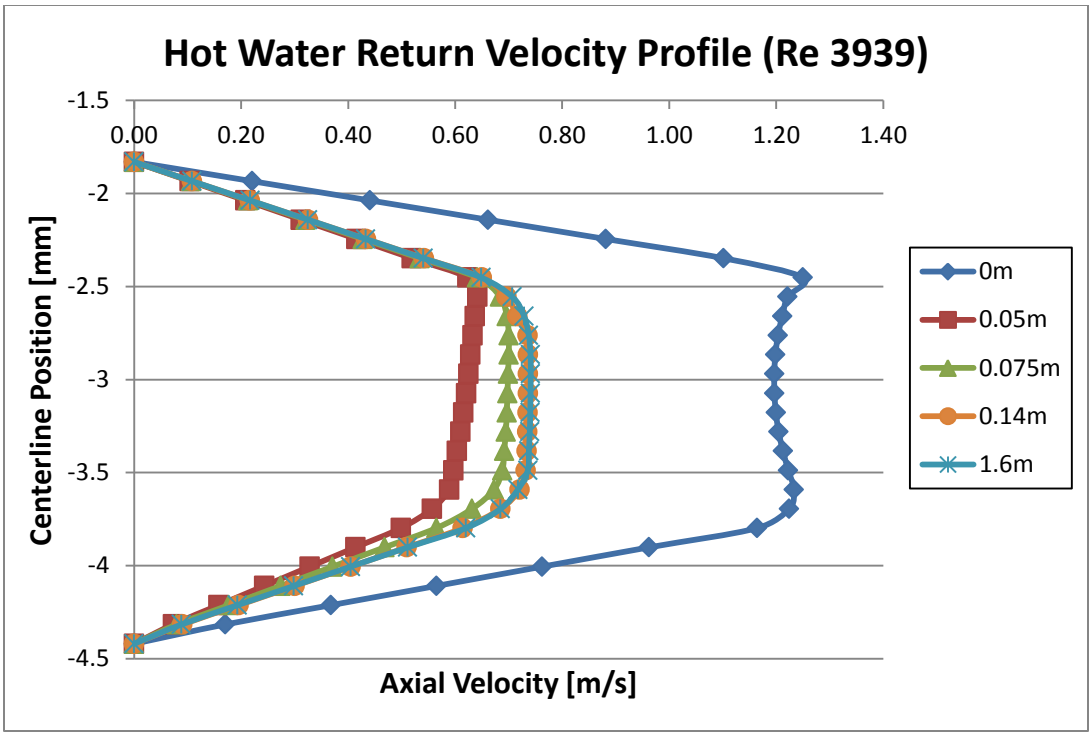

Figure 6.33 Axial Velocity Profile of Developing Flow After Elbow of Hot Water Region (1.8m HE)

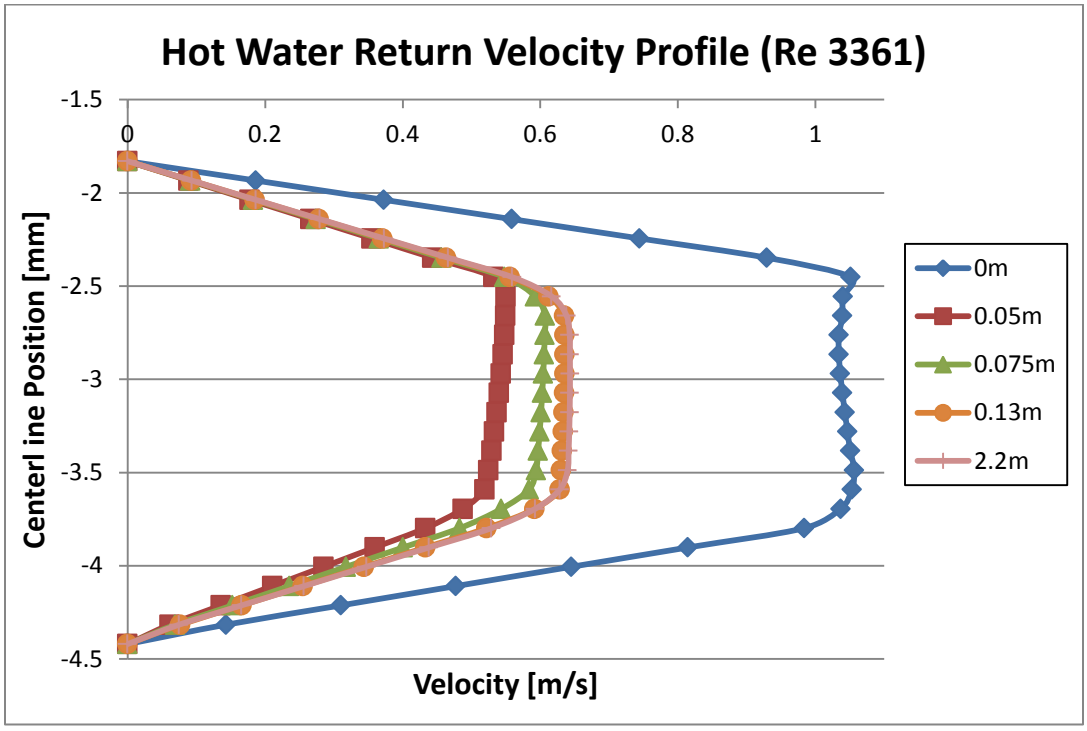

Figure 6.34 Axial Velocity Profile of Developing Flow After Elbow of Hot Water Region (2.4m HE)

Based on Figures 6.31-6.34, with increasing inlet volumetric flow rate of the Hot Water region (increasing Reynolds Number) the developing region increases. The hydrodynamic entrance lengths after the elbow section were determined to be 0.16m, 0.148m, 0.14m, and 0.13m for the respective heat exchanger lengths (0.6m, 1.2m, 1.8m, and 2.4m). The entrance length was determined to be when the axial velocity was 99% of the fully developed profile. Overall, the developing region immediately after the elbow section of the Hot Water region is relatively short when compared to the length of the heat exchanger. Entrance lengths under turbulent flow are typically much shorter when compared to laminar flow, which may account for the short developing regions observed.

To further characterize the hydrodynamic effects within the elbow section of the Hot Water region, plane sections at the apex and base were plotted for velocity magnitude and pressure. Figure 6.35 depicts the location of the plane sections in the Elbow of the Hot Water region. Figures 6.36-6.39 depict velocity magnitude and pressure plots in the Elbow section of the Hot Water region for the different heat exchanger lengths evaluated. A no-slip condition was applied at the wall of the Hot Water region, as such a velocity magnitude of 0m/s is observed at the wall. Inlet velocity of the Hot Water region was greatest for the 0.6m heat exchanger, which accounts for the higher velocity profile. Velocity magnitude is greatest at the inner surface of the Hot Water region for all heat exchanger lengths evaluated. Pressure plots at the elbow section of the Hot Water region reveal increasing pressure from the inner-wall toward the outer-wall of the Hot Water region. Increased pressure at the outer-wall of the Hot Water region concentrates the flow toward the inner-wall. Increased pressure and viscous drag forces near the wall of the elbow section results in the increased velocity profile further from the wall. This observation is consistent with increasing centrifugal forces present within the

elbow section which may account for the increased velocity magnitude and pressure profile observed.

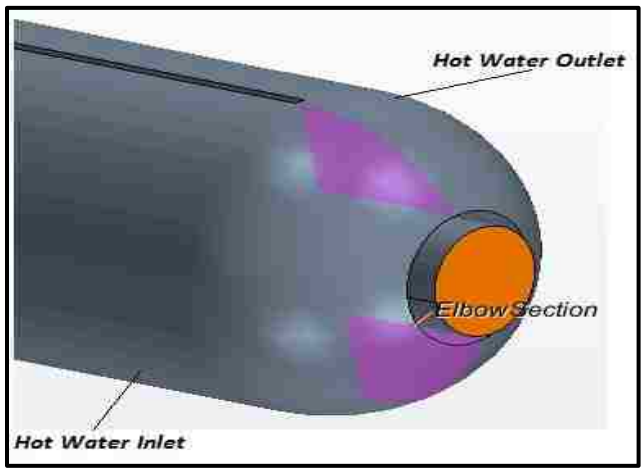

Figure 6.35 Location of Elbow Section Plane

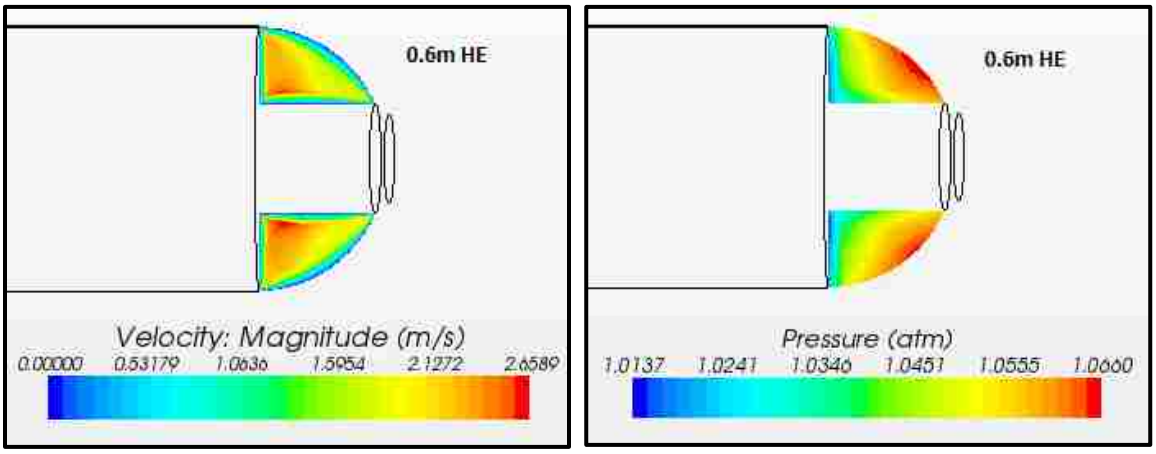

Figure 6.36 Velocity and Pressure Profile Elbow Section of the Hot Water Region (0.6m HE)

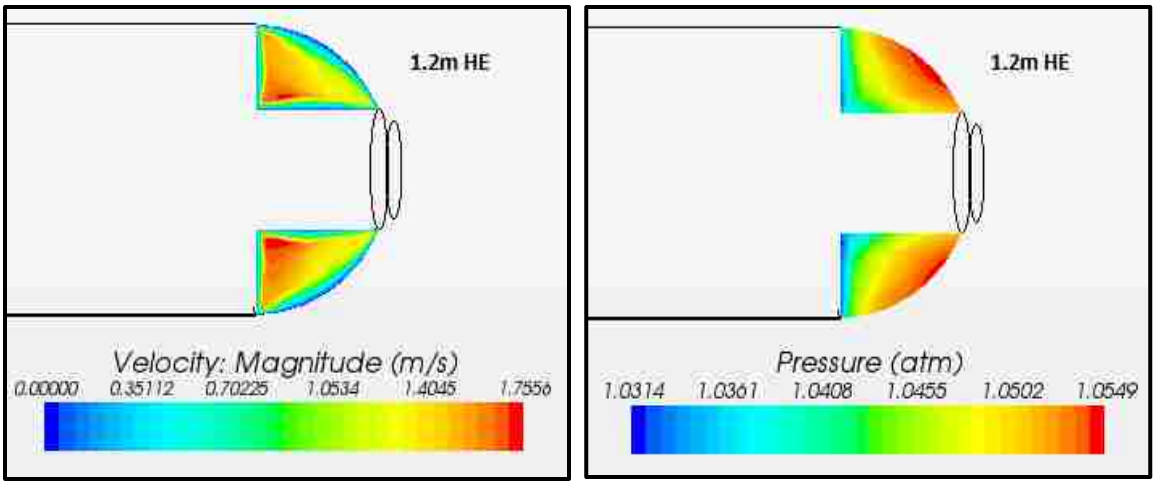

Figure 6.37 Velocity and Pressure Profile Elbow Section of the Hot Water Region (1.2m HE)

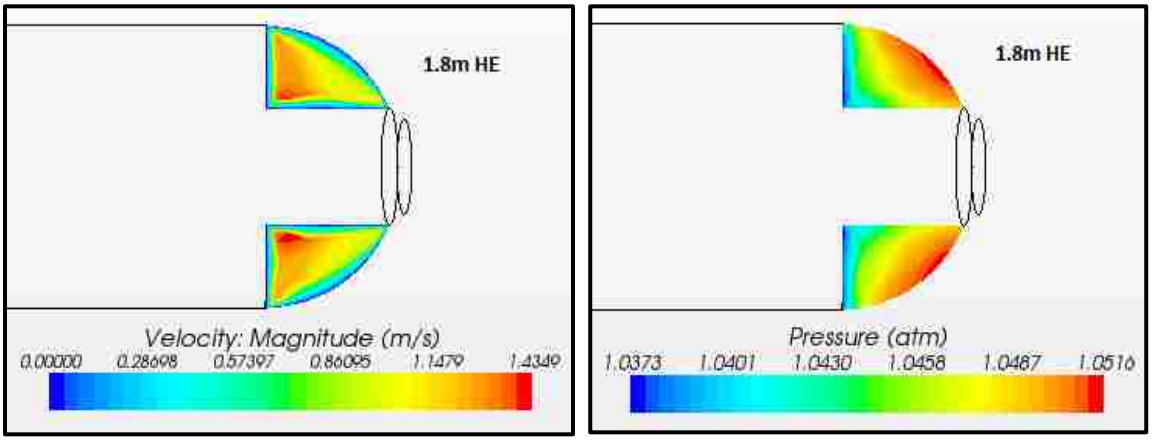

Figure 6.38 Velocity and Pressure Profile Elbow Section of the Hot Water Region (1.8m HE)

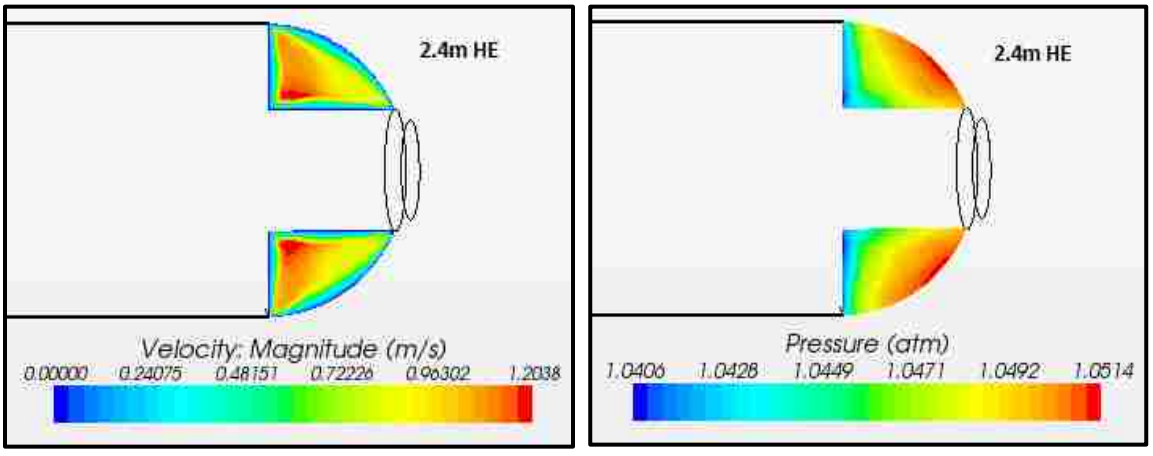

Figure 6.39 Velocity and Pressure Profile Elbow Section of the Hot Water Region (2.4m HE)

To further vizualize the flow characteristics of the elbow section within the Hot Water region, streamlines were plotted. Figure 6.40-6.43 show the streamlines along the entire length of the heat exchanger for the different lengths evaluated. Again the subsequent figures were scaled to accomadate the entire length of the heat exchanger into one image. The developing region at the inlet and after elbow sections of the Hot Water region are relatively short compared to the length of the heat exchanger. As such, a majority of the heat exchanger length consisists of parallel streamlines on both the entrance and return sections. The abrupt change in flow direction at the elbow section results in increased turbulence and velocity magnitude, which is observed in the subsequent streamline plots.

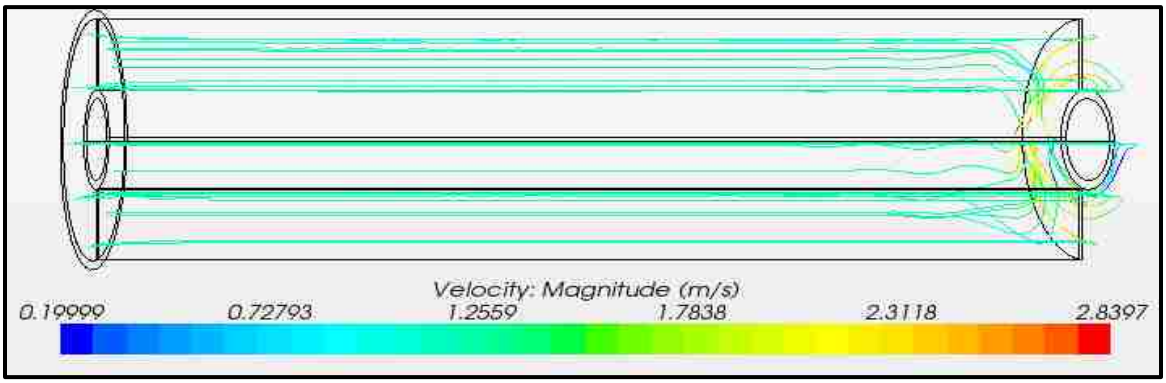

Figure 6.40 Streamlines Along Length of Heat Exchanger Within Hot Water Region (0.6m HE)

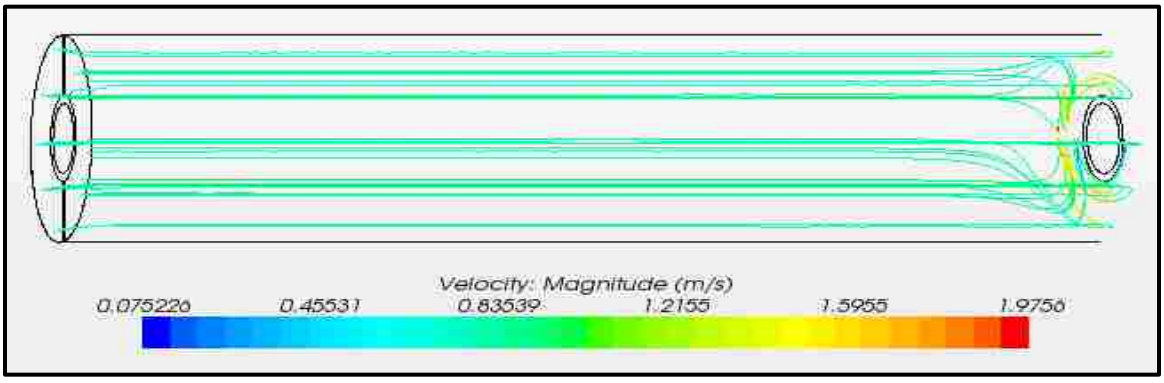

Figure 6.41 Streamlines Along Length of Heat Exchanger Within Hot Water Region (1.2m HE)

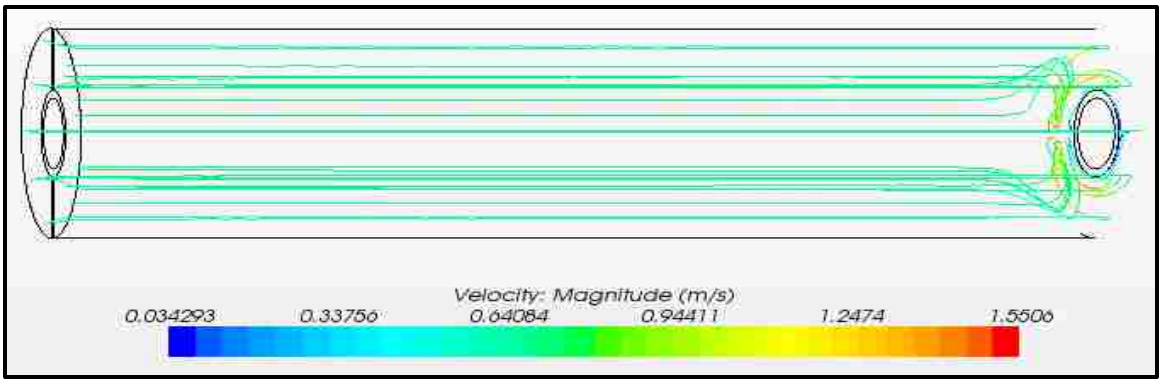

Figure 6.42 Streamlines Along Length of Heat Exchanger Within Hot Water Region (1.8m HE)

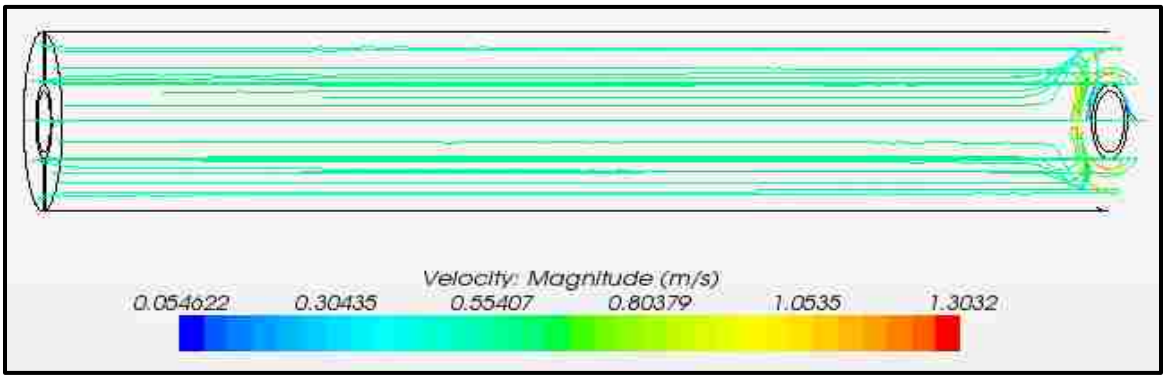

Figure 6.43 Streamlines Along Length of Heat Exchanger Within Hot Water Region (2.4m HE)

To highlight flow characteristics through the elbow section of the Hot Water region, unscaled images of the streamlines were plotted. Figures 6.44-6.47 depict the streamlines through the elbow section of the Hot Water region for the different heat exchanger lengths evaluated. The abrupt change in flow direction within the elbow section of the Hot Water region results in increased centrifugal forces within the flow area. The change in flow direction occurs over a short distance, relative to the length of the heat exchanger. This results in increased centrifugal forces leading to the turbulent flow and increased velocity magnitude obseved within the elbow section of the Hot Water region. Additionally, this yields a new develping flow region immediately after the elbow section of the Hot Wate region. The dimensions of the heat exchangers evaluated are identical except for increases in length. As such, despite the difference

in inlet volumetric flow rates, the flow profile within the elbow section is consistent for all heat exchanger lengths evaluated. Despite the influence of centrifugal forces within the elbow, no stagnation points were identified in the elbow section of the Hot Water region. However, near the outlet of the elbow section, mild circulation was observed for all heat exchanger lengths evaluated. The observed circulation is likely due to increased centrifugal forces within in the elbow section due to the abrupt change in flow direction.

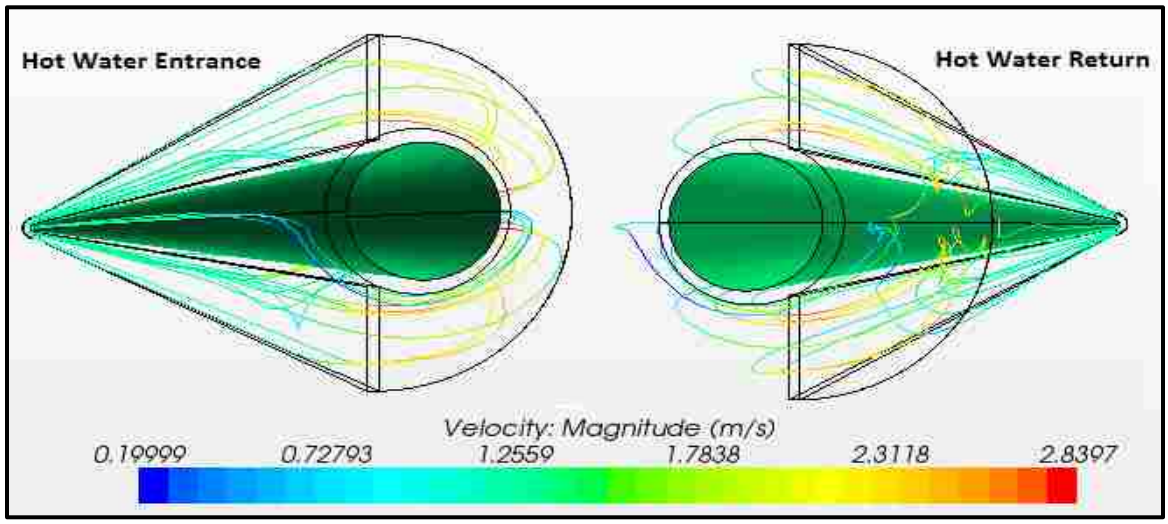

Figure 6.44 Streamlines Within Elbow Section of Hot Water Region (0.6m HE)

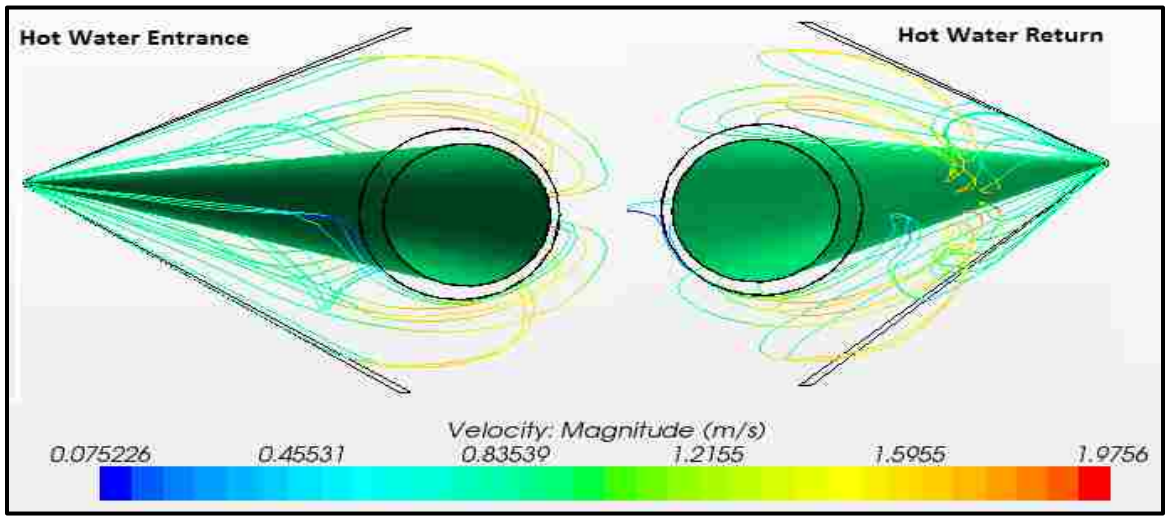

Figure 6.45 Streamlines Within Elbow Section of Hot Water Region (1.2m HE)

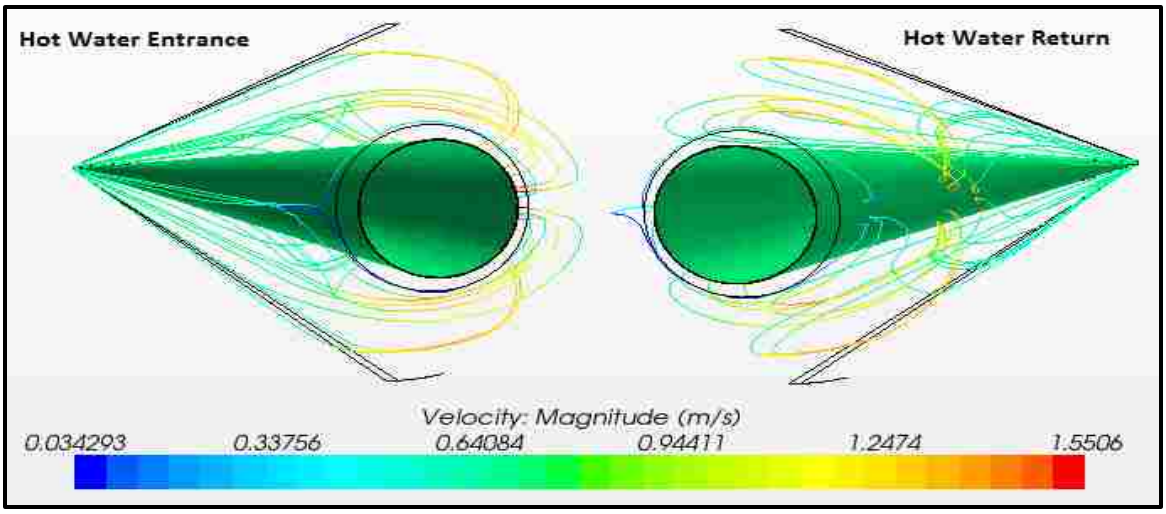

Figure 6.46 Streamlines Within Elbow Section of Hot Water Region (1.8m HE)

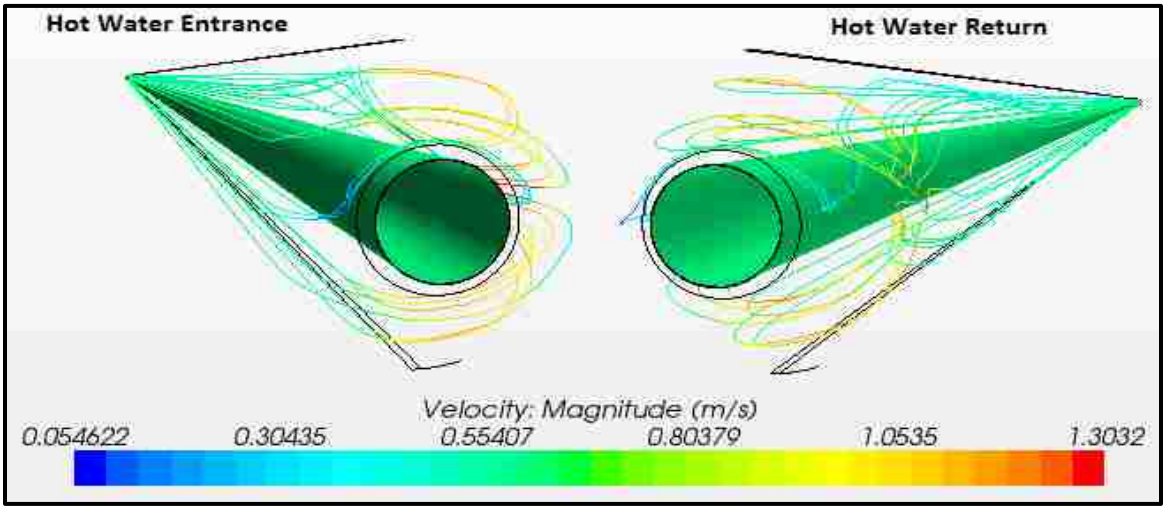

Figure 6.47 Streamlines Within Elbow Section of Hot Water Region (2.4m HE)

6.2 Outlet Temperature vs. Heat Exchanger Length (Increased Infusate Inlet Flow Rate)

The Infusate outlet temperature was again evaluated in terms of heat exchanger length. However, in these simulations the Infusate inlet mass flow rate was increased from 15ml/min to 50ml/min. The boundary conditions used for these simulations are given in Table 5.5. The results of the current CFD simulations were compared to experimental results collected in a paper published in 1998 [27]. Figure 6.48 compares the current CFD predicted outlet

temperatures with the experimental results. As previously mentioned, the experimental outlet temperatures were measured with a center-point temperature probe. The CFD predicted outlet temperatures (bulk temperature) were within 20% of the experimental values. However, when the outlet temperature from the CFD simulations was taken using a center-point probe the measurements were within 6% of the experimental values. Figures 6.49-6.50 show the temperature profile at the Infusate outlet for the different heat exchanger lengths evaluated. Compared to the previous simulations (Section 6.1), the increased Infusate mass flow rate results in a greater temperature gradient at the Infusate outlet for all heat exchanger lengths evaluated. This observation is most prominent for the shorter heat exchanger lengths evaluated. A 13^{o}C temperature difference was observed between the center-point and outer-surface of the Infusate outlet for the 0.6m heat exchanger.

Despite the improved relationship to the experimental data using a center-point temperature probe at the outlet, the thermodynamic properties of the Infusate region is more accurately characterized by using the bulk temperature. Additionally, evaluating in terms of bulk temperature may result in an increased effectiveness of Hypothermia treatment protocols. Evaluating outlet temperature using a center-point probe may result in fluid temperatures above 42^{o}C, which can cause hemolysis or cell degradation and be detrimental to patient care.

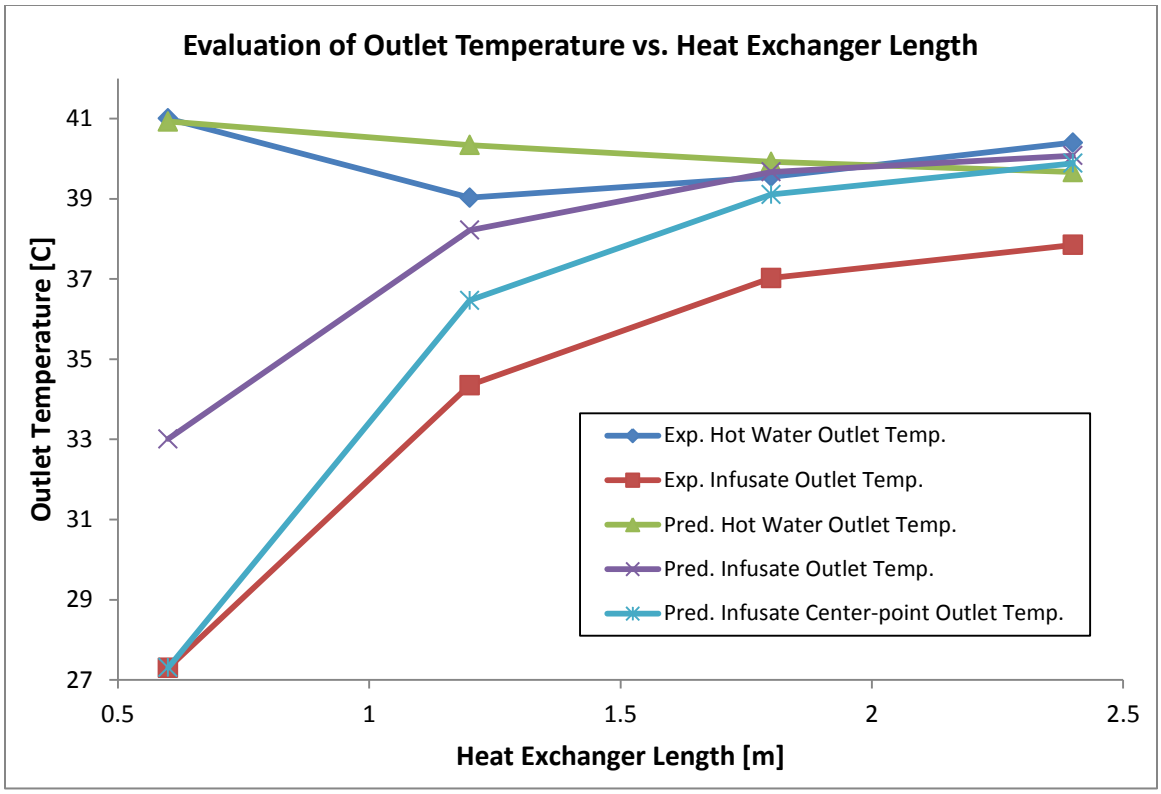

Figure 6.48 Comparison of Outlet Temperatures (CFD Predicted vs. Experimental Results [27])

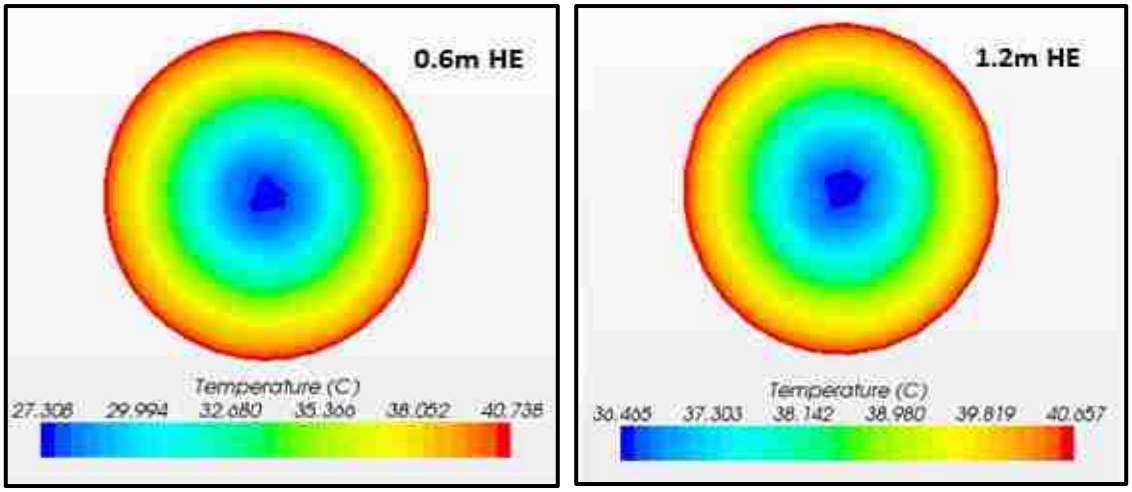

Figure 6.49 Infusate Outlet Temperature Profile (0.6m and 1.2m HE)

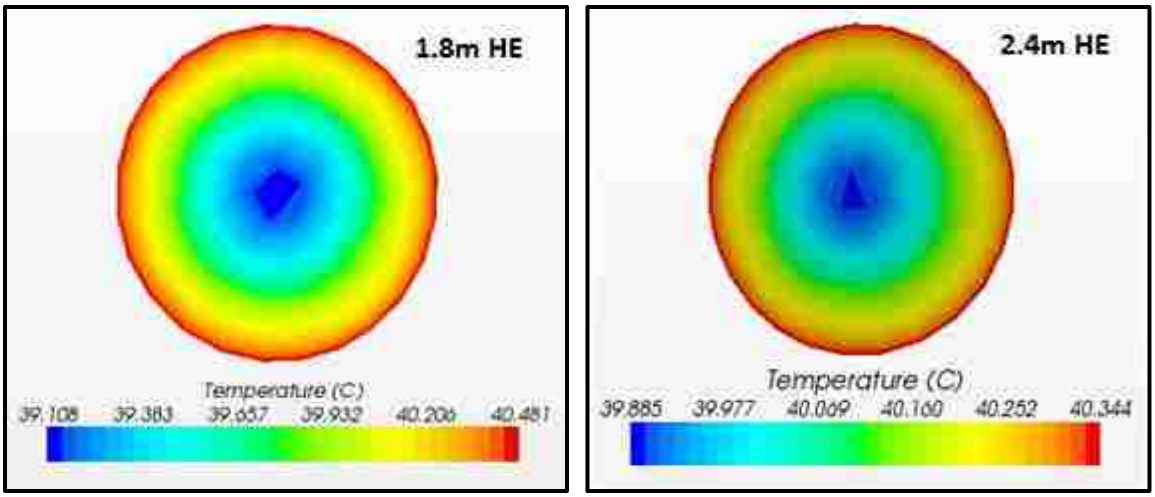

Figure 6.50 Infusate Outlet Temperature Profile (1.8m and 2.4m HE)

The flow conditions within the Hot Water region were identical to the previous set of simulations (Section 6.1). The only difference in this set of simulations was the increase in Infusate inlet mass flow rate. As such, only the thermal properties of the heat exchanger were evaluated. A center-plane section of the Infusate region was plotted in terms of temperature (Figures 6.51-6.54). Similar to the previous simulations, a parabolic thermal profile is seen within the cylindrical geometry of the Infusate region. In the previous set of simulations (Section 6.1), the Infusate region reached an approximate uniform temperature profile at the outlet for all heat exchanger lengths evaluated. By increasing the Infusate inlet mass flow rate to 50ml/min, only the 2.4m HE reached an approximate uniform temperature profile at the outlet. This is a direct function of HE length, as the Infusate inlet mass flow rate was the same for all heat exchanger lengths evaluated. Due to the laminar flow conditions within the Infusate region, the fully developed Nusselt number should be approximately constant. As such, increased heat exchanger length under the same laminar flow conditions would reach higher mean bulk temperatures at the outlet. Additionally, for lower flow rates a higher outlet temperature is

expected to satisfy the basic energy balance principle, which explains the decreased mean bulk temperatures observed at the outlet when compared to the previous simulations.

There was an approximately 13°C difference in temperature between the center-point and walls of the Infusate outlet for the 0.6m heat exchanger. This observation could potentially impact the respective Hypothermia treatment, as the fluid temperature delivered to the patient may not be as desired. Overall, the inlet Infusate mass flow rate of 50ml/min is much too fast to allow for adequate heat transfer in 0.6m, 1.2m, and 1.8m heat exchangers. However, the 2.4m heat exchanger length did produce a relatively uniform temperature profile at the Infusate outlet and may be acceptable for warming therapy.

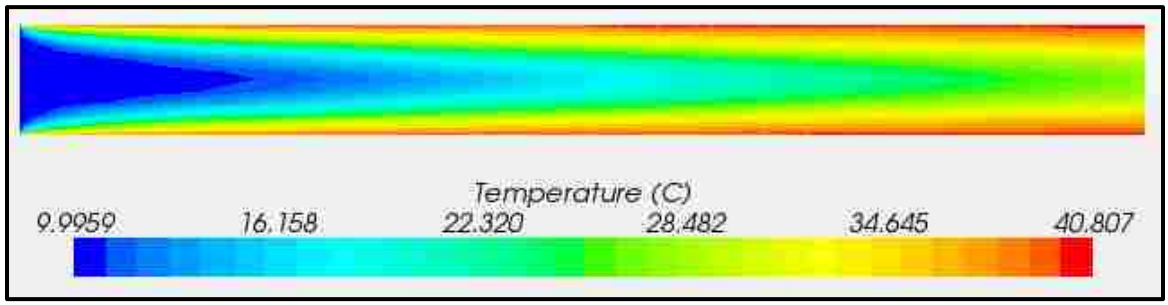

Figure 6.51 Infusate Center-Plane Temperature Profile (0.6m HE, Increased Infusate Flow Rate)

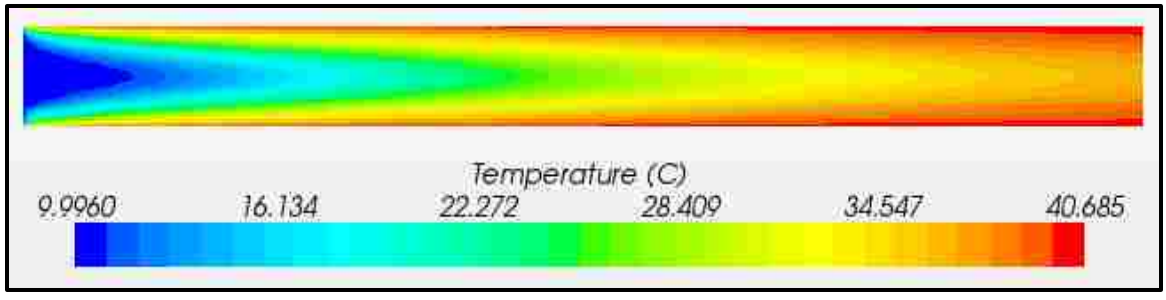

Figure 6.52 Infusate Center-Plane Temperature Profile (1.2m HE, Increased Infusate Flow Rate)

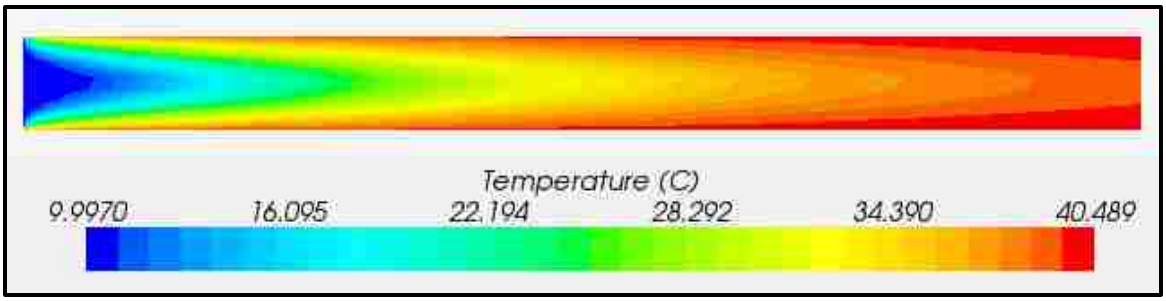

Figure 6.53 Infusate Center-Plane Temperature Profile (1.8m HE, Increased Infusate Flow Rate)

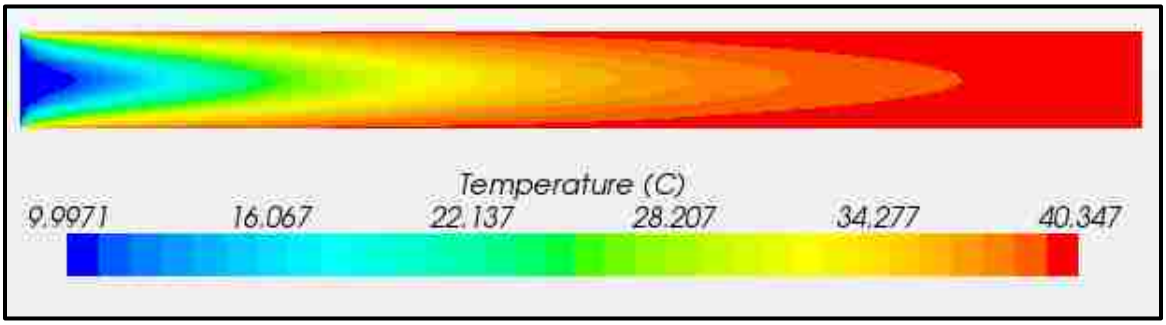

Figure 6.54 Infusate Center-Plane Temperature Profile (2.4m HE, Increased Infusate Flow Rate)

The temperature profile of the outer-surface of the Infusate region was also examined (Figures 6.55-6.58). Unlike the interior temperature profile of the Infusate region, the outer-surface reached a uniform temperature profile before the outlet. Again heat transfer is only allowed between the Infusate and Hot Water regions due to the adiabatic conditions at the heat exchanger surface. The outer-surface of the Infusate region is closer in proximity to the Hot Water region. This results in the outer-surface reaching a uniform temperature profile closer to the inlet than the interior of the Infusate region for all heat exchanger lengths examined.

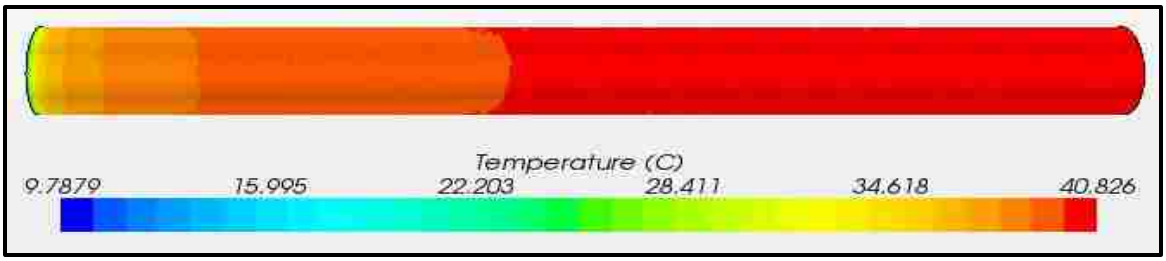

Figure 6.55 Infusate Outer-Surface Temperature Profile (0.6m HE, Increased Infusate Flow Rate)

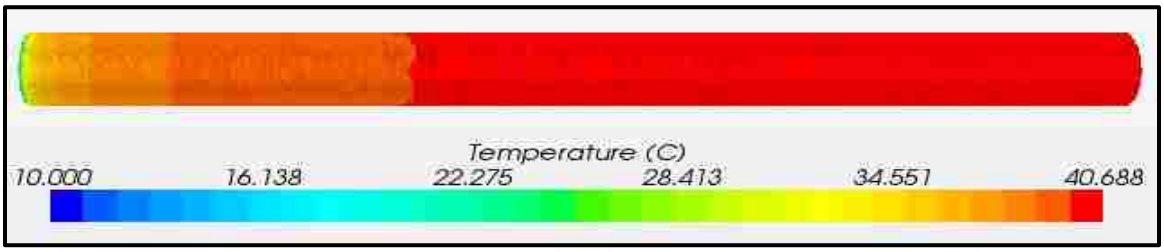

Figure 6.56 Infusate Outer-Surface Temperature Profile (1.2m HE, Increased Infusate Flow Rate)

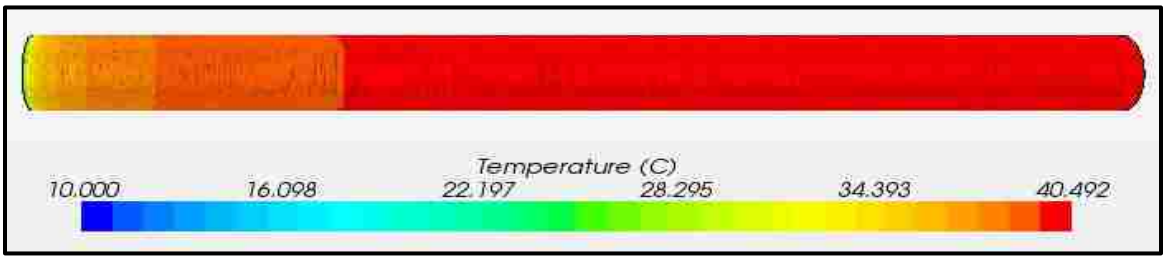

Figure 6.57 Infusate Outer-Surface Temperature Profile (1.8m HE, Increased Infusate Flow Rate)

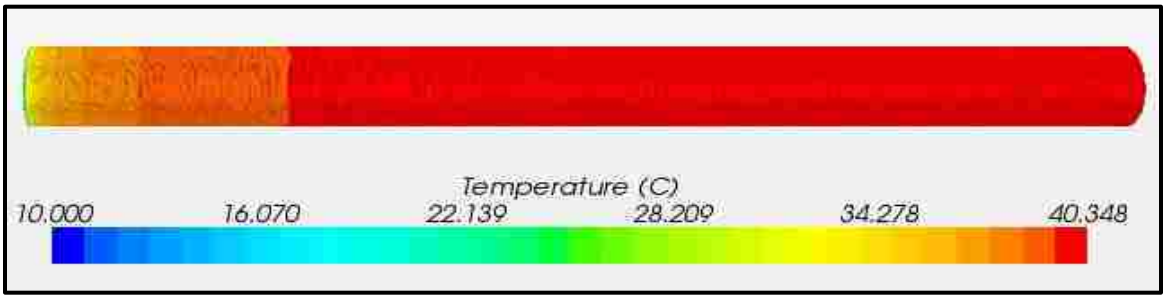

Figure 6.58 Infusate Outer-Surface Temperature Profile (2.4m HE, Increased Infusate Flow Rate)

To help visualize the thermal profile within the Hot Water region, a center-plane section along the length of heat exchanger was plotted in terms of temperature (Figure 6.59-6.62). Due

to the length of the heat exchanger, the subsequent figures were scaled to accommodate the entire length into one figure. The thermal profile is much more varied, when compared to the previous simulations (Section 6.1). The increased Infusate flow rate in these simulations would require lower outlet temperatures to satisfy the energy balance principle than the previous set of simulations (Section 6.1). This results in the decreased mean bulk temperature observed at the Infusate and Hot Water outlets for all heat exchanger lengths examined. Due to unique configuration of the heat exchanger thermal equilibrium was not reached between the Infusate and Hot Water sections for all heat exchanger lengths evaluated. This is likely due to the effects of heat transfer across both sides of the Infusate region, as a result of the parallel/counter-parallel orientation of the heat exchanger.

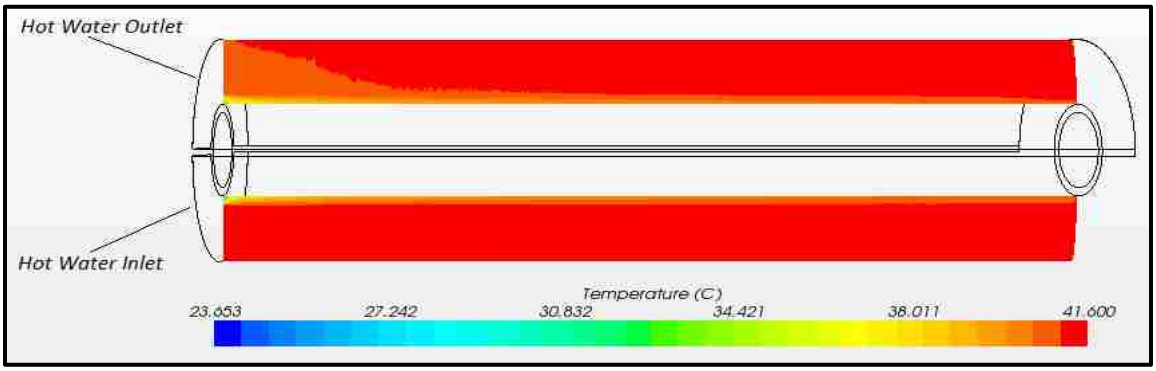

Figure 6.59 Hot Water Center-Plane Temperature Profile (0.6m HE, Increased Infusate Flow Rate)

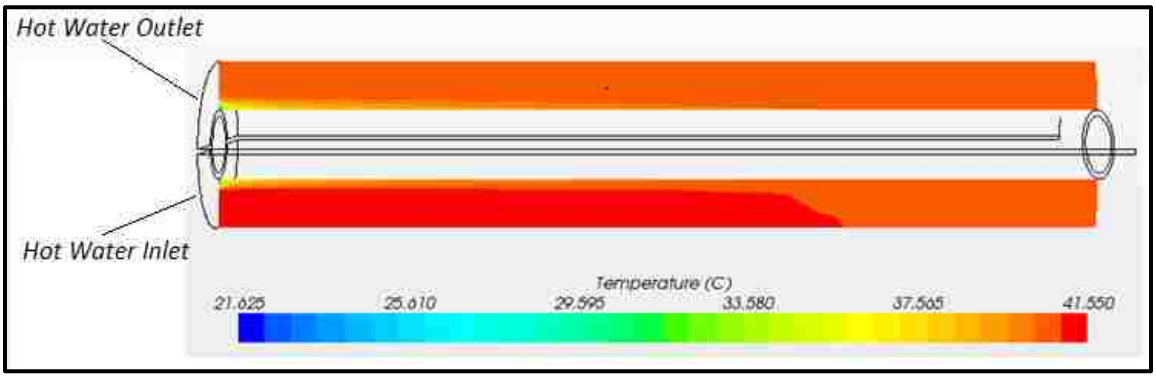

Figure 6.60 Hot Water Center-Plane Temperature Profile (1.2m HE, Increased Infusate Flow Rate)

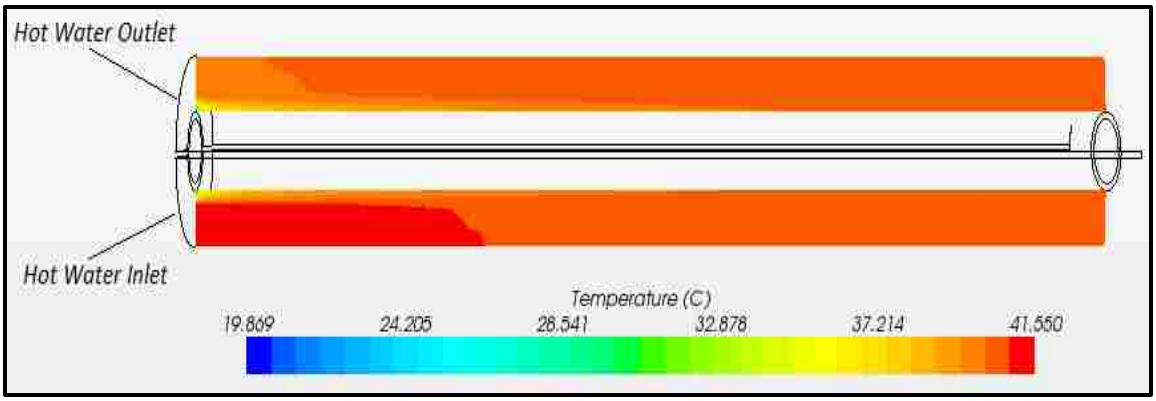

Figure 6.61 Hot Water Center-Plane Temperature Profile (1.8m HE, Increased Infusate Flow Rate)

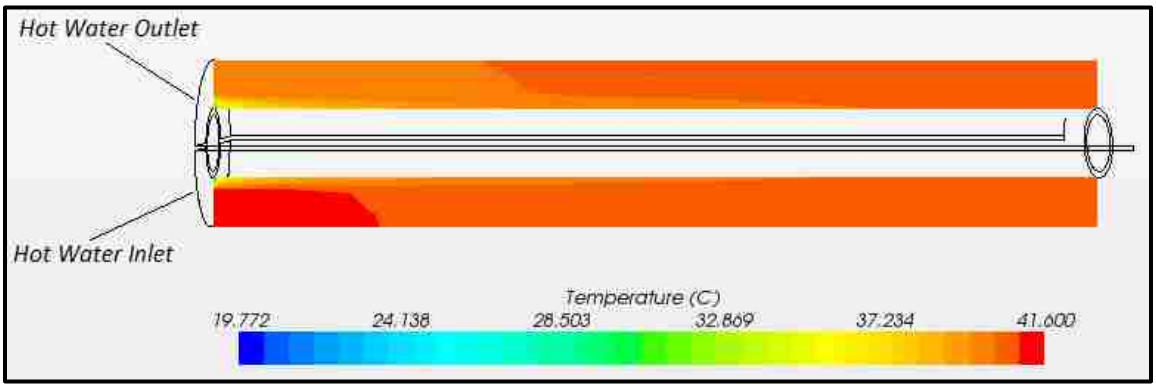

Figure 6.62 Hot Water Center-Plane Temperature Profile (2.4m HE, Increased Infusate Flow Rate)

6.3 Outlet Temperature vs. Infusate Inlet Flow Rate

In these simulations, the effect of increasing Infusate inlet mass flow rate on the Infusate outlet temperature was evaluated. The boundary conditions used for these simulations are given in Table 5.6. The results of the current CFD simulations were compared to previously collected experimental data [27]. Figure 6.63 compares the current CFD predicted outlet temperatures with the experimental results; no experimental data for the Hot Water region was available. As previously mentioned, the experimental outlet temperatures were measured with a center-point temperature probe, whereas bulk temperature was evaluated in the CFD simulations. The CFD predicted outlet temperatures were within 7% of the experimental values, and should be applicable for future design purposes. However, as experimental outlet

temperatures were only evaluated using a center-point temperature probe, more detailed temperature comparisons were not able to be made.

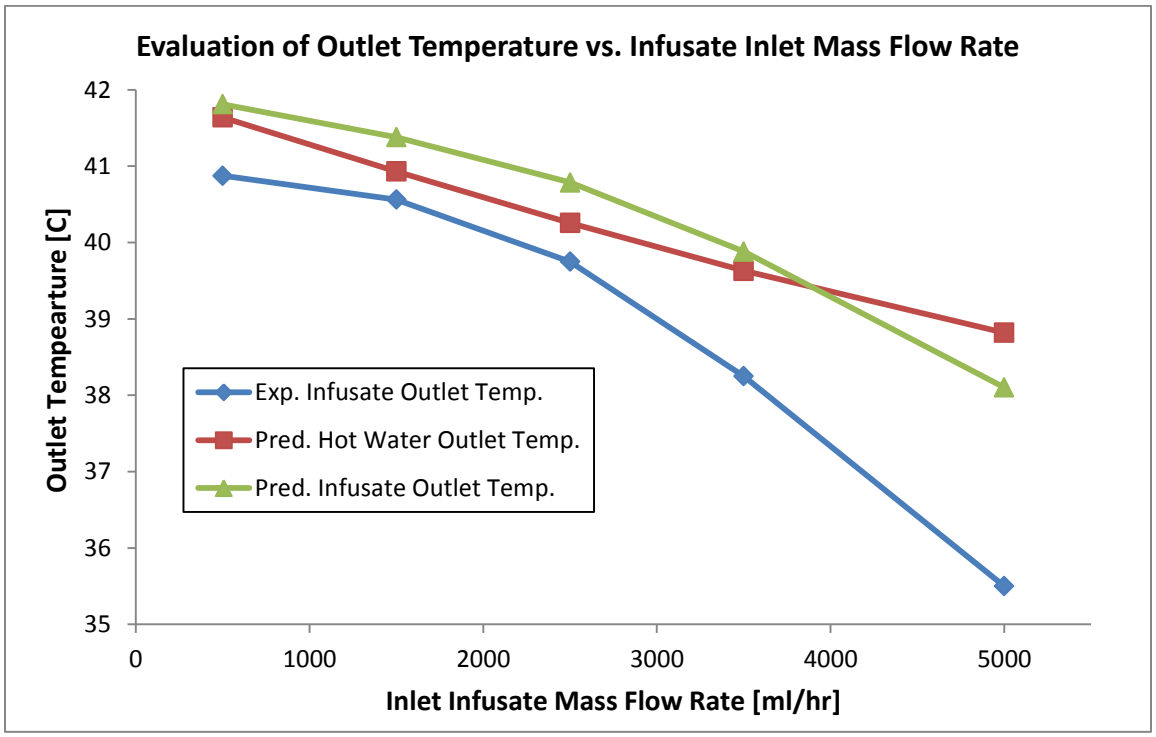

Figure 6.63 Comparison of Outlet Temperatures (CFD Predicted vs. Experimental Results [27])

The flow conditions within the Hot Water region were similar to the previous sets of simulations (Section 6.1 and 6.2). As such, this set of simulations was only evaluated in terms of the thermal properties. This study considered the effect of increasing Infusate inlet mass flow rate on heat transfer within the heat exchanger. Only the 2.4m heat exchanger was considered in these simulations. To characterize the thermal profile within the Infusate region, a center-plane was plotted along the length of the heat exchanger in terms of temperature (figures 6.64-6.68). Increasing Infusate inlet mass flow rate resulted in increased axial distance for the temperature profile to become uniform (to reach a minimum heat transfer rate on the Infusate side). Equilibrium between the Infusate and Hot Water regions is not reached due to the flow

configuration of the Hot Water region. The fully developed Nusselt number should be approximately constant within the laminar regime of the Infusate region. The Infusate inlet mass flow rate is the independent variable in this analysis. For increasing mass flow rate, the outlet mean bulk temperature is expected to decrease to satisfy basic energy balance principle. As such, increased axial distance from the inlet is required for a uniform temperature profile to be reached in the Infusate region for the higher flow rates examined. For the 5000ml/hr flow rate, the temperature profile within the Infusate region did not reach a uniform temperature profile before the outlet of the heat exchanger. Flow rates greater than 5000ml/hr for the Infusate region would require longer heat exchanger lengths to reach acceptable temperature profiles at the outlet. For the evaluated flow conditions, flow rates less than 5000ml/hr should be for a heat exchanger of 2.4m, as a uniform fluid temperature delivered to the patient is more optimal for Hypothermia treatment.

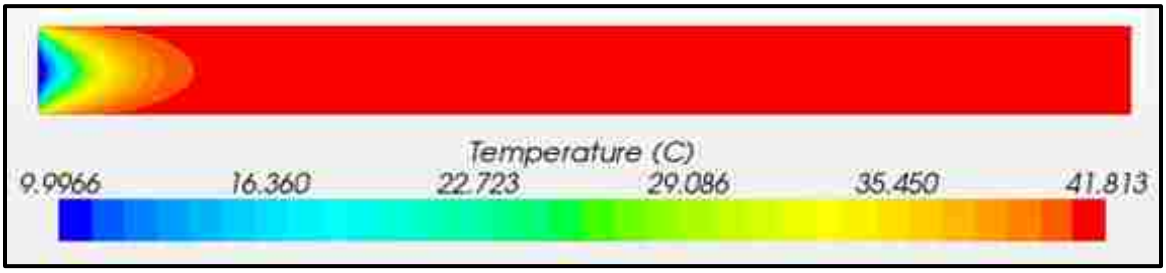

Figure 6.64 Infusate Center-Plane Temperature Profile (500ml/hr Infusate Flow Rate)

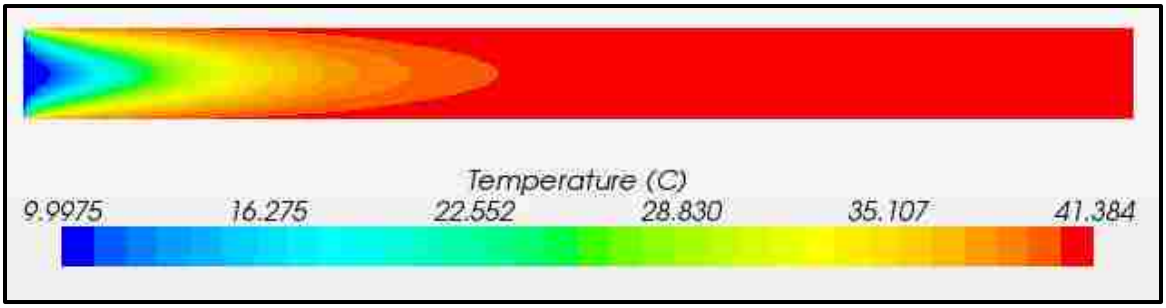

Figure 6.65 Infusate Center-Plane Temperature Profile (1500ml/hr Infusate Flow Rate)

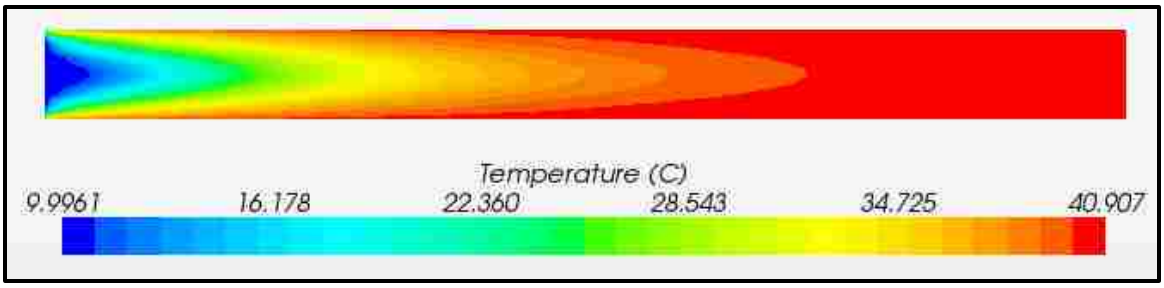

Figure 6.66 Infusate Center-Plane Temperature Profile (2500ml/hr Infusate Flow Rate)

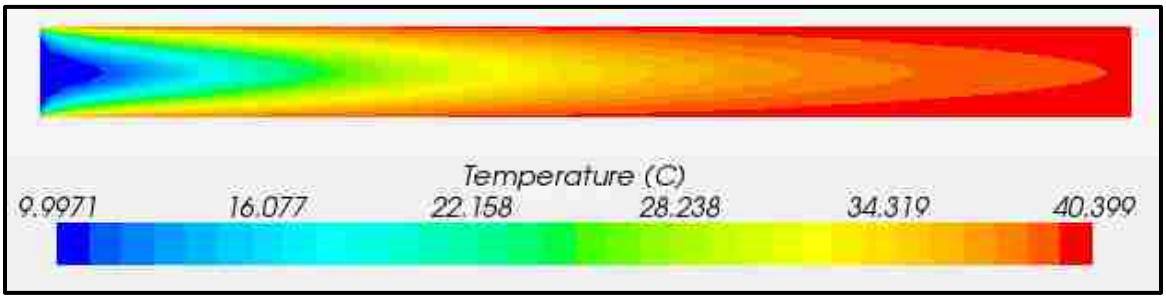

Figure 6.67 Infusate Center-Plane Temperature Profile (3500ml/hr Infusate Flow Rate)

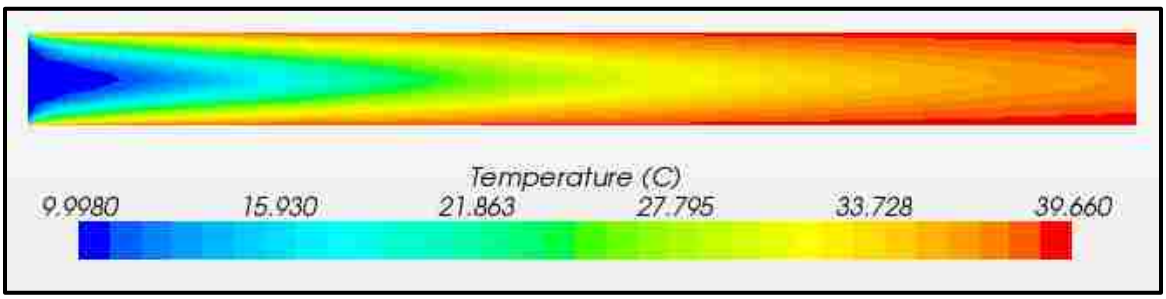

Figure 6.68 Infusate Center-Plane Temperature Profile (5000ml/hr Infusate Flow Rate)

The temperature profile on the outer-surface of the Infusate region was also examined (Figures 6.69-6.73). Similar to the previous simulations, the outer-surface reached a uniform temperature at a shorter distance from the inlet than the interior of the Infusate region. The outer-surface of the Infusate region reached a uniform temperature profile before the outlet for all Infusate flow rates evaluated. Again, this is directly related to the boundary conditions and proximity to the Hot Water region. Additionally, increasing Infusate flow rate results in

increased axial distance for a uniform temperature profile to be reached within the Infusate region. This is related to the impact of increased flow rates on the energy balance.

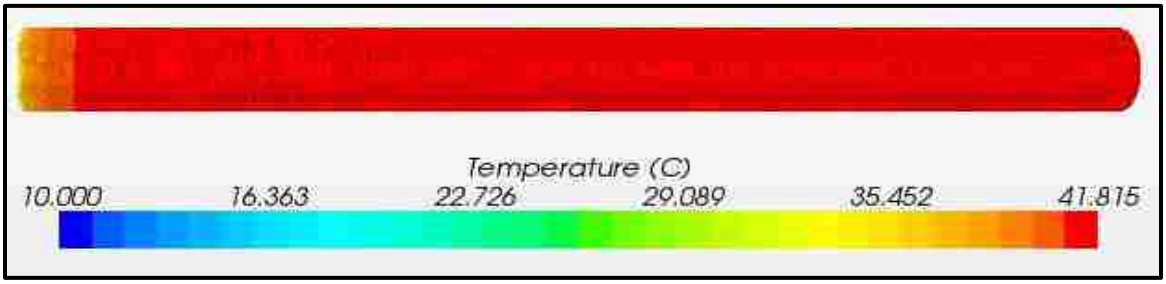

Figure 6.69 Infusate Outer-Surface Temperature Profile (500ml/hr Infusate Flow Rate)

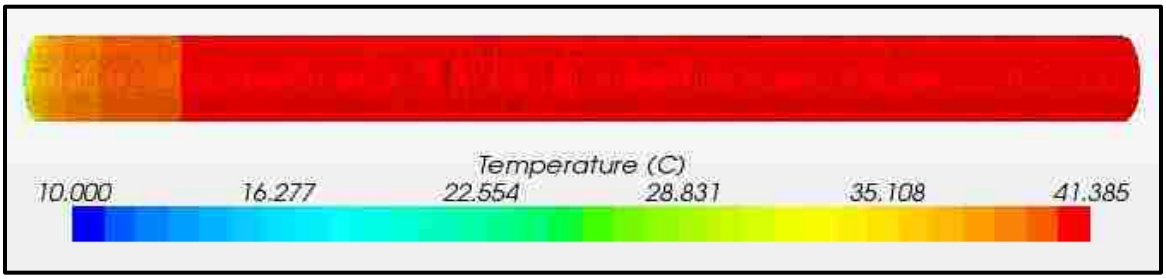

Figure 6.70 Infusate Outer-Surface Temperature Profile (1500ml/hr Infusate Flow Rate)

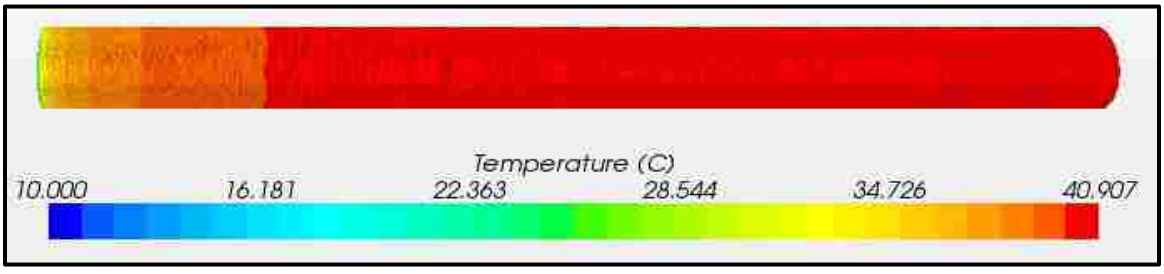

Figure 6.71 Infusate Outer-Surface Temperature Profile (2500ml/hr Infusate Flow Rate)

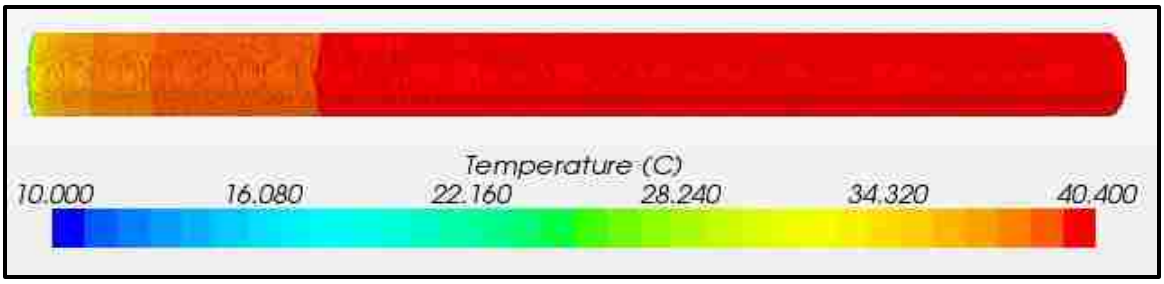

Figure 6.72 Infusate Outer-Surface Temperature Profile (3500ml/hr Infusate Flow Rate)

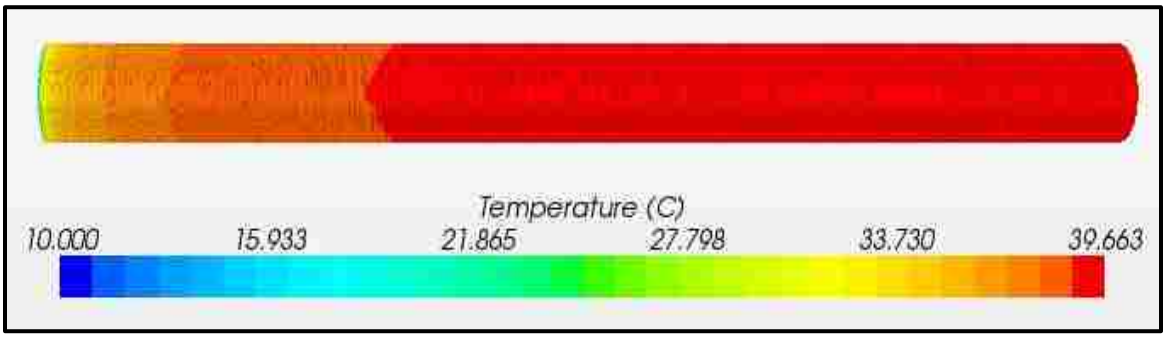

Figure 6.73 Infusate Outer-Surface Temperature Profile (5000ml/hr Infusate Flow Rate)

To visualize the thermal profile within the Hot Water region, a center-plane section along the length of heat exchanger was plotted in terms of temperature (Figure 6.74-6.78). Due to the length of the heat exchanger, the subsequent figures were scaled to accommodate the entire length into one figure. Increased temperature variation within the Hot Water region is seen with increasing Infusate mass flow rate. Specifically, temperatures within the Hot Water region decreased with increasing Infusate mass flow rate. The inlet boundary conditions for the Hot Water region were the same for all simulations evaluated; only the Infusate mass flow rate was varied. As such, the decreased temperature profile within the Hot Water region is directly related to the increase in Infusate mass flow rate. As the mass flow rate increases, outlet mean bulk temperature decreases to satisfy the basic energy balance principle. This results in the

decrease in outlet mean bulk temperature observed in the Infusate and Hot Water regions, as well as the thermal profile variation in the Hot Water region.

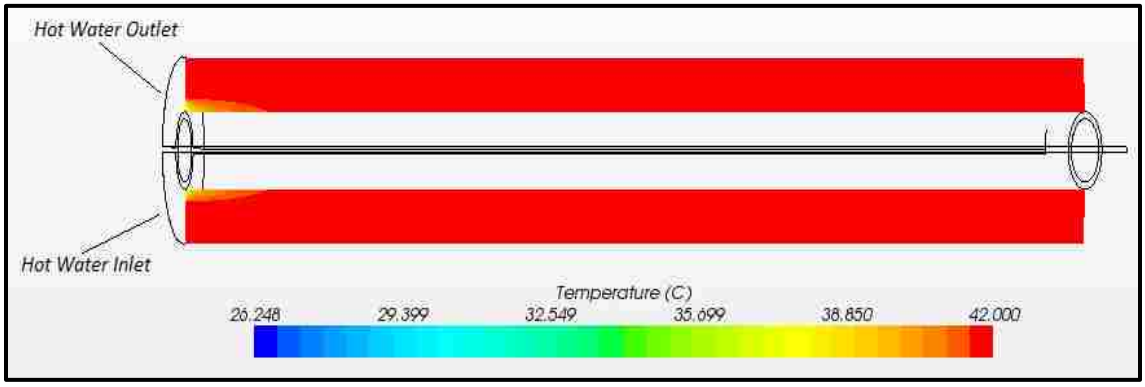

Figure 6.74 Hot Water Center-Plane Temperature Profile (500ml/hr Infusate Flow Rate)

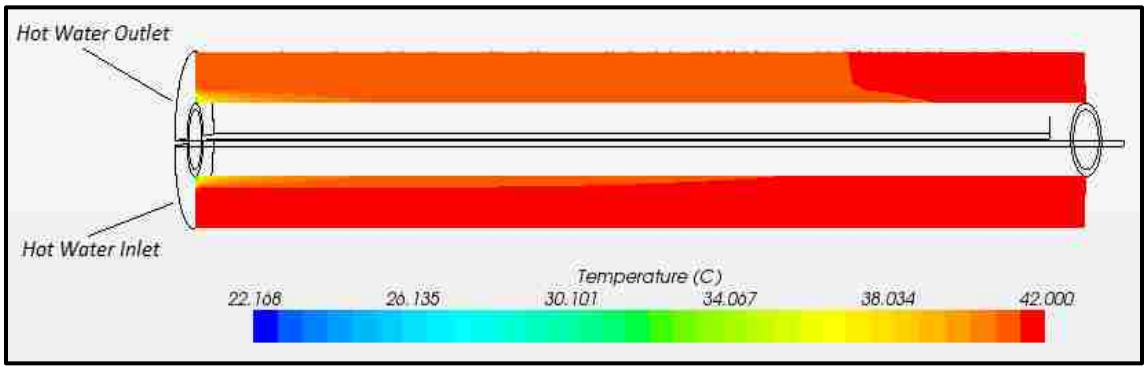

Figure 6.75 Hot Water Center-Plane Temperature Profile (1500ml/hr Infusate Flow Rate)

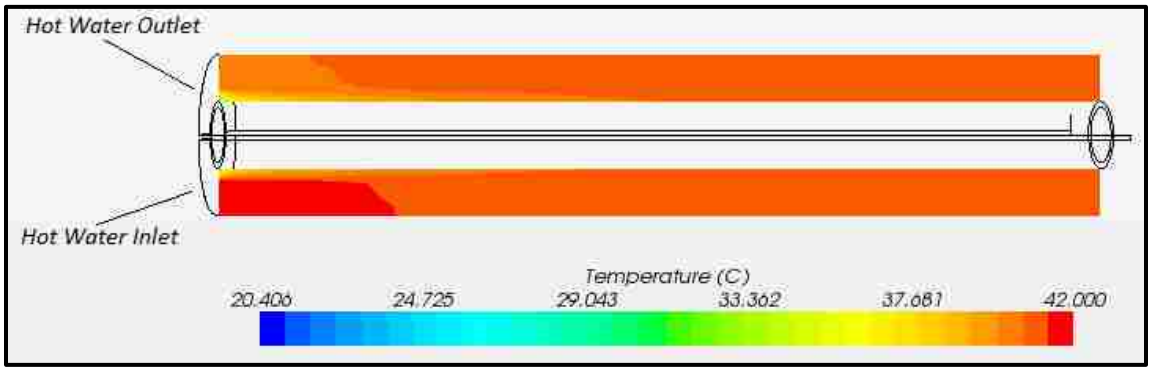

Figure 6.76 Hot Water Center-Plane Temperature Profile (2500ml/hr Infusate Flow Rate)

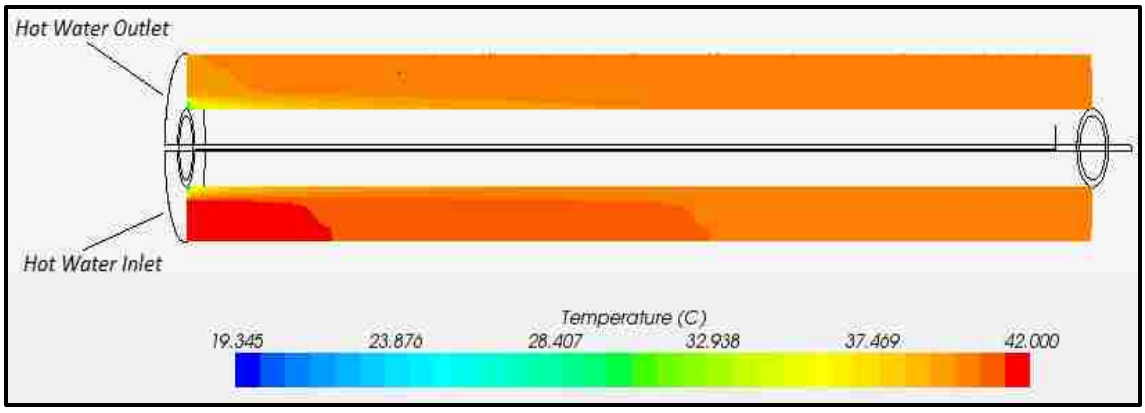

Figure 6.77 Hot Water Center-Plane Temperature Profile (3500ml/hr Infusate Flow Rate)

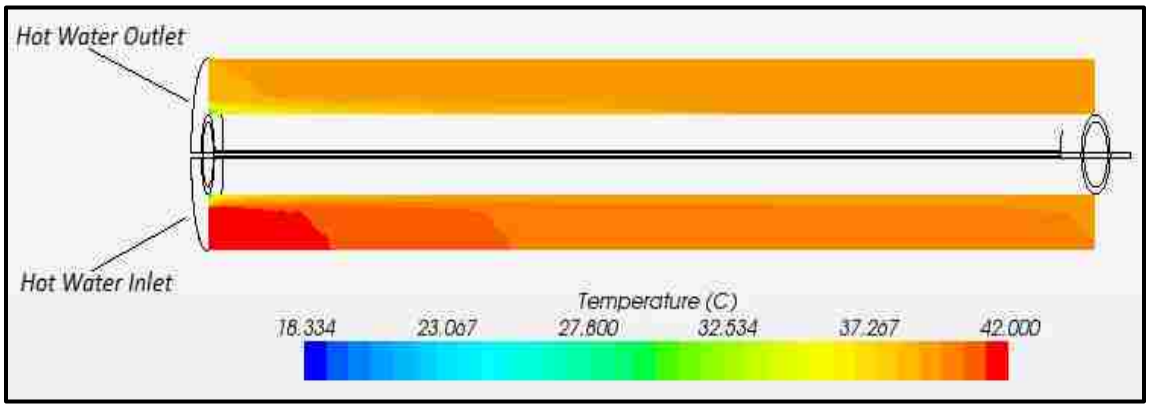

Figure 6.78 Hot Water Center-Plane Temperature Profile (5000ml/hr Infusate Flow Rate)

6.4 Outlet Temperature vs. Infusate Inlet Flow Rate (Increased Infusate Inlet Temperature)

In these simulations, the effect of increasing Infusate inlet mass flow rate on Infusate outlet temperature was again examined. However, the Infusate inlet temperature was increased from 10°C to 20°C. The boundary conditions used for these simulations are given in Table 5.7. The results of the current CFD simulations were compared to previously collected experimental data [27]. Figure 6.79 compares the current CFD predicted outlet temperatures with the experimental results; no experimental data for the Hot Water region was available. As previously mentioned, the experimental outlet temperatures were measured with a center-point temperature probe, whereas bulk temperature was determined in the CFD simulations.

The CFD predicted outlet temperatures were within 7% of the experimental values, and should be applicable for future design purposes. However, as experimental outlet temperatures were only evaluated using a center-point temperature probe, more detailed temperature comparisons were not able to be made.

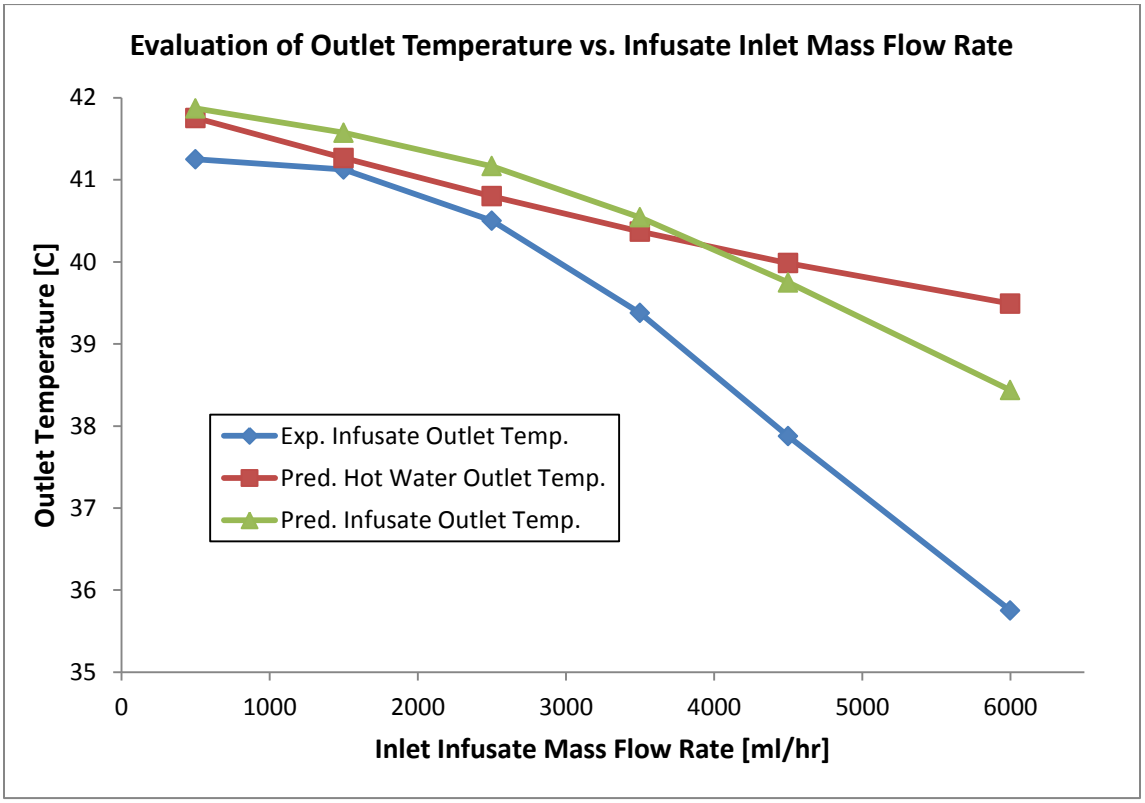

Figure 6.79 Comparison of Outlet Temperatures (CFD Predicted vs. Experimental Results [27])

Again only the thermal properties of the heat exchanger were considered. The boundary conditions are identical to the previous simulations (Section 6.3), except for an increase in the Infusate inlet temperature (10°C vs. 20°C). To visualize the thermal profile within the Infusate region, a center-plane section was plotted along the length of the heat exchanger in terms of temperature (figures 6.80-6.85). Similar to the previous simulations, increasing Infusate mass flow rate results in increased axial distance for a uniform temperature profile to be reached

within the Infusate region (minimum heat transfer rate on the Infusate side). However, in these simulations the heat transfer rate was not only affected by increased mass flow rate but also by a decrease in temperature gradient across the Infusate and Hot Water regions. Higher mass flow rates require increased heat exchanger length to approach uniform temperature profiles at the outlet. Convective heat transfer can be expressed using the following equation [20]:

$$q'' = hA(T_s - T_{amb}) \quad [23]$$

Where,

q" = Heat Transfer Rate
h = Heat Transfer Coefficient
A = Heat Transfer Surface Area
T_s = Solid Surface Temperature
T_{amb} = Ambient Temperature

Based on this relationship, the temperature gradient is proportional to the heat transfer rate. As such, a decreased temperature gradient across the Infusate and Hot Water regions result in a decrease in heat transfer rate. This decrease in heat transfer rate accounts for the decreased mean bulk outlet temperature in the Infusate and Hot Water regions observed for increasing Infusate mass flow rate. For the 4500ml/hr and 6000ml/hr flow rates, greater heat exchanger length is required for the thermal profile to stabilize. As such, when using these boundary conditions, flow rates less than 4000ml/hr should be considered within the Infusate region to ensure optimal Hypothermia treatment.

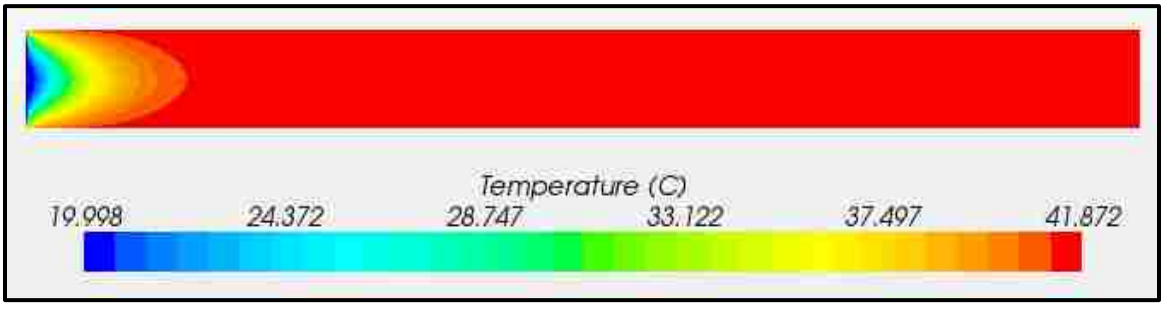

Figure 6.80 Infusate Center-Plane Temperature Profile (500ml/hr Infusate Flow Rate)

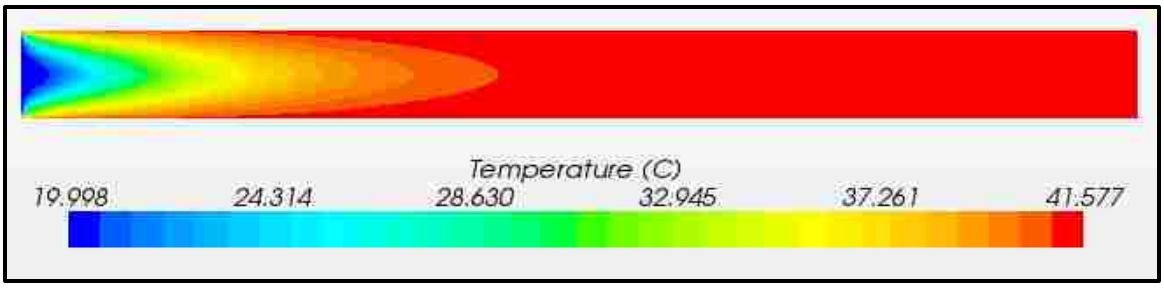

Figure 6.81 Infusate Center-Plane Temperature Profile (1500ml/hr Infusate Flow Rate)

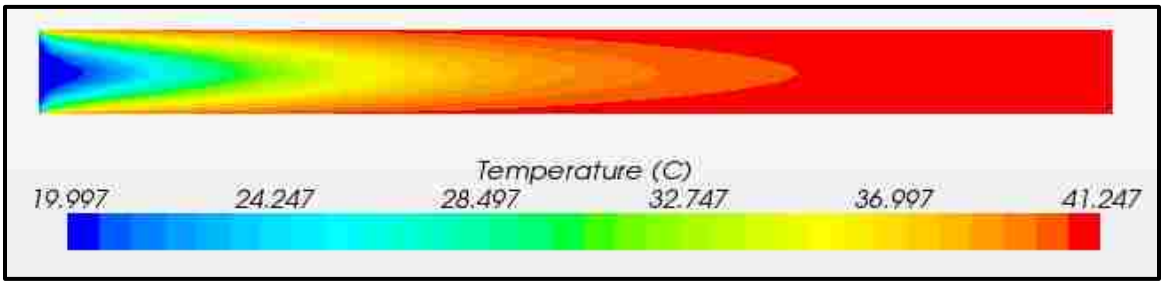

Figure 6.82 Infusate Center-Plane Temperature Profile (2500ml/hr Infusate Flow Rate)

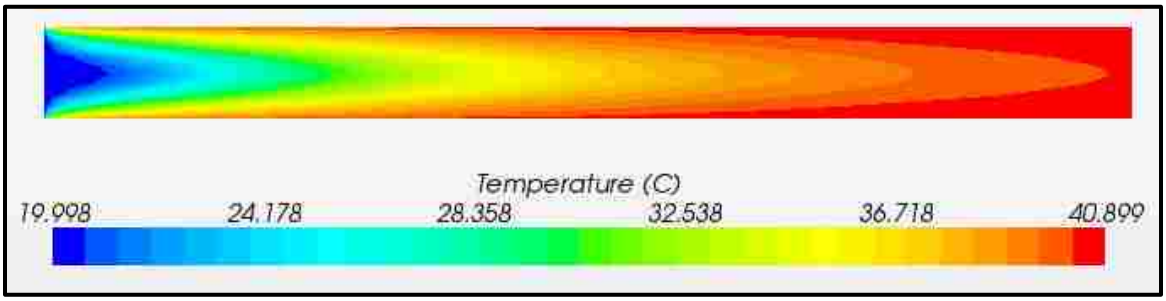

Figure 6.83 Infusate Center-Plane Temperature Profile (3500ml/hr Infusate Flow Rate)

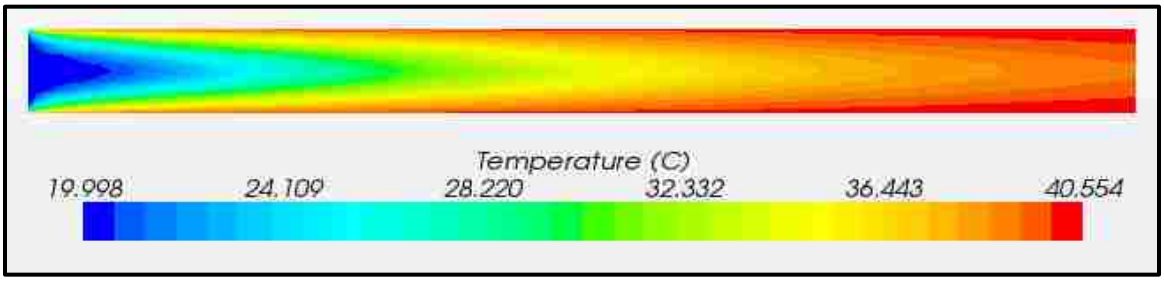

Figure 6.84 Infusate Center-Plane Temperature Profile (4500ml/hr Infusate Flow Rate)

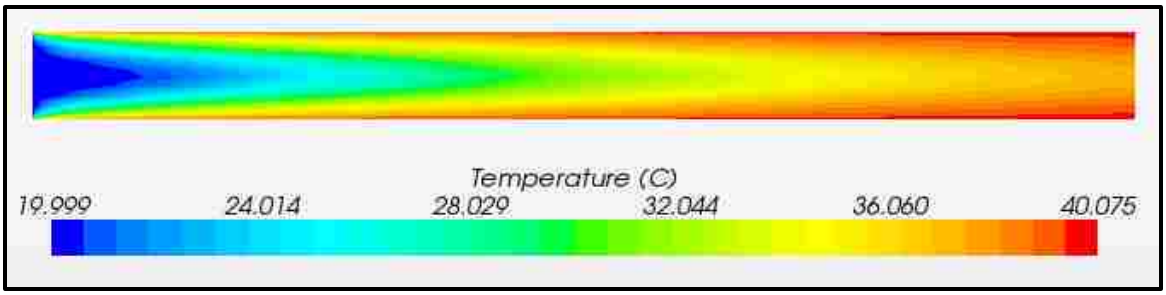

Figure 6.85 Infusate Center-Plane Temperature Profile (6000ml/hr Infusate Flow Rate)

The temperature profile on the outer-surface of the Infusate region was also examined (Figures 6.86-6.91). Similar to the previous simulations, the outer-surface reached a uniform temperature profile at a shorter distance from the inlet than the interior of the Infusate region. The outer-surface of the Infusate region reached a uniform temperature profile before the outlet for all Infusate flow rates evaluated. Again, this is directly related to the boundary conditions and proximity to the Hot Water region. Additionally, increasing Infusate flow rate results in increased axial distance for a uniform temperature profile to be reached within the Infusate region. This is related to the decrease in heat transfer rate due to the decreased temperature gradient between the Infusate and Hot Water regions.

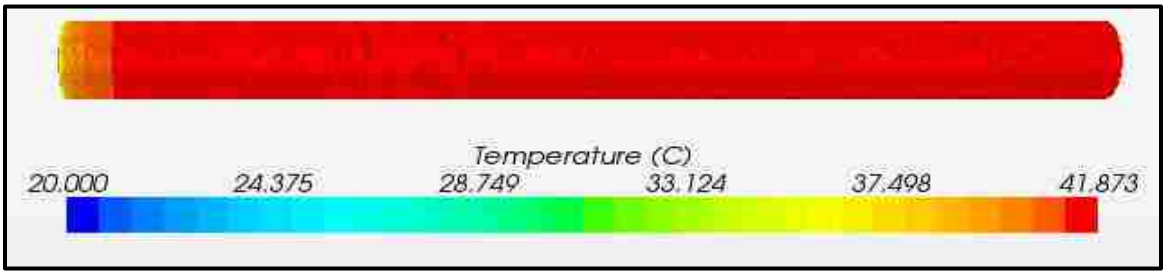

Figure 6.86 Infusate Outer-Surface Temperature Profile (500ml/hr Infusate Flow Rate)

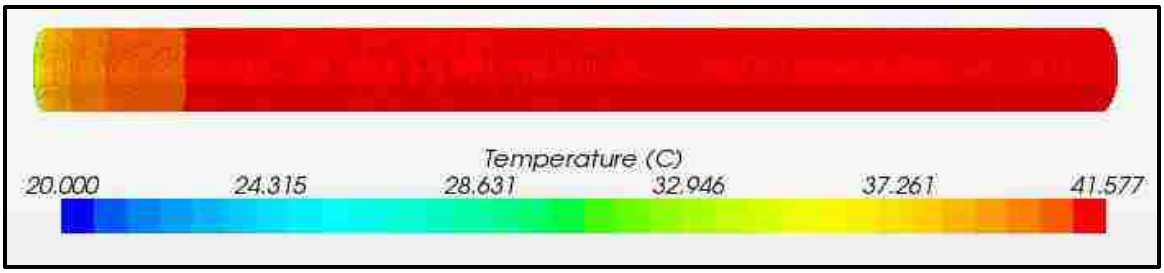

Figure 6.87 Infusate Outer-Surface Temperature Profile (1500ml/hr Infusate Flow Rate)

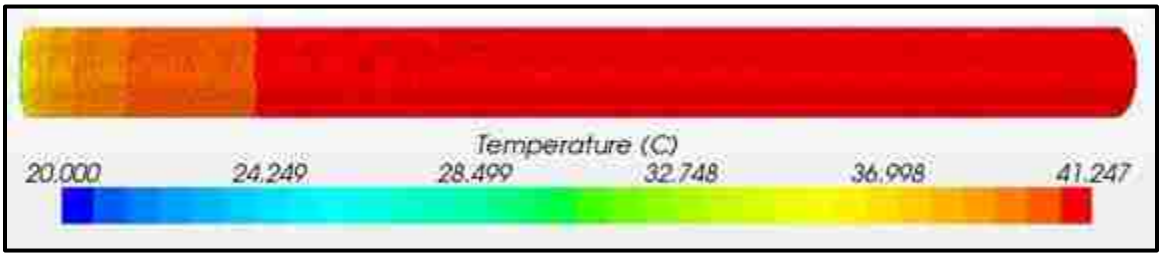

Figure 6.88 Infusate Outer-Surface Temperature Profile (2500ml/hr Infusate Flow Rate)

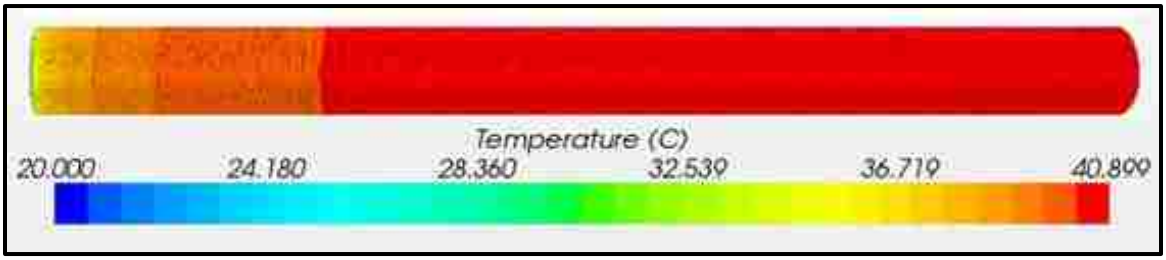

Figure 6.89 Infusate Outer-Surface Temperature Profile (3500ml/hr Infusate Flow Rate)

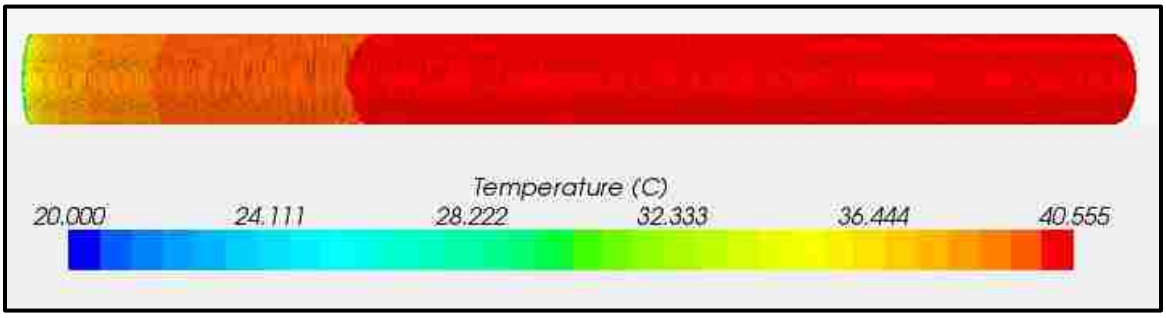

Figure 6.90 Infusate Outer-Surface Temperature Profile (4500ml/hr Infusate Flow Rate)

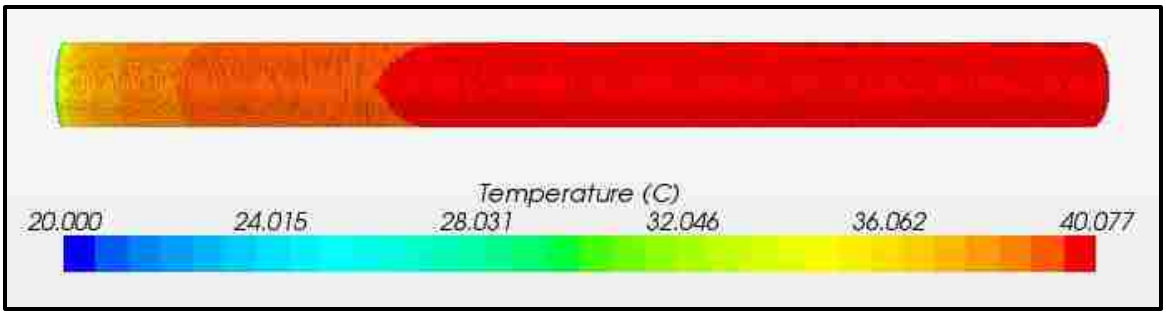

Figure 6.91 Infusate Outer-Surface Temperature Profile (6000ml/hr Infusate Flow Rate)

To visualize the thermal profile within the Hot Water region, a center-plane section along the length of heat exchanger was plotted in terms of temperature (Figure 6.92-6.97). Due to the length of the heat exchanger, the subsequent figures were scaled to accommodate the entire length into one figure. Increased temperature variation within the Hot Water region is seen with increasing Infusate mass flow rate. Specifically, temperatures within the Hot Water region decreased with increasing Infusate mass flow rate. These results are similar to the previous simulation. However the thermal variation is more pronounced, as the heat transfer rate is also impacted in these simulations due to the decreased temperature gradient between the Infusate and Hot Water regions. Again, the inlet boundary conditions for the Hot Water region were the same for all simulations evaluated; only the Infusate mass flow rate was varied. As such, the decreased temperature profile within the Hot Water region is directly related to the increase in Infusate mass flow rate. However, compared to the previous set of simulations (Section 6.3) the temperature profile is also impacted by a decrease in heat transfer rate due to the decreased temperature gradient between the Infusate and Hot Water regions. This results in the decrease in outlet mean bulk temperature observed in the Infusate and Hot Water regions, as well as the thermal profile variation in the Hot Water region.

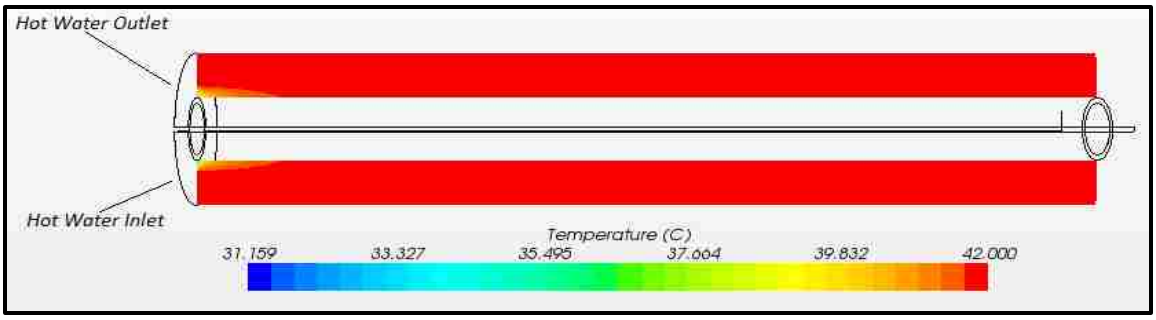

Figure 6.92 Hot Water Center-Plane Temperature Profile (500ml/hr Infusate Flow Rate)

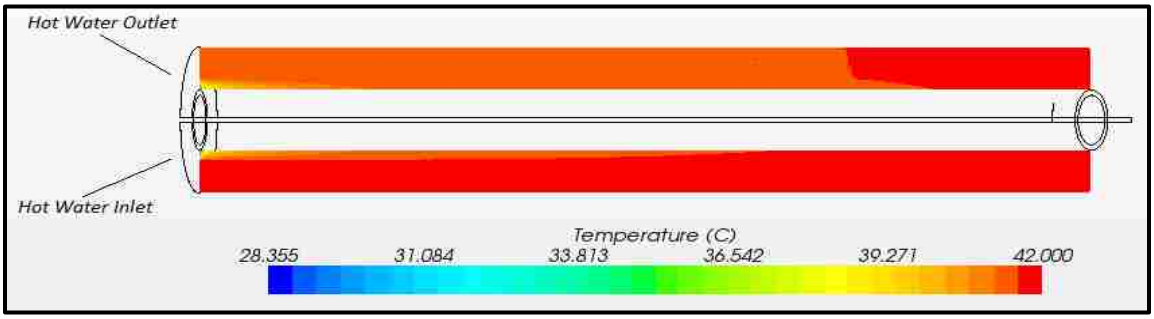

Figure 6.93 Hot Water Center-Plane Temperature Profile (1500ml/hr Infusate Flow Rate)

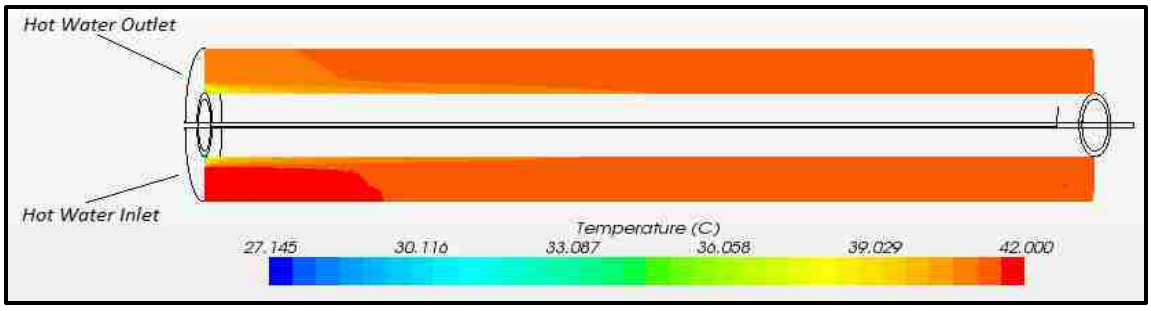

Figure 6.94 Hot Water Center-Plane Temperature Profile (2500ml/hr Infusate Flow Rate)

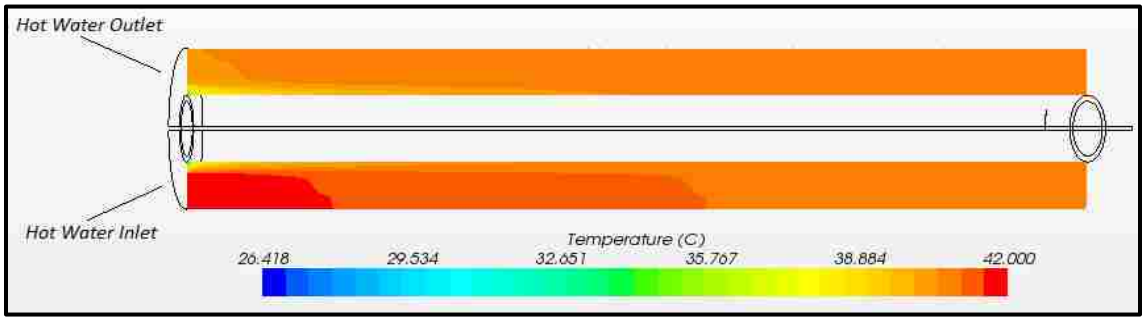

Figure 6.95 Hot Water Center-Plane Temperature Profile (3500ml/hr Infusate Flow Rate)

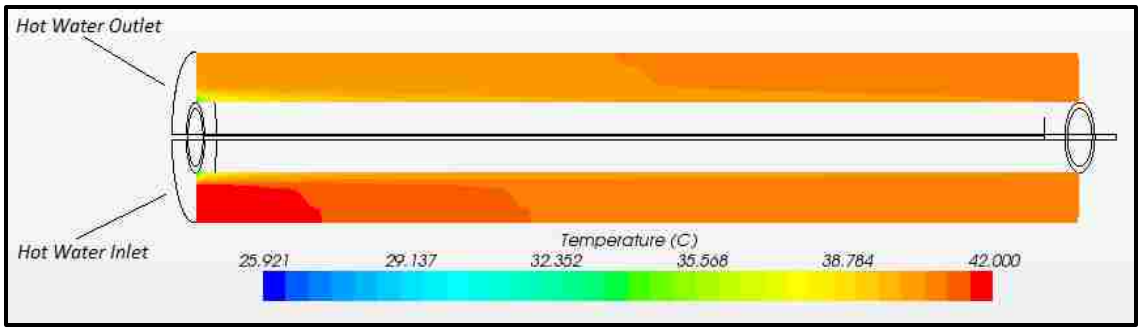

Figure 6.96 Hot Water Center-Plane Temperature Profile (4500ml/hr Infusate Flow Rate)

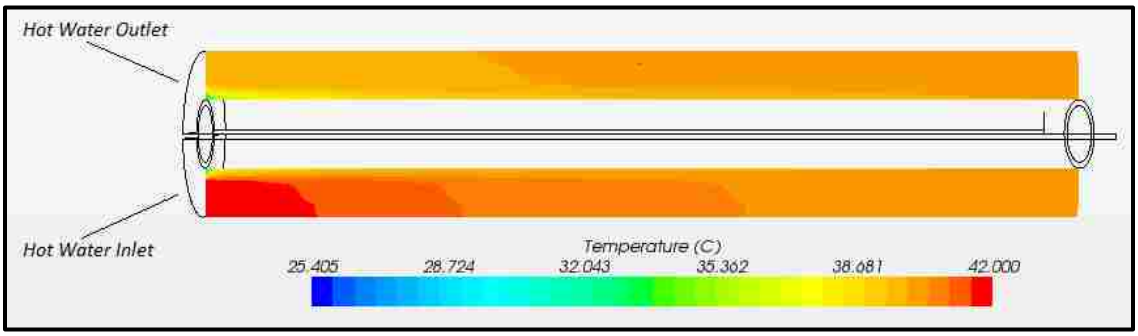

Figure 6.97 Hot Water Center-Plane Temperature Profile (6000ml/hr Infusate Flow Rate)

6.5 Determination of the Hot Water Region Entrance Length Correlation

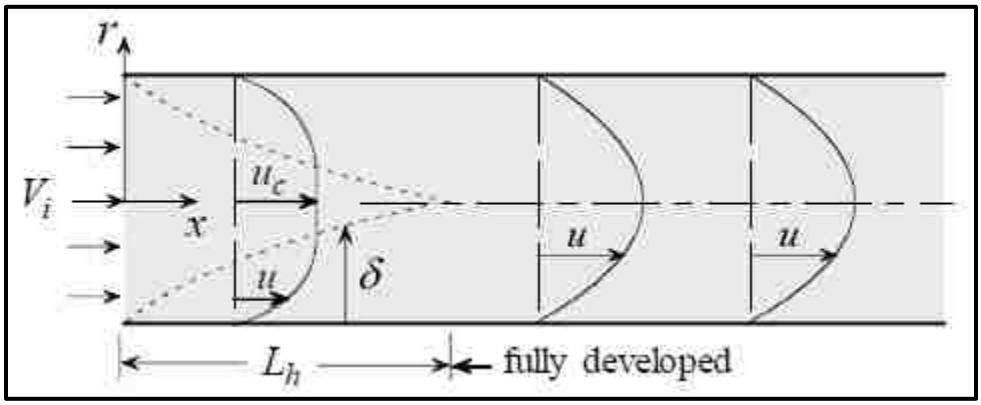

Figure 6.98 Developing Velocity Boundary Layer at the Entrance of a Pipe [20]

Entrance length (L_h) is the distance into a pipe or duct at which point the flow becomes fully developed, further increases in axial distance yield a constant uniform velocity profile.

Figure 6.98 depicts the developing boundary layer at the entrance of a pipe. The entrance region or developing region ($0 \leq x \leq L_h$) is characterized by the following features [20]:

- ($v_r \neq 0$), streamlines are not parallel.
- Core velocity (u_c) increases with axial distance (x) into the pipe.
- Pressure decreases with axial distance (x) into the pipe.
- Velocity boundary layer thickness (δ) is less than pipe radius.

The fully developed region ($x \geq L_h$) is characterized by the following features [20]:

- Streamlines are parallel ($v_r = 0$).
- Axial velocity profile is consistent along the remaining pipe length.

Previous studies have characterized the hydrodynamic entrance effects within concentric annular geometry. In the current study, the geometry of the Hot Water region is unique in that it features a separation along the center-plane, which confines the flow to half of the traditional concentric annular geometry. Figure 6.99 depicts the geometry of a true annulus, which consists of two concentric rings. A literature review did not return any previous studies concerning the unique geometry of the Hot Water region. As such, the focus of this current study was to compare the hydrodynamic properties of the studied Hot Water semi-annulus to that of a true concentric annulus. Additionally, the effects of the elbow section of the Hot Water region on flow characteristics were also considered.

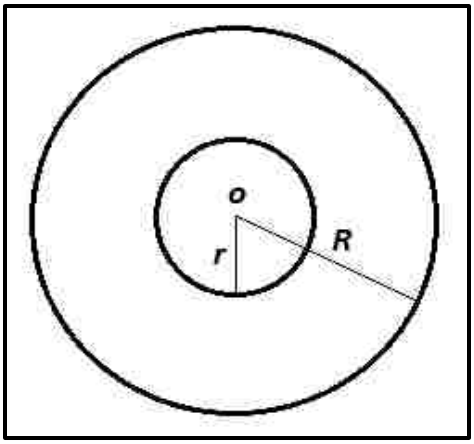

Figure 6.99 True Concentric Annulus Geometry

To understand the transition from laminar to turbulent flow within a true concentric annulus, the critical Reynolds Number was determined based on a comparison developed by Dou, Khou, and Tsai (2010). Figure 6.100 depicts the comparison of critical Reynolds Numbers for pipe and annular flow developed by Dou et al [11]. The term *k*, is defined as the ratio of the outer and inner radius of a concentric annulus. For the purposes of this study, the dimensions of the true annulus were based on the geometry of the studied Hot Water region. Refer to Figure 6.112 for the dimensions of the true annulus and Hot Water semi-annulus used in this comparative study. Based on these dimensions, the ratio of the outer and inner radius of the concentric annulus evaluated is k = 0.41. For the purposes of this study, the critical Reynolds Number for concentric annular flow was determined to be approximately Re_c = 2300. The critical Reynolds Number of 2300 was taken into account when evaluating laminar and turbulent flow within the studied semi-annulus and true concentric annulus.

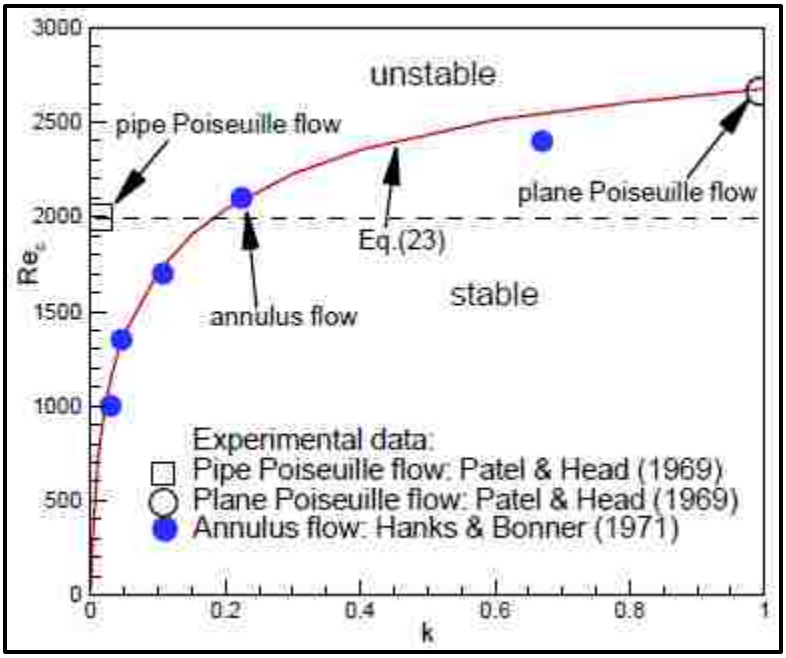

Figure 6.100 Comparison of Critical Reynolds Number for Pipe and Annular Flow [11]

The flow area of a concentric annulus is the difference in areas between the larger circle with diameter (R) and the smaller circle with diameter (r). The hydraulic diameter can be found with the following equation [14]:

$$D_h = D_o - D_i \quad [24]$$

Where:

D_o = Outer ring diameter
D_i = Inner ring diameter

Gupta and Garg (1981) characterized the developing region of a concentric annulus within the laminar regime. Traditionally, hydrodynamic entrance lengths have been defined as the length at which axial velocity at the centerline reaches 99% of the fully developed value [16]. Gupta and Garg described the hydrodynamic entrance length for a range of annulus radius ratios termed ($\gamma = r_i/r_o$), where r_i and r_o refer to the radii of the inner and outer walls of a concentric annulus. Using an implicit finite difference method, Gupta and Garg developed the following entrance length correlation for laminar flow within a concentric annulus [16]:

$$\frac{2L_h}{r_o - r_i} = CR_e \quad [25]$$

Where:

L_h = Entrance Length
r_o = Radius Outer Wall Concentric Annulus
r_i = Radius Inner Wall Concentric Annulus
R_e = Reynolds Number
C = Derived Constant based on γ (Table 6.1)

Table 6.1 Entrance Length Constant based on Radii Ratio of Concentric Annulus [16]

Entrance Length Constant for Radii Ratio Concentric Annulus						
γ	0.001	0.05	0.1	0.2	0.4	0.8
C	0.65	0.355	0.3	0.25	0.225	0.215

Gupta and Garg developed an entrance length correlation for a concentric annulus based on radii ratio of the inner and outer walls within the laminar regime. Table 6.1 lists the derived constants for the entrance length correlation based on the radii ratio (γ) [16]. For the purposes of this study, $\gamma \approx 0.4$ based on the dimensions of the studied heat exchanger.

This study focused on characterizing the hydrodynamic entrance properties for the unique geometry of the Hot Water region. Specifically, new empirical correlations for the entrance length were developed for Laminar and Turbulent flow within the unique semi-annular geometry. CFD simulations were run for increasing Reynolds Numbers. These results were then compared and an entrance length correlation developed. The developed entrance length correlation for the Hot Water region was then compared to the correlation developed by Gupta and Garg for a true concentric annulus within the laminar regime.

6.5.1 Entrance Length Correlation within the Laminar Regime:

A grid independency test was performed on the geometry of the Hot Water region to determine the optimum mesh density. New mesh conditions were required, as the previous simulations considered turbulent flow in the Hot Water region. As previously mentioned, selecting the appropriate mesh density is crucial in terms of final solution accuracy. A coarse mesh will require less computational power, but may lack solution accuracy. A finer mesh density increases solution accuracy, but requires more computational power and solution time. Grid independency is reached when further increases to mesh density do not result in changes to the final solution. Performing a grid independency ensures solution accuracy while efficiently utilizing computational resources.

A volumetric flow rate of 50ml/min (Reynolds number 241) was used for the grid independency of the Hot Water region. A coarse mesh of about 177,000 cells and a fine mesh of

about 522,000 cells were used for this analysis. Figure 6.101 depicts the generated volume mesh for the range of mesh densities evaluated (177,000 – 522,000 total cells). The axial velocity along the center line of the Hot Water outlet was evaluated (Figure 5.102). Table 6.2 documents the mesh conditions used for each iteration of increased mesh density.

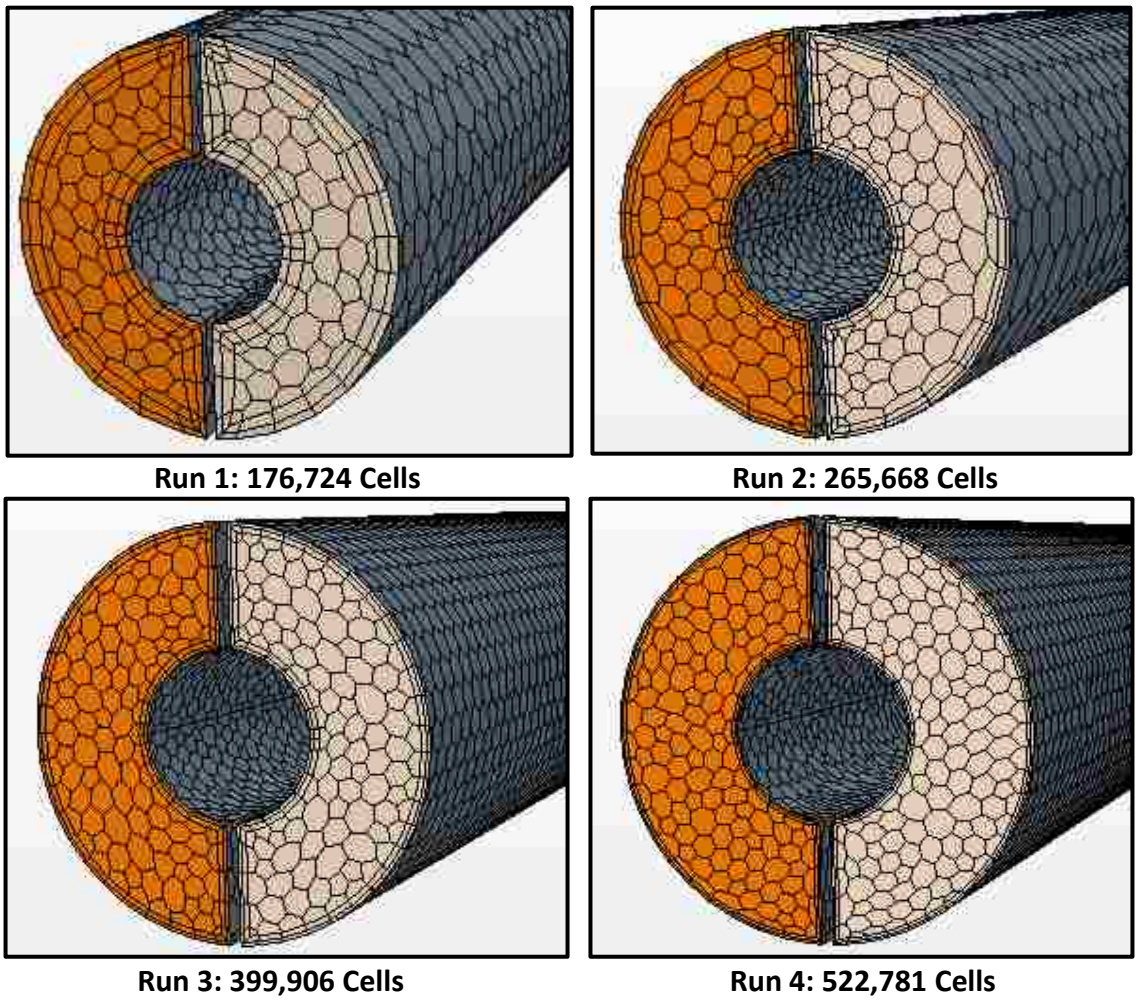

Figure 6.101 Generated Volume Mesh Densities Used in Hot Water Region Grid Independency

Table 6.2 Mesh Conditions Used for Variation of Mesh Density (176,000 – 500,000 total cells)

	Run 1	Run 2	Run 3	Run 4
Total Cells	176,724	265,668	399,906	522,781
Base Size [mm]	2.00	1.00	0.80	0.50
Number Prism Layers	2	2	2	2
Prism Layer Thickness [mm]	0.5	0.25	0.2	0.125
Target Surface Size [mm]	2	1	0.8	0.5

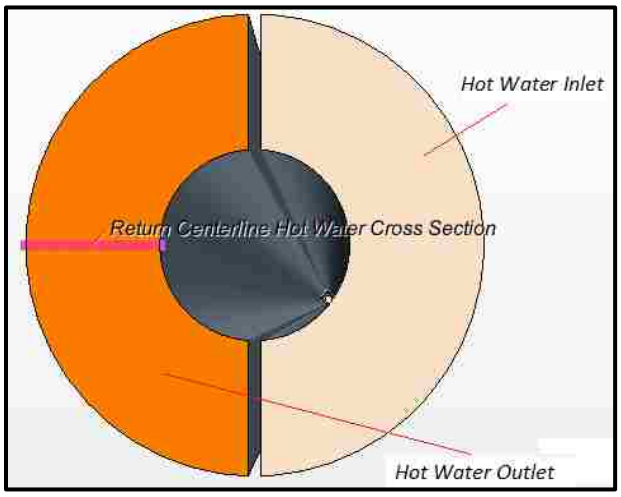

Figure 6.102 Cross Section Used for Axial Velocity Profile in the Grid Independency

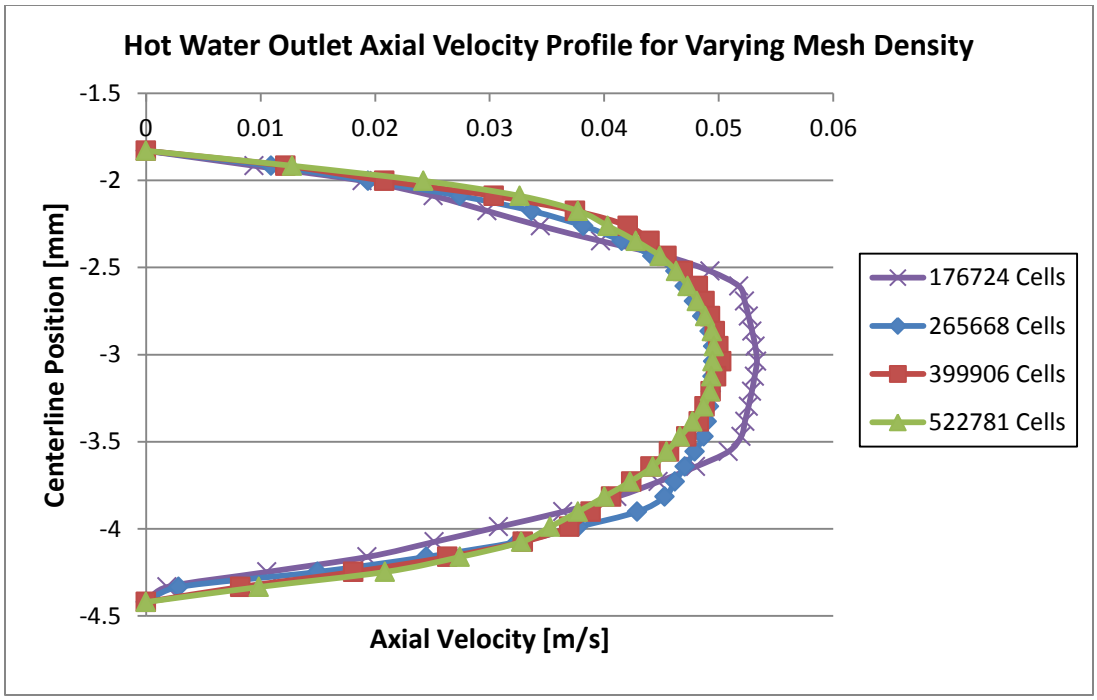

Figure 6.103 Comparison of Axial Velocity Profiles at Infusate Outlet for Increasing Mesh Density

Figure 6.103 depicts the axial velocity profile at the Hot Water outlet for the increasing mesh densities evaluated in the grid independency. The average difference between the axial velocity for the 400K and 500k mesh densities is less than 2%. As such, the mesh density of 400K was determined to be acceptable for the purposes of this study. As the total number of cells increase, the computational time increases proportionally. The chosen mesh conditions were determined to accurately capture the flow conditions while efficiently utilizing computational power. As such, the mesh conditions for the 400K mesh density were utilized for the production runs.

To determine a hydrodynamic entrance length correlation for laminar flow within the unique geometry of the Hot Water region, several CFD simulations were run for increasing Reynolds Number. The axial velocity was plotted along a centerline of the flow area with increasing distance into the Hot Water region. The entrance length was determined to be when

the axial velocity was 99% of the fully developed profile. Figure 6.104 depicts the centerline cross section and length profile used to plot the axial velocity profile. Figures 6.105 – 6.110 depict the entrance axial velocity profiles for increasing Reynolds Number. The boundary conditions used in the CFD simulations to determine an entrance length correlation for the inlet of the Hot Water region under laminar flow are given in Table 6.3.

Table 6.3 Boundary Conditions Used for Entrance Length Determination in Laminar Regime

Heat Exchanger Length [m]	Hot Water Volumetric Flow Rate [ml/min]	Mean Fluid Velocity [m/s]	Reynolds Number	Hot Water Outlet Pressure [atm]
0.6	5	0.003	21.41	1.0
0.6	20	0.013	85.64	1.0
0.6	50	0.034	214.09	1.0
0.6	100	0.067	428.19	1.0
0.6	200	0.135	856.37	1.0
0.6	300	0.202	1284.56	1.0

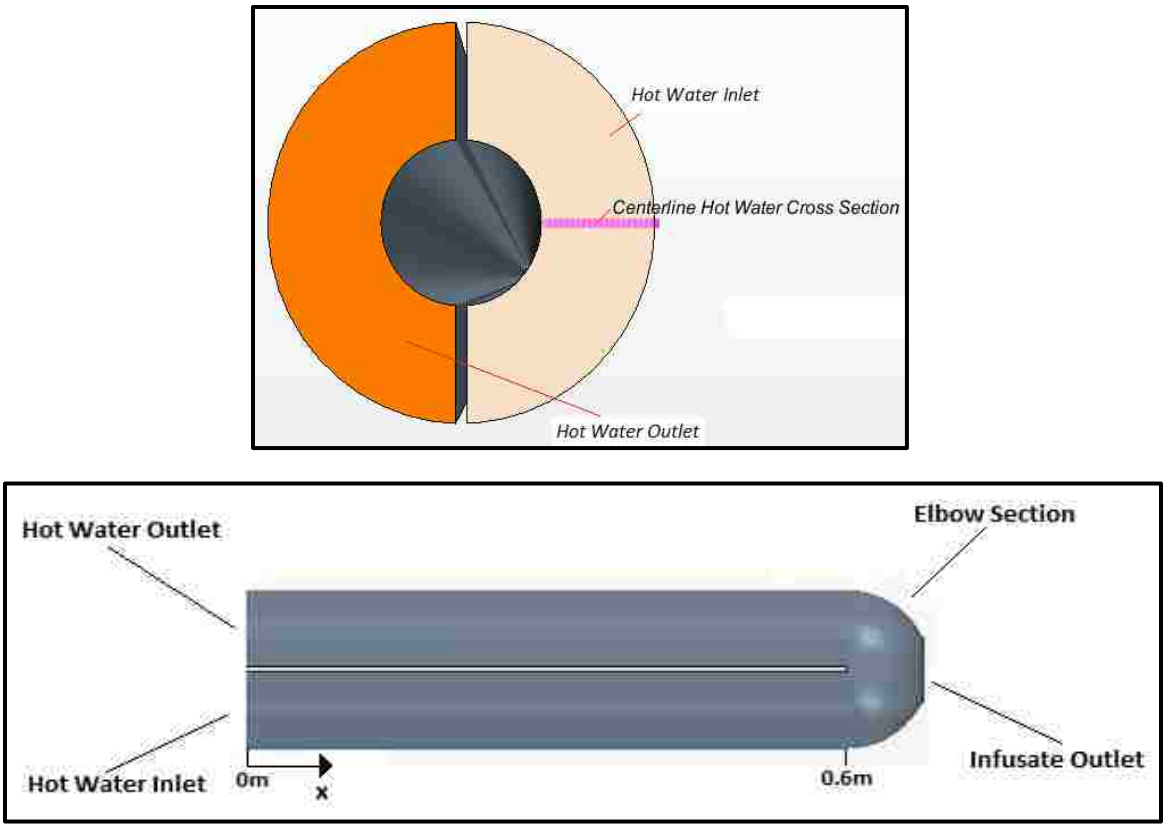

Figure 6.104 Hot Water Entrance Centerline Location/Axial Length for Subsequent Velocity Profile Data

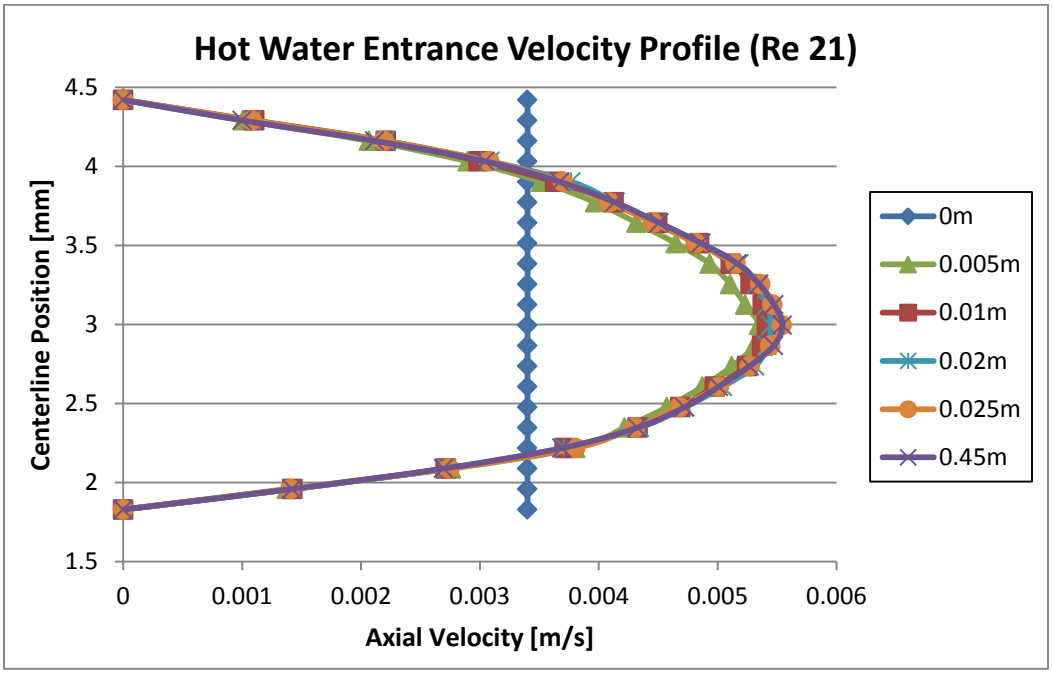

Figure 6.105 Axial Velocity Profile of Developing Region at Hot Water Inlet (Re 21)

Based on the cross section axial velocity profile of the Hot Water inlet section, it was determined that the flow becomes fully developed at approximately 0.025m from the entrance. As such, the entrance length (L_h) was determined to be 0.025m for a Reynolds Number of 21.

Hot Water Entrance Flow Region:

$R_e = 21$

$D_h = 4.076mm$

$L_h = 0.025m$

A dimensionless value can be obtained using the following relation:

$$\frac{L_h}{D_h} = \frac{25mm}{4.076mm} = 6.13$$

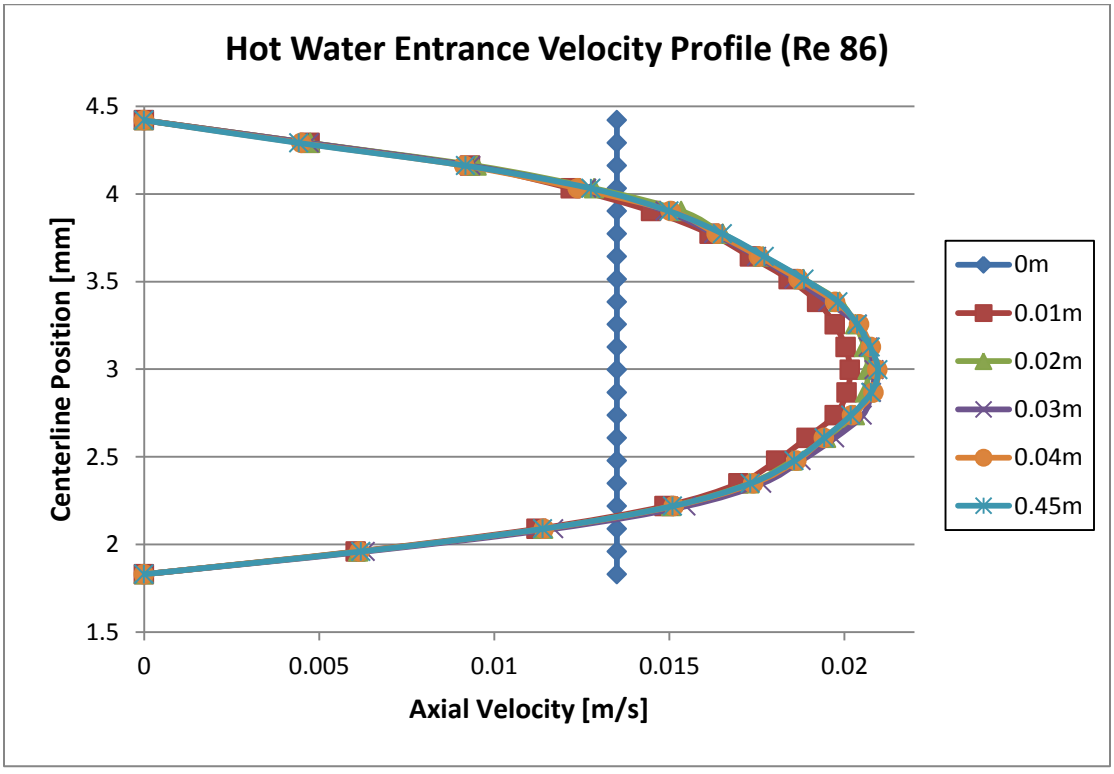

Figure 6.106 Axial Velocity Profile of Developing Region at Hot Water Inlet (Re 86)

Based on the cross section axial velocity profile of the Hot Water inlet section, it was determined that the flow becomes fully developed at approximately 0.04m from the entrance. As such, the entrance length (L_h) was determined to be 0.04m for a Reynolds Number of 86.

Hot Water Entrance Flow Region:

$R_e = 86$

$D_h = 4.076mm$

$L_h = 0.04m$

A dimensionless value can be obtained using the following relation:

$$\frac{L_h}{D_h} = \frac{40mm}{4.076mm} = 9.81$$

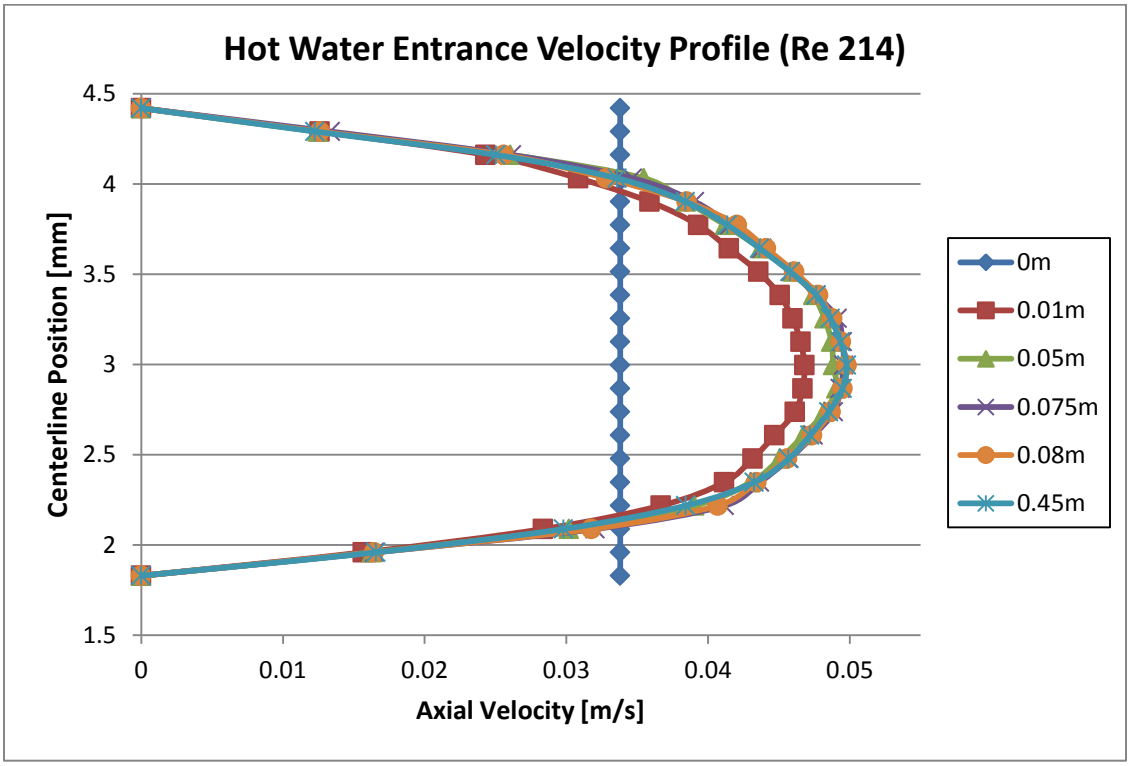

Figure 6.107 Axial Velocity Profile of Developing Region at Hot Water Inlet (Re 214)

Based on the cross section axial velocity profile of the Hot Water inlet section, it was determined that the flow becomes fully developed at approximately 0.08m from the entrance. As such, the entrance length (L_h) was determined to be 0.08m for a Reynolds Number of 214.

Hot Water Entrance Flow Region:

R_e = 214
D_h = 4.076mm
L_h = 0.08m

A dimensionless value can be obtained using the following relation:

$$\frac{L_h}{D_h} = \frac{80mm}{4.076mm} = 19.63$$

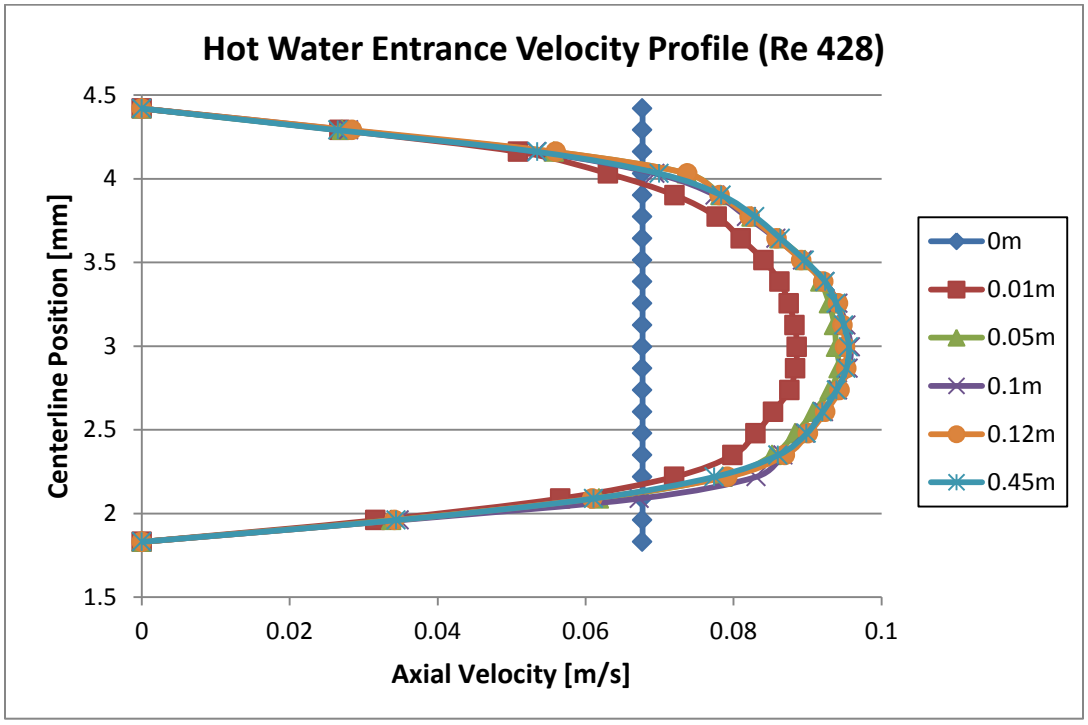

Figure 6.108 Axial Velocity Profile of Developing Region at Hot Water Inlet (Re 428)

Based on the cross section axial velocity profile of the Hot Water inlet section, it was determined that the flow becomes fully developed at approximately 0.12m from the entrance. As such, the entrance length (L_h) was determined to be 0.12m for a Reynolds Number of 428.

Hot Water Entrance Flow Region:

R_e = 428

D_h = 4.076mm

L_h = 0.12m

A dimensionless value can be obtained using the following relation:

$$\frac{L_h}{D_h} = \frac{120mm}{4.076mm} = 29.44$$

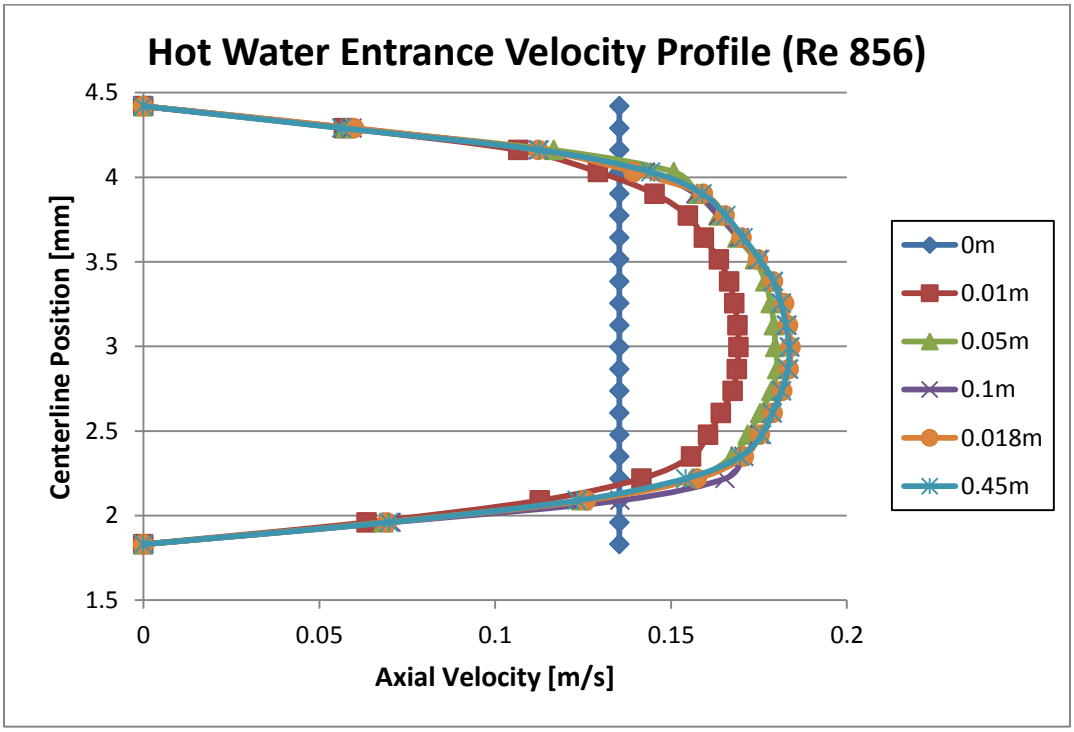

Figure 6.109 Axial Velocity Profile of Developing Region at Hot Water Inlet (Re 856)

Based on the cross section axial velocity profile of the Hot Water inlet section, it was determined that the flow becomes fully developed at approximately 0.18m from the entrance. As such, the entrance length (L_h) was determined to be 0.18m for a Reynolds Number of 856.

Hot Water Entrance Flow Region:

R_e = 856

D_h = 4.076mm

L_h = 0.18m

A dimensionless value can be obtained using the following relation:

$$\frac{L_h}{D_h} = \frac{180mm}{4.076mm} = 44.16$$

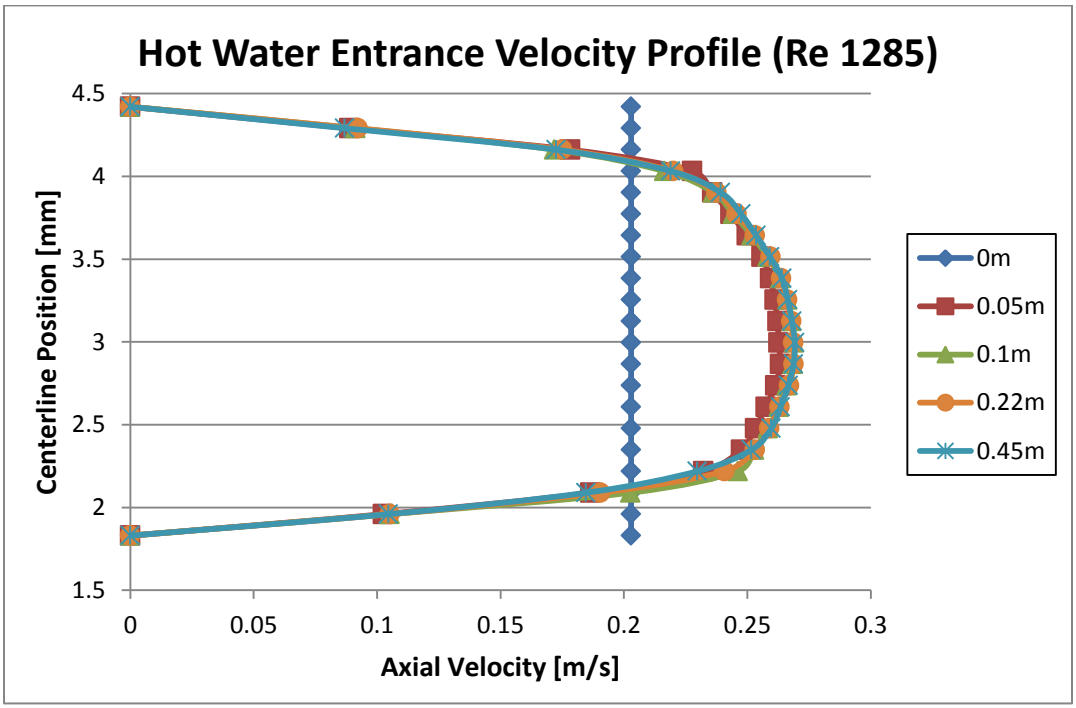

Figure 6.110 Axial Velocity Profile of Developing Region at Hot Water Inlet (Re 1285)

Based on the cross section axial velocity profile of the Hot Water inlet section, it was determined that the flow becomes fully developed at approximately 0.22m from the entrance. As such, the entrance length (L_h) was determined to be 0.22m for a Reynolds Number of 1285.

Hot Water Entrance Flow Region:

R_e = 1285
D_h = 4.076mm
L_h = 0.22m

A dimensionless value can be obtained using the following relation:

$$\frac{L_h}{D_h} = \frac{220mm}{4.076mm} = 53.97$$

Table 6.4 Entrance Length Results of CFD Simulations in Laminar Regime (At Inlet)

Entrance Velocity Profile (Laminar Regime)	
Reynolds Number	L_h/D_h
21.41	6.13
85.64	9.81
214.09	19.63
428.19	29.44
856.37	44.16
1284.56	53.97

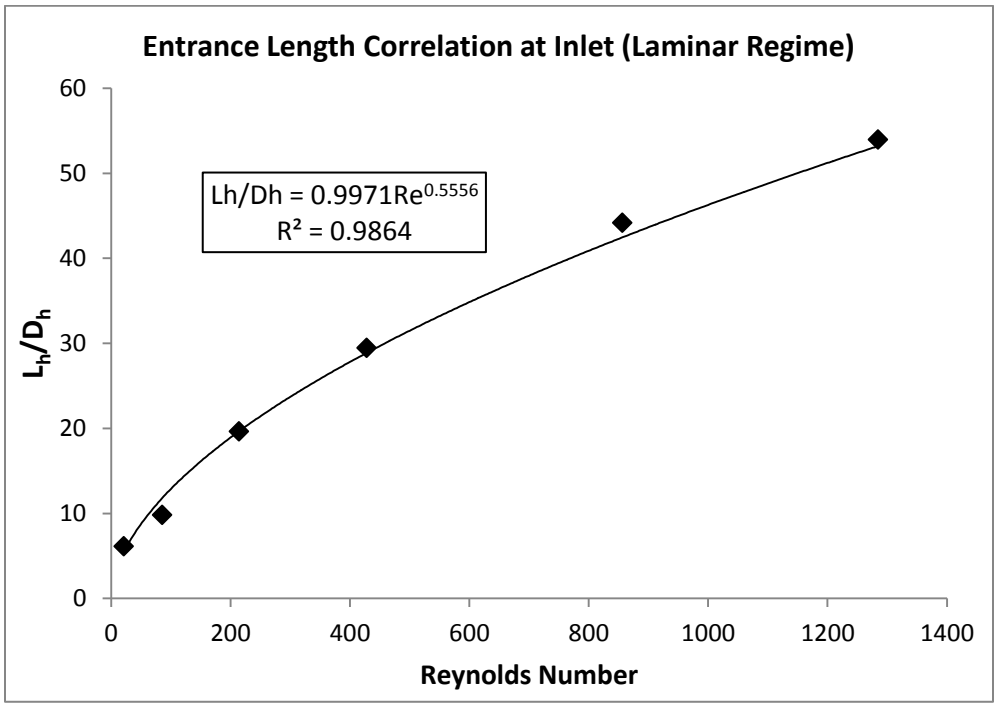

Figure 6.111 Equation Fitting to Results of CFD Simulations in Laminar Regime (At Inlet)

A Power function was fitted to the entrance length results of the CFD simulations within the laminar regime to approximate an entrance length correlation (Figure 6.111). Table 6.4 depicts the non-dimensionalized value (Lh/Dh) for the increasing Reynolds Numbers. A coefficient of determination (R^2) value of 0.9864 was obtained. The coefficient of determination

is a measure of how well the trendline correlates to the original data points. The coefficient of determination ranges from 0 – 1 and has no units. For a perfect fit, $R^2 = 1$ [8]. The R^2 value of 0.9864 indicates an excellent fit, and that the associated correlation should accurately predict entrance lengths for future design purposes. Based on the results of the CFD simulations, the entrance length correlation at the inlet of the Hot Water region under laminar flow was determined to be the following:

$$\frac{L_h}{D_h} = 0.9971 {R_e}^{0.5556} \quad [26]$$

Where:

L_h = Hydrodynamic Entrance Length
D_h = Hydraulic Diameter
R_e = Reynolds Number

Increasing Reynolds Numbers resulted in increased distance of the developing region within the Hot Water section. Increased mass flow rates result in increased forces within the flow area. This may explain the increased hydrodynamic entrance lengths observed for increasing Reynolds Numbers.

The CFD developed entrance length correlation (Eq. [26]) was compared to the entrance length correlation for a true concentric annulus developed by Gupta and Garg (1981). Figure 6.112 depicts the dimensions of a true concentric annulus compared to the perimeter dimensions of the flow area of the Hot Water region used for this comparison. The current study geometry is composed of two concentric rings, but includes a separation along the mid-plane of the annulus. Similar dimensions and flow conditions were used to compare hydrodynamic entrance lengths for a true concentric annulus and the studied Hot Water region semi-annulus.

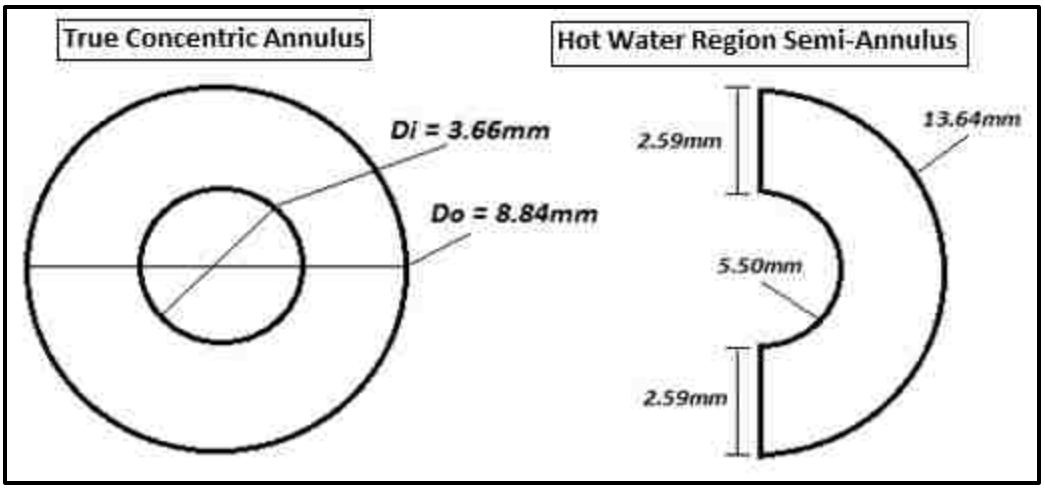

Figure 6.112 Schematic Diagram True Concentric Annulus vs. Current Study Geometry

The Reynolds Number for the true concentric annulus was determined using (Eq. [20]). The hydrodynamic diameter of the true concentric annulus was determined using (Eq. [24]). Table 6.5 gives the boundary conditions used for the true annulus entrance length calculation. The Flow area for the true annulus was determined using the following equation:

$$A_f = A_o - A_i = 50.854\text{mm}^2 \quad [27]$$

Where:

A_o = Area of outer-diameter ring = πR^2

A_i = Area of inner-diameter ring = πr^2

Table 6.5 Boundary Conditions Used for True Annulus Entrance Length Calculation

Dynamic Viscosity [Pa/s]	Volumetric Flow Rate [ml/min]	Mean Fluid Velocity [m/s]	Reynolds Number	Hydrodynamic Diameter [mm]
8.89×10^{-4}	8.0	0.00262	21.21	5.18
8.89×10^{-4}	32.5	0.01065	86.18	5.18
8.89×10^{-4}	81.0	0.02655	214.78	5.18
8.89×10^{-4}	161.5	0.05293	428.23	5.18
8.89×10^{-4}	323.0	0.10586	856.46	5.18
8.89×10^{-4}	484.0	0.15862	1283.36	5.18

Table 6.6 Comparison of Entrance Lengths in True Annulus and Semi-Annulus for Laminar Flow

Reynolds Number	True Annulus		Studied Semi-Annulus	
	Volumetric Flow Rate [ml/min]	L_h/D_h	Volumetric Flow Rate [ml/min]	L_h/D_h
21	8.0	2.39	5	6.13
86	32.5	9.69	20	9.81
214	81.0	24.16	50	19.63
428	161.5	48.18	100	29.44
856	323.0	96.35	200	44.16
1284	484.0	144.38	300	53.97

Table 6.6 gives the calculated hydrodynamic entrance lengths for the true concentric annulus (Eq. [25]) and the CFD determined hydrodynamic entrance lengths for the studied semi-annulus in the laminar regime. Figure 6.113 compares the hydrodynamic entrance lengths for a true concentric annulus and the studied geometry of the Hot Water region (semi-annulus). The entrance length of a concentric annulus is generally longer than the semi-annulus under laminar flow, and the difference is more prominent for increasing Reynolds Number.

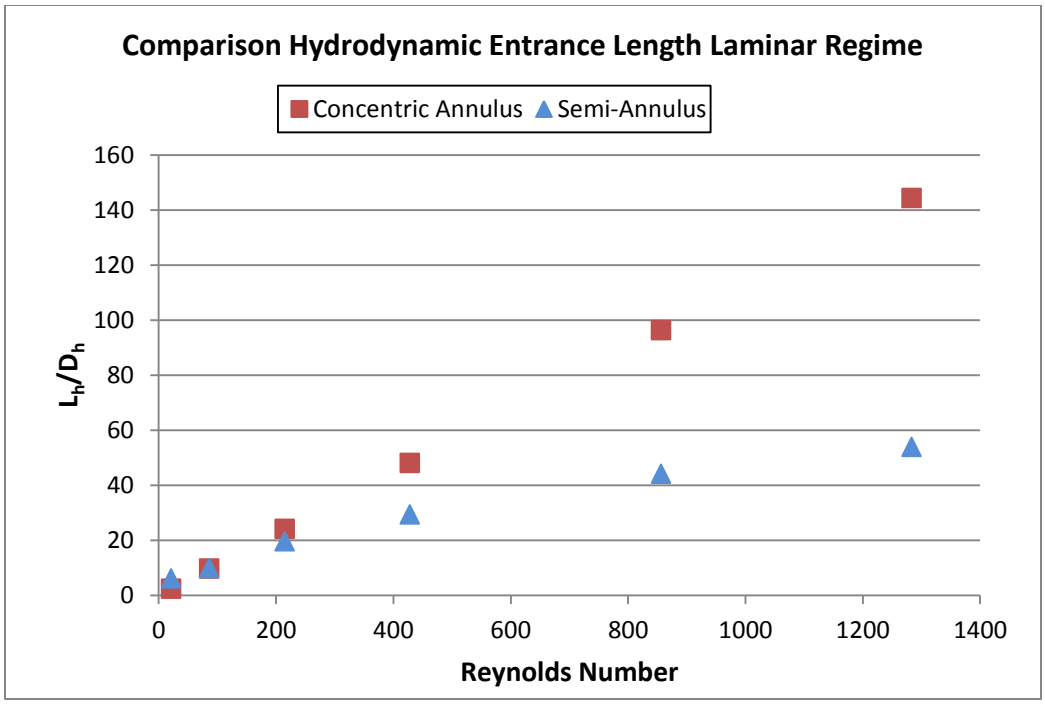

Figure 6.113 Comparison Entrance Length (True Annulus [16] vs. CFD Predicted Semi-Annulus)

Due to the separation along the center-plane of the Hot Water region, the flow area and wetted perimeter of a true concentric annulus is expected to be greater than that of the studied semi-annulus. As such, the shear and frictional forces within the semi-annulus is expected to be greater than those within a true concentric annulus, due to greater interaction with the wall resulting in increased viscous drag. This leads to the generally higher hydrodynamic developing lengths observed in the true semi-annulus when compared to a true concentric annulus.

In addition to the hydrodynamic entrance length at the inlet of the Hot Water region, an entrance length correlation was determined for the section immediately after the elbow. Flow is disrupted in the elbow of the Hot Water region, resulting in an additional developing region after the elbow. Again, the entrance length was determined to be when the axial velocity was 99% of the fully developed profile. The axial velocity was plotted along a centerline of the flow area with increasing distance into the Hot Water return region. Figure 6.114 depicts the

centerline cross section and length profile used to plot the axial velocity profile. Figures 6.115 – 6.120 depict the return axial velocity profiles for increasing Reynolds Number. The same boundary conditions used to determine the hydrodynamic entrance length correlation at the inlet were used to determine the entrance length correlation after the elbow (Table 6.3).

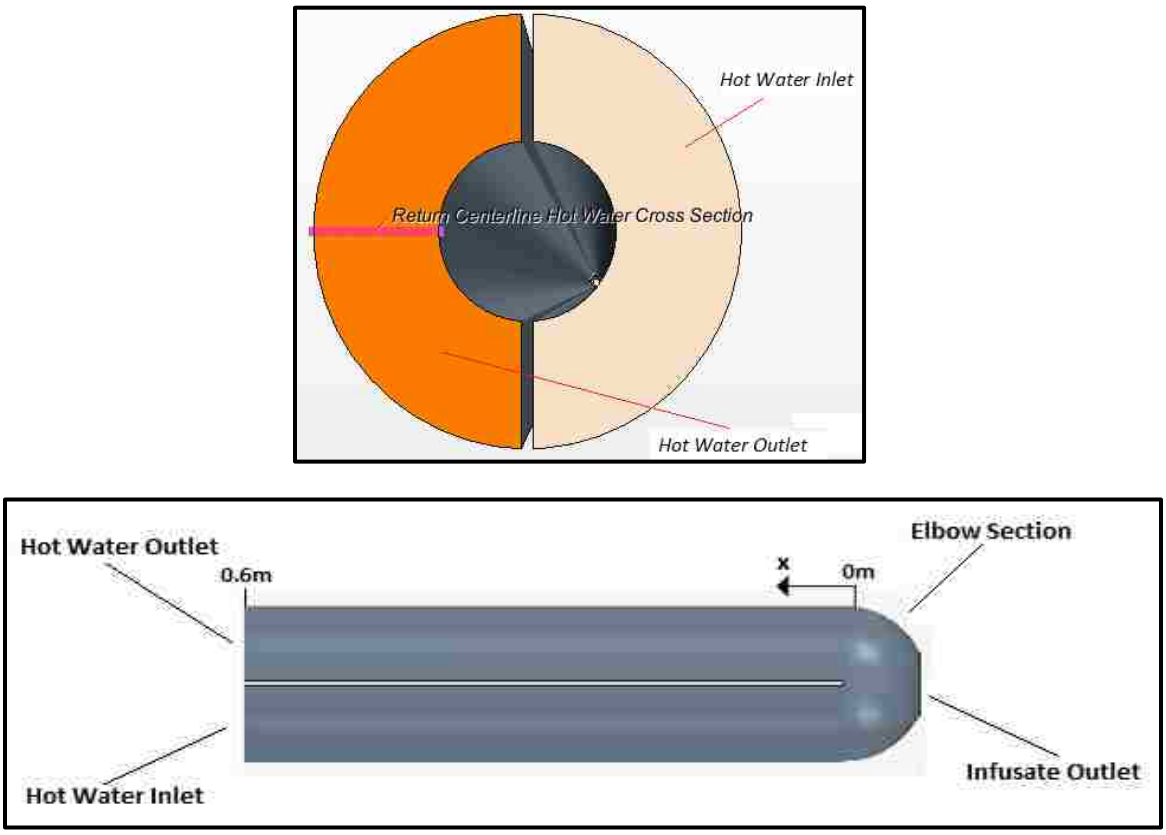

Figure 6.114 Hot Water Return Centerline/Axial length Locations for Subsequent Velocity Profile Data

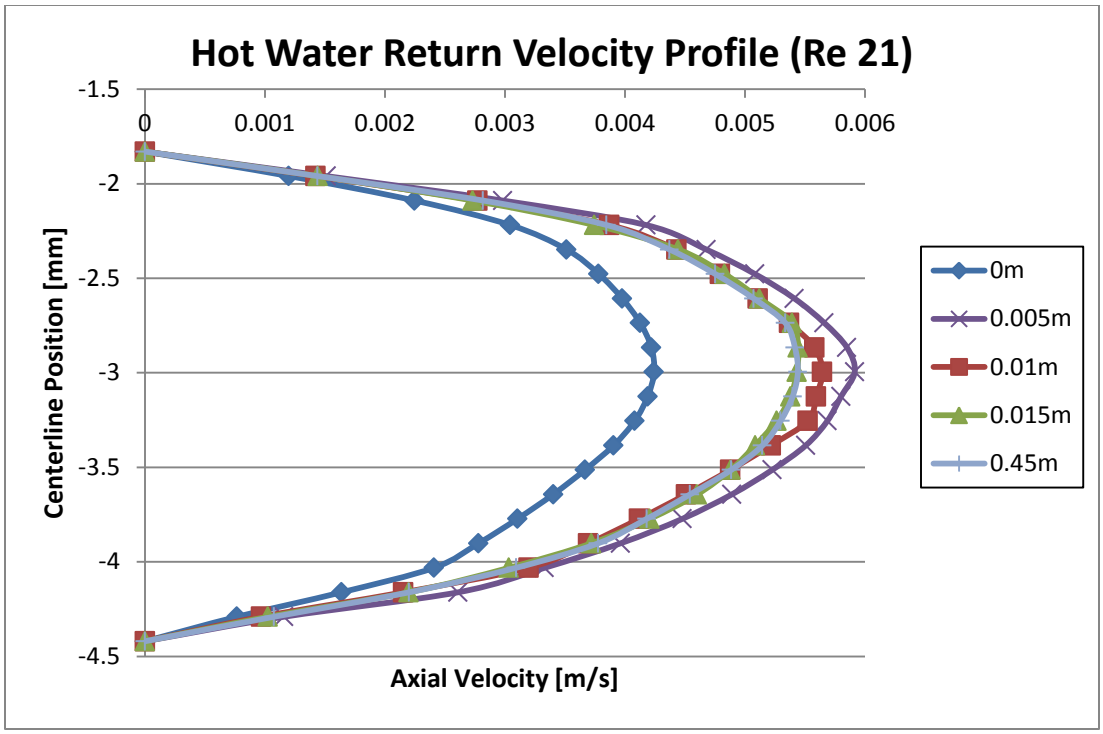

Figure 6.115 Axial Velocity Profile of Developing Region After Elbow Section (Re 21)

Based on the cross section axial velocity profile after the elbow of the Hot Water region, it was determined that the flow becomes fully developed at approximately 0.015m from the elbow. As such, the entrance length (L_h) was determined to be 0.015m for a Reynolds Number of 21.

Hot Water Entrance Flow Region:

$R_e = 21$

$D_h = 4.076mm$

$L_h = 0.015m$

A dimensionless value can be obtained using the following relation:

$$\frac{L_h}{D_h} = \frac{15mm}{4.076mm} = 3.68$$

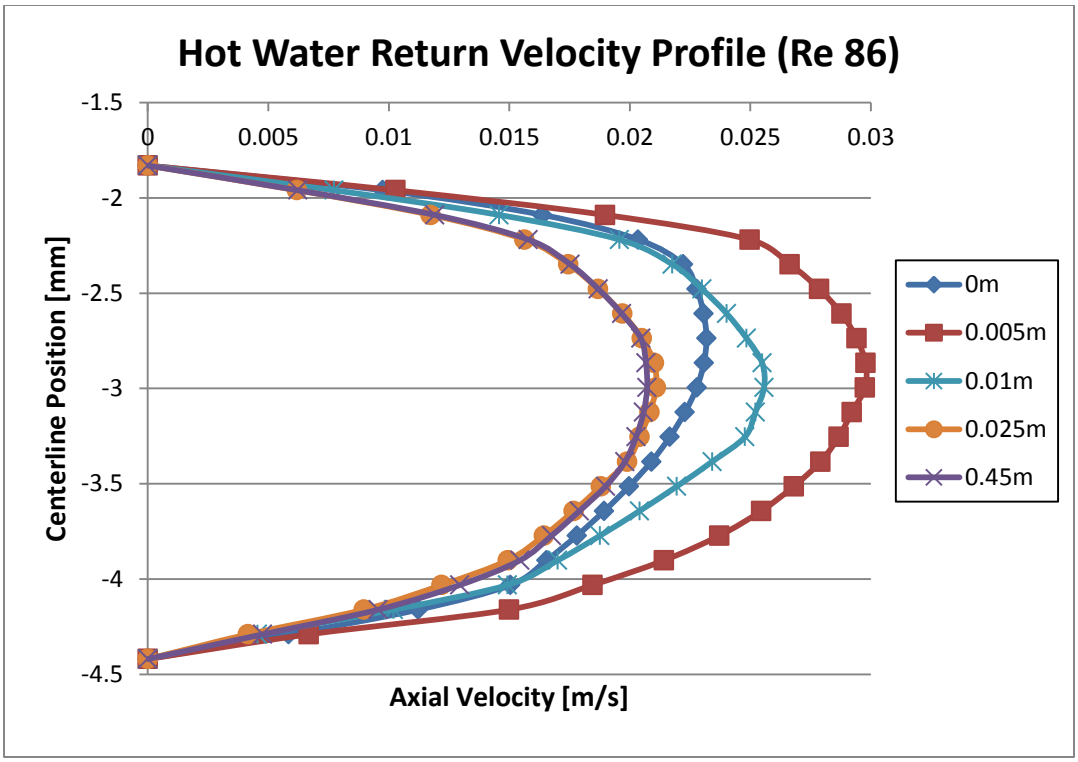

Figure 6.116 Axial Velocity Profile of Developing Region After Elbow Section (Re 86)

Based on the cross section axial velocity profile after the elbow of the Hot Water region, it was determined that the flow becomes fully developed at approximately 0.025m from the elbow. As such, the entrance length (L_h) was determined to be 0.025m for a Reynolds Number of 86.

Hot Water Entrance Flow Region:

$R_e = 86$

$D_h = 4.076mm$

$L_h = 0.025m$

A dimensionless value can be obtained using the following relation:

$$\frac{L_h}{D_h} = \frac{25mm}{4.076mm} = 6.13$$

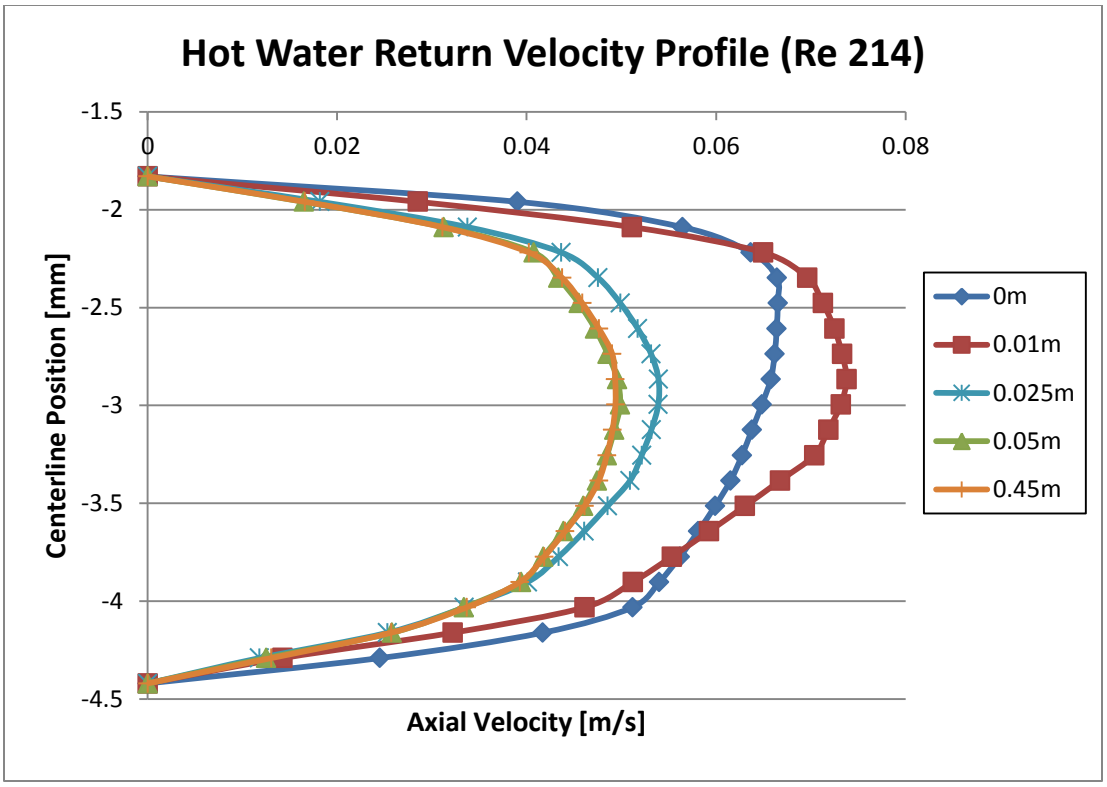

Figure 6.117 Axial Velocity Profile of Developing Region After Elbow Section (Re 214)

Based on the cross section axial velocity profile after the elbow of the Hot Water region, it was determined that the flow becomes fully developed at approximately 0.05m from the elbow. As such, the entrance length (L_h) was determined to be 0.05m for a Reynolds Number of 214.

Hot Water Entrance Flow Region:

$R_e = 214$

$D_h = 4.076mm$

$L_h = 0.05m$

A dimensionless value can be obtained using the following relation:

$$\frac{L_h}{D_h} = \frac{50mm}{4.076mm} = 12.27$$

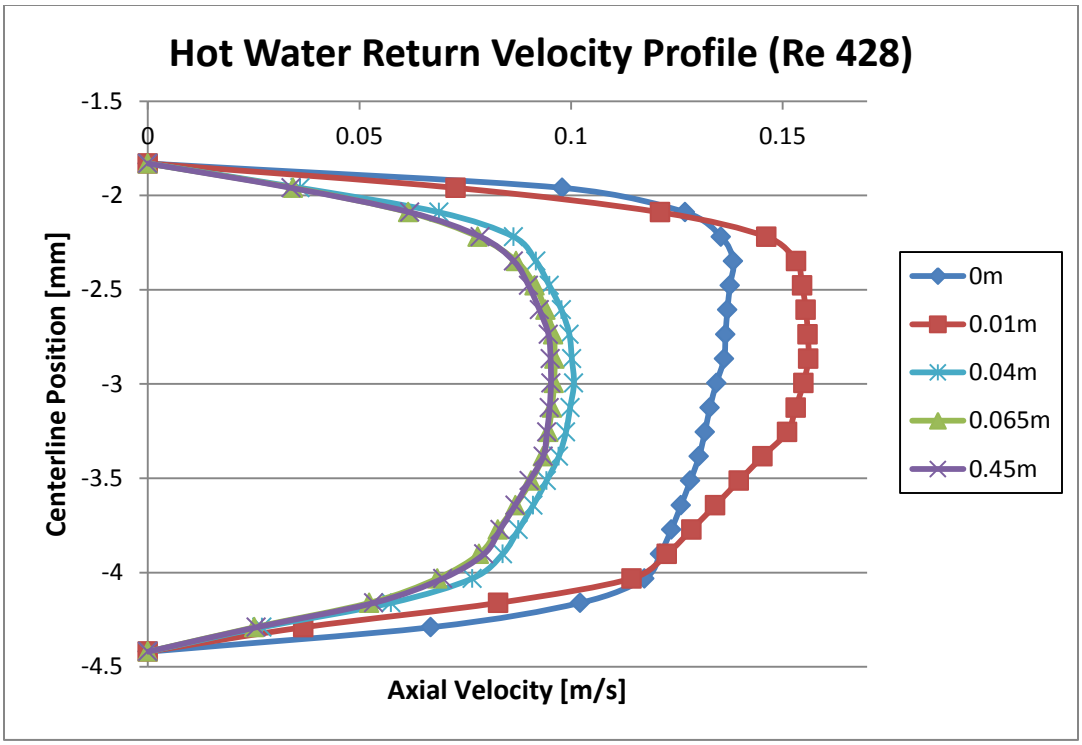

Figure 6.118 Axial Velocity Profile of Developing Region After Elbow Section (Re 428)

Based on the cross section axial velocity profile after the elbow of the Hot Water region, it was determined that the flow becomes fully developed at approximately 0.065m from the elbow. As such, the entrance length (L_h) was determined to be 0.065m for a Reynolds Number of 428.

Hot Water Entrance Flow Region:

$R_e = 428$

$D_h = 4.076mm$

$L_h = 0.065m$

A dimensionless value can be obtained using the following relation:

$$\frac{L_h}{D_h} = \frac{65mm}{4.076mm} = 15.95$$

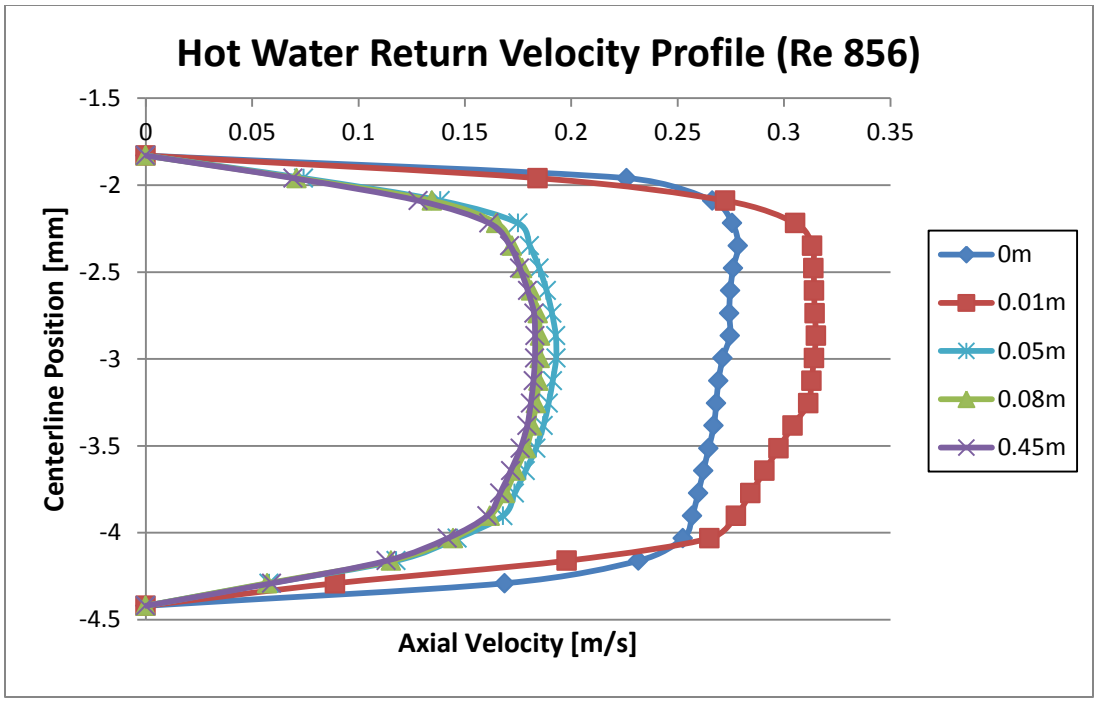

Figure 6.119 Axial Velocity Profile of Developing Region After Elbow Section (Re 856)

Based on the cross section axial velocity profile after the elbow of the Hot Water region, it was determined that the flow becomes fully developed at approximately 0.08m from the elbow. As such, the entrance length (L_h) was determined to be 0.08m for a Reynolds Number of 856.

Hot Water Entrance Flow Region:

$R_e = 856$

$D_h = 4.076mm$

$L_h = 0.08m$

A dimensionless value can be obtained using the following relation:

$$\frac{L_h}{D_h} = \frac{80mm}{4.076mm} = 19.63$$

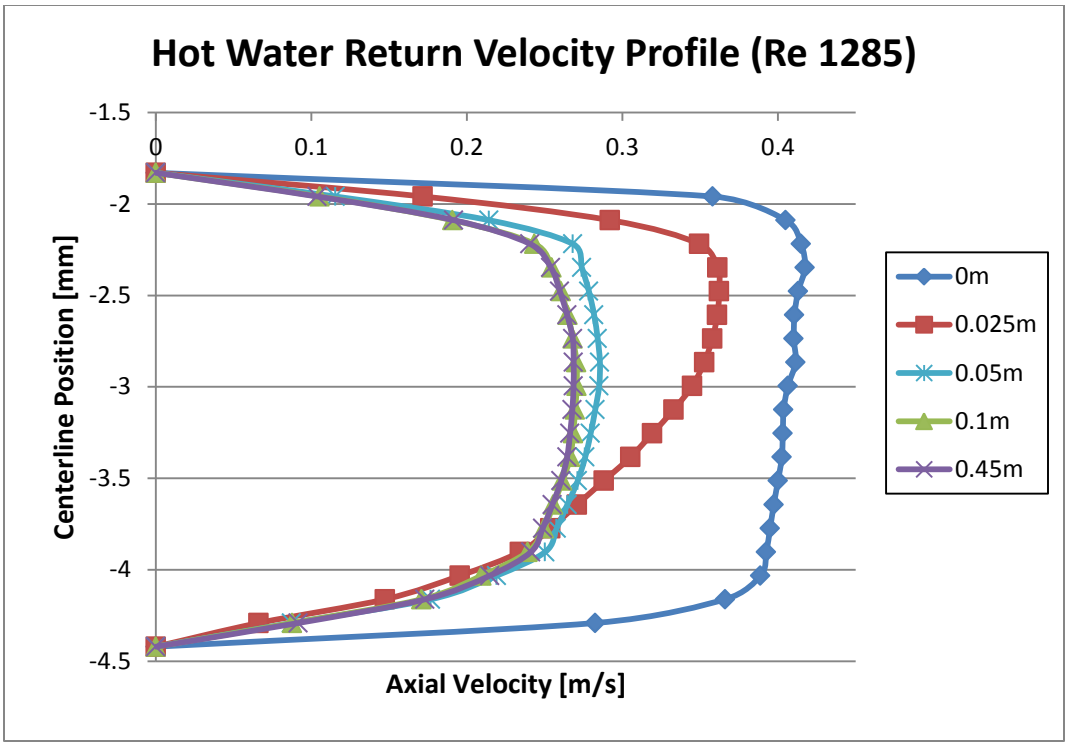

Figure 6.120 Axial Velocity Profile of Developing Region After Elbow Section (Re 1285)

Based on the cross section axial velocity profile after the elbow of the Hot Water region, it was determined that the flow becomes fully developed at approximately 0.1m from the elbow. As such, the entrance length (L_h) was determined to be 0.1m for a Reynolds Number of 1285.

Hot Water Entrance Flow Region:

R_e = 1285
D_h = 4.076mm
L_h = 0.1m

A dimensionless value can be obtained using the following relation:

$$\frac{L_h}{D_h} = \frac{100mm}{4.076mm} = 24.53$$

Table 6.7 Entrance Length Results of CFD Simulations in Laminar Regime (After Elbow)

Return Velocity Profile (Laminar Regime)	
Reynolds Number	L_h/D_h
21.41	3.68
85.64	6.13
214.09	12.27
428.19	15.95
856.37	19.63
1284.56	24.53

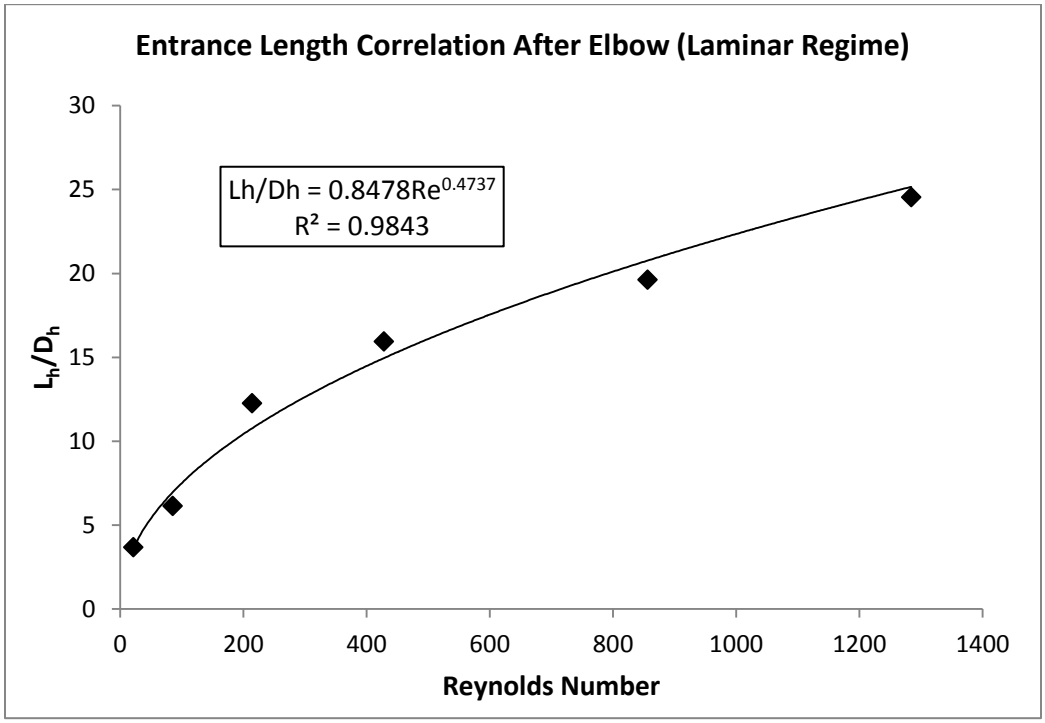

Figure 6.121 Equation Fitting to Results of CFD Simulations in Laminar Regime (After Elbow)

A Power function was fitted to the entrance length results of the CFD simulations within the laminar regime to approximate an hydrodynamic entrance length correlation after the elbow section (Figure 6.121). Table 6.7 depicts the non-dimensionalized value (Lh/Dh) for the increasing Reynolds Numbers. A coefficient of determination (R^2) value of 0.9843 was obtained.

The R^2 value of 0.9843 indicates an excellent fit, and that the associated correlation should accurately predict entrance lengths for future design purposes. Based on the results of the CFD simulations, the entrance length correlation after the elbow section of the Hot Water region under laminar flow was determined to be the following:

$$\frac{L_h}{D_h} = 0.8478 R_e^{0.4737} \quad [28]$$

Where:

L_h = Hydrodynamic Entrance Length
D_h = Hydraulic Diameter
R_e = Reynolds Number

Increasing Reynolds Numbers resulted in increased distance of the developing region within the Hot Water section. Increased mass flow rates can cause increased forces within the flow area. This may explain the increased hydrodynamic entrance lengths observed for increasing Reynolds Numbers.

6.5.2 Entrance Length Correlation within the Turbulent Regime:

To better characterize the hydrodynamic effects of the Hot Water region, an additional entrance length correlation was determined for the turbulent regime. A literature review did not return any previous studies evaluating the entrance length of a true concentric annulus in the turbulent regime. However, the hydrodynamic entrance length is typically much shorter for the turbulent regime compared to the laminar regime, and is often not considered in the analysis of turbulent flow [20]. As such, a more detailed comparison between the studied Hot Water region semi-annulus and a true concentric annulus within the turbulent regime was not able to be made.

To determine a hydrodynamic entrance length correlation for turbulent flow, several CFD simulations were run for increasing Reynolds Numbers. Similar to the laminar analysis, entrance length correlations were determined for the inlet and after elbow sections of the Hot Water region. Again, the entrance length was determined to be when the axial velocity was 99% of the fully developed profile. Similar to the laminar regime analysis, the axial velocity was plotted along a centerline of the flow area with increasing distance into the Hot Water region. Refer to Figure 6.104 for the centerline cross section and length profile used to plot the axial velocity at the inlet section of the Hot Water region. For this analysis, only the 0.6m heat exchanger was considered. The Reynolds Number for each volumetric flow rate evaluated was calculated using (Eqs. [20] and [21]). The boundary conditions used for the CFD simulations to determine the entrance length correlation within the turbulent regime are given in Table 6.8. Figures 6.122 – 6.126 depict the axial velocity profiles for increasing Reynolds Number at the inlet of the Hot Water region.

Table 6.8 Boundary Conditions Used for Entrance Length Determination Under Turbulent Flow

Heat Exchanger Length [m]	Hot Water Volumetric Flow Rate [ml/min]	Mean Fluid Velocity [m/s]	Reynolds Number	Hot Water Outlet Pressure [atm]
0.6	500	0.34	2140.93	1.0
0.6	1000	0.67	4281.86	1.0
0.6	1500	1.01	6422.78	1.0
0.6	2000	1.35	8563.71	1.0
0.6	2500	1.68	10704.64	1.0

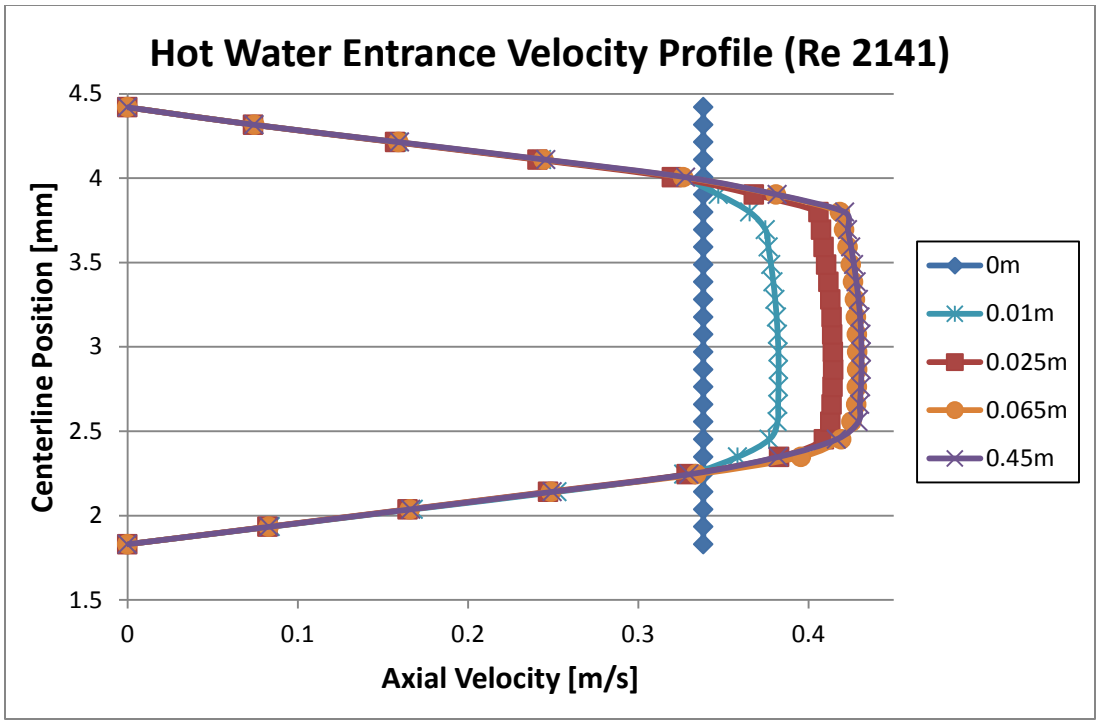

Figure 6.122 Axial Velocity Profile of Developing Region at Hot Water Inlet (Re 2141)

Based on the cross section axial velocity profile of the Hot Water inlet section, it was determined that the flow becomes fully developed at approximately 0.065m from the entrance. As such, the entrance length (L_h) was determined to be 0.065m for a Reynolds Number of 2141.

Hot Water Entrance Flow Region:

R_e = 2141

D_h = 4.076mm

L_h = 0.065m

A dimensionless value can be obtained using the following relation:

$$\frac{L_h}{D_e} = \frac{65mm}{4.08mm} = 15.95$$

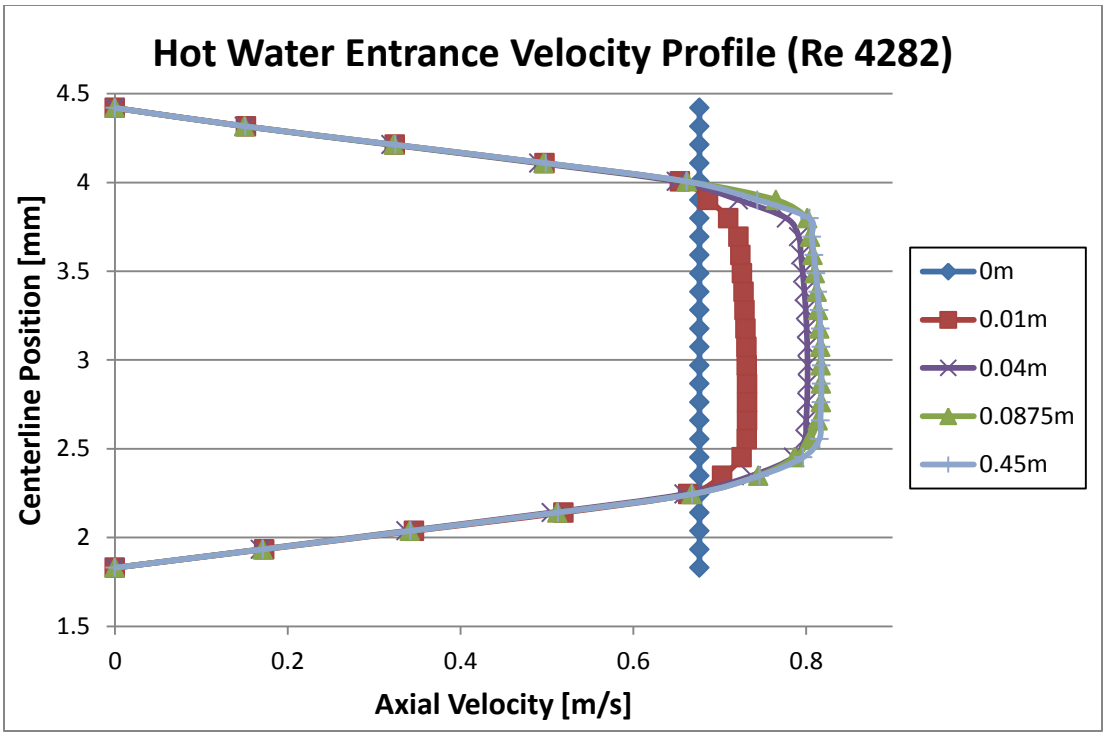

Figure 6.123 Axial Velocity Profile of Developing Region at Hot Water Inlet (Re 4282)

Based on the cross section velocity profile of the Hot Water inlet section, it was determined that the flow becomes fully developed at approximately 0.0875m from the entrance. As such, the entrance length (L_h) was determined to be 0.0875m for a Reynolds Number of 4282.

Hot Water Entrance Flow Region:

$R_e = 4282$

$D_h = 4.076mm$

$L_h = 0.0875m$

A dimensionless value can be obtained using the following relation:

$$\frac{L_h}{D_e} = \frac{87.5mm}{4.08mm} = 21.47$$

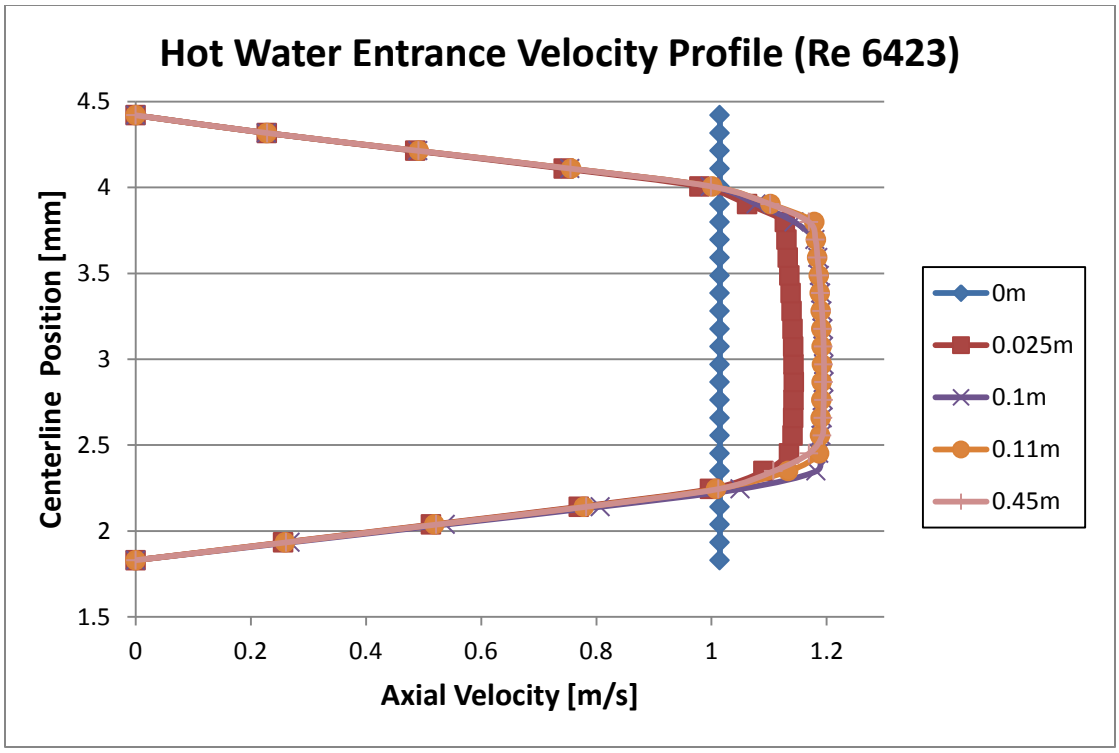

Figure 6.124 Axial Velocity Profile of Developing Region at Hot Water Inlet (Re 6423)

Based on the cross section axial velocity profile of the Hot Water inlet section, it was determined that the flow becomes fully developed at approximately 0.11m from the entrance. As such, the entrance length (L_h) was determined to be 0.11m for a Reynolds Number of 6423.

Hot Water Entrance Flow Region:

R_e = 6423
D_h = 4.076mm
L_h = 0.11m

A dimensionless value can be obtained using the following relation:

$$\frac{L_h}{D_e} = \frac{110mm}{4.08mm} = 26.99$$

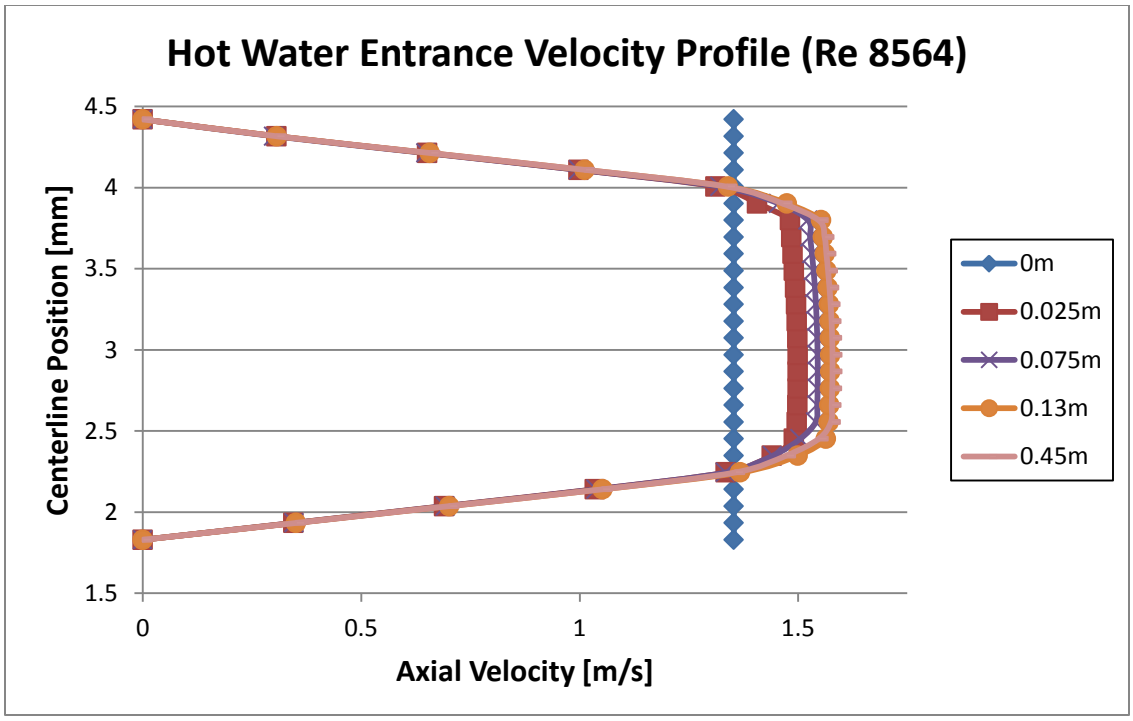

Figure 6.125 Axial Velocity Profile of Developing Region at Hot Water Inlet (Re 8564)

Based on the cross section axial velocity profile of the Hot Water inlet section, it was determined that the flow becomes fully developed at approximately 0.13m from the entrance. As such, the entrance length (L_h) was determined to be 0.13m for a Reynolds Number of 8564.

Hot Water Entrance Flow Region:

R_e = 8564

D_h = 4.076mm

L_h = 0.13m

A dimensionless value can be obtained using the following relation:

$$\frac{L_h}{D_e} = \frac{130mm}{4.08mm} = 31.89$$

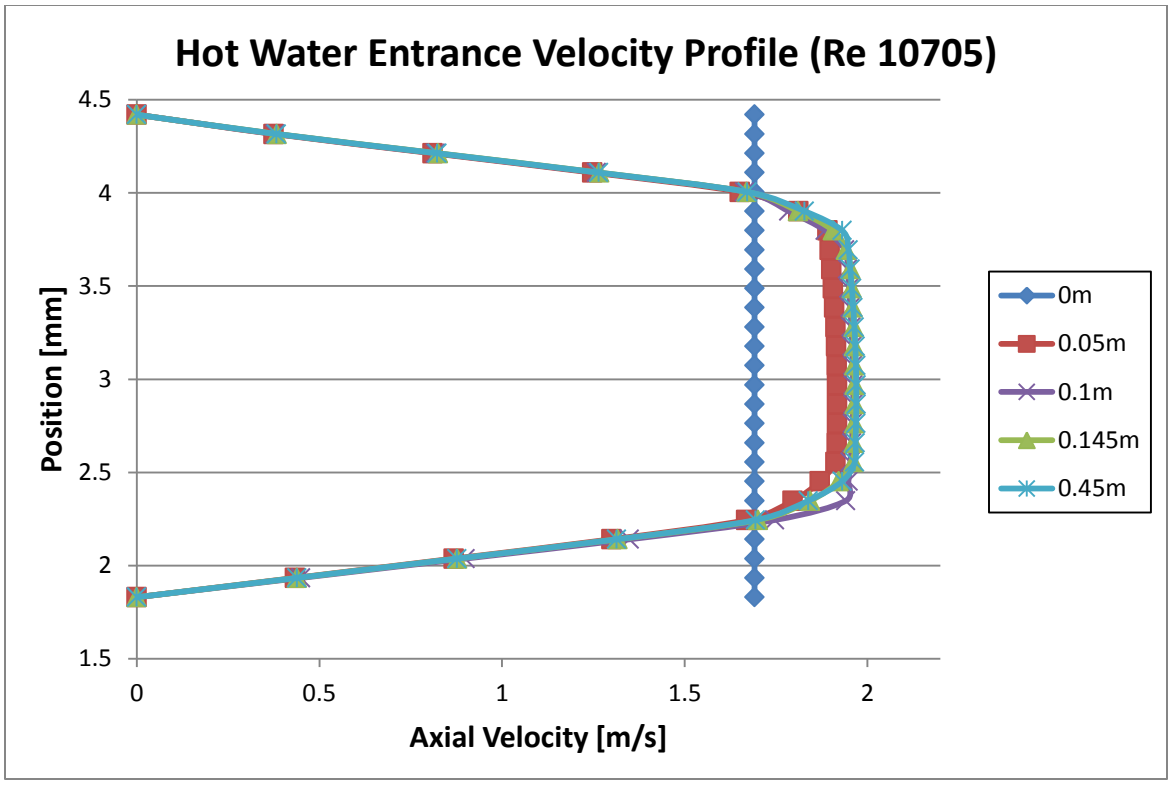

Figure 6.126 Axial Velocity Profile of Developing Region at Hot Water Inlet (Re 10705)

Based on the cross section axial velocity profile of the Hot Water inlet section, it was determined that the flow becomes fully developed at approximately 0.145m from the entrance. As such, the entrance length (L_h) was determined to be is 0.145m for a Reynolds Number of 10705.

Hot Water Entrance Flow Region:

R_e = 10705

D_h = 4.076mm

L_h = 0.145m

A dimensionless value can be obtained using the following relation:

$$\frac{L_h}{D_e} = \frac{145mm}{4.08mm} = 35.57$$

Table 6.9 Entrance Length Results of CFD Simulations in Turbulent Regime (At Inlet)

Entrance Velocity Profile (Turbulent Regime)	
Reynolds Number	L_h/D_h
2141	15.95
4282	21.47
6423	26.99
8564	31.89
10705	35.57

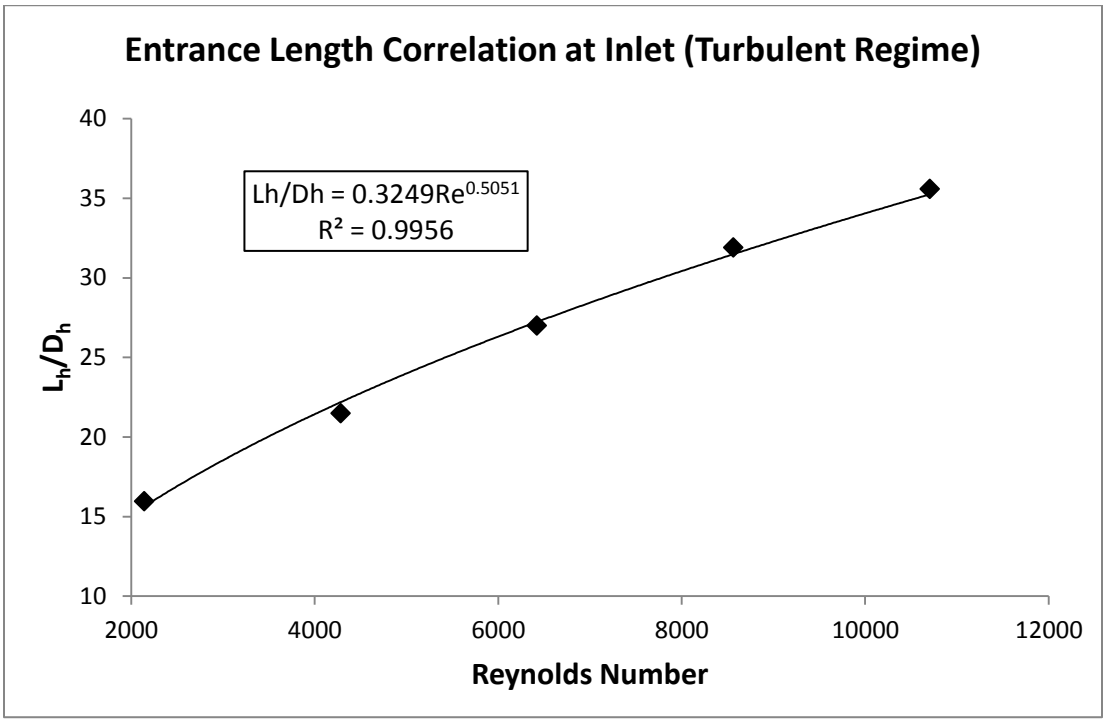

Figure 6.127 Equation Fitting to Results of CFD Simulations in Turbulent Regime (At Inlet)

A Power function was fitted to the entrance length results of the CFD simulations within the turbulent regime to approximate an entrance length correlation (Figure 6.127). Table 6.9 depicts the non-dimensionalized value (Lh/Dh) for the increasing Reynolds Numbers. A coefficient of determination (R^2) value of 0.9956 was obtained. The R^2 value of 0.9956 indicates an excellent fit, and that the associated correlation should accurately predict entrance lengths

for future design purposes. Based on the results of the CFD simulations, the entrance length correlation at the inlet of the Hot Water entrance region under turbulent flow was determined to be the following:

$$\frac{L_h}{D_h} = 0.3249 R_e^{0.5051} \quad [29]$$

Where:

L_h = Hydrodynamic Entrance Length
D_h = Hydraulic Diameter
R_e = Reynolds Number

Increasing Reynolds Numbers resulted in increased distance of the developing region within the Hot Water section. Increased mass flow rates can cause increased forces within the flow area and turbulent fluctuations. This may explain the increased hydrodynamic entrance lengths observed for increasing Reynolds Numbers.

In addition to the hydrodynamic entrance length at the inlet of the Hot Water region, an entrance length correlation was determined for the section immediately after the elbow under turbulent flow. Again, the entrance length was determined to be when the axial velocity was 99% of the fully developed profile. The axial velocity was plotted along a centerline of the flow area with increasing distance into the Hot Water return region. Refer to Figure 6.114 for the centerline cross section and length profile used to plot the axial velocity profile. Figures 6.128 – 6.132 depict the return axial velocity profiles for increasing Reynolds Number. The same boundary conditions used to determine the entrance length correlation at the inlet were used to determine the entrance length correlation after the elbow (Table 6.8).

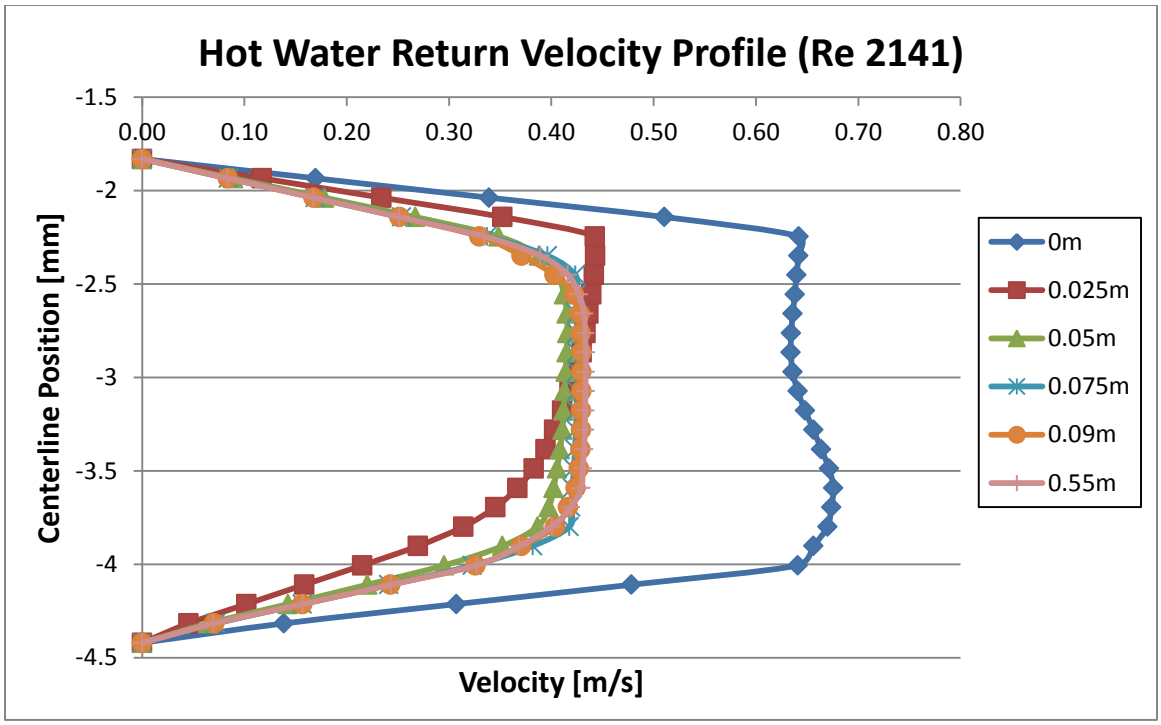

Figure 6.128 Axial Velocity Profile of Developing Region at Hot Water Elbow (Re 2141)

Based on the cross section axial velocity profile after the elbow of the Hot Water region, it was determined that the flow becomes fully developed at approximately 0.09m from the elbow. As such, the entrance length (L_h) was determined to be 0.09m for a Reynolds Number of 2141.

Hot Water Entrance Flow Region:

$R_e = 2141$

$D_h = 4.076mm$

$L_h = 0.09m$

A dimensionless value can be obtained using the following relation:

$$\frac{L_h}{D_h} = \frac{90mm}{4.08mm} = 22.08$$

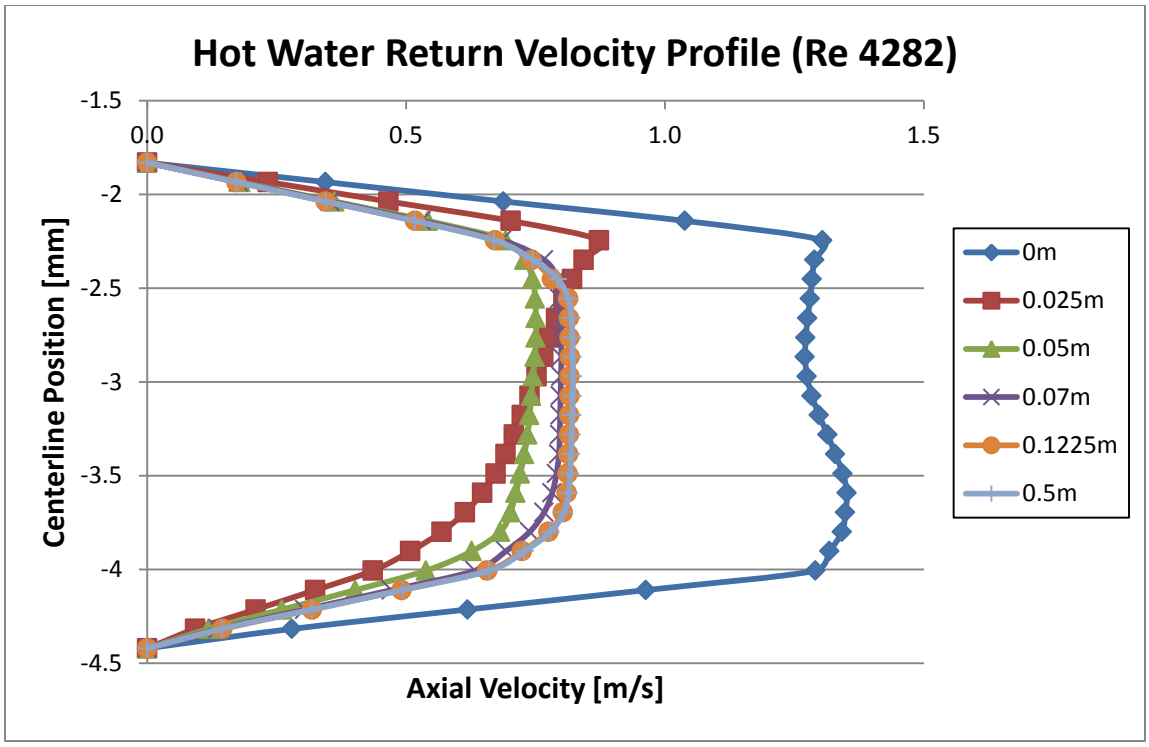

Figure 6.129 Axial Velocity Profile of Developing Region at Hot Water Elbow (Re 4282)

Based on the cross section axial velocity profile after the elbow of the Hot Water region, it was determined that the flow becomes fully developed at approximately 0.1225m from the elbow. As such, the entrance length (L_h) was determined to be 0.1225m for a Reynolds Number of 4282.

Hot Water Entrance Flow Region:

$R_e = 4282$

$D_h = 4.076mm$

$L_h = 0.1225m$

A dimensionless value can be obtained using the following relation:

$$\frac{L_h}{D_h} = \frac{122.5mm}{4.08mm} = 30.05$$

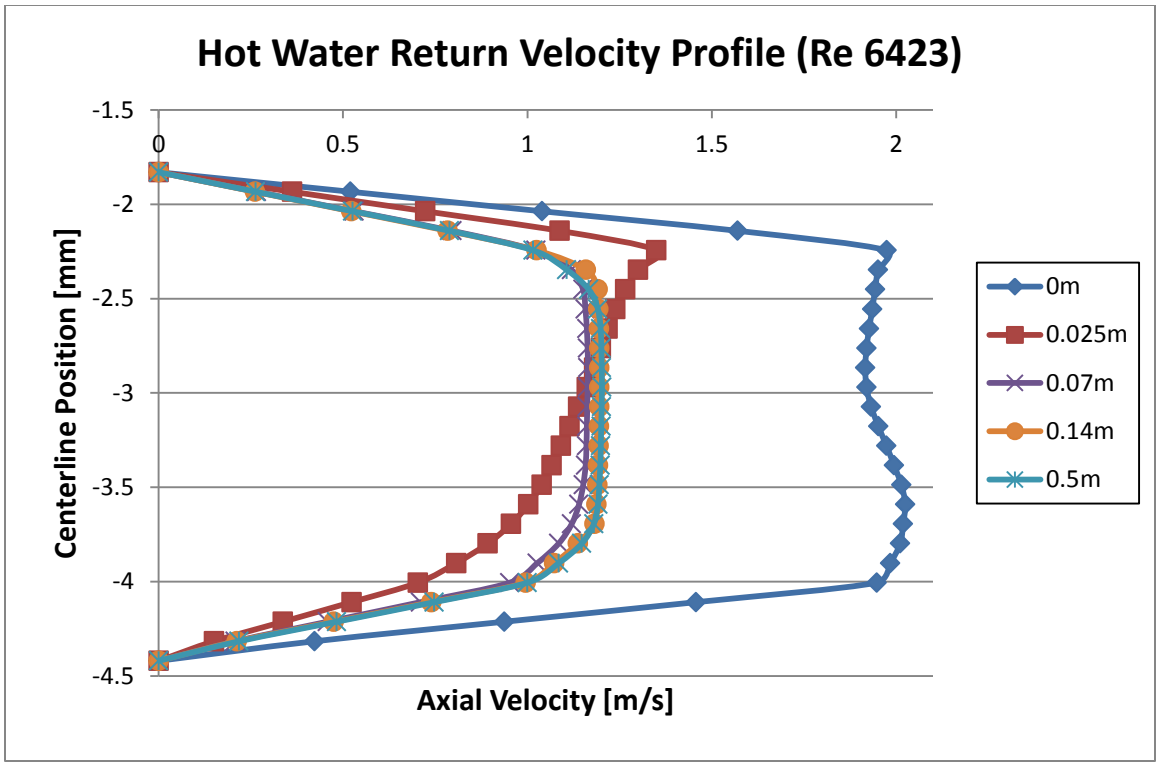

Figure 6.130 Axial Velocity Profile of Developing Region at Hot Water Elbow (Re 6423)

Based on the cross section axial velocity profile after the elbow of the Hot Water region, it was determined that the flow becomes fully developed at approximately 0.14m from the elbow. As such, the entrance length (L_h) was determined to be 0.14m for a Reynolds Number of 6423.

Hot Water Entrance Flow Region:

$R_e = 6423$

$D_h = 4.076mm$

$L_h = 0.14m$

A dimensionless value can be obtained using the following relation:

$$\frac{L_h}{D_h} = \frac{140mm}{4.08mm} = 34.35$$

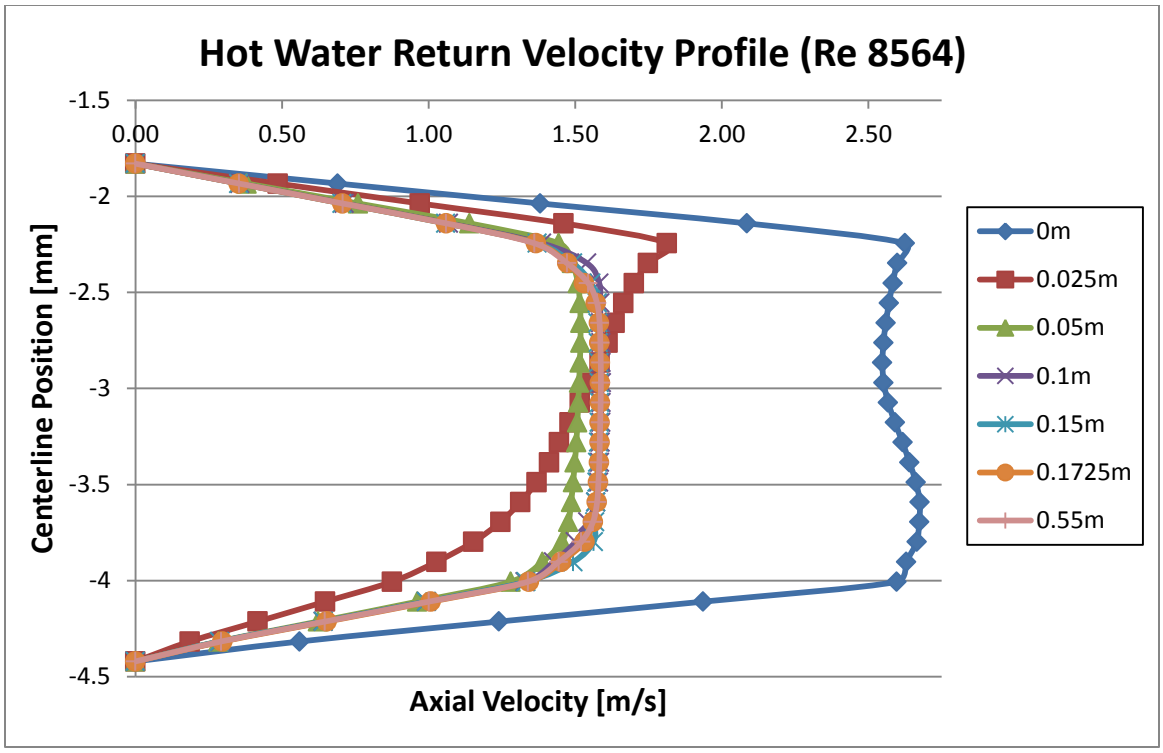

Figure 6.131 Axial Velocity Profile of Developing Region at Hot Water Elbow (Re 8564)

Based on the cross section axial velocity profile after the elbow of the Hot Water region, it was determined that the flow becomes fully developed at approximately 0.1725m from the elbow. As such, the entrance length (L_h) was determined to be 0.1725m for a Reynolds Number of 8564.

Hot Water Entrance Flow Region:

R_e = 8564

D_h = 4.076mm

L_h = 0.1725m

A dimensionless value can be obtained using the following relation:

$$\frac{L_h}{D_h} = \frac{172.5mm}{4.08mm} = 42.32$$

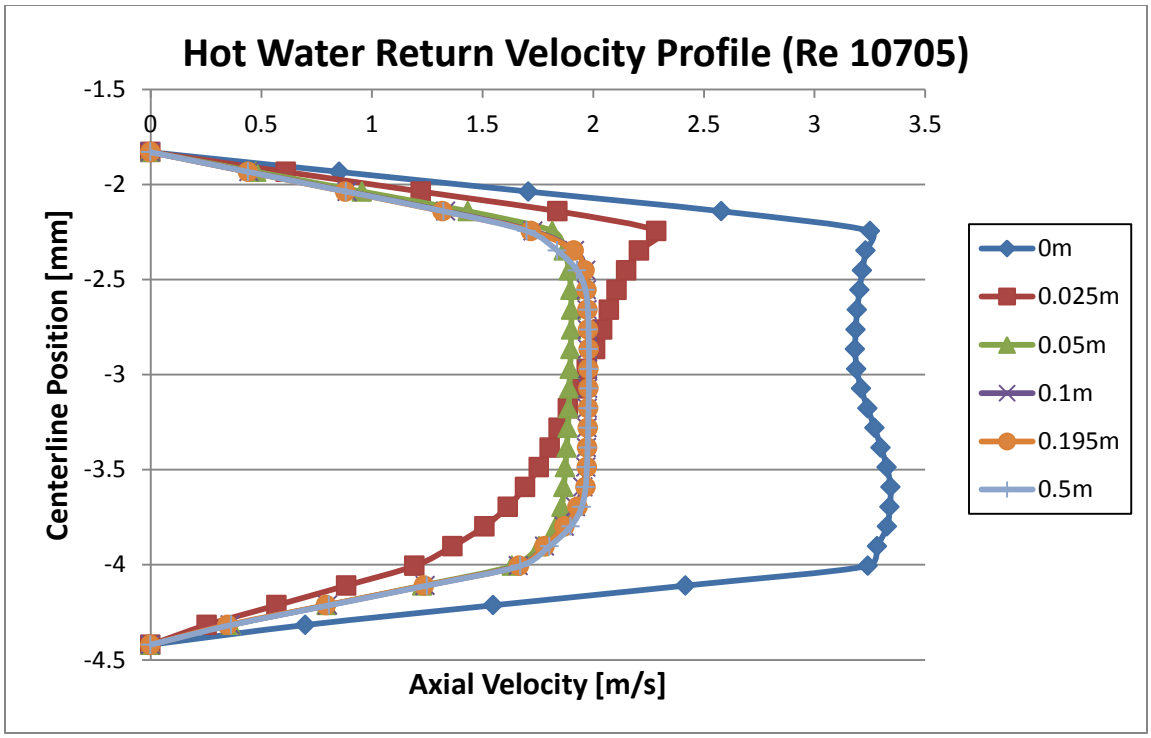

Figure 6.132 Axial Velocity Profile of Developing Region at Hot Water Elbow (Re 10705)

Based on the cross section axial velocity profile after the elbow of the Hot Water region, it was determined that the flow becomes fully developed at approximately 0.195m from the elbow. As such, the entrance length (L_h) was determined to be 0.195m for a Reynolds Number of 10705.

Hot Water Entrance Flow Region:

R_e = 10705

D_h = 4.076mm

L_h = 0.195m

A dimensionless value can be obtained using the following relation:

$$\frac{L_h}{D_h} = \frac{195mm}{4.08mm} = 47.84$$

Table 6.10 Entrance Length Results of CFD Simulations in Turbulent Regime (After Elbow)

Return Velocity Profile (Turbulent Regime)	
Reynolds Number	L_h/D_h
2141	22.08
4282	30.05
6423	34.35
8564	42.32
10705	47.84

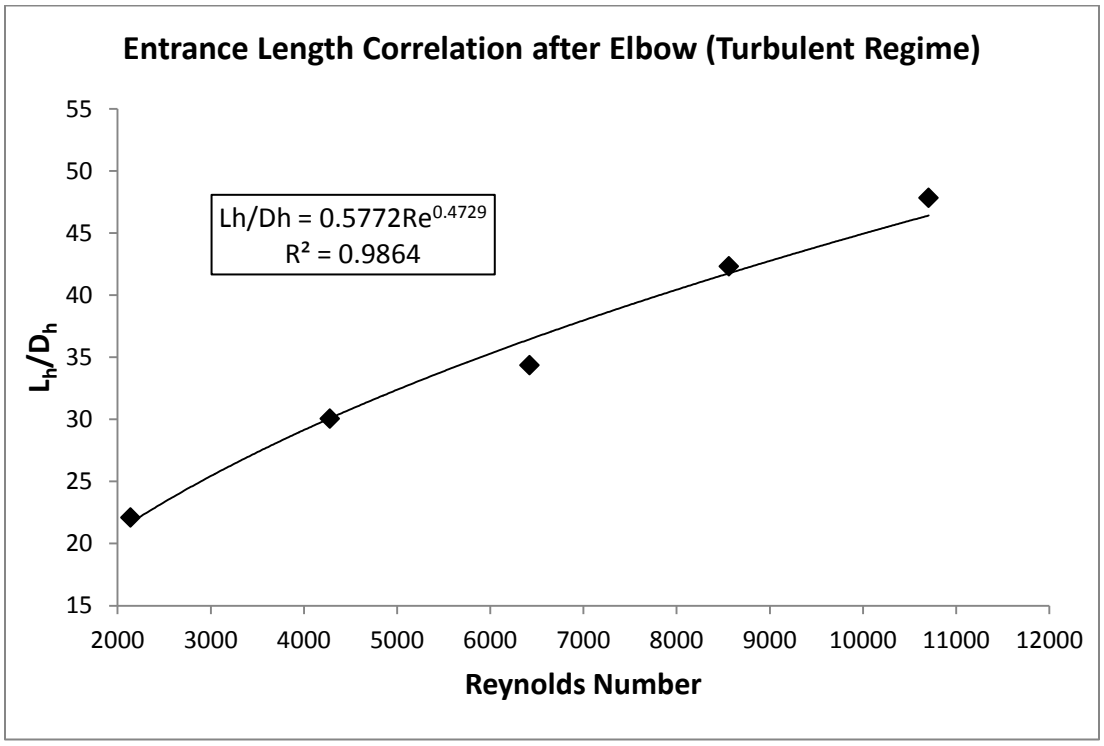

Figure 6.133 Equation Fitting to Results of CFD Simulations in Turbulent Regime (After Elbow)

A Power function was fitted to the entrance length results of the CFD simulations within the turbulent regime to approximate an entrance length correlation (Figure 6.133). Table 6.10 depicts the non-dimensionalized value (Lh/Dh) for the increasing Reynolds Numbers. A coefficient of determination (R^2) value of 0.9864 was obtained. The R^2 value of 0.9864 indicates

an excellent fit, and that the associated correlation should accurately predict entrance lengths for future design purposes. Based on the results of the CFD simulations, the entrance length correlation after the elbow of the Hot Water entrance region under turbulent flow was determined to be the following:

$$\frac{L_h}{D_h} = 0.5772 R_e^{0.4729} \quad [30]$$

Where:

L_h = Hydrodynamic Entrance Length
D_h = Hydraulic Diameter
R_e = Reynolds Number

Increasing Reynolds Numbers resulted in increased distance of the developing region within the Hot Water section. Increased mass flow rates can cause increased forces within the flow area and turbulent fluctuations. This may explain the increased hydrodynamic entrance lengths observed for increasing Reynolds Numbers.

6.6 Evaluation of Pressure Drop within Hot Water Region

To further characterize the hydrodynamic properties of the unique Hot Water geometry, pressure drop was evaluated axially within the Hot Water region. Pressure drop was evaluated for the studied semi-annular geometry of the Hot Water region using CFD simulations and compared to the properties of a true concentric annulus under similar boundary conditions. The hydrodynamic properties were evaluated under both laminar and turbulent flow.

6.6.1 Pressure Drop within the Laminar Regime

Pressure drop was evaluated for similar Reynolds Numbers for both the true concentric annulus and studied Hot Water region semi-annulus. Similar dimensions for the concentric annulus and studied semi-annulus were used (Refer to figure 6.112). The Reynolds Numbers for

the true concentric annulus were determined using (Eq. [20]). The hydraulic diameter of the true concentric annulus was determined using (Eq. [24]). Table 6.11 gives the boundary conditions used for the true concentric annulus pressure drop calculation. Table 6.12 gives the boundary conditions used for the CFD evaluation of pressure drop within the Hot Water region (semi-annulus) of the studied heat exchanger. The length of the heat exchanger evaluated was 0.6m. However, due to the unique configuration of the Hot Water region with the elbow section, the length of the Hot Water region is approximately 1.2m.

Table 6.11 Boundary Conditions for True Annulus Pressure Drop Calculation (Laminar Flow)

Dynamic Viscosity [Pa/s]	Volumetric Flow Rate [ml/min]	Mean Fluid Velocity [m/s]	Reynolds Number	Hydrodynamic Diameter [mm]
8.89×10^{-4}	8.0	0.00262	21.21	5.18
8.89×10^{-4}	32.5	0.01065	86.18	5.18
8.89×10^{-4}	81.0	0.02655	214.78	5.18
8.89×10^{-4}	161.5	0.05293	428.23	5.18
8.89×10^{-4}	323.0	0.10586	856.46	5.18
8.89×10^{-4}	484.0	0.15862	1283.36	5.18

Table 6.12 Boundary Conditions for CFD Evaluation of Pressure Drop (Laminar Flow)

Heat Exchanger Length [m]	Volumetric Flow Rate [ml/min]	Mean Fluid Velocity [m/s]	Reynolds Number	Hot Water Outlet Pressure [atm]
0.6	5	0.003	21.41	1.0
0.6	20	0.013	85.64	1.0
0.6	50	0.034	214.09	1.0
0.6	100	0.067	428.19	1.0
0.6	200	0.135	856.37	1.0
0.6	300	0.202	1284.56	1.0

To calculate the frictional pressure loss within a true concentric annulus, the following correlation was utilized for laminar flow [26]:

$$\frac{dp_f}{ds} = \frac{8\mu\bar{v}}{\left(r_o^2 + r_i^2 - \frac{r_o^2 - r_i^2}{ln\frac{r_o}{r_i}}\right)} \quad [31]$$

Where,

dp/ds = Frictional Pressure Drop with respect to Axial Length
μ = Dynamic Viscosity [Pa/s]
v = Mean Flow Velocity [m/s]
r_o = Outside Pipe Radius [m]
r_i = Inside Pipe Radius [m]

This correlation is valid within the fully developed regime. The elbow section of the studied heat exchanger results in two unique developing regions. As such, pressure drop was only considered within the fully developed velocity regions when making a comparison to the concentric annulus. Pressure drop within the true concentric annulus was calculated using (Eq. [31]). CFD simulations were run to determine the pressure drop within the studied Hot Water region. Figure 6.134 compares the pressure drop within a true concentric annulus and the studied semi-annulus under laminar flow. For the same Reynolds Numbers, the studied semi-annulus has a greater pressure drop than a true concentric annulus within the laminar regime. The flow perimeter of the studied semi-annulus is smaller than that of a true concentric annulus, resulting in increased viscous drag on the fluid. Increased viscous forces within the semi-annulus accounts for the greater pressure drop observed for the semi-annulus when compared to a true concentric annulus as a function of Reynolds Number.

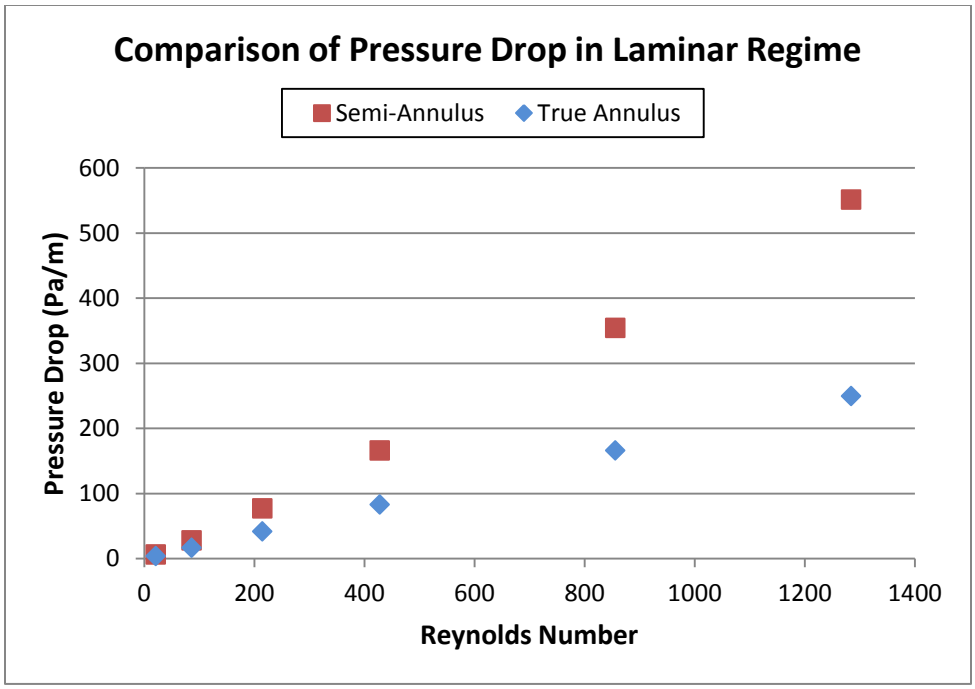

Figure 6.134 Comparison of Pressure Drop True Annulus vs. Semi-Annulus (Laminar Flow)

To further characterize the pressure drop within the Hot Water region of the studied heat exchanger, an axial pressure profile was plotted. Figure 6.135 depicts the axial positions on the heat exchanger used for the pressure measurements. Pressure was determined using surface averaged CFD data over the cross-sectional area of the Hot Water region at the specified axial locations. Figure 6.136 depicts the axial pressure profile within the Hot Water region for increasing Reynolds Number. The pressure drop along the length of the Hot Water region is approximately linear within the fully developed velocity regions. However, a more significant drop in pressure is observed at the elbow section, which is more prominent for the higher Reynolds Number flows. The elbow section of the Hot Water region creates an abrupt change in flow direction over a short distance (approximately 0.01m). This abrupt change in flow direction within the elbow generates centrifugal forces which increases shear and frictional forces resulting in the significant pressure drop observed.

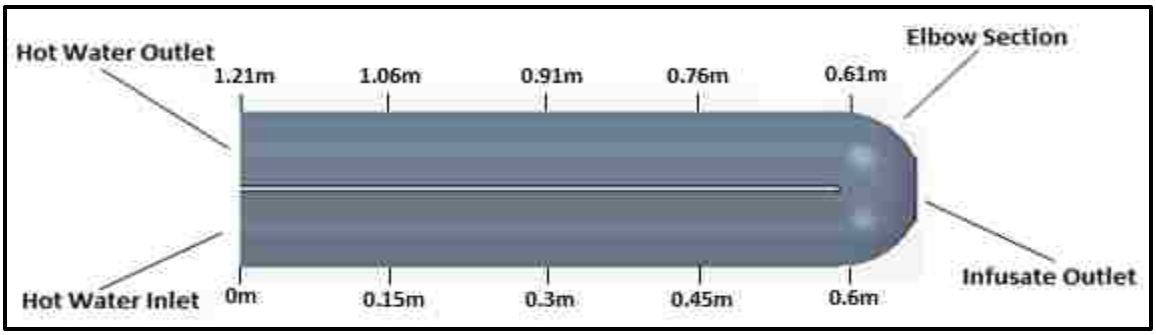

Figure 6.135 Axial Length Positions Used to Determine Axial Pressure Profile

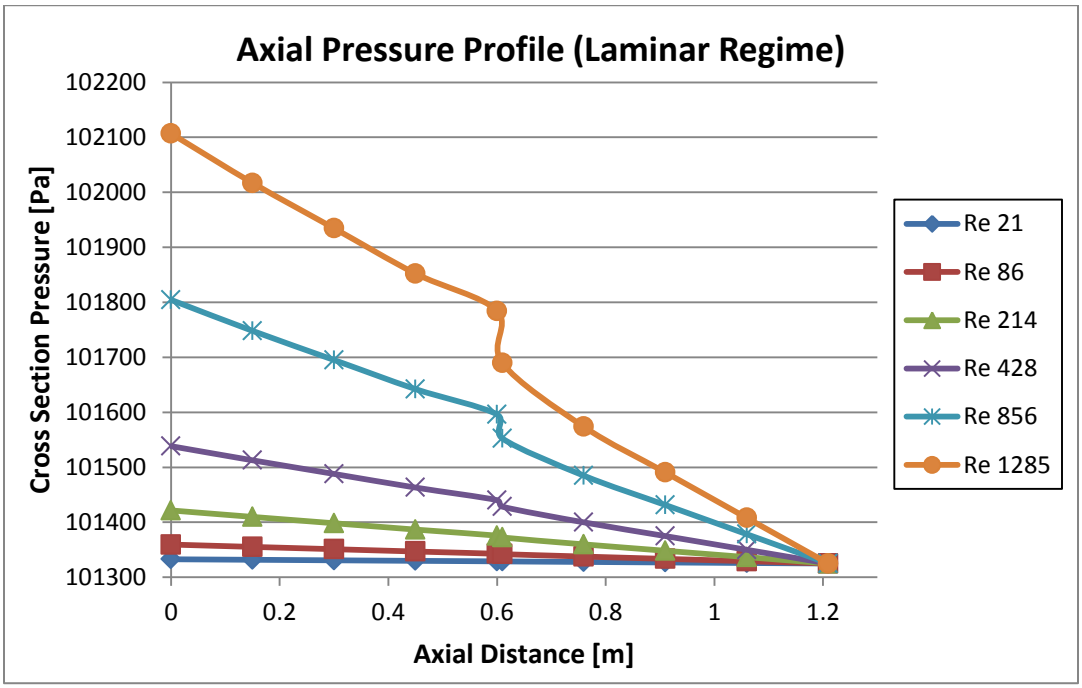

Figure 6.136 Axial Pressure Profile of Hot Water Region (Laminar Flow)

6.6.2 Pressure Drop within the Turbulent Regime

Pressure drop was evaluated for the studied annular geometry within the Hot Water region and compared to the properties of a true concentric annulus under similar boundary conditions within the turbulent regime. Pressure drop was evaluated for similar Reynolds Numbers for both the true concentric annulus and studied Hot Water region semi-annulus. Similar dimensions for the concentric annulus and studied semi-annulus were used (Refer to

figure 6.112). The Reynolds Numbers for the true concentric annulus were determined using (Eq. [20]). The hydrodynamic diameter of the true concentric annulus was determined using (Eq. [24]). Table 6.13 gives the boundary conditions used for the true concentric annulus pressure drop calculation. Table 6.14 gives the boundary conditions used for the CFD evaluation of pressure drop within the Hot Water region of the studied heat exchanger. The length of the heat exchanger evaluated was 0.6m. However, due to the unique configuration of the Hot Water region with the elbow section, the length of the Hot Water region is approximately 1.2m.

Table 6.13 Boundary Conditions for True Annulus Pressure Drop Calculation (Turbulent Flow)

Dynamic Viscosity [Pa/s]	Volumetric Flow Rate [ml/min]	Mean Fluid Velocity [m/s]	Reynolds Number	Hydrodynamic Diameter [mm]
8.89×10^{-4}	807	0.26448	2139.82	5.18
8.89×10^{-4}	1615	0.52929	4282.29	5.18
8.89×10^{-4}	2422	0.79378	6422.11	5.18
8.89×10^{-4}	3229.5	1.05842	8563.26	5.18
8.89×10^{-4}	4037	1.32307	10704.41	5.18

Table 6.14 Boundary Conditions for CFD Evaluation of Pressure Drop (Turbulent Flow)

Heat Exchanger Length [m]	Volumetric Flow Rate [ml/min]	Mean Fluid Velocity [m/s]	Reynolds Number	Hot Water Outlet Pressure [atm]
0.6	500	0.34	2140.93	1.0
0.6	1000	0.67	4281.86	1.0
0.6	1500	1.01	6422.78	1.0
0.6	2000	1.35	8563.71	1.0
0.6	2500	1.68	10704.64	1.0

To calculate the frictional pressure loss within a true annulus under turbulent flow, a modified correlation for pipe flow was utilized [26]:

$$\frac{dp_f}{ds} = \frac{0.1582\rho^{0.75}\bar{v}^{1.75}\mu^{0.25}}{{d_e}^{1.25}} \quad [32]$$

Where,

dp/ds = Frictional Pressure Drop with respect to Axial Length
μ = Dynamic Viscosity [Pa/s]
v = Mean Flow Velocity [m/s]
ρ = Fluid Density [kg/m^3]
d_e = Equivalent Diameter

The equivalent diameter for a concentric annulus is given by:

$$d_e = d_o - d_i \quad [33]$$

Where:

d_o = Outer Ring Diameter
d_i = Inner Ring Diameter

For the geometry of a concentric annulus, the equivalent diameter is equal to the hydraulic diameter. Additionally, this correlation is valid within the fully developed regime. The elbow section of the studied heat exchanger results in two unique developing regions. As such, pressure drop was only considered within the fully developed velocity regions when making a comparison to the concentric annulus. Pressure drop within the true concentric annulus was calculated using (Eq. [32]). CFD simulations were run to determine the pressure drop within the studied Hot Water region. Figure 6.137 compares the pressure drop within a true annulus and the studied semi-annulus under turbulent flow. For the same Reynolds Numbers, the studied semi-annulus has a larger pressure drop than a true concentric annulus within the turbulent regime. Again, the flow perimeter of the studied semi-annulus is smaller than that of a true concentric annulus, resulting in increased viscous drag on the fluid. Increased viscous forces within the semi-annulus accounts for the greater pressure drop observed for the semi-annulus when compared to a true concentric annulus as a function of Re. Increased viscous drag forces may also produce increased turbulent fluctuations near the wall. As such, the studied semi-

annulus would likely enter the turbulent regime at a lower Reynolds Number than a true concentric annulus.

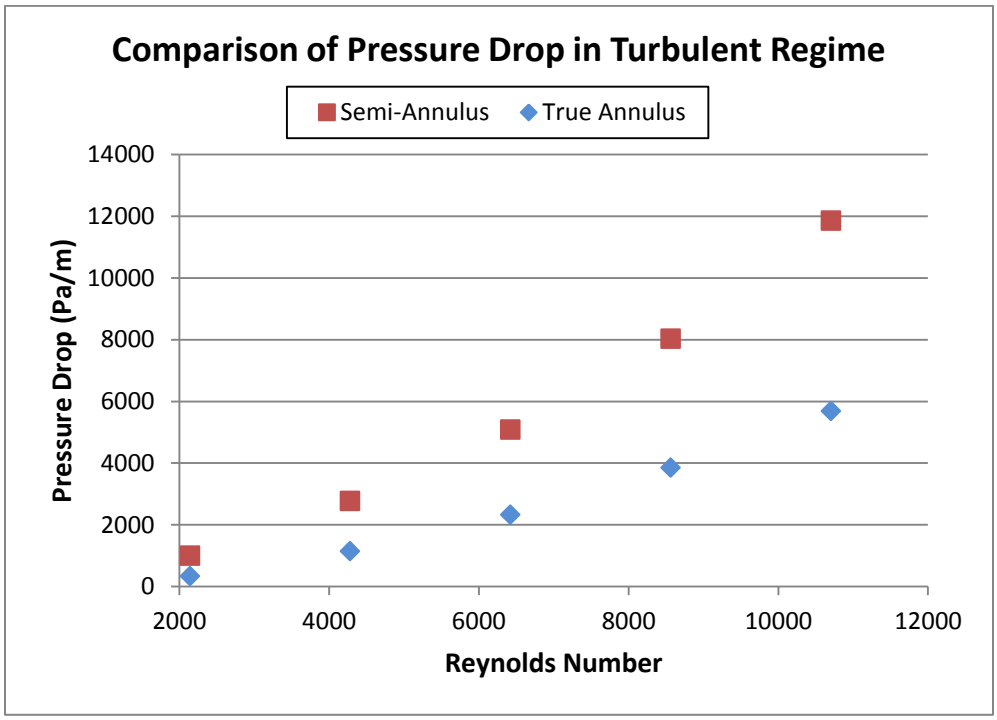

Figure 6.137 Comparison of Pressure Drop True Annulus vs. Semi-Annulus (Turbulent Flow)

To further characterize the pressure drop within the Hot Water region of the studied heat exchanger, an axial pressure profile was plotted. Refer to Figure 6.135 for the axial positions on the heat exchanger used for the pressure measurements. Figure 6.138 depicts the axial pressure profile within the Hot Water region for increasing Reynolds Number. Similar to the laminar regime, the pressure drop along the length of the Hot Water region is approximately linear within the fully developed velocity regions. However, a more significant drop in pressure is observed at the elbow section, which is more prominent for the higher Reynolds Number flows. The elbow section of the Hot Water region creates an abrupt change in flow direction over a short distance (approximately 0.01m). Again the abrupt change in flow direction

produces centrifugal forces which may account for the significant pressure drop observed in the elbow section of the Hot Water region.

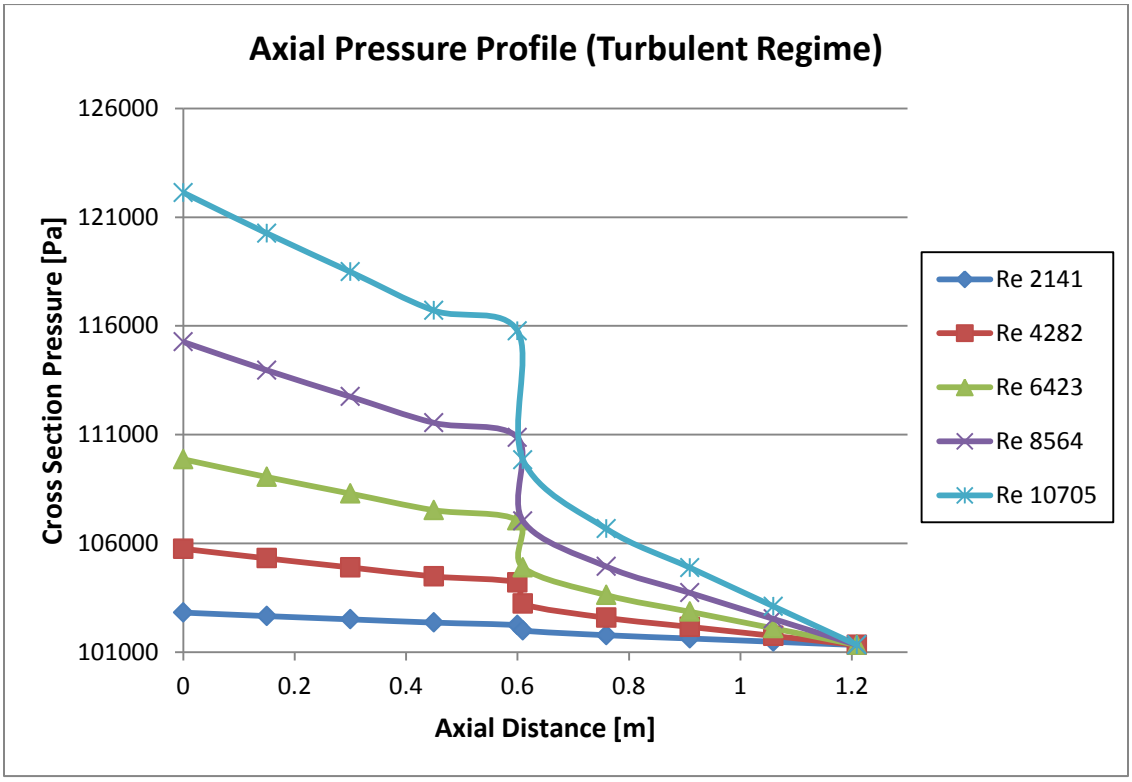

Figure 6.138 Axial Pressure Profile of Hot Water Region (Turbulent Flow)

6.7 Evaluation of Thermal Developing Length within Hot Water Region

To further characterize the thermal properties of the unique semi-annular geometry, the thermal developing length within the Hot Water region of the heat exchanger was evaluated. Only turbulent flow was considered, as the typical flow rates used in Hypothermia treatment protocols would fall into the turbulent regime.

Typically, thermal developing length can be evaluated by plotting axial temperature profiles along the length of the geometry to determine the fully developed profile. However, because heat transfer is present along the length of the heat exchanger this method is not

feasible. To determine the thermal developing length when heat transfer is present, a dimensionless temperature θ is considered [20]:

$$\theta = \frac{T_s - T_{(x,y)}}{T_s - T_m} \quad [34]$$

Where,

T_s = Surface Temperature
T_m = Mean Bulk Temperature
$T_{(x,y)}$ = Fluid Temperature at Specified Radius

The dimensionless temperature θ was evaluated along a cross section of the Hot Water region for increasing axial distance from the inlet. For the temperature value ($T_{(x,y)}$), a specified radius is chosen and evaluated downstream with increasing axial distance. Since heat transfer occurs along the length of the heat exchanger, the mean fluid temperature varies with axial distance. A fully developed temperature profile exists when θ no longer varies with increasing axial distance.

Only the 0.6m heat exchanger length was considered. The thermal developing length was evaluated for increasing Reynolds Number. Table 6.15 gives the boundary conditions used for the CFD simulations to determine the thermal developing length. The thermal developing length was evaluated at the inlet section and after the elbow section of the Hot Water region. Both sections were considered due to the parallel/counter-parallel flow arrangement of the Hot Water region.

Table 6.15 Boundary Conditions Used for Thermal Developing Length Determination

Hot Water Inlet Temperature [C]	Hot Water Volumetric Flow Rate [ml/min]	Mean Fluid Velocity [m/s]	Reynolds Number	Hot Water Outlet Pressure [atm]
41.6	500	0.34	2140.93	1.0
41.6	1000	0.67	4281.86	1.0
41.6	1500	1.01	6422.78	1.0
41.6	2000	1.35	8563.71	1.0
41.6	2500	1.68	10704.64	1.0

Figure 6.139 depicts the axial positions on the heat exchanger used for the θ calculations. Figure 6.140 and 6.141 depicts the Hot Water cross-sections used for the calculation of θ at the inlet and after elbow sections. All temperature values were evaluated at planar axial cross sections within the flow area. The mean bulk temperature (T_m) was evaluated over the cross-sectional area of the Hot Water region. The surface temperature (T_s) was evaluated as a surface average of the wall temperature at axial cross-sections along the Hot Water region. The fluid temperature ($T_{(x,y)}$), was specified as a specific point near the center of flow area and evaluated axially along the length of the heat exchanger.

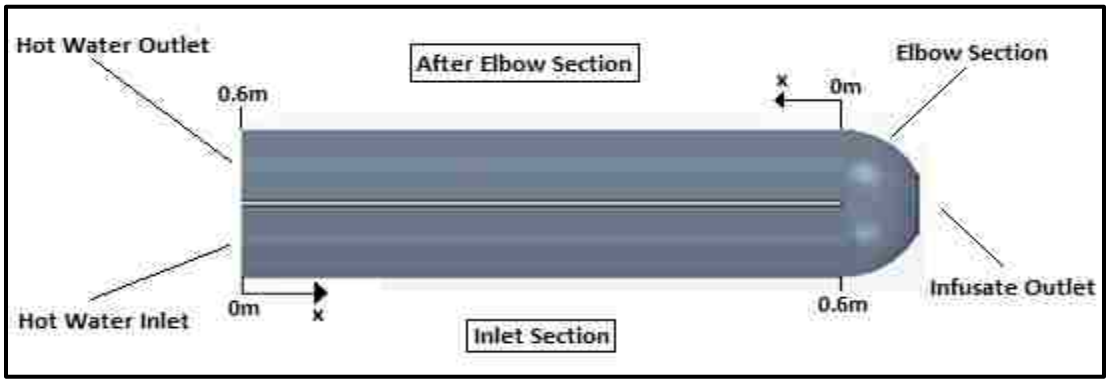

Figure 6.139 Axial Length Positions Used to Determine Dimensionless Temperature Profile

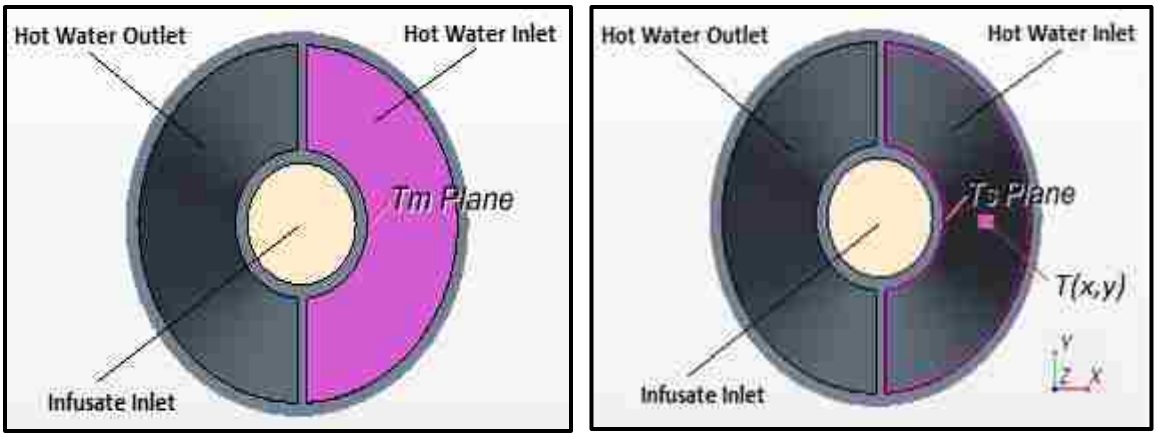

Figure 6.140 Hot Water Sections Used for Dimensionless Temperature Calculation (At Inlet)

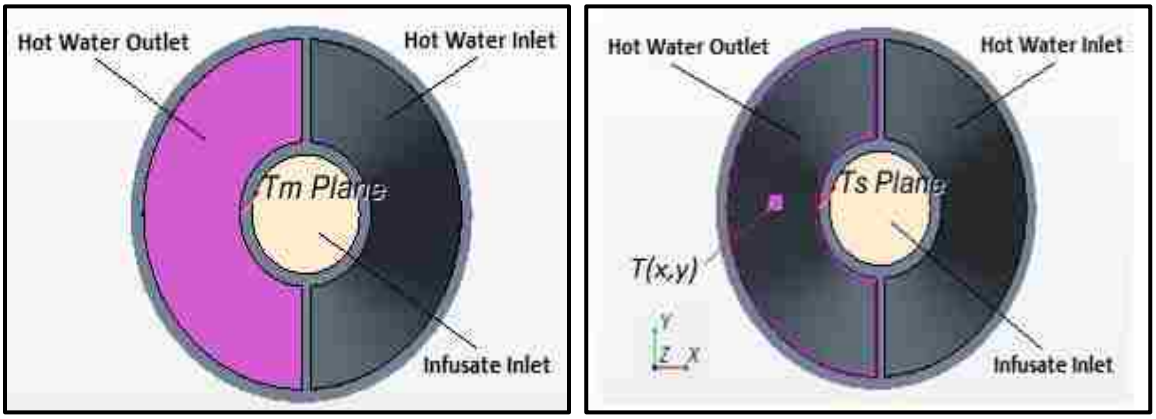

Figure 6.141 Hot Water Sections Used for Dimensionless Temperature Calculation (After Elbow)

The dimensionless temperature θ was calculated for increasing axial distance along the length of the heat exchanger. Figures 6.142-143 depict the thermal developing profile of the Hot Water region for increasing Reynolds Number. As expected, θ reached an approximate asymptotic value with increasing axial distance, or became independent of increasing axial distance. At this point the temperature profile was determined to be fully developed and described as the thermal developing length.

The thermal developing length of the Hot Water region increased with increasing Reynolds Number at both the inlet and after elbow sections. As previously mentioned, the outer-surface of the heat exchanger was specified as adiabatic and heat transfer was limited to

the temperature gradient between the Infusate and Hot Water regions. As mass flow rate increases, greater heat exchanger length is required to reach similar temperature profiles. Additionally, for lower flow rates higher outlet temperatures are expected to satisfy the basic energy balance principle. This results in the increased length of the thermal developing region observed with increasing Reynolds Number at both the inlet and after elbow sections of the Hot Water region.

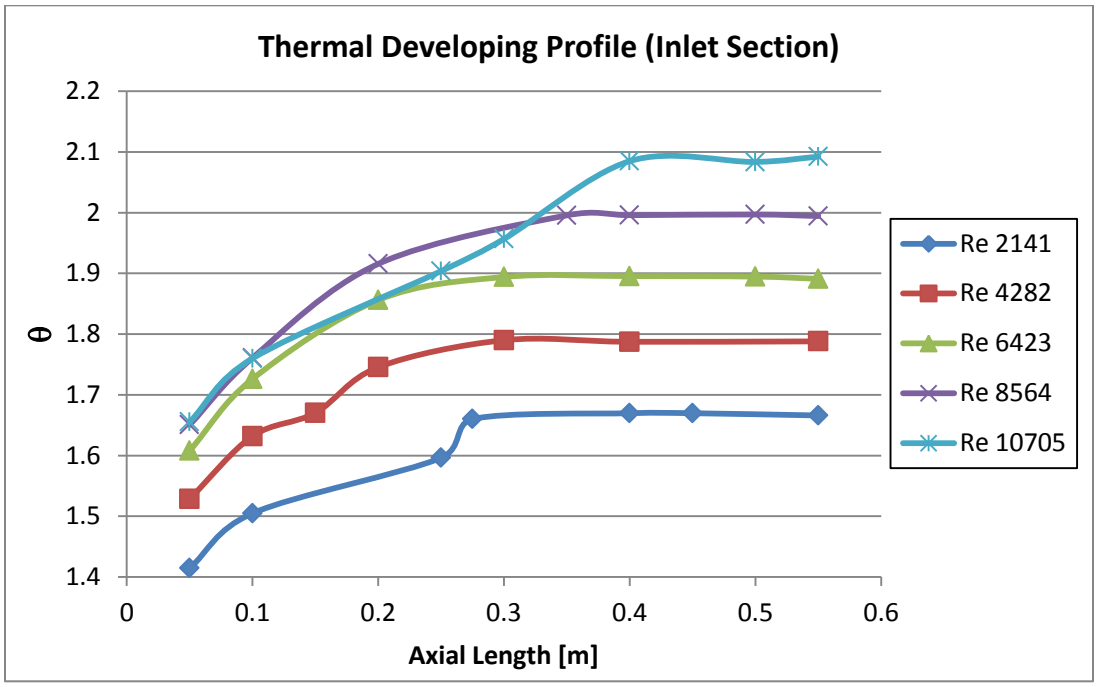

Figure 6.142 Evaluation of θ for Increasing Axial Length (At Inlet)

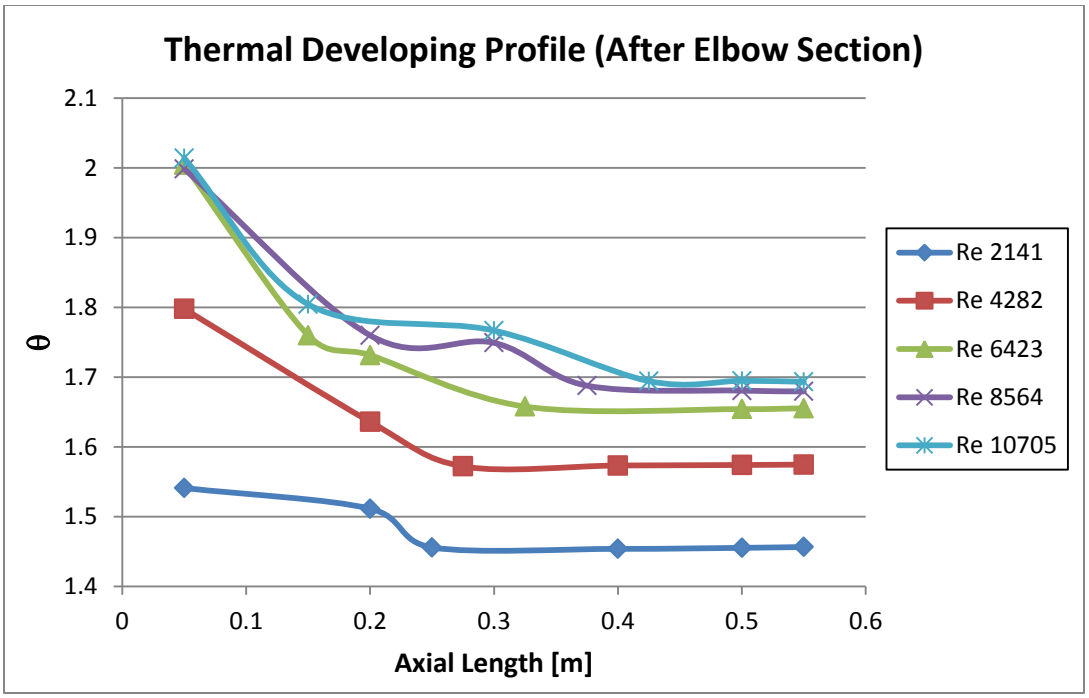

Figure 6.143 Evaluation of θ for Increasing Axial Length (After Elbow)

Figure 6.144 depicts a comparison of the CFD determined thermal developing length for the inlet and after elbow sections of the Hot Water region. The CFD simulations were conducted for the 0.6m heat exchanger with increasing Reynolds Number. Based on the CFD simulations, it appears that the thermal developing length (L_t) increases with increasing Reynolds Number at both the inlet and after elbow sections. An approximate correlation for the thermal developing length within the Hot Water region was developed using the following dimensionless relation:

$$\frac{L_t}{D_h} \qquad [35]$$

Where,

L_t = Thermal Developing Length
D_h = Hydraulic Diameter

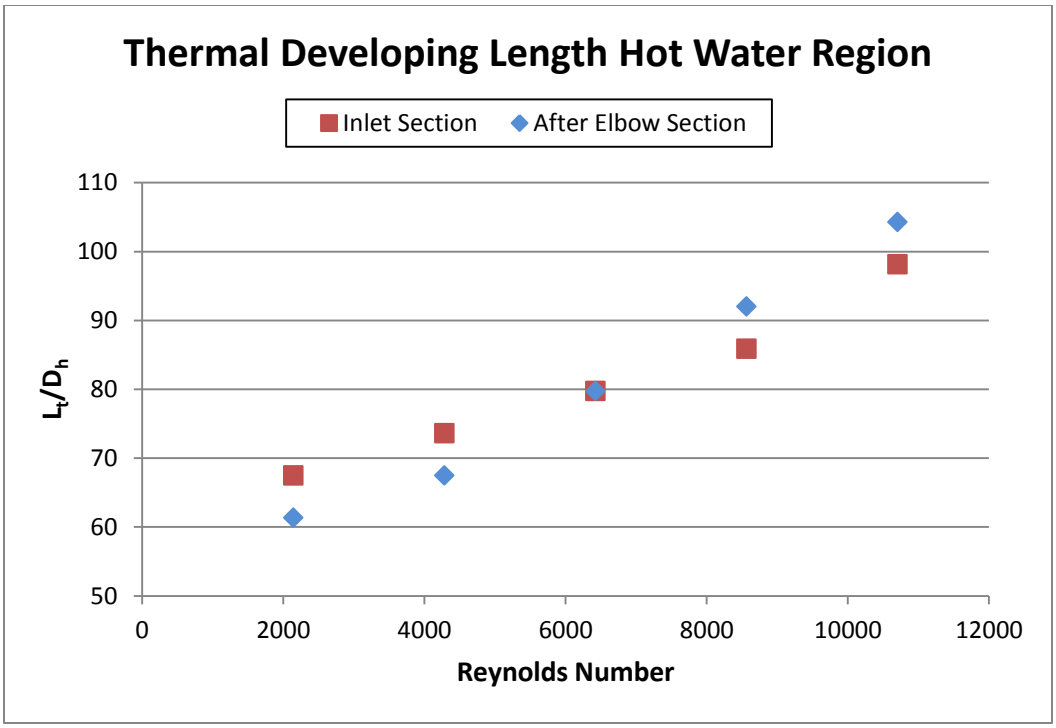

Figure 6.144 CFD Determined Thermal Developing Length for Hot Water Region

As expected, an increase in Reynolds Number (increased flow rate) results in increased thermal developing length as the hydrodynamic conditions of the flow help to stabilize and reach fully developed thermal conditions. Thermal developing lengths at the inlet section were greater than after the elbow section for Re < 6400. However, thermal developing lengths after the elbow section were greater than the inlet section for Re > 6400. Pressure drop at the elbow increases exponentially for increasing Reynolds Number. The greater thermal developing lengths observed at after elbow section is likely the result of increased centrifugal forces and circulation through the elbow which requires increased axial length to stabilize the thermal/hydrodynamic profile.

Table 6.16 Thermal Developing Length Results of CFD Simulations in Hot Water Region

Inlet Thermal Profile		After Elbow Thermal Profile	
Reynolds Number	L_t/D_h	Reynolds Number	L_t/D_h
2141	67.47	2141	61.33
4282	73.60	4282	67.47
6423	79.74	6423	79.74
8564	85.87	8564	92.00
10705	98.14	10705	104.27

A Power function was fitted to the thermal developing length results of the CFD simulations to approximate thermal developing length correlations at the inlet and after elbow sections of the Hot Water region (Figures 6.145 – 6.146). Table 6.16 depicts the non-dimensionalized value (Lt/Dh) for increasing Reynolds Numbers within the inlet and after elbow sections of the Hot Water region.

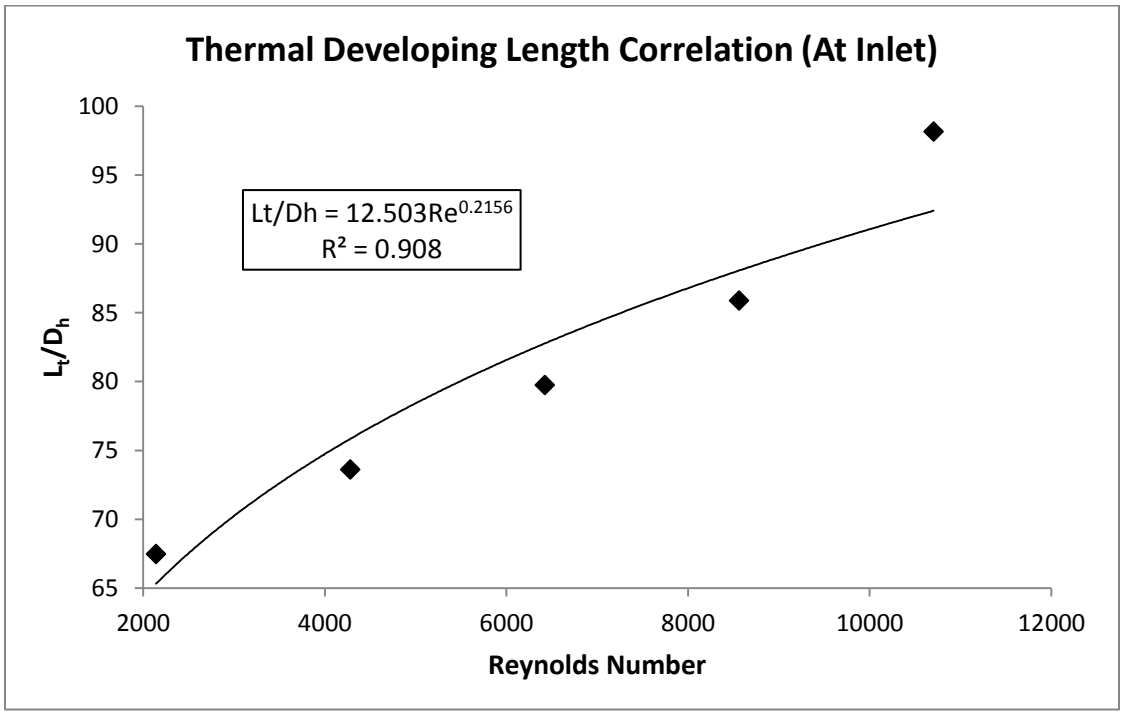

Figure 6.145 Equation Fitting to Results of CFD Simulations to Determine L_t (At Inlet)

A coefficient of determination (R^2) value of 0.908 was obtained for the correlation at the inlet section. The R^2 value of 0.908 indicates an acceptable fit, and that the associated correlation should accurately predict thermal developing lengths for future design purposes. Based on the results of the CFD simulations, the thermal developing length correlation for the inlet section of the Hot Water region under turbulent flow was determined to be the following:

$$\frac{L_t}{D_h} = 12.503 R_e^{0.2156} \quad [36]$$

Where:

L_t = Thermal Developing Length
D_h = Hydraulic Diameter
R_e = Reynolds Number

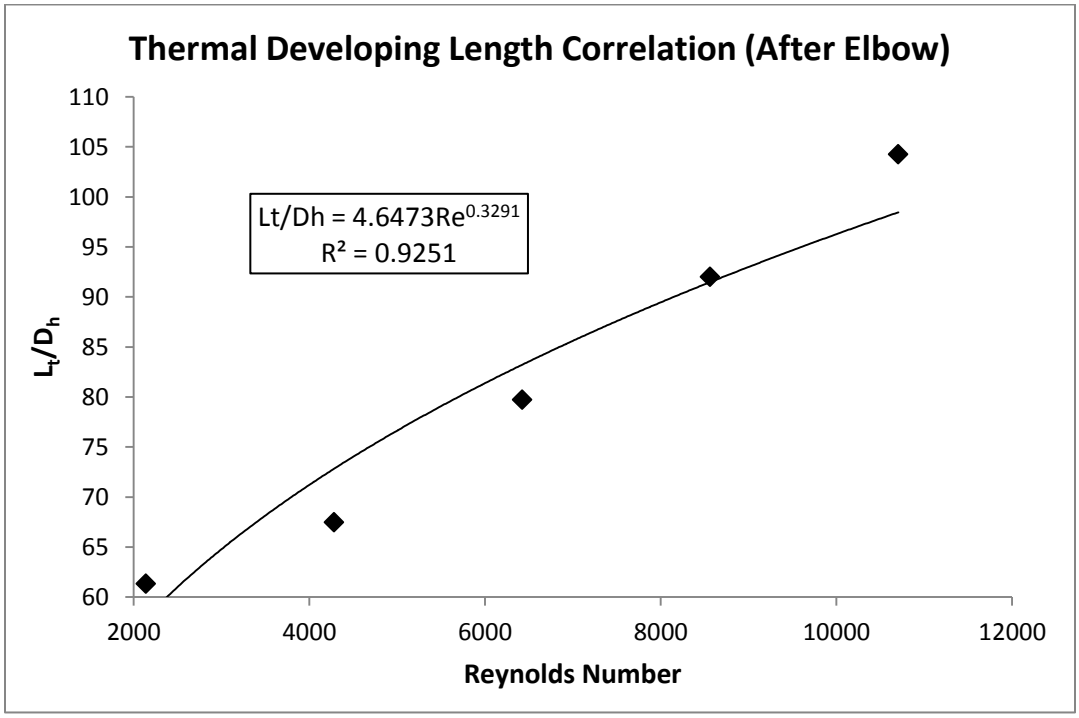

Figure 6.146 Equation Fitting to Results of CFD Simulations to Determine L_t (After Elbow)

A coefficient of determination (R^2) value of 0.9251 was obtained for the correlation after the elbow section. The R^2 value of 0.9251 indicates an acceptable fit, and that the associated correlation should accurately predict thermal developing lengths for future design purposes. Based on the results of the CFD simulations, the thermal developing length correlation after the elbow section of the Hot Water region under turbulent flow was determined to be the following:

$$\frac{L_t}{D_h} = 4.6473 R_e^{0.3291} \quad [37]$$

Where:

L_t = Thermal Developing Length
D_h = Hydraulic Diameter
R_e = Reynolds Number

CHAPTER 7

CONCLUSION

Four different lengths of the heat exchanger were evaluated (0.6m, 1.2m, 1.8m, and 2.4m) to determine the effects of heat exchanger length on the outlet temperatures. Additionally, the inlet mass flow rate of the Infusate region was evaluated to determine its effect on outlet temperatures. Temperature and velocity profiles were evaluated using commercial CFD software.

These CFD simulations demonstrate the effects of flow rate and inlet temperature on the heat transfer characteristics of the studied heat exchanger. Based on the significant temperature gradient at the Infusate outlet, more accurate temperature measurements need to be considered (specifically mean bulk temperature). The temperature difference between the center-point and walls of the Infusate outlet was as much as 13^{o}C. This may have detrimental effects on the treatment of a Hypothermic patient, as the fluids delivered may not be at the desired temperature.

This study shows that 3D CFD modeling can be used to accurately predict the outlet temperatures relative to the experimental data collected in a paper by Moujaes and Oliver [27]. Using a center-point temperature probe, the CFD simulations were within 8% of the experimental values. Additionally, bulk temperature was evaluated at the outlets using CFD modeling to more accurately represent the thermodynamic averaged temperature. However, experimental outlet temperatures were only evaluated using a center-point temperature probe, so more detailed temperature comparisons were not able to be made. Despite this difference, it was concluded that the CFD model accurately represented the thermodynamic characteristics of the heat exchanger and can be used for future design purposes.

This study also provides insight into the hydrodynamic and thermal properties within the Hot Water region, specifically related to the elbow section. Hydrodynamic Entrance length correlations were developed for the Hot Water region under laminar and turbulent flow. The CFD determined hydrodynamic entrance lengths within the studied Hot Water region (semi-annulus) were compared to that of a true concentric annulus under similar boundary conditions and laminar flow. The entrance length of a concentric annulus is generally longer than the semi-annulus within the laminar regime, and the difference is more prominent for increasing Reynolds Number. Additionally, Thermal developing length correlations were developed for the Hot Water region under turbulent flow, which demonstrated increasing thermal developing length for increasing Reynolds Numbers.

Pressure drop along the length of the Hot Water region (semi-annulus) was also evaluated and compared to pressure drop within a true concentric annulus with similar dimensions. Under both laminar and turbulent flow, the studied semi-annulus demonstrated greater pressure drop when compared to a concentric annulus. Significant pressure drop was observed at the elbow section of the Hot Water region, which is likely due to increased centrifugal forces and recirculating zones as a result of the abrupt change in flow direction.

The thermal and hydrodynamic properties revealed in the CFD simulations can be used to improve future design considerations, which may lead to improved Hypothermia treatment protocols.

7.1 Future Work

This thesis utilized some basic assumptions to simplify the analysis. Water was used as the working fluid for both the Infusate and Hot Water region. Typically, fluid warmers are used to warm IV fluid such as saline or blood. For the purpose of CAVR, blood would be the working

fluid. Future analysis should consider the thermal properties of the heat exchanger when blood is used as the working fluid.

Additionally, when considering CAVR, the flow within the Infusate region would be driven by the pumping action of the human circulatory system. Typically, the flow within the human circulatory system is intermittent due to the contraction and relaxation of the heart. It would be interesting to simulate pulsatile flow within the Infusate region to mimic the human circulatory system. Further characterization of the temperature and velocity profiles within the Infusate region would need to be considered for pulsatile flow.

This thesis developed an entrance length correlation for the Hot Water region under laminar and turbulent flow. Additionally, thermal developing length and pressure drop were evaluated within the Hot Water region. Experimental studies should be considered to verify the results of the CFD simulations in terms of the hydrodynamic and thermal properties within the Hot Water region.

REFERENCES

[1] 3M. (2014, March 24). *3M Forced Air Warming Blanket – Bair Hugger.* Retrieved from http://solutions.3m.com/wps/ portal/3M/en_US/IPD-NA/3M-Infection-Prevention/products/catalog/~?N=7570550&rt=c3

[2] Aragon, D. (1999). Temperature management in trauma patients across the continuum of care: the TEMP Group. Temperature Evaluation and Management Project. *AACN Clin Issues, 10(1),* 113-23.

[3] Bernabel, A.F., Levison, M.A., & Bender, J.S. (1992). The effects of hypothermia and injury severity on blood loss during trauma laparotomy. *Journal of Trauma, 33*, 835-839.

[4] Bondok, R.S. (2009). Hypothermia in Trauma: Fluid and Blood Warming. *Ain Shams Journal of Anesthesiology, 2,* 45-47.

[5] Boyan, C.P., & Howland, W.S. (1961). Blood temperature: a critical factor in massive transfusion. *Anesthesiology, 22*, 559-563.

[6] Bracker, M.D. (1992). Environmental and thermal injury. *Clinics Sports Medicine, 11*, 419-431.

[7] Cerny, F.J., & Burton, H.W. (2001). *Exercise Physiology for Health Care Professionals*. Champaign, IL: Human Kinetics.

[8] Chapra, S.C., & Canale, R.P. (2010). *Numerical Methods for Engineers* (6th ed.). New York: McGraw-Hill.

[9] Cincinnati Sub Zero. (2014, March 24). *Cincinnati Sub Zero Circulating Water Blanket – Blanketrol III*. Retrieved from http://www.cszmedical.com/Products/Hyper-Hypothermia.aspx

[10] Comunale, M.E. (2000). IV fluid warmers create air embolus danger. *Anesthesia Patient Safety Foundation Newsletter, 15(3),* 41-42.

[11] Dou, H.S., Khoo, B.C., & Tsai, H.M. (2010). Determining the Critical Condition for Turbulent Transition in a Full-Developed Annulus Flow. *Journal of Petroleum Science and Engineering, 73*, 41-47.

[12] Fritsch, D.E. (1995). Hypothermia in the trauma patient. *AACN Clin Issues, 6(2),* 196-211.

[13] Gentilello, L.M., Cortes. V., Moujaes, S., Viamonte, M., Malinin, L., Ho, C., & Gomez, G.A. (1990). Continuous Arteriovenous Rewarming: Experimental Results and Thermodynamic Model Simulation of Treatment for Hypothermia. *Journal of Trauma, 30(12)*, 1436-1449.

[14] Gnielinski, V. (2009). Heat Transfer Coefficients for Turbulent Flow in Concentric Annular Ducts. *Heat Transfer Engineering, 30(6),* 431-436.

[15] Gregory, J.S., Flancbaum, L., Townsend, M.C., Cloutier, C.T., & Jonasson, O. (1991). Incidence and timing of hypothermia in trauma patients undergoing operations. *Journal of Trauma, 31(6)*, 795-800.

[16] Gupta, S.C., & Garg, V.K. (1981). Developing Flow in a Concentric Annulus. *Computer Methods in Applied Mechanics and Engineering, 28,* 27-35.

[17] Heaton, H.S., Reynolds, W.C., & Kays, W.M. (1964). Heat Transfer in Annular Passages. *International Journal Heat Mass Transfer, 7*, 763-781.

[18] Incropera, F.P., Dewitt, D.P., Bergman, T.L., & Lavine, A.S. (2007). *Introduction to Heat Transfer* (1st ed.). New Jersey: John Wiley & Sons.

[19] Jayatilleke, C.L. (1969). The influence of Prandtl number and surface roughness on the resistance of the laminar sub-layer to momentum and heat transfer. *Progress in Heat and Mass Transfer, 1*, 193-330.

[20] Jiji, L.M. (2009). *Heat Convection* (2nd ed.). Germany: Springer.

[21] Jolly, B.T., & Ghezzi, T. (1992). Accidental hypothermia. *Emerg Med Clin North Am, 10(2)*, 311-327.

[22] Jongen, T. (1998). *Simulation and Modeling of Turbulent Incompressible Flows* (Doctoral Dissertation). Lausanne: EPFL.

[23] Jurkovich, G.J., Greiser, W.B., Luterman, A., & Curreri, P.W. (1987). Hypothermia in trauma victims: an ominous predictor of survival. *Journal of Trauma, 27(9),* 1019-1024.

[24] Lin, M.J., Wang, Q.W, & Tao, W.Q. (2000). Developing Laminar Flow and Heat Transfer in Annular-Sector Ducts. *Heat Transfer Engineering, 21*, 53-61.

[25] Mikhail, J. (1999). The trauma triad of death: Hypothermia, Acidosis, and Coagulopathy. *AACN Clinical Issues, 10*, 85-94.

[26] Mitchell, R.F., & Miska, S.Z. (2011) *Fundamentals of Drilling Engineering* (Vol. 12). United States: Society of Petroleum Engineers.

[27] Moujaes, S., & Oliver, D. (1998). Computer simulation of the thermal performance of a parallel/countercurrent flow heat exchanger for patient thermal comfort in medical applications. *Preceding ASME heat transfer division, 361*, 303-307.

[28] Nouar, C., Ouldrouis, M., Salem, A., & Legrand, J. (1995). Developing Laminar Flow in the Entrance Region of Annuli – Review and Extension of Standard Resolution Methods for the Hydrodynamic Problem. *International Journal Engineering Science, 33(10),* 1517-1534.

[29] Pitoni, S., Sinclair, H.L., & Andrews, P.J.D. (2011). Aspects of thermoregulation physiology. *Current Opinion in Critical Care, 17(2),* 115-121.

[30] Poole, R.J. (2010). Development-Length Requirements for Fully Developed Laminar Flow in Concentric Annuli. *Journal of Fluids Engineering, 132(6),* (4 pages).

[31] Rodi, W. (1991). *Experience with Two-Layer Models Combining the k-e Model with a One-Equation Model Near the Wall*. Paper presented at the 29th Aerospace Sciences Meeting, Reno, NV, 7-10 January AIAA 91-0216.

[32] Shih, T.H., Liou, W.W., Shabbir, A., Yang, Z., Zhu, J. (1994). A New k- Eddy Viscosity Model for High Reynolds Number Turbulent Flows -- Model Development and Validation. *NASA,* TM-106721.

[33] Sinclair, W.H., Rudzki, S.J., Leicht, A.S., Fogarty, A.L., Winter, S.K., & Patterson, M.J. (2009). Efficacy of field treatments to reduce body core temperature in hyperthermia subjects. *Medicine and Science in Sports and Exercise, 41(11),* 1984-1990.

[34] Smalley, B., Janke, R.M., & Cole, D. (2003). Exertional heat illness in Air Force basic military trainees. *Military Medicine, 168(4)*, 298-303.

[35] Smith, C.E., & Wagner, K. (2008). Principles of Fluid and Blood Warming in Trauma. *International Trauma Care, 18(1),* 71-79.

[36] Smiths Medical. (2014, March 24). *Smiths Medical Fast Flow Fluid/Blood Warmer – Level 1*. Retrieved from http://www.smiths-medical.com/catalog/fluid-warming/fast-flow/hardware/level-1-h-1200.html.

[37] Sparrow, E.M., & Lin, S.H. (1964). The Developing Laminar Flow and Pressure Drop in the Entrance Region of Annular Ducts. *Journal Fluids Engineering, 86(4),* 827-834.

[38] STAR-CCM+ user manual, version 9.02.005. CD-Adapco.

[39] Tsuei, B.J., & Kearney, P.A. (2004). Hypothermia in the trauma patient. *Injury, 35(1)*, 7-15.

[40] Zikanov, O. (2010). *Essential Computational Fluid Dynamics* (1st ed.). New Jersey: John Wiley & Sons.

VITA

Graduate College
University of Nevada, Las Vegas

Alex J. Heller

Degrees:

Bachelor of Science, Mechanical Engineering, 2009
University of Nevada Reno

Special Honors and Awards:

Engineering Intern (EI), OT6100
Inducted Tau Beta Pi National Engineering Honor Society, 2013

Thesis Title: CFD Simulation of the Thermal Performance of a Parallel Counter-Parallel Flow Heat Exchanger for the Treatment of Hypothermia

Thesis Examination Committee:

Chairperson, Dr. Samir F. Moujaes, Ph.D.
Committee Member, Dr. Alexander Barzilov, Ph.D.
Committee Member, Dr. Hui Zhao, Ph.D.
Graduate Faculty Representative, Dr. Moses Karakouzian, Ph.D.